U.S. DEPARTMENT OF ENERGY

PNNL-20472

Prepared for the U.S. Department of Energy
Under Contract DE-AC05-76RL01830

BIOSYNGAS TO ALCOHOL CATALYST IMPROVEMENT PROJECT

Final Report for CRADA No. PNNL/297 with Range Fuels, Inc.

MA Lilga
KO Albrecht
A Andersen
MH Engelhard
RT Hallen
CJ Howard
SM Kathmann
G Li
D Mei
KK Ramasamy
LV Saraf
JJ Strohm
T Varga
ED Walter
C Wang
JL White

June 2011

Pacific Northwest NATIONAL LABORATORY

DISCLAIMER

PACIFIC NORTHWEST NATIONAL LABORATORY
operated by
BATTELLE
for the
UNITED STATES DEPARTMENT OF ENERGY
under Contract DE-AC05-76RL01830

Printed in the United States of America

Available to DOE and DOE contractors from the Office of Scientific and Technical Information,
P.O. Box 62, Oak Ridge, TN 37831-0062
www.osti.gov
ph: (865) 576-8401
fax: (865) 576-5728
email: reports@osti.gov

Available to the public from the National Technical Information Service
5301 Shawnee Rd., Alexandria, VA 22312
ph: (800) 553-NTIS (6847)
or (703) 605-6000
email: info@ntis.gov
Online ordering: http://www.ntis.gov

PNNL-20472

BIOSYNGAS TO ALCOHOL CATALYST IMPROVEMENT PROJECT

Final Report for CRADA No. PNNL/297
with Range Fuels, Inc.

MA Lilga
KO Albrecht
A Andersen
MH Engelhard
RT Hallen
CJ Howard
SM Kathmann
G Li
D Mei
KK Ramasamy
LV Saraf
JJ Strohm
T Varga
ED Walter
C Wang
JL White

June 2011

Prepared for
the U.S. Department of Energy
under Contract DE-AC05-76RL01830

Pacific Northwest National Laboratory
Richland, Washington 99352

Executive Summary

Biofuels have garnered a high level of recent attention as a replacement for petroleum-based liquid transportation fuels and to potentially mitigate the effects of anthropogenic global warming. Ethanol is a biofuel that has found wide application as a blendstock to petroleum-based gasoline. Currently, ethanol is produced by the fermentation of sugars, which limits the feedstocks to crops such as corn and sugarcane. Alternatively, mixed alcohols, including ethanol and longer chain alcohols suitable as gasoline blendstocks or stand-alone fuels, could be produced thermochemically via a multi-step process that could utilize a large variety of biomass feedstocks, including non-edible feeds.

MoS_2-based catalysts are being developed by Range Fuels, Inc., who have built a thermochemical biomass-to-syngas-to-alcohol fuels demonstration facility in Soperton, Georgia. Range Fuels enlisted the help of PNNL to use its expertise in catalyst characterization and computational modeling to help improve the performance of its catalyst. This report describes PNNL's characterization and modeling work and presents recommendations for improved catalyst synthesis.

The focus of the current project was two-fold: (1) characterization of several bulk Mo-Co-K sulfide mixed alcohol synthesis catalysts provided by Range Fuels and (2) DFT computational modeling of the interactions of potassium with MoS_2 and of K/MoS_2 with CO. Characterization and modeling results were used to understand catalyst behavior and modes of deactivation with the goals of:

- Increasing the selectivity of alcohols while diminishing hydrocarbon selectivity
- Improving catalyst lifetime
- Increasing catalyst activity

Characterization techniques were chosen to identify the properties of catalyst materials subjected to a variety of reaction conditions in a reactor producing mixed alcohols. Catalyst samples were obtained prior to activation; after a short activation period; after runs with methanol as co-feed both with and without H_2S; and after extended time on stream. Each sample was subjected to x-ray diffraction (XRD) testing for bulk crystalline phase identification and scanning electron microscopy/energy dispersive spectroscopy (SEM/EDS) for surface chemical analysis. Transmission electron microscopy (TEM) analysis

was performed on selected catalyst samples in order to understand the morphology of the catalysts at the tens-of-nanometers scale. X-ray photoelectron (XPS) analysis was also performed on all samples in order to gather information on the quantity of elements at the surface of the catalyst as well as to identify chemical differences in the elements through changes in the characteristic binding energies of the electrons associated with surface elements. Electron paramagnetic resonance (EPR) was performed to characterize materials containing unpaired electrons. Selected samples were also subjected to diffuse reflectance IR Fourier transform spectroscopy (DRIFTS) to probe the functionality of the catalyst. Temperature programmed experiments including reduction (TPR) and desorption (TPD) as well as CO chemisorption were also performed on selected samples.

This study identified modes of deactivation and selectivity change from alcohols to hydrocarbons for Range Fuel's K-Co-Mo-S higher alcohol synthesis catalyst. Undesirable K segregation into the catalyst binder likely increases hydrocarbon selectivity, especially for catalysts that have been on stream for a long time. Segregation of the Co promoter from the active site and clustering to other phases is expected to decrease the ethanol yield and decrease catalyst activity. The Co phases formed are inactive (Co_9S_8) or have different selectivities to products (Co_2C, Co(0)). The formation of cobalt metal is believed to be a major contributor to the increased selectivity to methane.

The catalyst composition and form may not be ideal. Only the exterior surface of the bulk catalyst appears to be used in the catalysis. This results in a lower activity than might otherwise be obtained and represents an inefficient use of expensive metal components in the catalyst. The cation-exchange material as a binder may contribute to decreased selectivity with time. Excess Co in the catalyst recipe forms Co_9S_8, one possible precursor to Co(0), a good Fischer-Tropsch catalyst.

Some steps could be taken to address the technical challenges of preventing promoter (K and Co) segregation, avoiding paths to cobalt metal, and using metals more efficiently, thereby improving the performance of the catalyst. A supported catalyst would use catalytic materials more efficiently and avoid early formation of Co_9S_8. Nearly all of the catalyst would be accessible to the syngas, minimizing the cost of materials per pound of product. Higher surface areas could be attained, increasing overall catalyst activity. Use of a binder other than Bentolite (or other cation exchange materials) could slow the loss of potassium from the active sites, thereby improving long-term activity and selectivity to ethanol. A surface-supported catalyst likely would not need a binder at all, further decreasing costs.

Careful control of the Co:Mo ratio would minimize the formation of Co_9S_8 and would minimize metal costs. Minimization of Co_9S_8 formation may also decrease formation of cobalt metal, which would decrease hydrocarbon (methane) formation. Keeping the catalyst sulfided is also an important strategy that Range Fuels is already aware of. Finally, use of mono-layer MoS_2 in the catalyst preparations could reduce the amount of potassium that intercalates, thereby decreasing the amount of cobalt metal that forms.

Implementation of these recommendations could lead to higher and more stable catalyst activities, enhancing catalyst longevity. Selectivity to ethanol would also be stabilized and methane yields decreased. Catalyst costs per pound of ethanol could be decreased by more efficiently using expensive metal catalyst components and by increasing activity.

Contents

Figures

Tables

1 Introduction

Biofuels have garnered a high level of recent attention as a replacement for petroleum-based liquid transportation fuels and to potentially mitigate the effects of anthropogenic global warming. Ethanol is a biofuel that has found wide application as a blendstock to petroleum-based gasoline. Currently, ethanol is produced by the fermentation of sugars, which limits the feedstocks to crops such as corn and sugarcane. Alternatively, mixed alcohols, including ethanol and longer chain alcohols suitable as gasoline blendstocks or stand-alone fuels, could be produced thermochemically via a multi-step process that could utilize a large variety of biomass feedstocks, including non-edible feeds. The first step in thermochemical mixed alcohol production is gasification of an organic feedstock to produce syngas, which is a mixture of CO and H_2. The syngas would subsequently be converted catalytically to higher alcohols. In order to make the thermochemical route to mixed alcohols commercially viable, several technological advancements are still required, including catalysts with greater activity and selectivity to alcohols versus hydrocarbons. Modified Fischer-Tropsch catalysts, methanol synthesis catalysts, and MoS_2 based catalysts have been investigated for mixed alcohol production.

MoS_2-based catalysts are being developed by Range Fuels, who have built a thermochemical biomass to alcohol fuels demonstration facility in Soperton, Georgia. Range Fuels enlisted the help of PNNL to use its expertise in catalyst characterization and computational modeling to help improve the performance of its catalyst. This report describes PNNL's characterization and modeling work and presents recommendations for improved catalyst synthesis.

MoS_2 has been used for decades in the gas and oil industry in the hydrodesulfurization (HDS) of sulfur-contaminant compounds such as thiophene in crude oil.[1] MoS_2 is also active for syngas conversion to hydrocarbons (primarily methane).[2] However, with the addition of basic alkali metal promoters, the MoS_2-based catalysts become more selective for the formation of linear alcohols with a high selectivity toward ethanol.[2] Early independent studies by the Dow Chemical Company[3,4] and the Union Carbide Corporation[5] suggested that both supported and unsupported MoS_2 catalysts are active for alcohol synthesis from syngas with an alcohol selectivity range of 75-90%.[6,7] Moreover, due to unique physical and chemical properties of MoS_2, MoS_2-based catalysts are sulfur-resistant, slow to coking deactivation, and have less CO_2 sensitivity compared with other catalysts for alcohol synthesis.[2]

Cobalt is another common promoter added to alkali-promoted MoS_2 catalysts. The Co has been reported to enhance and maintain selectivity to C_{2+} alcohols.[8] While studying hydrodesulfurization (HDS) catalysts, Chianelli and Berhault[9] reported that Co and Mo sulfides are immiscible but that a "symmetrical synergy" existed between the sulfide phases. This symmetrical synergy resulted in a MoS_2 crystalline phase that was surface enriched by Co sulfide in which the Co resided at the edges, but not at the basal planes, of the MoS_2 crystallites. For HDS catalysts, the optimum Co/Mo ratio was reported to be 0.10-0.30. When the Co/Mo ratio was ≥0.4, Co_9S_8 was formed[10]. Surisetty et al.[11] reported that Co addition to carbon-nanotube-supported K-Mo-S catalysts increased the number of surface Mo sites. Clearly, a K-Mo-Co sulfided catalyst for mixed alcohol production is a complex system in which the catalytically active sites are difficult to identify due to the dynamic nature of the catalyst surface.

Little is known about the exact role that alkali metal promoters play in the alcohol selectivity of MoS_2-based catalysts. Alkali-promoted Mo-based catalysts (MoS_2-based or Mo/MoO_x/Mo-C-based treated with H_2S) for alcohol synthesis have been characterized with a wide range of microscopy, spectroscopy, and diffraction characterization techniques, each providing limited insight into the complex reaction mechanism.[12-21] The results of these studies suggest that the addition of basic alkali promoters decreases the surface acidity of the catalyst, thus suppressing various side reactions such as isomerization, dehydrogenation, and coking as well as reducing the number of active sites for CO dissociation that are responsible for hydrocarbon formation.[22] The observed general trend for the alkali metal promoters in terms of increased higher alcohol production for MoS_2-based catalysts is Li < Na < K < Cs < Rb (incidentally, in order of increased basicity).[2] Light alkali metals (Li and Na) are not the most suitable MoS_2 promoters for high alcohol selectivity, and, unlike the heavy alkali metals (K, Rb, and Cs), light alkali metals are known to profoundly disrupt the 2H phase structure of MoS_2.

Potassium is typically delivered to supported or unsupported MoS_2 catalysts in salt form (e.g., K_2CO_3, KOH, K_2S, K_2SO_4, KCl), and this salt is either added as an aqueous solution or by mechanically grinding it into the MoS_2.[14] Lee et al.[14] have shown that, for certain promoter salts, such as KOH, K_2S, and K_2CO_3, the potassium spreads uniformly over the catalyst after an induction period under syngas/H_2S reactor conditions. For promoter salts with anions of strong acids, such as KCl and K_2SO_4, non-uniform spreading of potassium was observed, indicating that the salt particles largely stay intact. Lee et al. suggested that a uniform distribution of the K over the catalyst is correlated with high selectivity toward alcohol synthesis. A similar observation with a combination of X-ray photo-spectroscopy (XPS), scanning

electron microscopy (SEM), and energy dispersive spectroscopy (EDS) measurements for their (K, Cs) promoted Co-MoS_2/clay catalysts was reported by Iranmahboob et al.[12, 13, 23] Woo et al. have shown through various spectroscopic techniques (XPS, FTIR, and XPS) that intentional oxidation of the catalyst leads to T_d and C_{2v} symmetry sulfates on the MoS_2 surface. [16, 17]

In addition to molybdenum sulfide-based catalysts, related sulfided catalysts prepared from molybdenum oxides also provide insight into potential reactive surface features. Materials such as MoO_x and Mo supported on oxide or carbon supports form MoS_x phases (including 2H MoS_2) under sulfiding conditions in a syngas/H_2S atmosphere.[1] Because of the transitional nature of these Mo-based catalysts (i.e., intergrowth of intermediate domains of Mo oxides and sulfides), a variety of chemical species with oxidation state and magnetic property signatures may be present and in higher concentrations compared to catalyst materials based on MoS_2 alone. Thus, characterization of these systems can give insight into possible surface species that can influence the mechanistic understanding of higher alcohol creation. For example, electron spin resonance (ESR) and XPS studies of $MoO_3/K_2CO_3/SiO_2$ and K_2MoO_3/SiO_2 for the production of methanethiol (a potential competing product to alcohols) under syngas and H_2S atmosphere show diverse surface species. Yang et al. observed "oxo-Mo(V)", "thio-Mo(V)", and S species signatures in their ESR spectra, and S^{2-}, $[S\text{-}S]^{2-}$, S^{6+}, Mo^{4+}, Mo^{5+}, and Mo^{6+} species signatures in their XPS spectra.[24,25] They found through XPS that the K_2CO_3 promoter also enhances the sulfiding and reduction of Mo^{6+} high oxidation state species to MoS_2 and "oxo-Mo(V)" species. The creation of persulfide $[S\text{-}S]^{2-}$ and S^{2-} species is enhanced as well. These observations were confirmed in a more recent study by Chen et al. on the same catalyst system used by Yang et al. as well as a Co-doped version of the catalyst.[20] Chen et al. also noted a promotion of the water-gas-shift reaction over the potassium-promoted catalysts that they attributed to a higher Mo^{5+}/Mo^{4+} ratio.

It is generally accepted that the most catalytically active sites of MoS_2-based catalysts are located at the MoS_2(100) edge surface. Supporting this convention, previous STM experiments of thiophene adsorption on nanoparticulate, single-layered, gold-supported MoS_2 catalyst where the higher edge surface area in comparison to bulk MoS_2 coupled with DFT simulations show enhanced catalytic activity for HDS.[26] Potassium can decorate the surfaces of and, under appropriate conditions, intercalate into the interstitial space of MoS_2.[27,28] Though the intercalation may have an electronic effect on the catalytic properties of MoS_2, Fourier transform infrared spectroscopy (FTIR) studies indicate that surface

potassium provides additional CO adsorption sites and that these sites may be a key feature of this catalyst's alcohol synthesis selectivity.[14]

The focus of the current project was two-fold: (1) characterization of several bulk Mo-Co-K sulfide mixed alcohol synthesis catalysts provided by Range Fuels and (2) DFT computational modeling of the interactions of potassium with MoS_2 and of K/MoS_2 with CO. Characterization and modeling results were used to understand catalyst behavior and modes of deactivation with the goals of:

1. Increasing the selectivity of alcohols while diminishing hydrocarbon selectivity
2. Improving catalyst lifetime
3. Increasing catalyst activity

Characterization techniques were chosen to identify the properties of catalyst materials subjected to a variety of reaction conditions in a reactor producing mixed alcohols. Catalyst samples were obtained prior to activation; after a short activation period; after runs with methanol as co-feed both with and without H_2S; and after extended time on stream. Each sample was subjected to x-ray diffraction (XRD) testing for bulk crystalline phase identification and scanning electron microscopy/energy dispersive spectroscopy (SEM/EDS) for surface chemical analysis. Transmission electron microscopy (TEM) analysis was performed on selected catalyst samples in order to understand the morphology of the catalysts at the tens-of-nanometers scale. X-ray photoelectron spectroscopy (XPS) analysis was also performed on all samples in order to gather information on the quantity of elements at the surface of the catalyst as well as to identify chemical differences in the elements through changes in the characteristic binding energies of the electrons associated with surface elements. Electron paramagnetic resonance (EPR) was performed to characterize materials containing unpaired electrons. Selected samples were also subjected to diffuse reflectance IR Fourier transform spectroscopy (DRIFTS) to probe the functionality of the catalyst. Temperature programmed experiments including reduction (TPR) and desorption (TPD) as well as CO chemisorption were also performed on selected samples.

2 Experimental

2.1 Catalyst and Reference Samples

Range Fuels denoted the baseline catalyst for analysis at PNNL as RF-101. RF-101 nominally contained a 1:1 molar ratio of Mo:Co as precipitated sulfides. Ammonium tetrathiomolybdate was used as the molybdenum precursor while cobalt acetate was used for the cobalt precursor. Sulfuric acid was added to the initial solution such that precipitation occurred at a pH of 3. The Mo-Co precipitate contained 50% excess sulfur. Potassium was added to the catalyst via physical grinding in the form of K_2CO_3. A catalyst binder, which was referred to according to its commercial name as Bentolite-L, and a lubricant known as Stearotex were also added to the material prior to tableting. After tableting, RF-101 required several hours of conditioning in a mixed alcohol synthesis reactor at 280°C under 1200-1500 psig syngas in order to produce an active catalyst. Range Fuels reported that an activated catalyst had an approximate (Mo + Co)/S molar ratio of 1.7.

Table 1 reports the samples delivered to PNNL from Range Fuels for characterization. Samples of RF-101 that had been activated or subjected to mixed alcohol synthesis were air sensitive and were therefore shipped under an inert atmosphere. Range Fuels had previously observed that activated tablets of RF-101 that were exposed to air had greatly diminished crush strength. Thus, in order to maintain the physical and chemical integrity of the samples, samples were stored in an Ar glovebox at PNNL and transported only in Sample Saver™ containers from Electron Microscopy Sciences.

2.1.1 Preparation of Co_9S_8 Reference Material

A sample of Co_9S_8 was prepared in the open atmosphere for use as a reference material to aid the characterization of the samples received from Range Fuels. The sample preparation was performed according to the method employed by Liu.[29] $CoCl_2 \cdot 6H_2O$ (0.75 mmol) and $(NH_2)_2CS$ (0.75 mmol) were added to a 25 mL Teflon-lined autoclave. Next, 15 ml of hydrazine hydrate ($N_2H_4 \cdot H_2O$, 50 wt% in water) was slowly added. After stirring for several minutes, the autoclave was sealed and heated at 160°C for 24 h. The temperature inside the reactor was 162°C. The Parr reactor reached 600 psig pressure during the reaction. Upon cooling, the residual pressure was released slowly to atmospheric pressure. A black precipitate was collected by filtration and washed with ethanol followed by distilled water in sequence several times. The final product was dried in a vacuum oven at 60°C for 6 h. The material was given the sample number 11-1.

Table 1. Samples received from Range Fuels and analyzed by PNNL.

PNNL #	Range Fuels #	Description
3-1	RFCG0001-38-10	Fresh RF-101
3-2*	RFCG0001-38-13	RF-101 discharged from near the bottom of Tube 1 of K2A after about 4200 h of exposure to syngas.
3-3*	RFCG0001-38-16	RF-101 discharged from near the top of Tube 1 of K2A after about 4200 h of exposure to syngas.
3-4	RFCG0001-38-19	Catalyst discharged under moderately inert conditions from CC-400 Run 33, which involved co-feed of methanol with syngas.
3-5	RFCG0001-39-4	K_2MoS_4 reference Material
4-1	RFCG0001-48-12	CC-400 Reactor, Run 34, top of reactor, easily unloaded under inert conditions
4-2	RFCG0001-48-14	CC-400 Reactor, Run 34, bottom of reactor, unloaded under potentially less inert conditions than 4-1#.
9-1	RFCG0001-52-7	CC-400 Reactor Run 35, a reactor run with 47 ppm H_2S added and a MeOH co-feed.
9-2	RFCG0001-52-12	Nominally anhydrous K_2CO_3
9-3	Bentolite-L	Catalyst binder material packed in air.

*These samples were unloaded from the Range Fuels reactor CC-400 and stored in sealed vials under N_2, but outside the glovebox. Analyses indicated they were air oxidized on receipt.
EPR testing indicated, however, that the sample was not air oxidized

A second batch of Co_9S_8 was prepared "anaerobically." The preparation of the second batch of Co_9S_8 was performed such that after the initial mixing of the reactants and sealing of the Parr reactor, the material was only handled in an inert atmosphere. $CoCl_2 \cdot 6H_2O$ (2.25 mmol) and $(NH_2)_2CS$ (2.25 mmol) were added to a 100 mL Teflon-lined Parr reactor. Next, 45 ml of hydrazine hydrate ($N_2H_4 \cdot H_2O$, 50 wt% in water) was slowly added to the mixture. After stirring for several minutes, the autoclave was sealed and heated to an external temperature of 170°C for 24 h. The measured solution temperature inside the reactor was 162°C. The Parr reactor reached 900 psig pressure at the reaction temperature within an

hour after the experiment started. At this point the pressure relief valve (PRV) actuated and the experiment was paused.

The experiment was restarted the following day. The reactor pressure increase was closely monitored and only reached a maximum pressure of approximately 170 psig. The interior of the reactor only reached 140^{o}C. Thus, it was likely that much of the reaction had occurred previously and that the reaction most likely proceed to completion more safely at the lower temperature. The reactor was heated for 24 h total.

The autoclave was allowed to cool down to room temperature after heat treatment and the residual pressure was released slowly to reach atmospheric pressure. The autoclave was moved to the glovebox under Ar and a black precipitate was collected by filtration and washed several times with degassed absolute ethanol and distilled water in sequence. Finally, the sample was washed with methylene chloride to remove any sulfur in the product. To dry the sample, the sample container was kept open in the glove box overnight. The material was given the sample number 12-1.

2.1.2 Preparation of the Co_2C Reference Material

The Co_2C reference material was prepared according to the methods of Hofer and Peebles[30] as well as Clarke and Jack.[31] A schematic of the fixed bed tubular reactor used for the preparation is shown in Figure 1. The glass tube reactor has an inner diameter, outer diameter, and length of 0.315”, 0.395”, and 14”, respectively. Both ends of the reactor were connected to Swagelok ball valves using graphite or PTFE ferrules. The ball valves allowed the reactor to be shut for transport to the glove box for sampling and unloading under an inert atmosphere. The glass tube was vertically mounted and encased in a small tube furnace, which was controlled with a Watlow temperature controller. A thermocouple placed in the center of the oven, external to the reactor tube, was used for temperature control and readout. CO, H_2, and N_2 were plumbed to the system and fed from regulators set to about 100 psi. For safety, the CO cylinder was kept inside the fume hood and supported with the existing Unistrut framework. A pressure relief valve on the gas inlet upstream of the mass flow controller was set to 800 psi. Only one gas was fed at any given time. The system was flushed with N_2 prior to the introduction of CO or H_2. A mass flow controller was used to control the gas flow rate. A pressure relief valve was set to 2 psi and positioned between the mass flow controller outlet and the reactor tube. The system also included a gas-liquid separator on the outlet to collect any condensable water formed during reduction

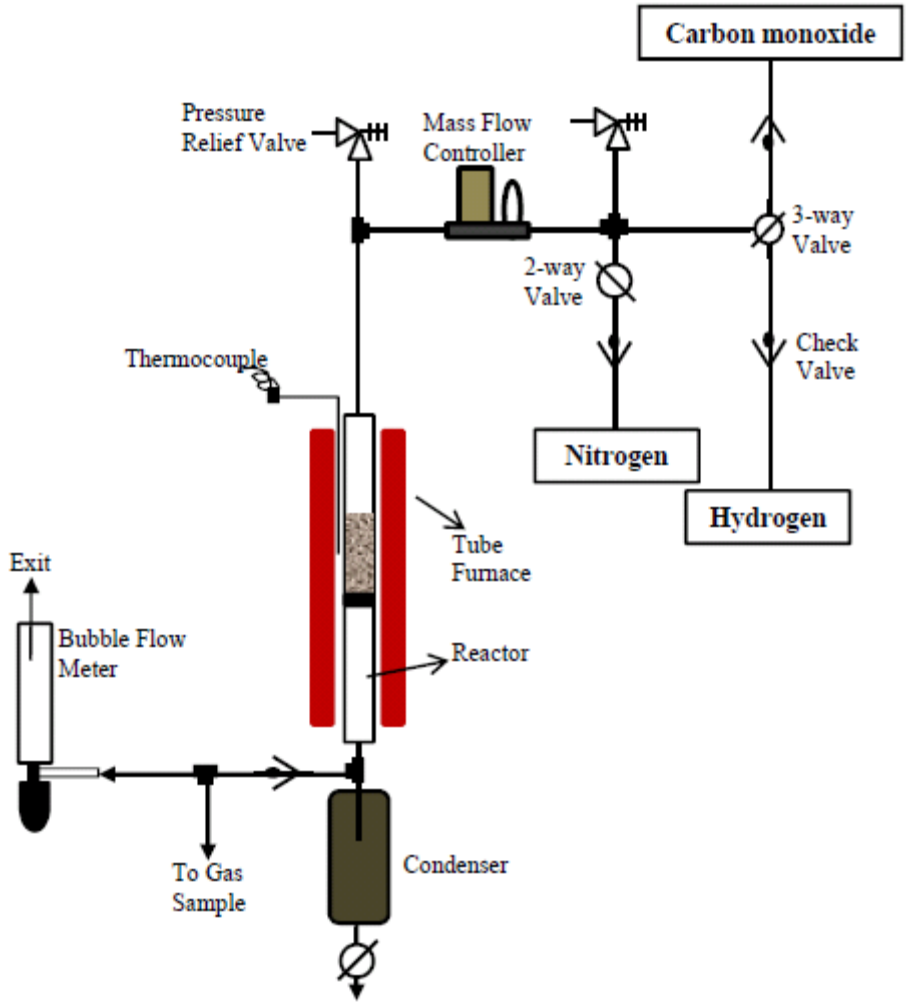

Figure 1. Process Flow Diagram for Reaction Setup to Produce Cobalt Carbide

of metal oxides. The exit gases passed a gas sampling port followed by a bubble flow meter, which measured gas flow rates, before being vented. A CO monitor with alarm was kept at the face of the fume hood any time CO was in use. Hood sashes were closed during operation to the maximum extent possible.

Cobalt (II, III) oxide (99.995%) was acquired from Sigma Aldrich. The Co (II,III) oxide (4.09 g) was first reduced under flowing H_2 at 350°C for 8 h in the tubular fixed bed reactor to produce metallic Co. Next, the metallic Co was converted to Co_2C by reaction with flowing CO (10 cm^3/min) at 243°C for 40 days. To determine the extent of the reaction from Co to Co_2C, samples were periodically drawn from the reactor in an Ar filled glove box. Material at the top of the reactor (inlet) was sampled with use of a 1.5

mm melting point capillary tube. A portion of each sample was ground and transferred to a 0.5 mm glass capillary for XRD analysis. Samples were transported for analysis under an inert atmosphere. Table 2 lists the sample numbers given to the samples of Co_2C sampled at various times as well as an overall summary of all reference materials prepared at PNNL.

Table 2. A summary of reference samples prepared at PNNL.

PNNL #	Description
	Co_9S_8 Reference Samples
11-1	Co_9S_8 prepared aerobically in the hood.
12-1	Co_9S_8 prepared anaerobically in a sealed Parr reactor and unloaded in the Ar glovebox.
	Co_2C Reference Samples
15-1	Sample drawn from the Co_2C reactor after Co oxide reduction and before carbidization.
16-1	Sample drawn from the Co_2C reactor after 4 days on stream.
17-1	Sample drawn from the Co_2C reactor after 2 weeks on stream.
18-1	Sample drawn from the Co_2C reactor after 3 weeks on stream.
18-2	Sample drawn from the Co_2C reactor after 4.5 weeks on stream.
19-1	Sample drawn from the Co_2C reactor after 6 weeks on stream.

2.2 Characterization and Computation Methods

2.2.1 SEM/EDS

Scanning electron microscopy (SEM) was used to characterize the samples received from Range Fuels as well as several reference materials. Energy dispersive spectroscopy (EDS) was utilized for chemical analysis of the samples. A dual-beam focused ion beam / scanning electron microscope (FIB/SEM) from FEI (Quanta 3D FEG) was used to analyze the surface morphology. The SEM imaging was performed using an electron beam energy of 1-5 kV in order to mitigate sample charging effects and in order to produce high resolution micrographs of the catalyst surface. The EDS analysis was acquired at 30 kV electron beam energy using analytical mode with the high current option. An electron beam energy of 30 kV was selected for EDS measurements in order to excite the Mo kα line at 17.5 keV, which would not have been possible if the lower beam energy used during SEM imaging had been used. The chemical analysis and post-processing of the data was performed using the Genesis interface from EDAX.

2.2.2 XRD

MicroXRD (x-ray diffraction) data were collected using a Rigaku D/Max Rapid II instrument with a 2D image plate detector. X-rays were generated with a MicroMax 007HF generator fitted with a rotating Cr anode (Lambda = 2.2897 Å), and focused on the specimen through a 300 μm diameter collimator. 2DP, Rigaku 2D Data Processing Software (Ver. 1.0, Rigaku, 2007) was used to integrate the diffraction rings captured by the 2-D image plate detector. The analysis of diffraction data was done using JADE 8.5 from Materials Data Inc., and the PDF4+ database from ICSD. Special care was taken not to expose the samples to air. Samples 3-1, 3-2, 3-3, 3-4, 4-1, 4-2, and 9-1 were run both as finely ground powders loaded into Kapton capillaries sealed inside the glove box as well as pellet pieces wrapped in Kapton tape inside the glove box. The pelletized samples were cut in half using a razor blade inside the glove box. Data was subsequently collected at three locations on the pellet. Samples 3-5, 11-1, 15-1, 16-1, 17-1, and 18-1 were only measured as fine powders loaded into glass capillaries. The rest of the samples (9-2, and 9-3) were not air sensitive. Hence, these powders were dispersed on a double-sided tape and measured in air. Samples were measured immediately after being taken out of the glove box. The actual XRD scans took 5 minutes.

"XRD_Sample ID_A_B" sample naming scheme was applied to the XRD analysis, where "A" refers to which pellet or sample was analyzed (A=1 for the first pellet analyzed, A=2 for the second pellet analyzed, etc), and "B" corresponds to the location of the analysis on the cross section of a complete pellet (1 = center, 2 = between center and exterior, 3 = exterior, 4 = a ground pellet or non-site specific analysis). For example, "XRD_ 3-3_2_1" refers to XRD analysis of a second pellet of sample 3-3 in the center of a cross-section of the pellet.

2.2.3 XPS

X-ray photoelectron spectroscopy (XPS) was used to acquire quantitative chemical information at the surface of the catalyst samples. Samples were received and stored inside a N_2-purged recirculated glove box. Samples were mounted for analysis inside another nitrogen recirculated glove box that operated at <1ppm O_2. The sample was pressed onto clean double sided Nichiban tape supported by 1 cm x 3 cm flat Si wafers. To minimize exposure to the atmosphere, the Si wafer pieces containing the catalysts were sealed into new VWR trace clean sample vials for the short (~1 min) transfer into the glove bag attached to the XPS system. The Si wafer substrates supporting the pellets were mounted for XPS inside a nitrogen-purged I^2R glove bag attached to the XPS sample introduction chamber. The pellets were

exposed to the glove bag environment for only about 1 to 2 minutes during the transfer into the spectrometer. The glove bag is continually purged with nitrogen (<1 ppm oxygen) from LN_2 evaporation. The oxygen concentration in the glove bag during the XPS sample mounting was measured at <30 ppm oxygen. The sample holder was then placed into the XPS vacuum introduction system and pumped to $<1x10^{-6}$ Torr using a turbomolecular pumping system prior to introduction into the main ultra high vacuum system. The main vacuum system pressure was maintained at $<5x10^{-9}$ Torr during analysis and pumped using a series of sputter ion pumps.

XPS measurements were performed using a Physical Electronics Quantum 2000 Scanning ESCA Microprobe. This system uses a focused monochromatic Al Kα x-ray (1486.7 eV) source and a spherical section analyzer. The instrument has a 16 element multichannel detector. The X-ray beam used was a 100 W, 100 μm diameter beam that was rastered over a 1.3 mm by 0.2 mm rectangle on the sample. The X-ray beam is incident normal to the sample and the photoelectron detector was at 45° off-normal. The high energy resolution photoemission spectra were collected using a pass energy of 46.95 eV. For the $Ag3d_{5/2}$ line, these conditions produced a full width at half maximum (FWHM) of 0.98 eV. The binding energy (BE) scale is calibrated using the $Cu2p_{3/2}$ feature at 932.62 ± 0.05 eV and Au 4f at 83.96 ± 0.05 eV for known standards. The sample experienced variable degrees of charging. Low energy electrons at ~1 eV, 20μA and low energy Ar^+ ions were used to minimize this charging.

2.2.4 EPR

EPR spectra were obtained with a Bruker E-580 spectrometer equipped with either a TE102 or SHQE resonator, which were considered to be equivalent for the analyses performed. The spectrometer was also equipped with an Oxford 935 variable temperature cryostat. Samples were loaded in 3 mm ID quartz tubes and, unless noted, sealed under inert nitrogen atmosphere.

2.2.5 TEM

The sample was prepared by dusting the catalyst powder particles on a 200 mesh TEM grid, which minimized artificial sample charging. High resolution TEM analysis was carried out on a JEOL JEM 2010 microscope fitted with a LaB_6 filament and an acceleration voltage of 200 kV. The point-to-point resolution of the microscope was 0.194 nm. Elemental composition of the sample was analyzed using energy dispersive x-ray spectroscopy (EDS) that attached to the microscope (Oxford, ISIS analysis system). Particle crystallinity was analyzed using electron diffraction. Images were recorded with a 1k

by 1k CCD camera and processed using Digital Micrograph (Gatan, USA). The following four samples were analyzed: 4-1, 4-2, 3-4, and 9-1.

Quantification with EDS was not performed on any of the samples for two reasons. First, there was some degree of peak overlap in the low energy end, which may have lead to errors in the subtraction of the background. Secondly, there was no standard sample for experimentally measuring the k-factor for quantitative analysis. Using a theoretical k-factor normally leads to very large deviations in the result.

2.2.6 DRIFTS

In-situ diffuse reflectance infrared Fourier transform spectroscopy (DRIFTS) was performed using a conventional Vertex 70 FTIR spectrometer from Bruker. The spectrometer was equipped with a praying mantis diffuse reflection optical accessory from Harrick Scientific. The praying mantis accessory was also installed with a high temperature reaction chamber for in-situ evaluation of a catalyst at temperature under various atmospheres. The reported DRIFTS spectra were the culmination of 256 scans. A resolution of 4 cm^{-1} was specified for the spectra. All DRIFTS spectra were collected into Kubelka–Munk units using the commercial OPUS program. Samples were handled in a glove box purged with N_2 gas; the oxygen level of the glove box was less than 2 ppm. Samples were ground to powder with an agate mortar and pestle and loaded into the DRIFTS reaction chamber while in the glove box in order to minimize exposure to the atmosphere.

DRIFTS was also applied to various samples under oxidative or reductive atmospheres. An oxidative environment was obtained by flowing 2% O_2 buffered in He while the reductive atmosphere was achieved by flowing 2% H_2 buffered in He (99.9999%). A 2% CO stream buffered in Ar (99.9999%) was used for CO chemisorption experiments.

2.2.7 TPR/TPD/CO Chemisorption

Temperature programmed reaction (TPR), temperature programmed desorption (TPD), and CO chemisorption experiments were performed with a Micromeritics AutoChem II 2920. A thermal conductivity detector (TCD) was utilized to monitor changes in the composition of the gas passing over the catalyst sample during experiments. The instrument was supplied with the optional CryoCooler attachment to allow for cryogenic temperature testing down to -100°C in chemisorption experiments.

TPD, TPR, and CO chemisorption experiments were conducted on sulfided materials. Samples were prepared at various temperatures by heating the sample at 10°C/min to the pretreatment temperature in flowing ultra-high purity (UHP) He and holding at the desired temperature for 1 h. TPD experiments consisted of passing He over a sample while ramping the temperature at 10°C/min. TPR experiments with sulfides were conducted in a stream of pure H_2 to investigate the evolution of H_2S. All gas flows had a volumetric flow rate of 50 cm^3/min in these experiments.

CO chemisorption experiments on sulfide samples were conducted with 10% CO/He. The amount of CO chemisorbed was measured by pulsing a known amount of CO onto the sample by first passing the gas through a calibrated sample loop. The sample was considered saturated with CO when several pulses in succession were determined to be of similar volume, indicating that CO was passing over the catalyst without being adsorbed. After saturation with CO, samples were flushed with He for 2 h at the chemisorption temperature to remove any physically adsorbed CO. TPD was then conducted to examine loss of CO and other species.

TPR experiments with metal oxides were performed. Molybdenum oxide, MoO_3, and two samples of cobalt oxide, the first reported as nominally CoO and another reported as nominally Co(II,III) oxide, were supplied by Sigma-Aldrich. The Co(II,III) oxide was reported to have a formula weight of 240.8 g/mol. A stream of 9.8 vol% H_2 in Ar was passed over about 100 mg of sample at 25 cm^3/min. The temperature was then ramped from 35°C to 800°C at 5°C/min. Hydrogen consumption was measured by changes in the concentration of the gas flowing over the sample as compared to a stream of identical 9.8 vol% H_2 in Ar passing over the reference side of the TCD.

2.2.8 Computational

2.2.8.1 Density functional theory calculations

Spin-polarized periodic density functional theory (DFT) calculations were performed with the CP2K code.[32] These calculations employ a mixed Gaussian and planewave basis set. Core electrons were represented with norm-conserving Goedecker-Teter-Hutter pseudopotentials,[33-35]and the valence electron wavefunction was expanded in a double-zeta basis set with polarization functions[36] along with an auxiliary plane wave basis set used to solve the coulombic part of the Kohn-Sham equation. Semicore pseudopotentials were used for molybdenum and potassium ($4s^2 4p^6 5s^1 4d^5$ and $3s^2 3p^6 4s^1$, respectively), and a valence-only pseudopotential was used for sulfur ($3s^2 3p^4$). The generalized gradient

approximation exchange-correlation function of Perdew, Burke, and Enzerhof (PBE)[37] was used for all calculations. The energy cutoff for the planewave basis set was set at 300 Ry. The convergence criteria for the RMS and maximum changes in geometry between the previous and current structures were set to 3.0×10^{-3} and 1.5×10^{-3} bohr, respectively, and the root mean square (RMS) force and maximum force component convergence criteria were set to 3×10^{-4} and 4.5×10^{-4} Hartree/bohr, respectively.

Bader analysis using the code of Henkelman et al.[38-40] and projected density of states (PDOS) generated from a projection of the total density of states onto spherical harmonics were used in the electronic structure analysis. Work function calculations were also performed by subtraction of the vacuum electrostatic potential (half-way between the slab surface and its image slab surface) and the Fermi energy, i.e., $\Phi = V_{vacuum} - \varepsilon_{Fermi}$.

2.2.8.2 Construction of MoS_2(100) edge surfaces with different surface sulfur concentrations

The bulk MoS_2 unit lattice structure was constructed using crystallographic data in the literature.[41,42] The hexagonal 2H polymorph structure of MoS_2 (space group $P6_3/mmc$) has the following unit cell lattice parameters a=b=3.160 Å, c=12.294 Å, α = β= 90° and γ=120°. This bulk structure was then cleaved at the (100) plane to give a molybdenum-terminated ($10\bar{1}0$) edge and a sulfur-terminated ($\bar{1}010$) edge. This edge surface was expanded to four units along the x and to four units in depth. A vacuum layer of 20 Å was added above the cleaved surface slab to give a volume of 12.640×12.294×29.1221 Å. All the atoms in the model edge surface slab were relaxed with only the bottom layer held fixed. The resulting "as-cleaved" structure, referred to as Mo0-S100 in this work, is shown in Figure 2(a). Two other sulfur concentrations at the MoS_2(100) surface were considered in addition to the Mo0-S100 system. A 50%-50% concentration of sulfur at each of the edge surfaces (referred to as Mo50-S50) was created by moving half of the Mo0-S100 model's sulfur-terminated edge sulfur atoms to the molybdenum-terminated edge surface Figure 2(b). The Mo50-S50 surface is the most energetically stable under HDS working conditions (having H_2S present as with the mixed alcohol synthesis studies) by previous DFT calculations.[43] The third model is a fully sulfur-covered edge surface system (referred to as Mo100-S100) and was created by added a full coverage of sulfur at the bare molybdenum edge of the original Mo0-S100 system (Figure 2(c)). A fully sulfur-covered surface approximates the initial state of a newly-synthesized MoS_2 catalyst. Both the Mo50-S50 and Mo100-S100 model surfaces were relaxed in the same manner as with the Mo0-S100 system. In addition to the above models, a fourth model with 37.5% sulfur coverage at the Mo edge and 50% sulfur coverage at the S edge (referred to as Mo37.5v-

S50) was constructed from the Mo50-S50 model to study the effect a sulfur “vacancy” at the Mo edge has on the potassium interaction (Figure 2(d)). Brillouin zone sampling at the Γ-point was sufficient.

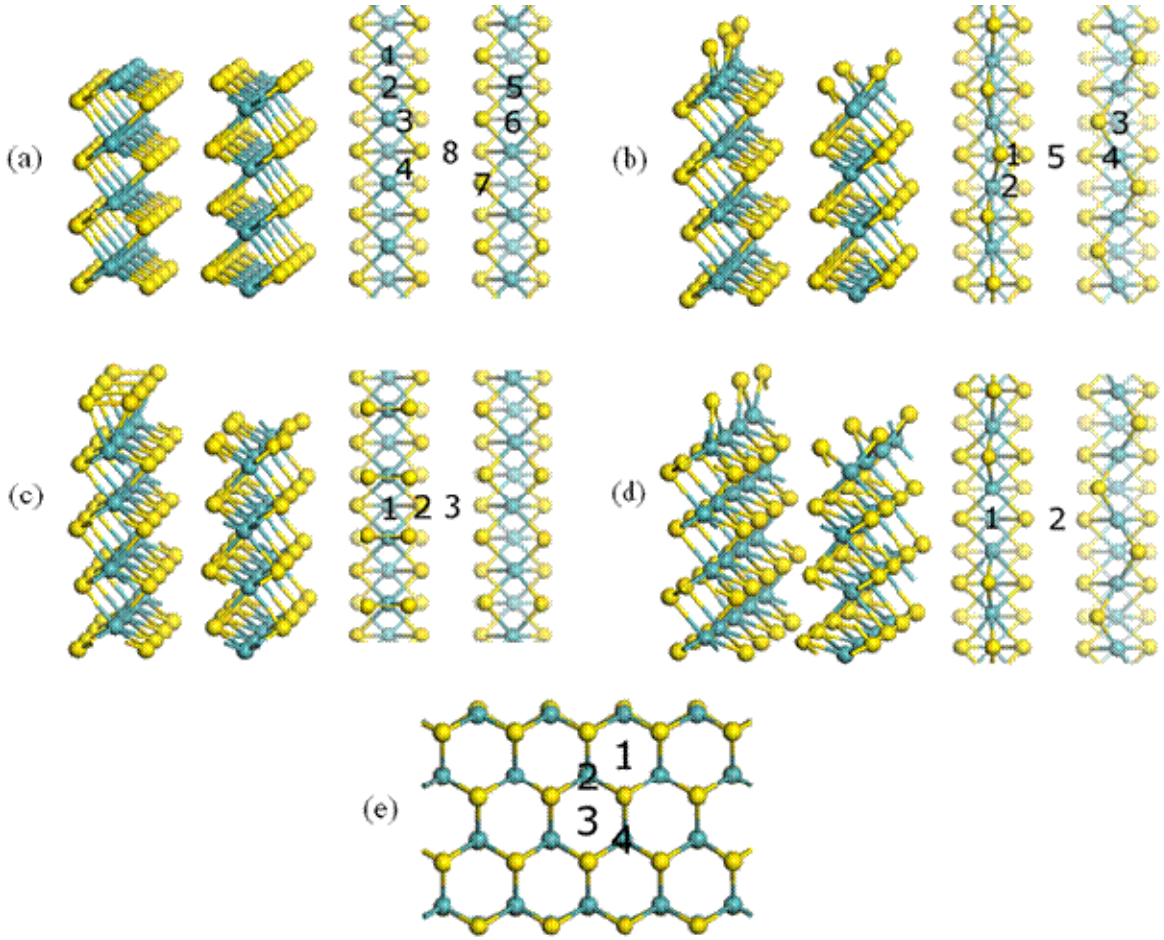

Figure 2. MoS_2(100) surface with (a) ``as-cleaved'', (b) 50%-50%, (c) 100-100%, and (d) 37.5%-50% Mo edge and S edge sulfur coverages. The top view to the right of the side, interstitial view of the surface models are numerically labeled with the K adsorption sites considered in this study. The basal view of (e) shows the interstitial sites considered here. Blue-green balls represent molybdenum atoms and yellow balls represent sulfur atoms. Fading of atoms according to surface depth is used to enhance the top-most features in each top view depiction.

2.2.8.3 Placement of potassium on edge surface models

Potassium atoms were placed at hollow, atop, bridging, and near-surface interstitial sites on the surface (see right-side figures in Figure 2(a-d)). The stability of potassium in the interstitial at subsurface sites (1 and 2, respectively, in Figure 2(e) and deeper sites below the surface (3 and 4, respectively, in Figure 2(e) were also explored in this work. Each of these configurations were optimized with the Broyden-Fletcher-Goldfarb-Shanno (BFGS) algorithm to locate their respective energy minima. The convergence

criteria for the RMS and maximum changes in geometry between the previous and current structures were set to 3.0×10^{-3} and 1.5×10^{-3} bohr, respectively, and the root mean square (RMS) force and maximum force component convergence criteria were set to 3×10^{-4} and 4.5×10^{-4} Hartree/bohr, respectively. As previously noted, potassium-promoted MoS_2-based catalysts have been experimentally prepared with neutral potassium metal (vapor phase or ammonia-dissolved) and with potassium salts such as K_2CO_3 and KOH under reducing conditions. Herein, we consider two cases: neutral K and oxidized ("K^+") model systems. For the charged "K^+" case system, a uniform +1 charge was applied to the system (i.e., "hole-doping"). In the case of the neutral K system, the multiplicity of the system was assumed to be a doublet. However, as discussed later on, the edge surface possesses magnetic properties,[44-46] which can be affected by the presence of alkali metal atoms/ions. The charged case was considered only for the low single K atom doping coverage. With increasing K atom coverage where two or more K atoms were placed on the 4×1 model surfaces, only neutral systems were considered. The computational research has implications for the catalytic properties of K-doped MoS_2 at the edge surface due to changes in its electronic structure.

Potassium adsorption energies were computed as follows:

$$E_{ad}(K) = E_{tot}(K + surf) - [E_{tot}(K) + E_{tot}(surf)] \quad (1)$$

where $E_{tot}(K+surf)$ is the energy for the potassium adsorbed to the surface, $E_{tot}(K)$ is the energy for the isolated potassium atom in vacuum, and $E_{tot}(surf)$ is the energy of the clean surface without the adsorbed potassium atom. Based on this definition, a negative value of $E_{ad}(K)$ indicates stable adsorption. For the charged systems where a uniform charge for the cation was applied, the $[E_{tot}(K)+E_{tot}(surf)]$ is replaced by the total energy of the surface slab with the potassium placed 10 Å above the surface. For multiple K atoms adsorbed on the edge surfaces, average adsorption energy per K atom was calculated as follows:

$$E_{ad}(K) = \{E_{tot}(N_K K + surf) - [N_K E_{tot}(K) + E_{tot}(surf)]\} / N_K \quad (2)$$

where N_K is the number of K atoms adsorbed on the surface.

3 Results

3.1 SEM and EDS Analysis Results

SEM as well as complimentary and simultaneous EDS results were collected on the catalyst samples. SEM is a microscopy technique that allows for sample morphological characterization through visualization of the surface at magnifications greater than what can be achieved with optical microscopy. EDS analysis is based on the principle that the electron beam used to produce SEM micrographs also releases electrons for the sample energy characteristic of the elements present. Because the electron beam is rastered across the surface sample, spatial resolution of where elements are located within a given SEM micrograph can be determined. By shading a SEM micrograph with the location of an element identified during rastering, an "elemental map" can be produced for a given element. Thus, SEM/EDS analysis is valuable for its ability to not only relay information on the surface texture and morphology of the catalyst samples but also for the location and concentration of the elements present.

The data in Figure 3 was obtained from SEM/EDS analysis of sample 3-1 (freshly prepared, unactivated RF-101). Figure 3(a) is the SEM micrograph illustrating the surface texture of the sample while Figure 3(b)-(f) are EDS elemental maps that illustrate the location of various elements of interest in the sample. As shown in Figure 3(c), (e), and (f), Mo, Co and S appear to be well dispersed and lack any identifiably concentrated areas. In contrast, Si and O, which are strongly associated with each other and present due to the Bentolite®binder, exhibit clustering as illustrated in Figure 3(a) and (b). K, which was present as K_2CO_3 physically mixed into the catalyst, was heterogeneously dispersed throughout the sample. K was observed at low magnification. However, it was not observed at higher magnification, presumably because, by chance, the areas sampled did not contain detectable amounts.

The data in Figure 3 from freshly prepared RF-101 can best be compared with samples 4-1 and 4-2, which were samples of RF-101 that had been activated but not utilized for mixed alcohol synthesis for an extended period. During activation, sample 4-1 was located near the top of the mixed alcohol synthesis reactor while sample 4-2 was located near the bottom of the reactor. Figure 4 and Figure 5 illustrate the results of SEM/EDS testing on samples 4-1 and 4-2, respectively. Analysis of the EDS elemental maps in Figure 4 and Figure 5 reveals that Co, Mo, and S appear to be associated with each other, are generally well dispersed, and are not associated with Si in the binder material. In contrast, K appears to be spread uniformly across regions associated with Mo, Co, and S, as well as regions

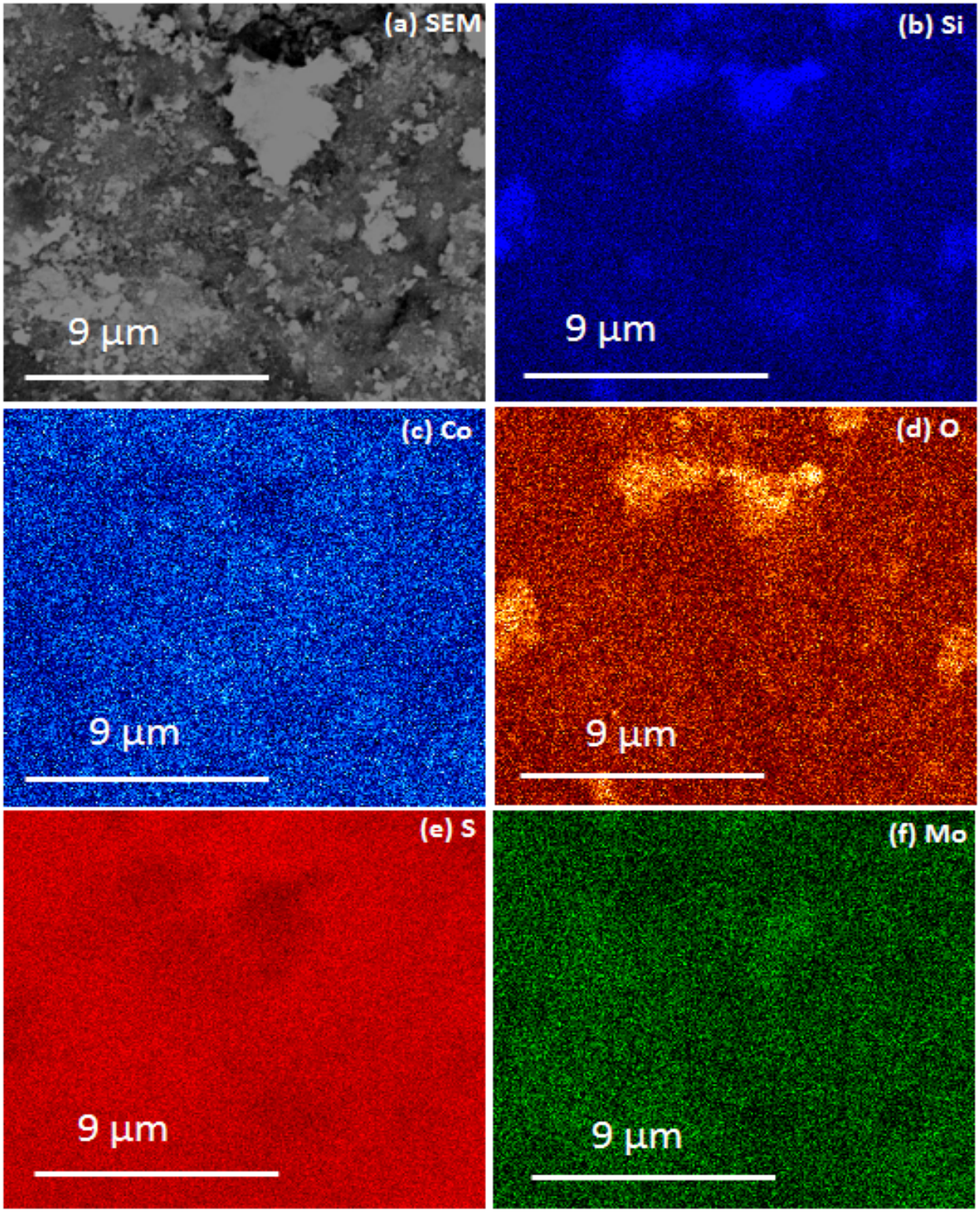

Figure 3. (a) SEM micrograph exhibiting the surface morphology of sample 3-1, which was fresh, unactivated RF-101 (b) Si Kα EDS map (c) Co Kα EDS map (d) O Kα EDS map (e) S Kα EDS map (f) Mo Kα EDS map .

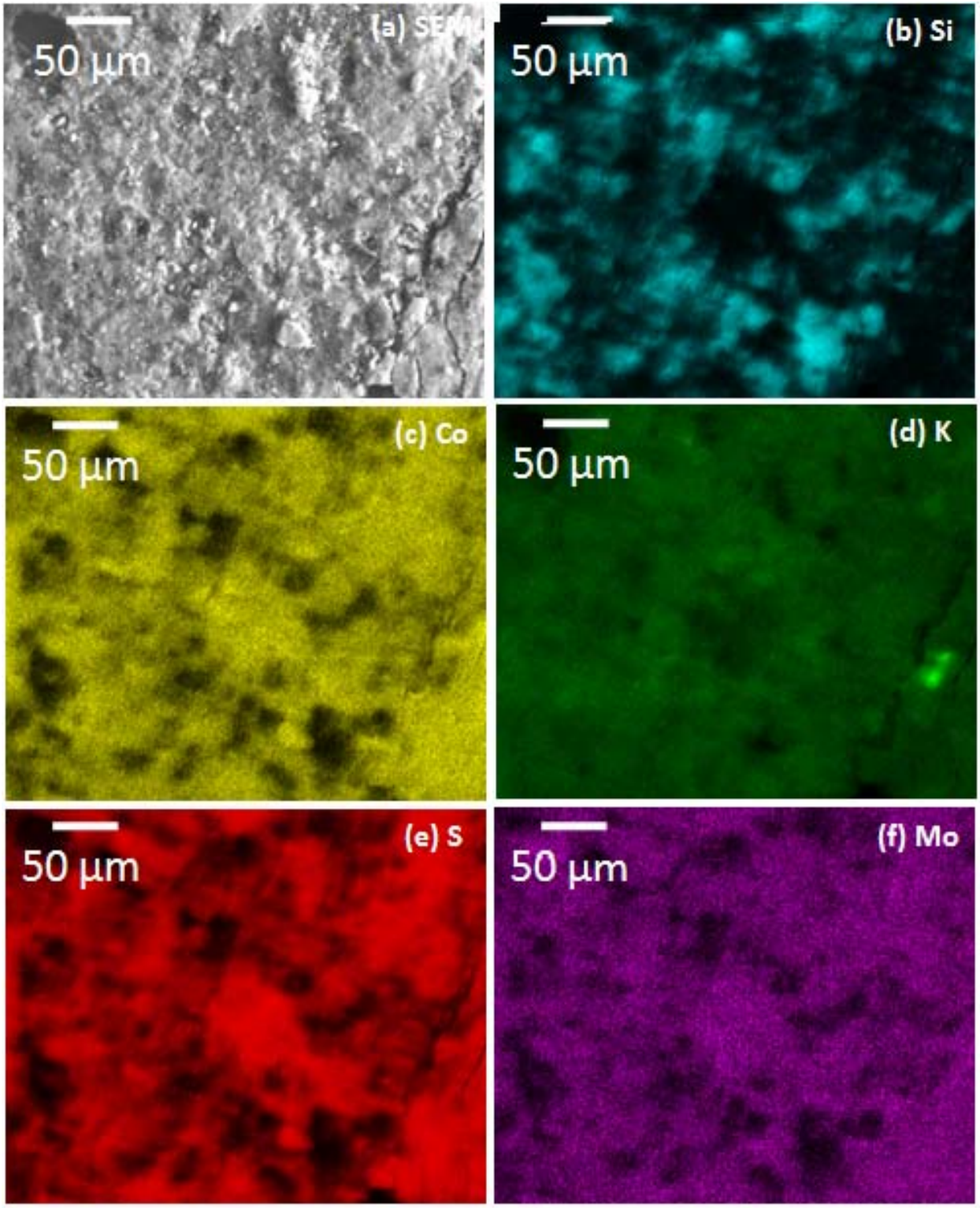

Figure 4. (a) SEM micrograph exhibiting the surface morphology of sample 4-1, which was activated RF-101 near the top of the mixed alcohol synthesis reactor (b) Si Kα EDS map (c) Co Kα EDS map (d) K Kα EDS map of (e) S Kα EDS map (f) Mo Kα EDS map .

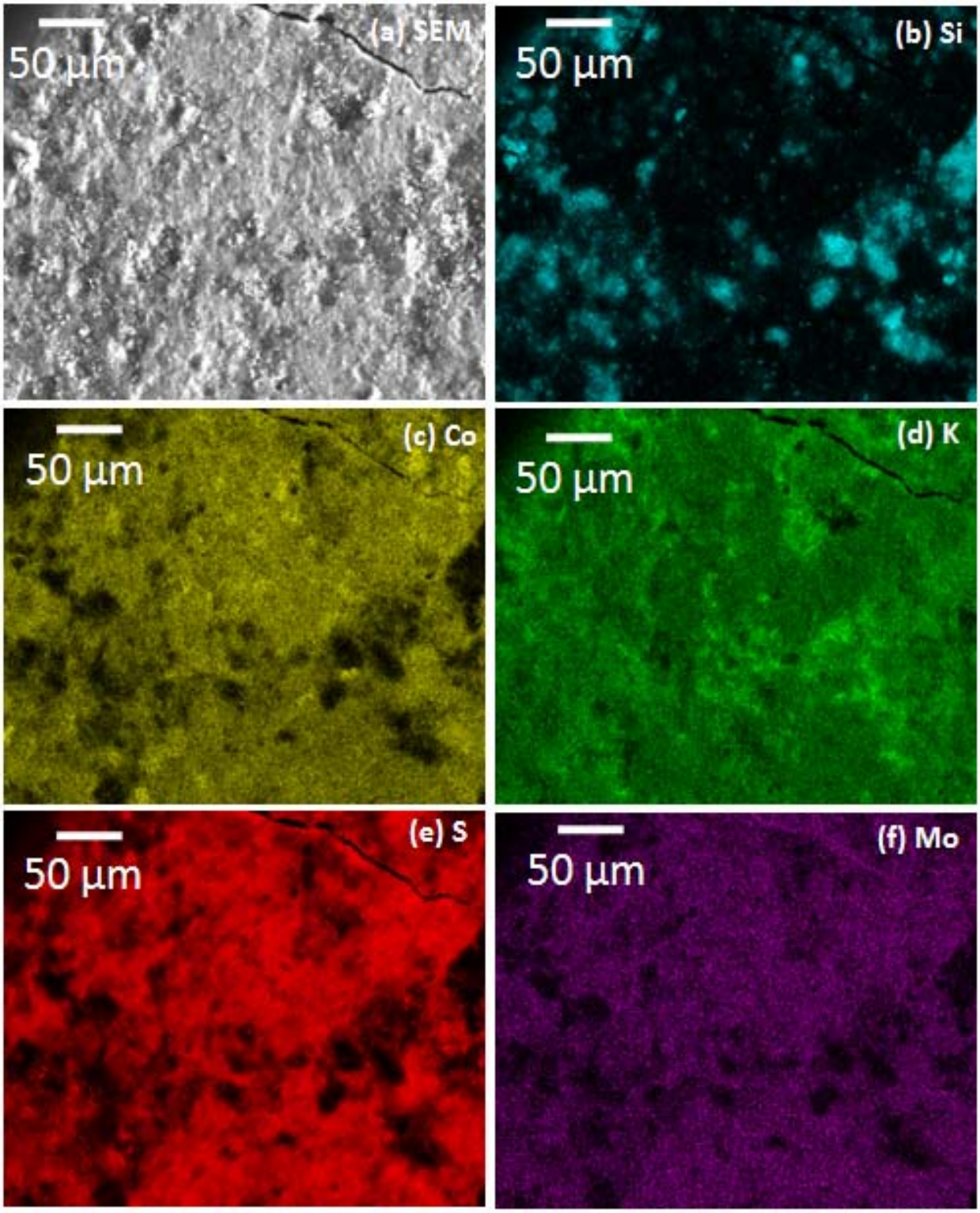

Figure 5. (a) SEM micrograph exhibiting the surface morphology of sample 4-2, which was activated RF-101 near the bottom of the mixed alcohol synthesis reactor (b) Si Kα EDS map (c) Co Kα EDS map (d) K Kα EDS map of (e) S Kα EDS map (f) Mo Kα EDS map .

containing binder material. Uniform dispersion of K is desirable since K is necessary in Co-Mo-S catalysts for selectivity to alcohols over hydrocarbons, On the other hand, K associated with the binder material may not effectively promote the catalyst.

Next, sample 3-2, which was a catalyst sample that had been activated and subjected to ~4200 h of mixed alcohol synthesis, was characterized with SEM/EDS measurements. Two analyses of a representative sample of 3-2 were performed: the first was outside the catalyst pellet at the exterior and the second was inside the catalyst pellet after slicing the pellet open. Results obtained at the pellet exterior are shown in Figure 6 while the interior analysis results are shown in Figure 7. Several interesting results were obtained with the analysis of sample 3-2. First, Figure 6(c) and Figure 7(c) clearly illustrate the presence of Co clusters with a size distribution in the range of 300 nm- 1µm. As noted by several researchers including Chianelli and Berhault,[9] Co effectively promotes MoS_2 at MoS_2 edges. Agglomerated Co is undesirable as Co clusters are not able to efficiently decorate MoS_2 edge sites. The chemical nature of the Co clusters cannot be determined via SEM/EDS measurements alone. However, it is interesting to note that the Co clusters in Figure 7(c) appear to correspond to sulfur poor regions in Figure 7(e). Yet, in other regions of this same sample, Co (Figure 6(c)) and S (Figure 6(e)) appear to be associated. Based on XRD measurements discussed in the next section, it is likely that the observable Co clusters consist largely of Co_2C and Co_9S_8, although the presence of other Co carbide and sulfide species, cannot be conclusively ruled out.

The location of K in sample 3-2 at the exterior of the pellet is also interesting as shown in Figure 6(d). Specifically, K was not as dispersed as in the activated catalyst but instead appears to have a greater concentration in areas rich with Si and O. A correlation between Si, O, and K suggests that the binder material can act as a K "sink," potentially due to undesirable cation exchange properties. The strong correlation between K, Si, and O illustrated in Figure 6 was an extreme case, not widely observed in other samples. However, Figure 7 appears to suggest that K agglomeration may also take place in regions not associated with the siliceous binder. Similar to Co agglomeration, K agglomeration with increasing time on stream is almost certainly an undesirable process that negatively impacts the catalyst's performance.

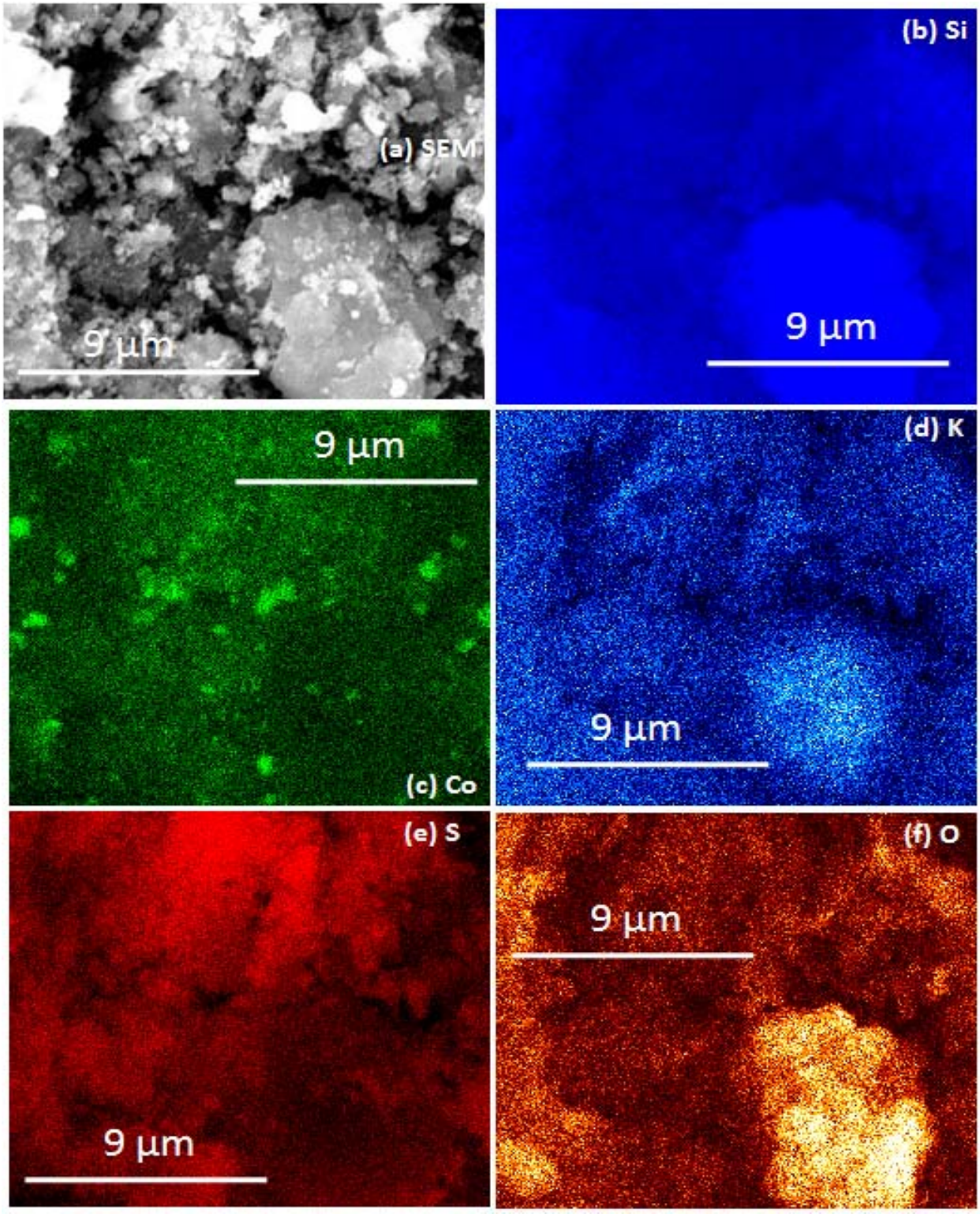

Figure 6. (a) Surface morphology of the exterior of sample 3-2, which was activated RF-101 used for mixed alcohol synthesis for an extended period removed from near the top of the reactor. (b) K EDS map of the surface shown in (a). (c) O EDS map of the surface shown in (a). (d) Si EDS map of the surface shown in (a).

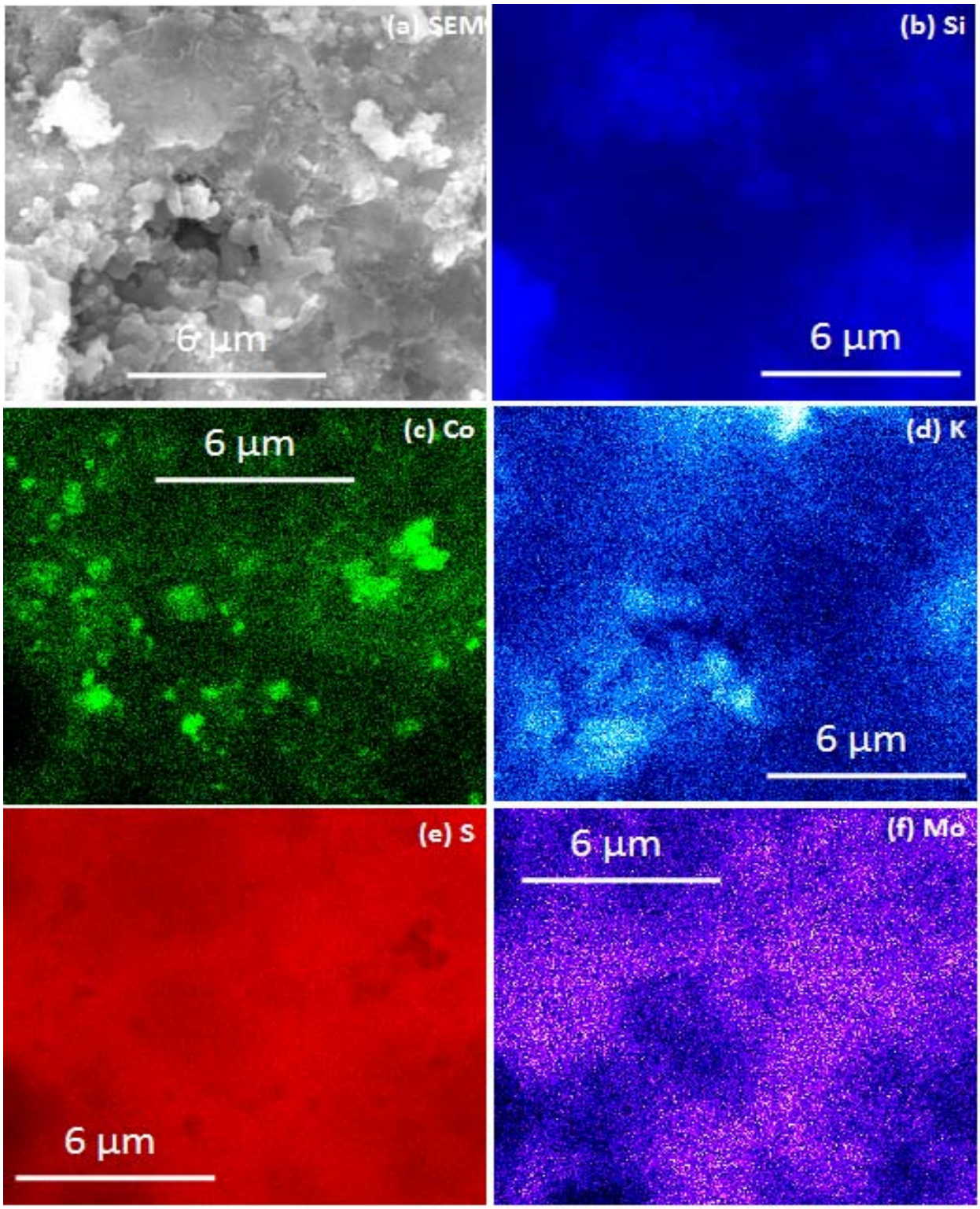

Figure 7. (a) Surface morphology of the interior of sample 3-2, which was activated RF-101 used for mixed alcohol synthesis for an extended period removed from near the top of the reactor. (b) K EDS map of the surface shown in (a). (c) O EDS map of the surface shown in (a). (d) Si EDS map of the surface shown in (a).

Sample 3-4 was also analyzed. Sample 3-4 was RF-101 that had been activated and utilized for the production of mixed alcohols but also aged in an accelerated fashion via a methanol co-feed. Range Fuels had reported that the methanol co-feed rapidly altered the catalytic activity, possibly due to sulfur stripping from the catalyst. While several regions were measured by SEM/EDS, only one region at different magnifications is illustrated in Figure 8 and Figure 9. The features of Figure 8 and Figure 9 are similar to those of the activated samples of RF-101 in Figure 4 and Figure 5 (4-1 and 4-2). Areas of Co, Mo, and S appear to be strongly correlated but are separate from areas with Si and O (O is not shown). K is again observed to be dispersed indiscriminately across the Co-Mo-S and Si-O regions. Figure 8(c) and Figure 9(c) suggest that Co agglomeration has initiated as indicated by the points of small relatively brighter areas. However, it is difficult to determine from these data if Co agglomeration was promoted by the methanol co-feed.

Finally, sample 9-1 was analyzed via SEM/EDS. Sample 9-1 was a sample of activated RF-101 that was utilized for mixed alcohol synthesis from syngas while also injecting methanol and H_2S in the co-feed. SEM/EDS results of a similar area are presented at varying magnifications in Figure 10 and Figure 11. In Figure 10, which illustrates the lower magnification SEM/EDS analysis on sample 9-1, the Mo, Co, and S are clearly associated with each other. Si, which is likely from the binder, is segregated into areas not associated with Mo, Co, or S. As observed with other samples, K appears to be uniformly distributed across both the Mo/Co/S as well as the Si rich regions.

The lower magnification analysis (2000x) of sample 9-1 in Figure 10 did not show Co clustering, but the higher magnification (50,000x) did (Figure 11(c)). The Co clusters were in the size range of about 200-400 nm. Some localized regions rich in Si were also observed in Figure 11(b). Even at high magnification, K, S, and Mo were dispersed evenly throughout the sample as illustrated in Figure 11(d), (e) and (f), respectively.

Methanol was used by Range Fuels staff to age catalyst 3-4 (Figure 8 and Figure 9). In one hypothesis formulated by Range Fuels, methanol aged the catalyst in an accelerated fashion due to the removal of S from the catalyst. In the run that generated sample 9-1 methanol and H_2S were co-fed in order to understand if the catalyst could be stabilized by adding S along with methanol to the reactor. The EDS was used to quantify the concentration of S in various samples in order to understand if methanol removed S and if the H_2S co-feed increased the S concentration. The S concentration in freshly activated

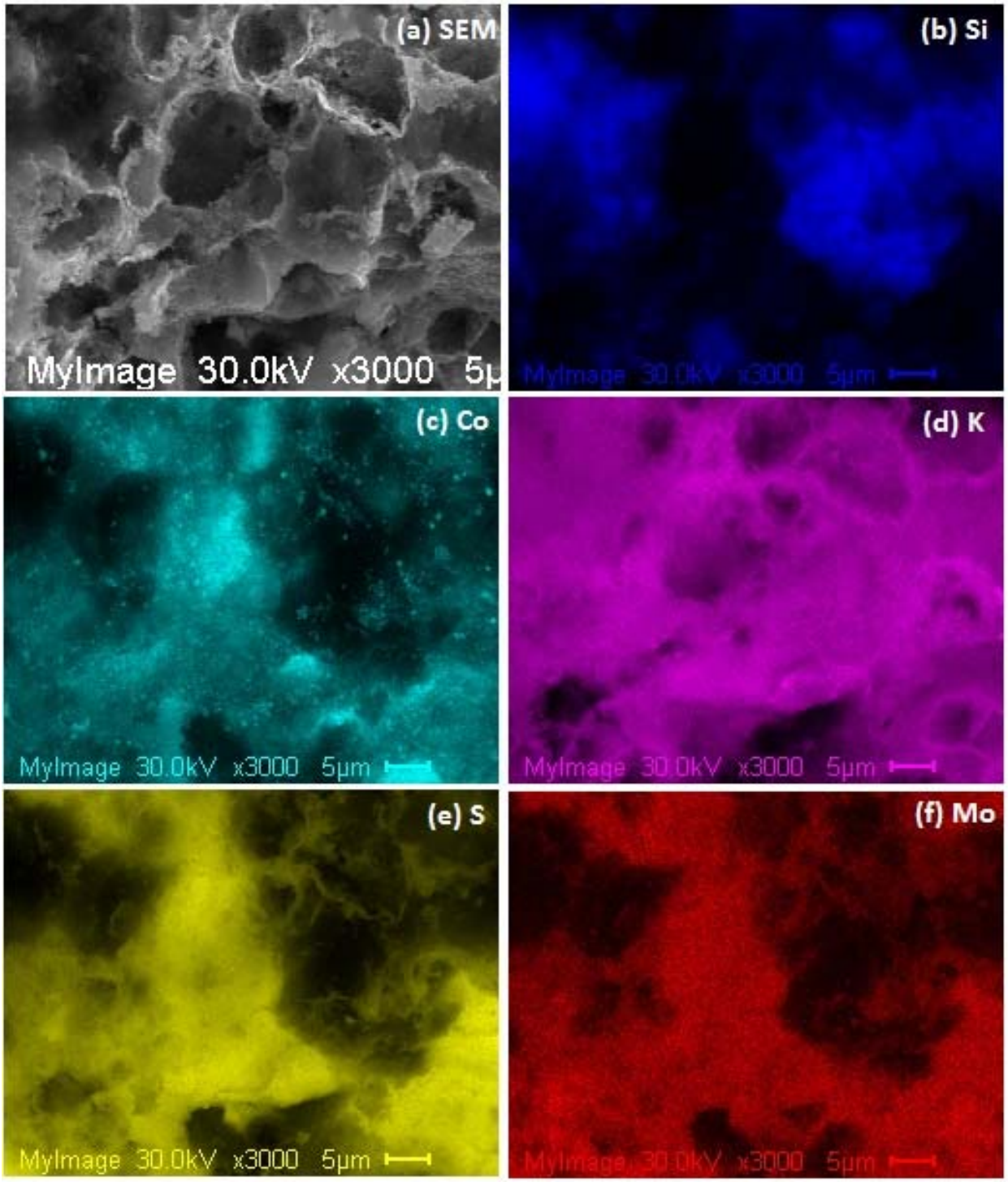

Figure 8. Data from sample 3-4, which was methanol aged RF-101, at 3000x magnification (a) SEM micrograph exhibiting the surface morphology (b) Si Kα EDS map (c) Co Kα EDS map (d) K Kα EDS map of (e) S Kα EDS map (f) Mo Kα EDS map.

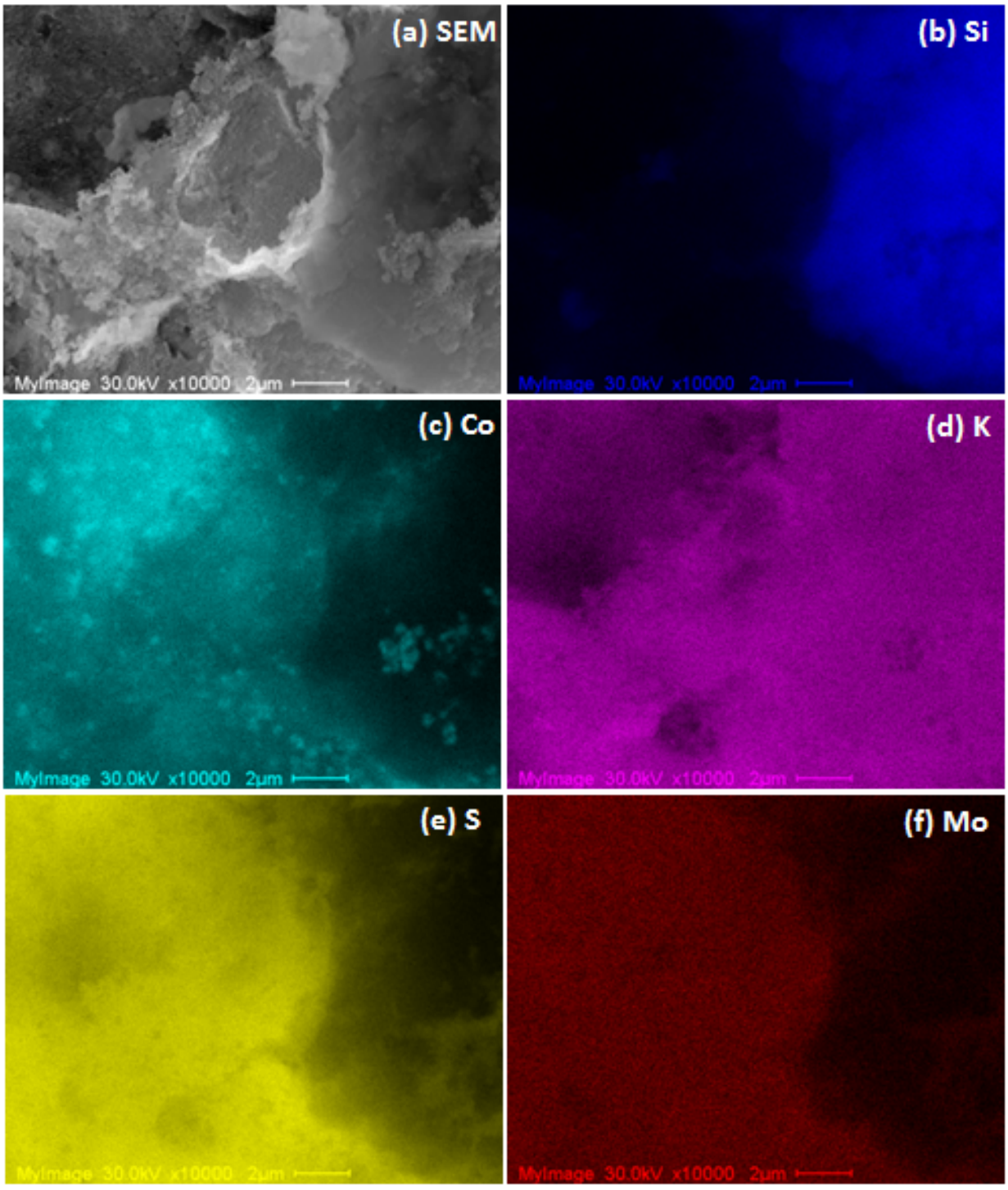

Figure 9. Data from sample 3-4, which was methanol aged RF-101, at 10,000x magnification (a) SEM micrograph exhibiting the surface morphology (b) Si Kα EDS map (c) Co Kα EDS map (d) K Kα EDS map of (e) S Kα EDS map (f) Mo Kα EDS map.

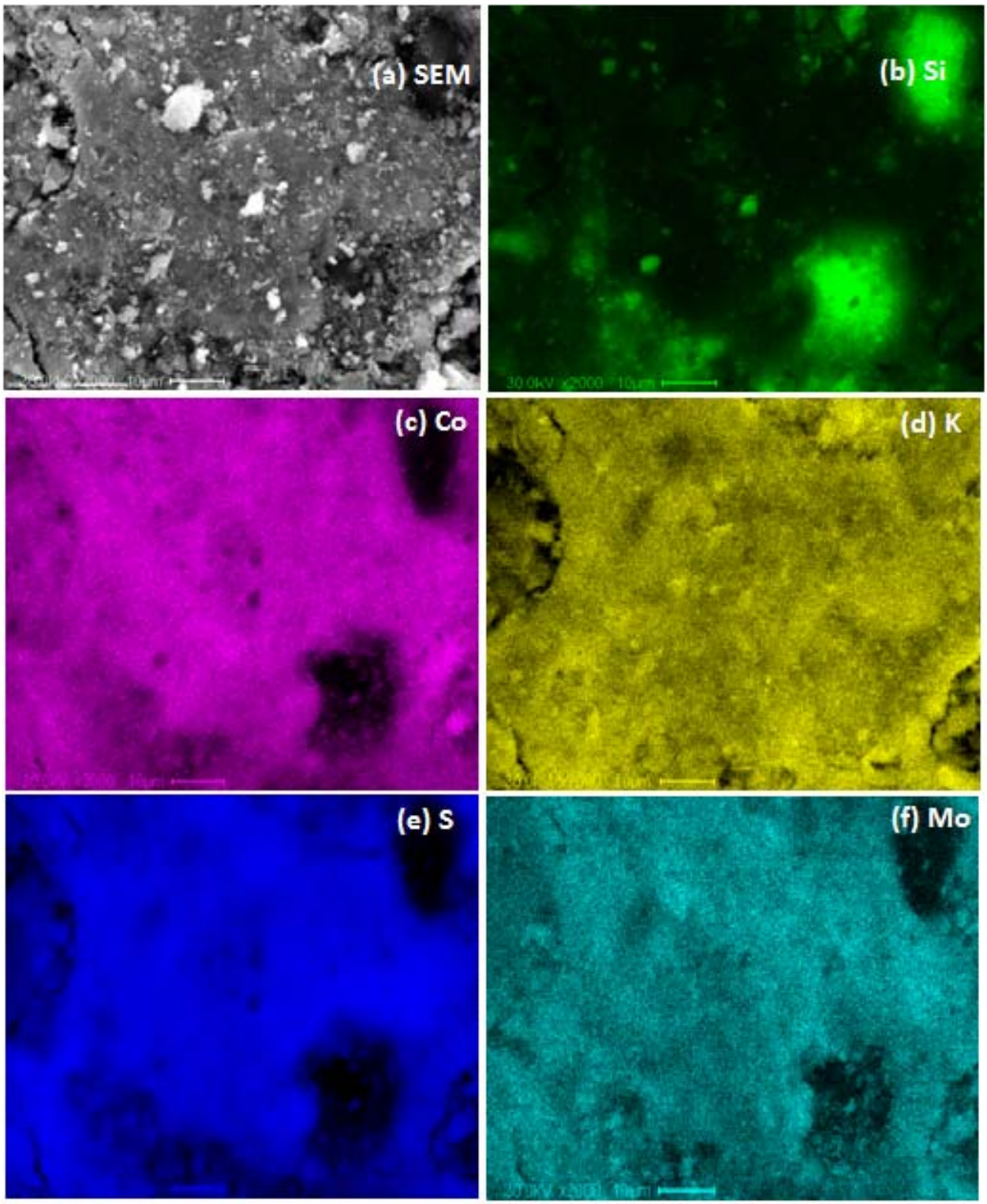

Figure 10. (a) SEM micrograph showing the surface morphology of sample 9-1, which was RF-101 used for mixed alcohol synthesis with methanol and H_2S co-feeds, at 2,000x magnification. (b) Si Kα EDS map (c) Co Kα EDS map (d) K Kα EDS map of (e) S Kα EDS map (f) Mo Kα EDS map.

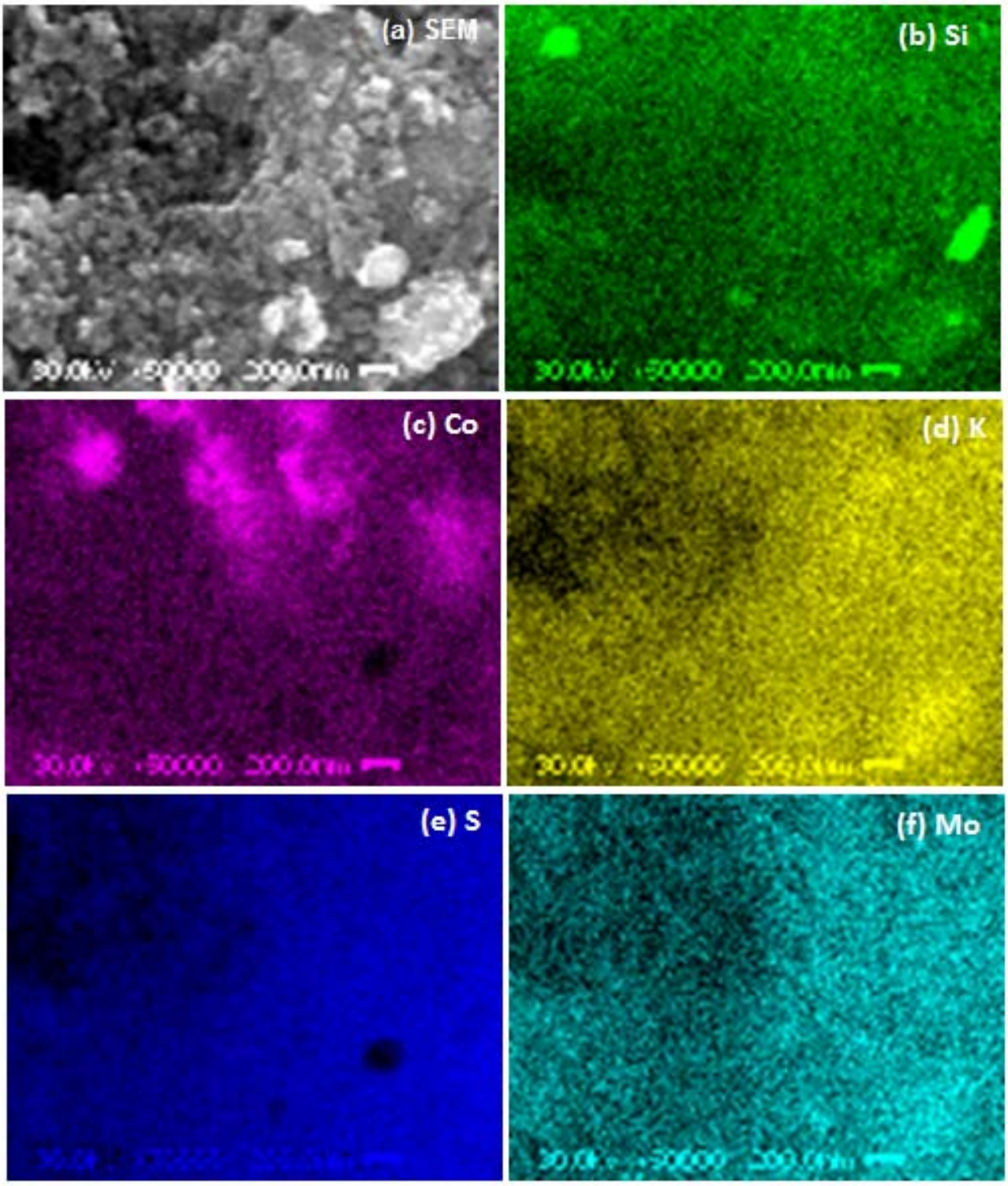

Figure 11. (a) SEM micrograph showing the surface morphology of sample 9-1, which was RF-101 used for mixed alcohol synthesis with methanol and H_2S co-feeds, at 50,000x magnification. (b) Si Kα EDS map (c) Co Kα EDS map (d) K Kα EDS map of (e) S Kα EDS map (f) Mo Kα EDS map.

samples (4-1 and 4-2) was about 35 atomic%. Sample 3-4, the sample with methanol added, was found to have about 25 atomic% S. In contrast, sample 9-1, which experienced both a methanol and H_2S co-feed, exhibited about 37 atomic% S. Thus, methanol did appear to remove S, but the presence of the H_2S co-feed appeared to significantly increase the concentration of the S in the sample when methanol was co-fed. Sample 3-2, which was RF-101 utilized for mixed alcohol synthesis for 4200 h, was found to contain only 12-20 atomic% S. Therefore, sulfur was lost from the catalyst during long-term production of mixed alcohols even when methanol was not added as a co-feed.

Zn and La impurities were identified in sample 3-2. In other samples, impurities such as Zn, Na, Mg, La, and Fe were observed in very small quantities. The Zn and La impurities were not observed in the K_2CO_3 potassium precursor (9-2), or in a stainless steel wire received from Range Fuels that had been used to unpack the catalyst from the reactor. Nor were they found in the binder used in synthesis of the catalyst. Therefore, the source of the La and Zn impurities could not be determined. Ca and Fe were identified as impurities to the Si, Mg, Al, and O expected from the Bentolite® binder.

3.2 XRD Analysis Results

XRD analysis was performed on several reference samples as well as the catalyst samples obtained from Range Fuels. XRD utilizes elastic x-ray scattering to determine the presence of crystalline species within a sample. In this analysis, the x-rays were produced using Cr Kα electrons with a characteristic wavelength of 2.2897 Å. Phases were identified or proposed with the Powder Diffraction File library from the International Centre for Diffraction Data.

The XRD analysis was primarily performed with a Micro-XRD apparatus. In contrast to the more traditional powder XRD analytical technique, the Micro-XRD apparatus could utilize an un-ground catalyst pellet. Furthermore, the Micro-XRD x-ray beam could be focused on specific points on a catalyst pellet. This allowed for spatial resolution of the catalyst pellet to be performed. However, many of the catalyst samples were revealed to be very poorly crystalline (i.e. highly amorphous), resulting in poor signal-to-noise ratio. Therefore, some catalyst pellet samples were ground and placed in a sealed capillary utilizing the Micro-XRD. Analysis of the ground samples was found to increase the signal-to-noise ratio with the trade-off that spatial resolution was lost due to the grinding of the sample.

3.2.1 Reference Samples

3.2.1.1 Sample 3-5 (K_2MoS_4 reference material)

The K_2MoS_4 reference material was received from Range Fuels staff, who hypothesized that it could be a phase present in the catalytic samples. The material was analyzed as a ground powder in a capillary. The presence of the expected K_2MoS_4 phase was confirmed as shown in Figure 12. Additional phases were also present. Most of the additional peaks were accounted for by the viewcards of $CaSO_4$ (anhydrite) and SiC (moissanite).

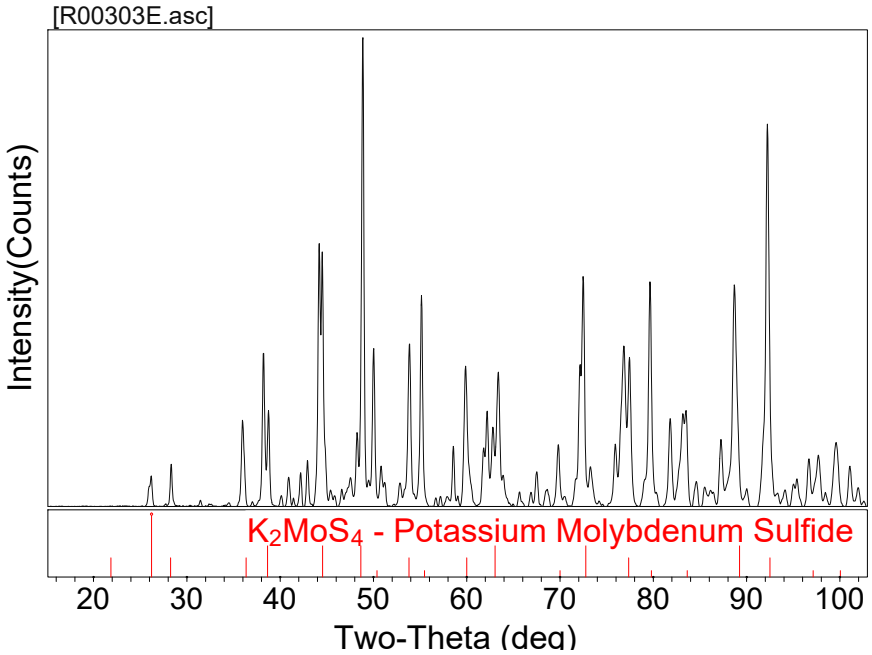

Figure 12. Data collected during XRD analysis of sample 3-5, which was a nominally K_2MoS_4 reference material received from Range Fuels. Measurements were performed on ground powder in a capillary. The presence of K_2MoS_4 was confirmed. The pattern is background-subtracted. Data collected using Cr radiation (2.2897 Å).

3.2.1.2 Sample 9-2 (Nominally anhydrous K_2CO_3)

XRD measurements were performed on sample 9-2, which was a sample of the K_2CO_3 used in the preparation of RF-101 (Figure 13). Data was collected on the powder sample using a flat sample holder. Measurements revealed that K_2CO_3 was the main phase. Some of the hydrated form of the compound, $K_2CO_3 \cdot 1.5H_2O$, was also present as a secondary phase; $K_2CO_3 \cdot 1.5H_2O$ has a different monoclinic structure than that of K_2CO_3.

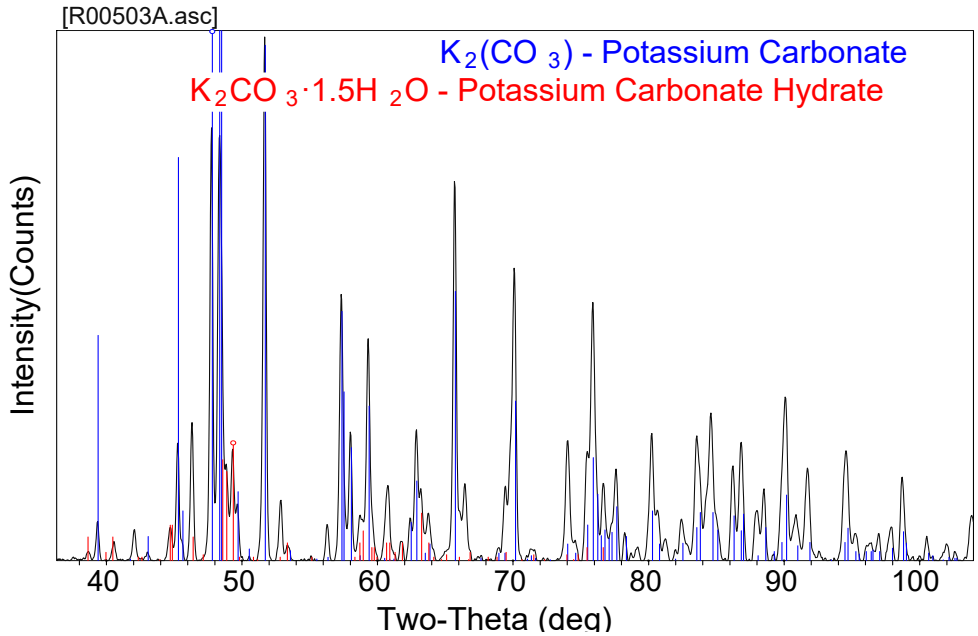

Figure 13. Data collected during the measurements of 9-2, which was a nominally anhydrous K_2CO_3 material used in the preparation of RF-101. Analysis was performed on ground powder on a flat sample holder. Analysis revealed the presence of K_2CO_3 and $K_2CO_3 \cdot 1.5H_2O$. The pattern is background-subtracted. Data collected using Cr radiation (2.2897 Å).

3.2.1.3 Sample 9-3 (BentoLite® binder material)

Data collected on a powder sample of the Bentolite® binder revealed that the binder was primarily the mineral Montmorillonite (which is a form of bentonite). The crystal structure is $(Ca,Na)_{0.3}Al_2(Si,Al)_4O_{10}(OH)_2 \cdot xH_2O$. In addition to Montmorillonite, Tridymite (SiO_2) and forsterite (Mg_2SiO_4) were matched as possible impurity phases (see Figure 14).

3.2.1.4 Sample 11-1 (cobalt pentlandite, Co_9S_8)

A sample of Co_9S_8 prepared at PNNL was examined via XRD. The sample analyzed, 11-1, was prepared in the open air. The nominal Co_9S_8 sample was measured as a ground powder on a flat sample holder, and confirmed to be cobalt pentlandite, Co_9S_8. Minor impurity peaks were present, which may be attributed to CoS or elemental S (see Figure 15). It should be noted that the cubic Co_4S_3 phase is practically isostructural with Co_9S_8 and displays an XRD spectrum nearly identical to Co_9S_8. While no attempt was made to determine which of these phases was present in the Co_9S_8 reference material and Range Fuels catalyst samples, the Co_9S_8 phase was assumed based on reports that Co_4S_3 is only stable above about 800°C and that Co_9S_8 is the most thermodynamically stable phase below this temperature.[47]

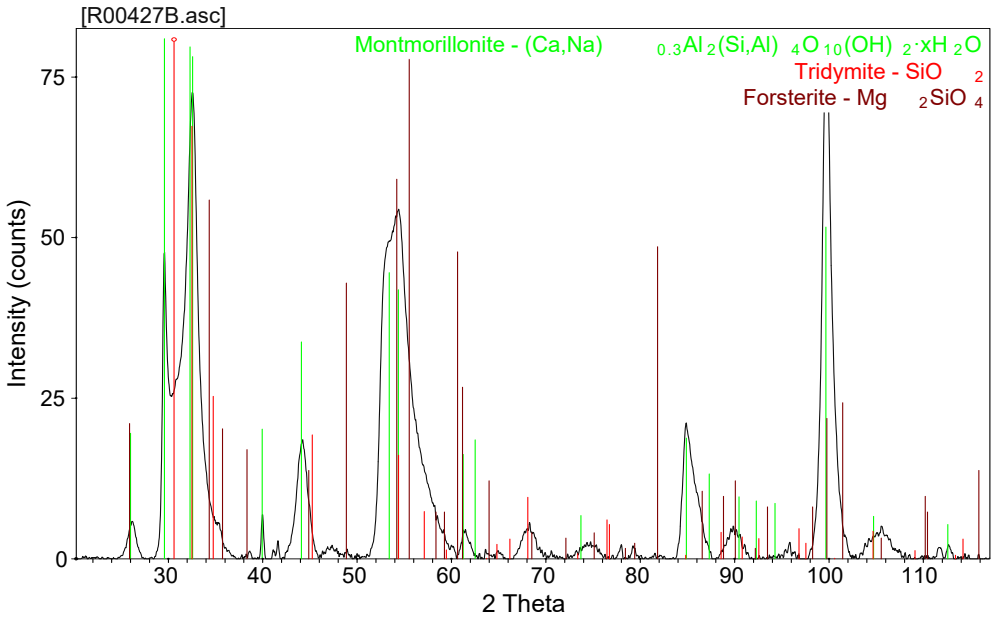

Figure 14. Data collected during XRD analysis on powdered sample of 9-3, the BentoLite® binder used in the preparation of RF-101. The powder was analyzed on a flat sample holder. Analyse revealed the presence of montmorillonite (bentonite), tridymite (SiO_2), and forsterite (Mg_2SiO_4). The pattern is background-subtracted.

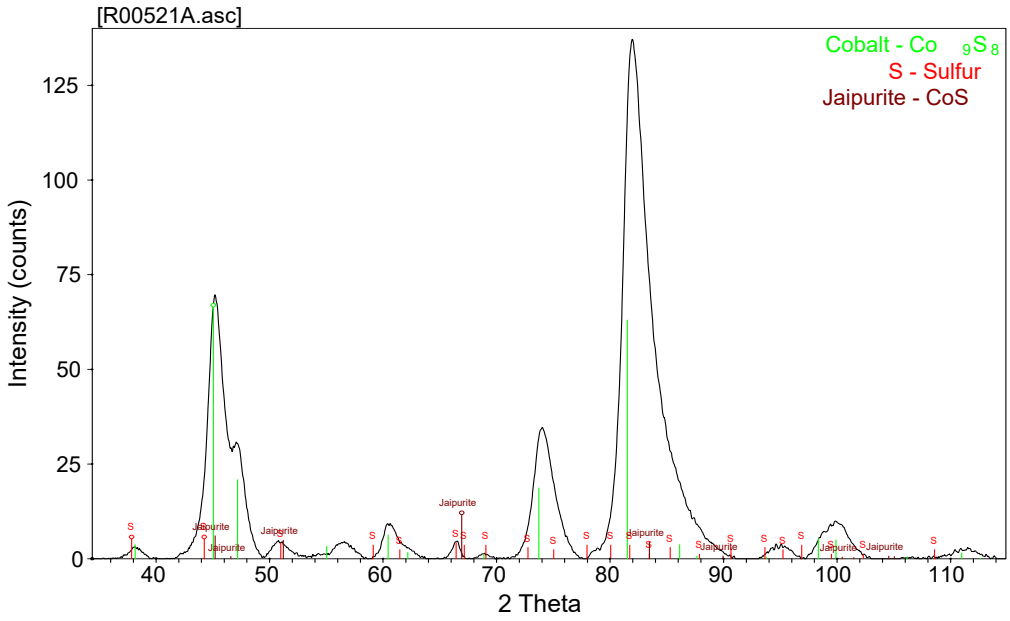

Figure 15. XRD data collected on the ground powder of sample 11-1, which was a sample of the reference material Co_9S_8 prepared at PNNL. The powdered sample was analyzed on a flat sample holder. XRD measurements revealed the presence of Co_9S_8, with possibly CoS or S as impurities. The pattern is background-subtracted. Data collected using Cr radiation (2.2897 Å).

3.2.1.5 Co_2C Reference Samples (16-1, 17-1, 18-1, 18-2, 19-2)

During the course of the project, a reference sample of Co_2C was prepared for characterization by various techniques. XRD was utilized as an analytical technique to monitor the progress of the carbidization reaction, which was extremely slow. Sample 15-1 is metallic Co obtained by the reduction of cobalt oxide under H_2. The pattern in Figure 16 confirms that elemental Co was obtained prior to carbidization.

Following reduction, Co(0) was reacted with CO to produce Co_2C. The XRD phase analysis shows that Co_2C formation continued throughout the experiment, while the amount of Co(0) in the product steadily decreased (Figure 17). The amount of Co_2C increased substantially but Co(0) was still present in all samples.

From the semi-quantitative phase analysis of the XRD spectra, the estimated amount of Co metal from sample to sample was: ~75 wt% (16-1) $\rightarrow$ ~54 wt% (17-1) $\rightarrow$ ~37 wt% (18-1) $\rightarrow$ ~28 wt% (18-2) $\rightarrow$ ~20 wt% (19-1). Figure 18 illustrates that the concentration of unreacted Co(0) decreased in a non-linear fashion. This may be indicative of Co(0) conversion to Co_2C via the shrinking core mechanism, where increasing amounts of Co_2C formed at a particle surface increasingly impedes continued reaction.

3.2.2 Catalyst Samples

X-ray diffraction analysis of the Mo-Co-K-S RF-101 catalyst samples revealed that the samples were generally amorphous with very small intensity crystalline reflections superimposed on broad backgrounds. Analyses obtained from Micro-XRD measurements on pellet fragments wrapped in Kapton tape were unacceptably noisy. Better signal-to-noise ratios were achieved with scans performed on ground powders loaded in capillaries. In all of the reported patterns, the baseline was manually fit and subtracted prior to phase-matching. Figure 19 illustrates an example of raw diffractograms on sample 3-1 (unactivated RF-101) at various points in the pellet and is representative of the raw data. Figure 20 is representative of a baseline-subtracted pattern after baseline fitting. All of the diffractograms on the catalyst samples were background subtracted unless otherwise noted.

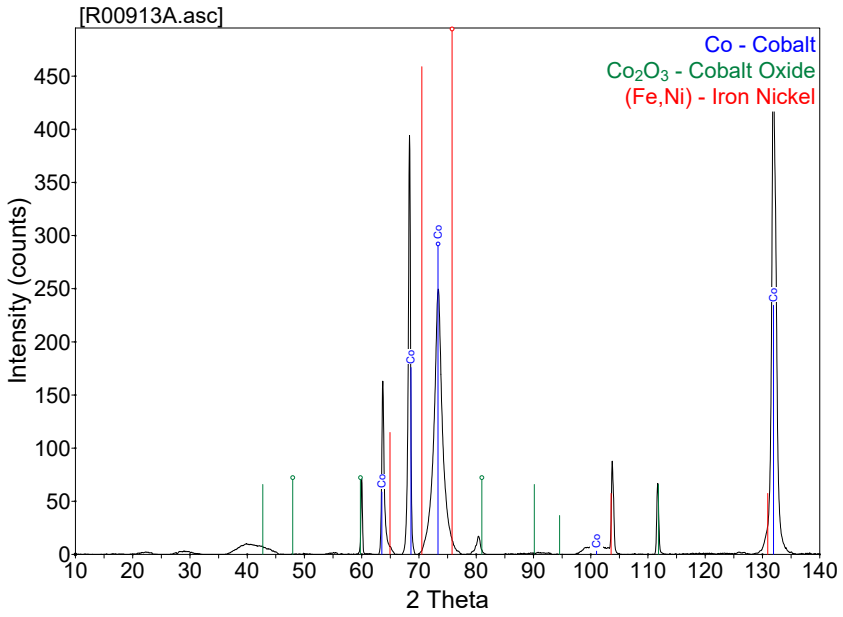

Figure 16. XRD_15-1: data collected on the ground powder on a flat sample holder showing the presence of elemental Co, traces of Co_3O_4, and possible contribution from the sample holder (FeNi). The pattern is background-subtracted. Data collected using Cr radiation (2.2897 Å).

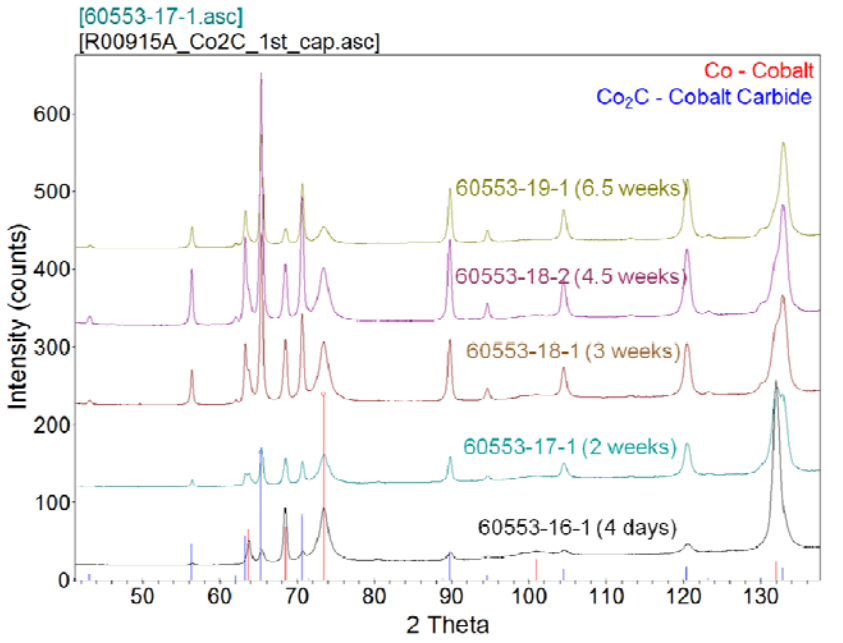

Figure 17. XRD data collected on ground powders loaded in glass capillaries showing the increasing presence of Co_2C and the concomitant decrease of elemental Co. Data collected using Cr radiation (2.2897 Å).

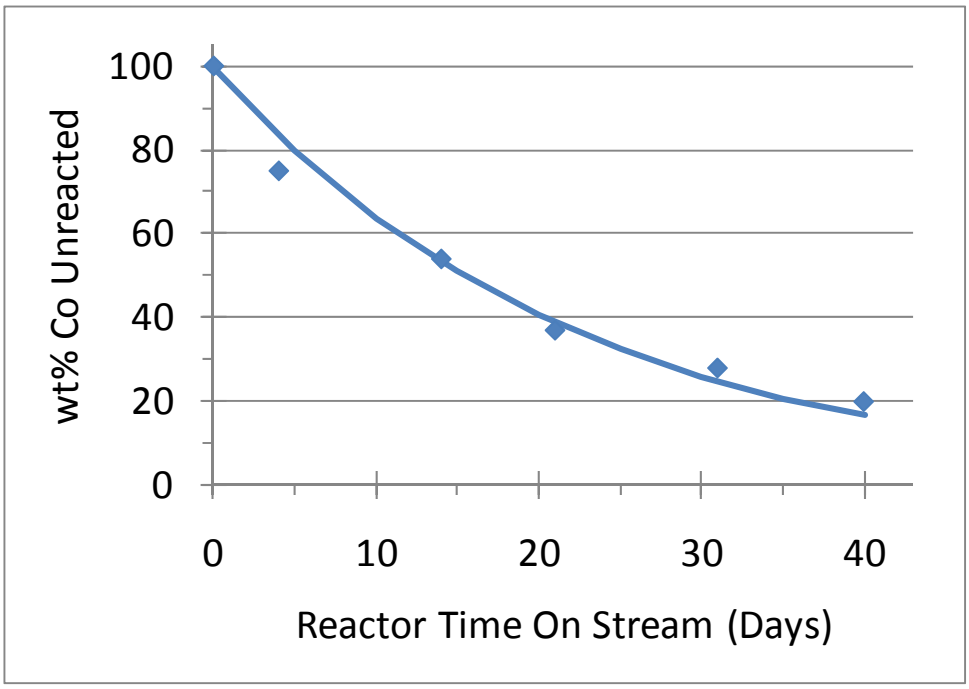

Figure 18. The amount of unreacted metallic Co remaining in the Co_2C synthesis reactor as estimated via XRD measurements of the samples and data illustrated in Figure 17.

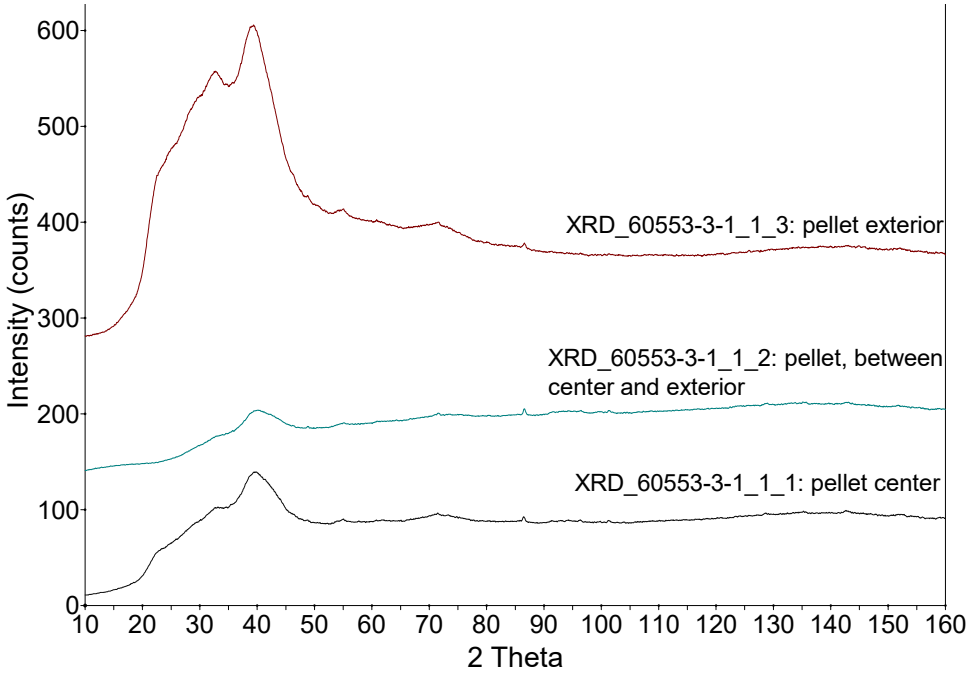

Figure 19. The raw XRD patterns collected during measurements at various points on a pellet of 3-1 (unactivated RF-101). The data was collected using Cr radiation (2.2897 Å).

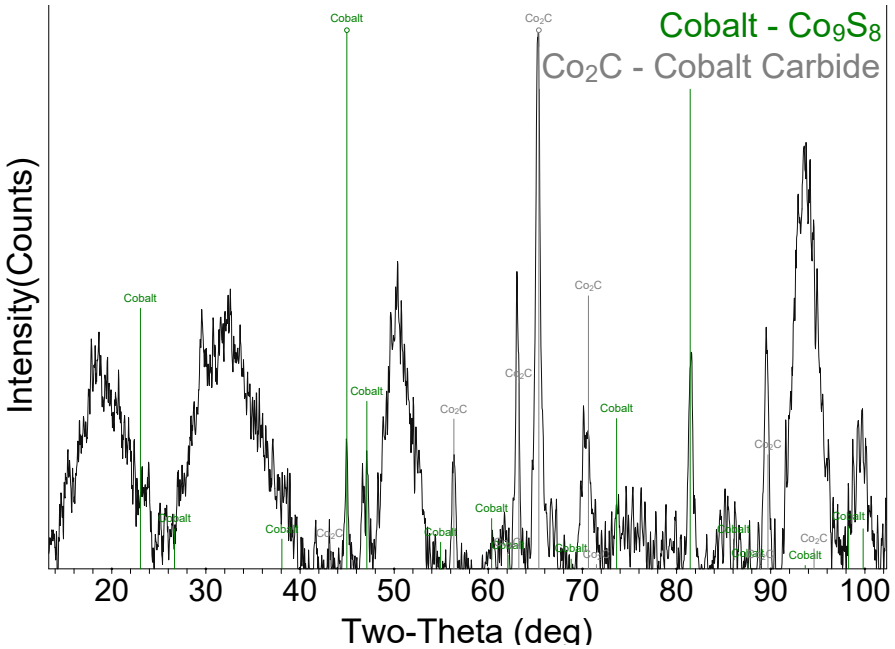

Figure 20. Background-subtracted pattern of sample 3-2_2_4 with viewcards of Co_9S_8 and Co_2C. Data collected using Cr radiation (2.2897 Å).

The large hump at ~42° 2-θ in Figure 19 is present in several samples. The hypothesis that the large amorphous hump was characteristic of the samples and not the sample holder (glass capillary or Kapton tape) was confirmed by running scans on a blank capillary as well as on Kapton tape placed on the sample holder. Neither the capillary nor the tape exhibited the large amorphous registry and, therefore, the hump was considered to be from the catalyst samples. Unfortunately, after extensive analysis, no positive identification could be made as to the identity of the poorly crystalline species that resulted in the broad peak.

3.2.2.1 Sample 3-1 (Unactivated RF-101)

Figure 21 illustrates data collected during analysis of sample 3-1, which was pelletized but unactivated RF-101. Figure 21(a) shows the results of XRD measurements on a sample of the 3-1 pellet ground and sealed in a thin walled capillary. The results of XRD measurements on the sample indicated the presence of CoS_2 and MoS_2. Next, measurements were performed on a single pellet that had been fractured. Measurements were taken at the exterior, center and part-way between the center and exterior radially to determine if differences in the crystalline phases could be observed within the pellet. The diffractograms measured at various points throughout the pellet exhibited similar crystalline phases. However, the best signal was obtained at the catalyst exterior. Thus, Figure 21(b) only

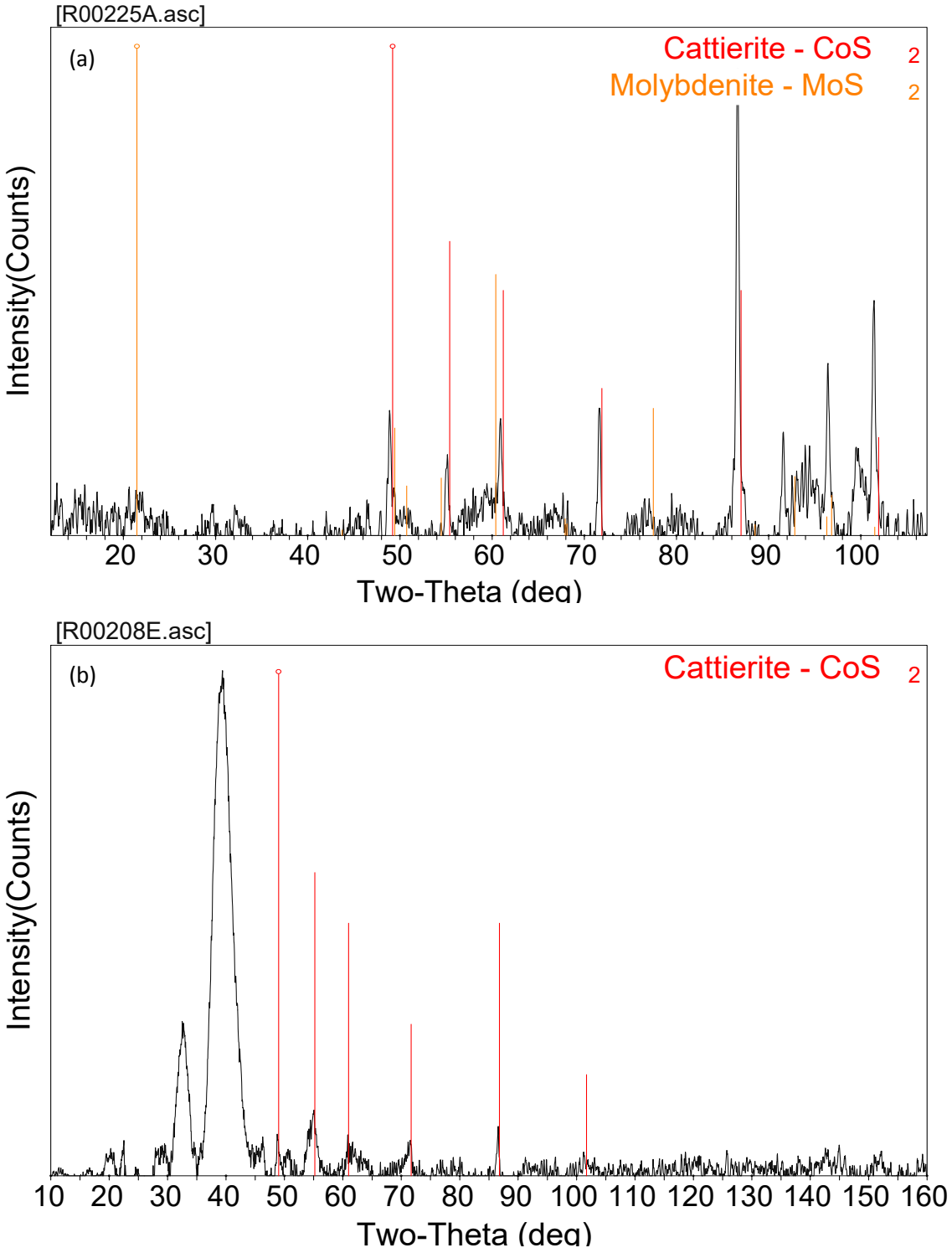

Figure 21. (a) Data collected on the ground powder of sample 3-1 (unactivated RF-101) in a capillary showing the presence of CoS_2 and MoS_2. (b) Data collected at the pellet exterior showing the presence of CoS_2. The data was collected using Cr radiation (2.2897 Å).

illustrates the diffractogram measured at the exterior of the pellet. Throughout the pellet, CoS_2 was identified. In addition, MoS_2 was found to be a likely match at the pellet center, but was less likely at the exterior. Co_9S_8 and CoS were also considered as possibilities throughout the pellet, but these two phases could not be correlated with any major reflections with certainty. Where the reflections for Co_9S_8 and CoS coincided with a major reflection peak in the sample, the reflections overlapped with each other, making positive confirmation impossible.

It is interesting to note that for sample 3-1, the large amorphous hump at approximately 42° 2-θ is present in the pelletized sample, but not in the sample that was ground to powder. Thus, the concentration of the species responsible for the hump may be significantly diluted by grinding and may only be present sporadically throughout the pellet. It is also interesting that differences in the crystallinity of the pellet appear to exist radially throughout the pellet. Presumably, the pellet should be homogenous throughout as sample 3-1 had not experienced heat treatment or activation prior to testing. The pressing process may have introduced inhomogeneities in the catalyst pellet.

3.2.2.2 Sample 4-1 (Activated RF-101 from near the top of the reactor)

Sample 4-1 was a sample of RF-101 that had been activated under syngas, but not utilized for the production of mixed alcohols for an extended time. Pellets comprising sample 4-1 had been located near the top of the mixed alcohol synthesis reactor. XRD data were collected on ground powder in a capillary as well as on a fragmented pellet. Analysis of the ground powder revealed the presence of Co_9S_8 and MoS_2 as shown in Figure 22(a). Co_2C and CoS_2 were possibly present at low concentrations. The raw patterns also exhibited the large, amorphous hump centered at about 42° 2-θ. This hump is similar to what was observed in sample 3-1 that could not be correlated with any expected crystalline phases.

Spatially resolved XRD analysis at different locations radially within a fractured pellet of sample 4-1 revealed that the signal was of higher intensity for the data collected at the exterior of the pellet. At the centered of the fractured pellet, Co_9S_8 and MoS_2 were identified while the presence of CoS_2 was also possible (see Figure 22(b)). Between the pellet center and the exterior, only Co_9S_8 was detected and identified. The same phases were found at the pellet exterior (4-1_2_3) as in the pellet center (Co_9S_8 and MoS_2, with possible presence of CoS_2). No Co_2C was found with certainty in this sample.

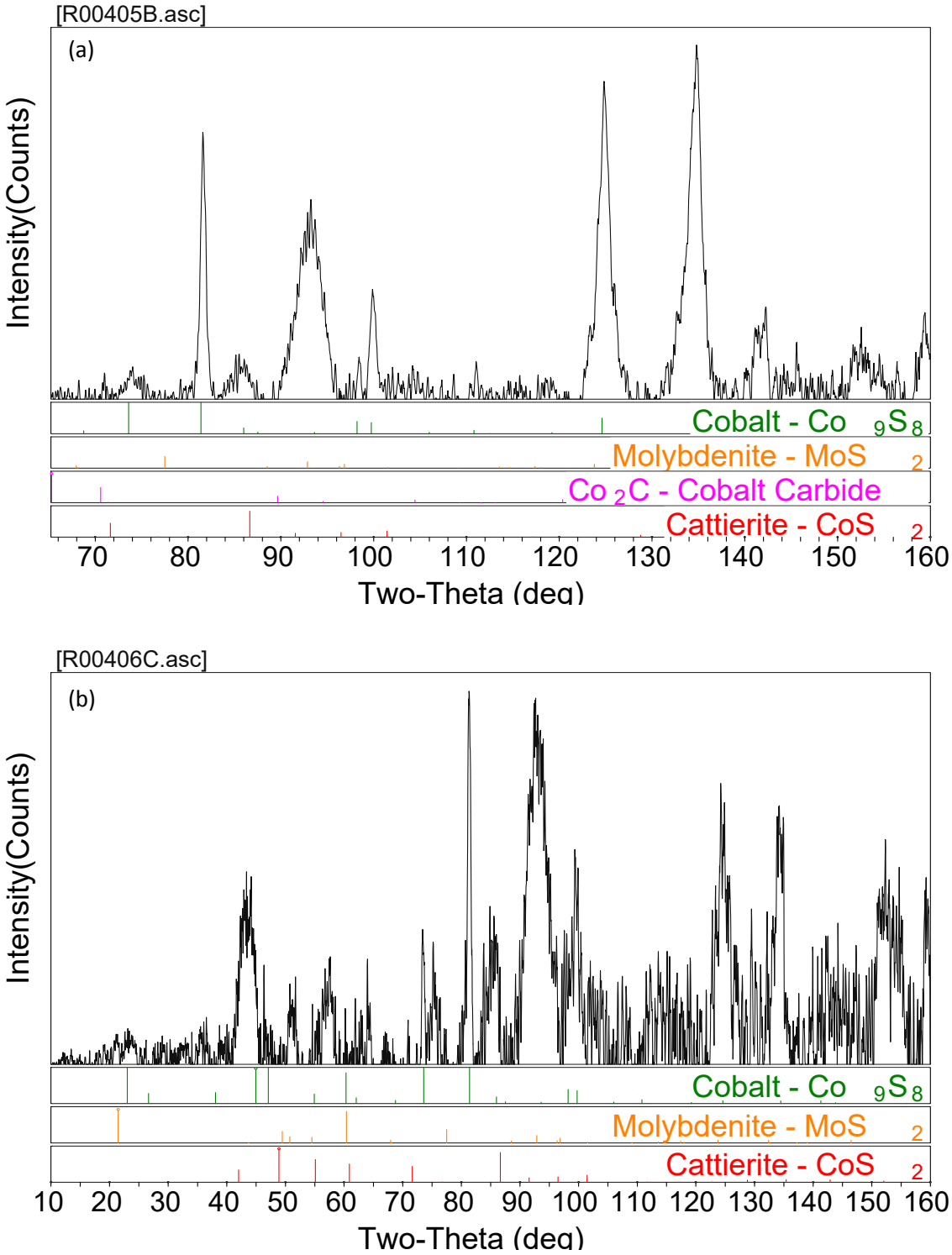

Figure 22. (a) XRD data collected from measurements on the ground powder of sample 4-1 (activated RF-101). (b) XRD data collected at the center of a fractured pellet of sample 4-1. The data was collected using Cr radiation (2.2897 Å).

3.2.2.3 Sample 4-2 (RF-101, activated, subjected to mixed alcohol synthesis for a long period)

Sample 4-2 was taken from the same reactor as 4-1 except that 4-2 pellets were located near the bottom of the reactor during activation. XRD measurements were performed on ground powder as well as on a fractured pellet. The XRD data collected on the ground powder revealed the presence of Co_9S_8 along with the possible presence of CoS_2 and MoS_2 (see Figure 23(a)). Co_2C, which would have exhibited a major reflection near 65° 2-θ, was not observed.

Next, a fractured pellet was analyzed at varying positions radially within the pellet. It was found that the signal was of higher intensity for the data collected at the exterior of the pellet. Interestingly, all of the patterns collected on the fractured pellet again exhibited the large, unassignable amorphous humps. At the pellet center, only Co_9S_8 and MoS_2 were identified. Between the pellet center and the exterior, Co_9S_8, MoS_2, and CoS_2 were identified as the crystalline phases present. At the pellet exterior as in the pellet center, Co_9S_8 and MoS_2 were detected, while CoS_2 was possible but not positively confirmed (see Figure 23(b)). Co_2C was specifically sought, but its presence was deemed to be unlikely at any of the points measured. Generally, the presence of Co_2C could not be confirmed in either 4-1 or 4-2.

3.2.2.4 Sample 3-2 (RF-101 near the top of the reactor used for mixed alcohol synthesis for ~4200 h)

Sample 3-2 consisted of pellets that had been collected from the top of the mixed alcohol synthesis reactor after being utilized for 4200 h. Data was again collected on a sample ground into powder as well as on a fractured pellet at various points radially within the pellet. XRD measurements collected on the ground powder revealed Co_9S_8 and Co_2C (see Figure 24(a)). The amorphous hump centered at about 42° 2-θ was again apparent when the exterior of the pellet was analyzed (Figure 24(b))

When the patterns collected at different locations of a pellet of 3-2 were compared, it was found that the signal was stronger for the scan run at the pellet center. In the center of the pellet, Co_9S_8 was probably present but was not matched with certainty (Figure 24(b)). Co_2C may have been present at very low concentration at the pellet interior given the presence of the peaks at approximately 65° and 62° 2-θ. However, it was difficult to definitively identify Co_2C at any point radially within the pellet, including the exterior. The definitive presence of Co_2C in the ground powder but not at any point measured on the fractured pellet may suggest that Co_2C formation is highly localized. The areas of the

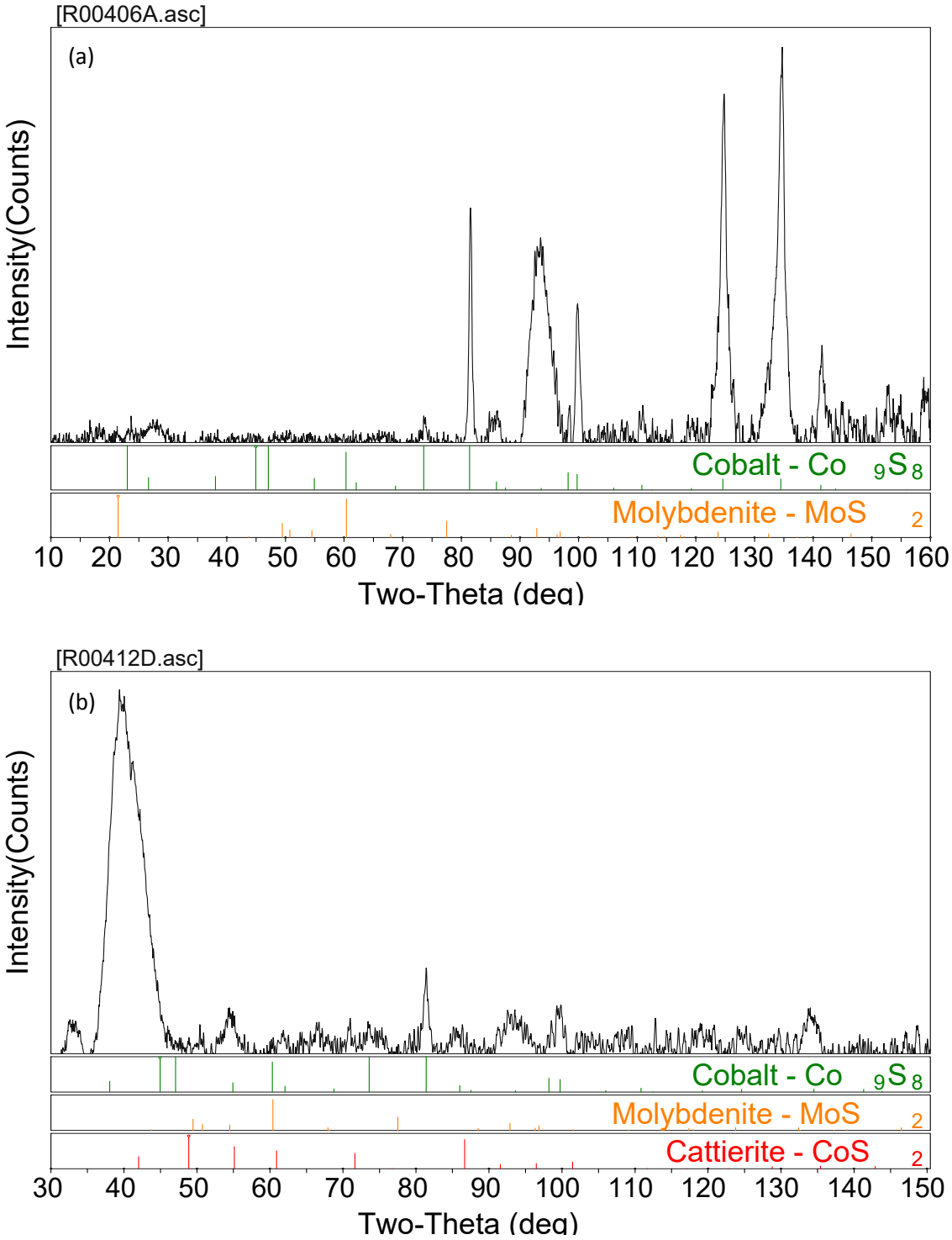

Figure 23. (a) Data collected during XRD measurements on ground powder of sample 4-2 in a capillary. The data is shown with the tickmarks for Co_9S_8 and MoS_2. (b) Data collected during XRD measurements at the pellet exterior with the tickmarks of Co_9S_8, MoS_2, and CoS_2. The data was collected using Cr radiation (2.2897 Å).

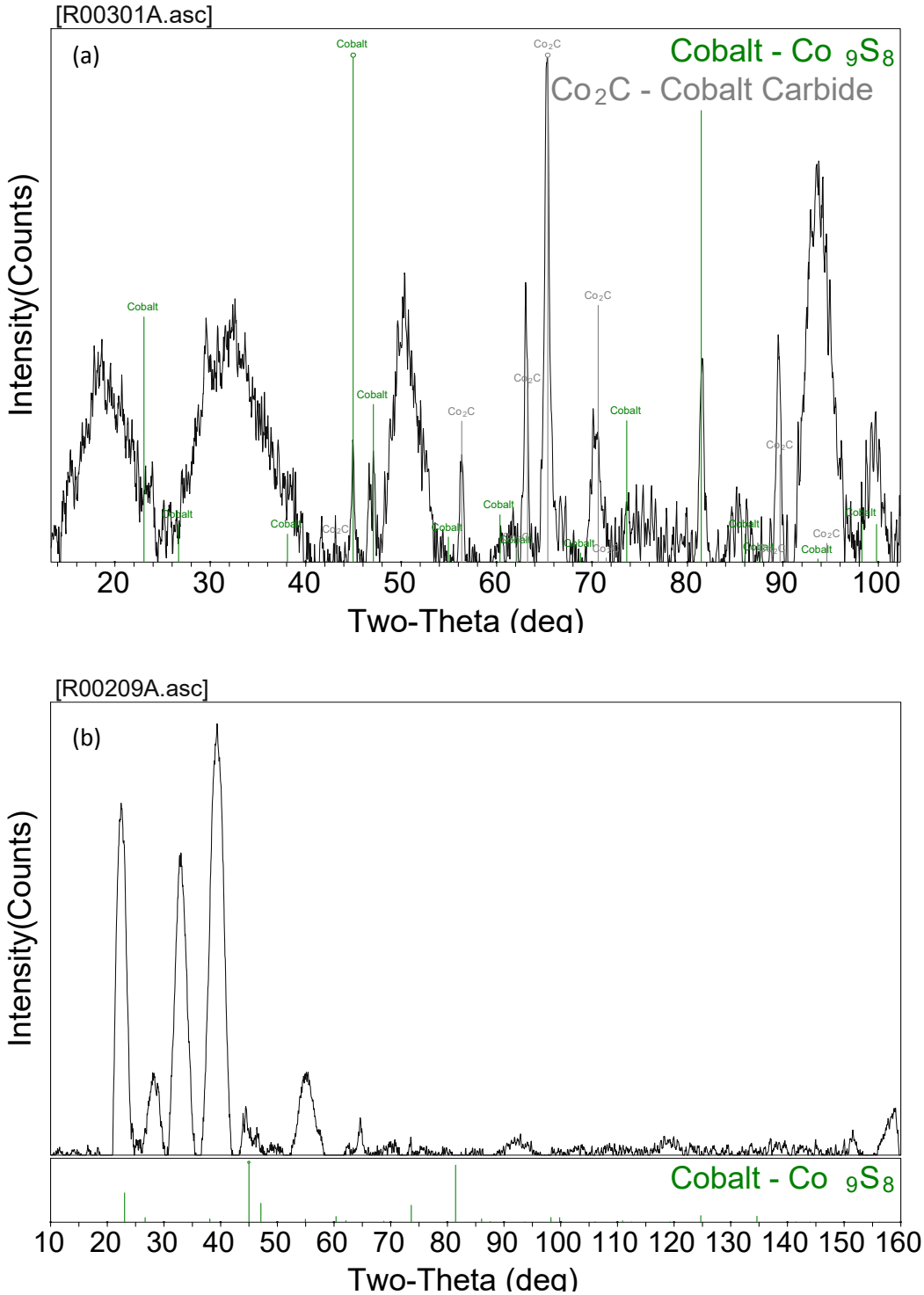

Figure 24. (a) XRD measurements collected on ground powder of sample 3-2 showing the presence of Co_9S_8 and Co_2C. (b) XRD data collected at the center of fractured pellet showing the presence of Co_9S_8. Co_2C may be present in low concentration as evidenced by the peak at approximately 65° 2-θ. The data was collected using Cr radiation (2.2897 Å).

fractured pellet scanned may have been relatively low in Co_2C while, speculatively, other areas may have contained much greater concentrations of the Co_2C phase. The localized model of Co_2C formation may fit with the observation of Co clusters revealed by SEM/EDS measurements.

3.2.2.5 Sample 3-3 (RF-101 near the bottom of the reactor used for mixed alcohol synthesis for ~4200 h)

Sample 3-3 consisted of pellets that had been utilized to produce mixed alcohols from syngas for approximately 4200 h. While the same reactor run produced samples 3-3 and 3-2, sample 3-3 was located near the bottom of the reactor. XRD measurements were performed on powder produced by grinding a pellet as well as points inside of a fractured pellet. The data collected on the ground powder sample of 3-3 revealed only the presence of Co_2C with certainty. However, Co_9S_8 and MoS_2 were also considered as shown in Figure 25(a). While the presence of Co_9S_8 seemed to be more likely than MoS_2, both phases were missing at least one of the major reflections associated with the phase.

The XRD data obtained from various points radially within a fractured pellet revealed that the signal was of higher intensity for the data collected at the exterior of the pellet. Data collected in the pellet center showed very weak signal. Only Co_2C was identified with certainty throughout the pellet from the interior to the exterior. The presence of Co_9S_8 was also a possibility. In addition to Co_9S_8 and Co_2C, the expected reflections of MoS_2 are shown in Figure 25(b) because some minor reflections match the diffractogram (e.g. between 90-100° 2-θ). However, the major reflections of MoS_2 do not match the sample diffractogram, which makes it unlikely that crystalline MoS_2 was present.

3.2.2.6 Sample 3-4 (RF-101 with methanol co-feed)

Sample 3-4 was another sample of RF-101 that had been utilized to produce mixed alcohols under typical synthesis conditions except with addition of methanol to the feed stream. Measurements were again taken on a sample of ground powder as well at various spots within a fractured pellet. In the pattern collected on the ground powder in a capillary, Co_9S_8 was identified. MoS_2 as well as CoS_2 were also possible, but, as shown in Figure 26(a), the match was not absolute. Interestingly, Co_2C was not detected in the ground material diffractogram.

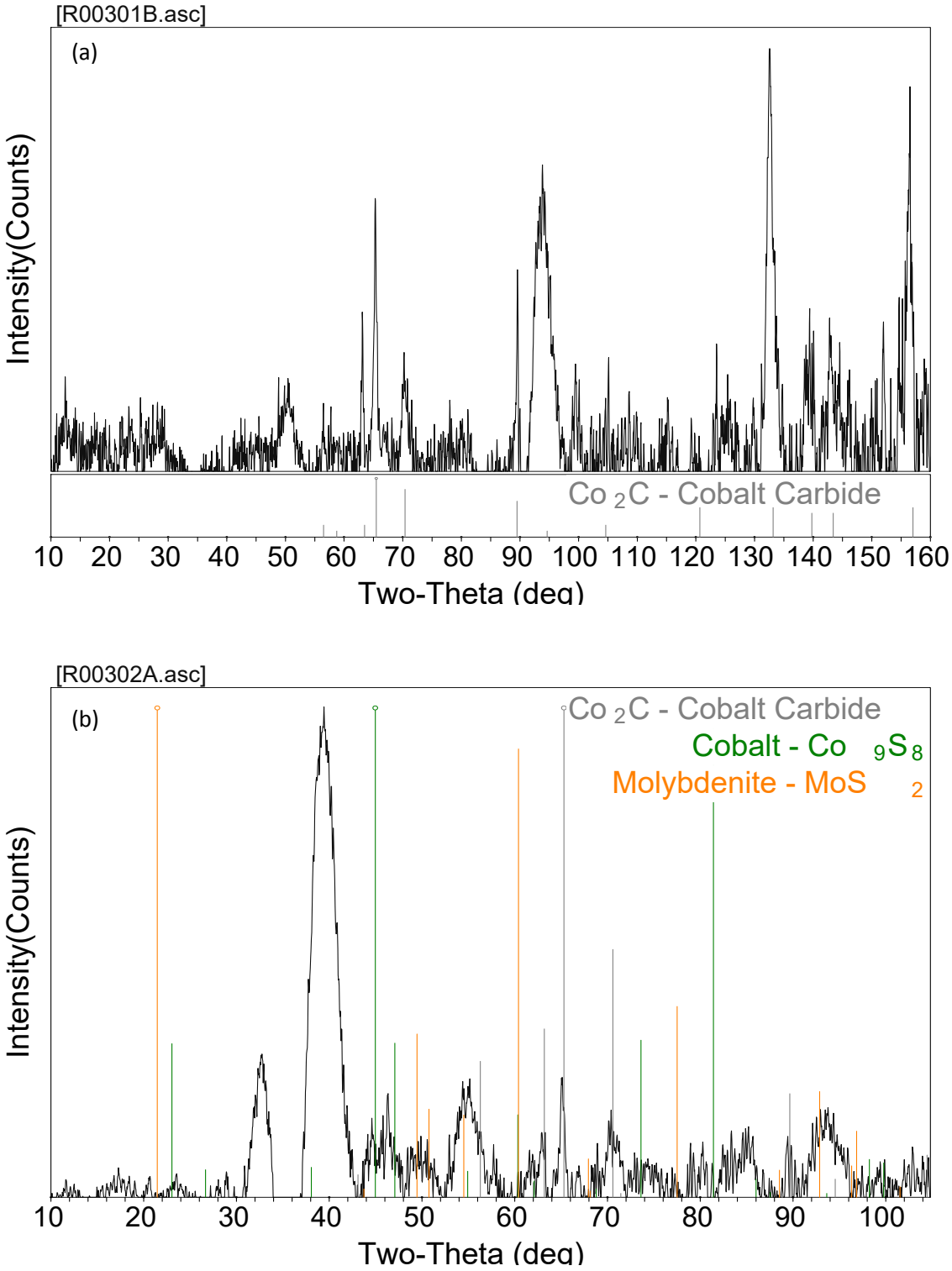

Figure 25. (a) XRD data collected on ground powder from sample 3-3 showing the presence of Co_2C. (b) Diffractogram of data collected at the pellet exterior with the tickmarks of Co_9S_8, Co_2C, and MoS_2. The data was collected using Cr radiation (2.2897 Å).

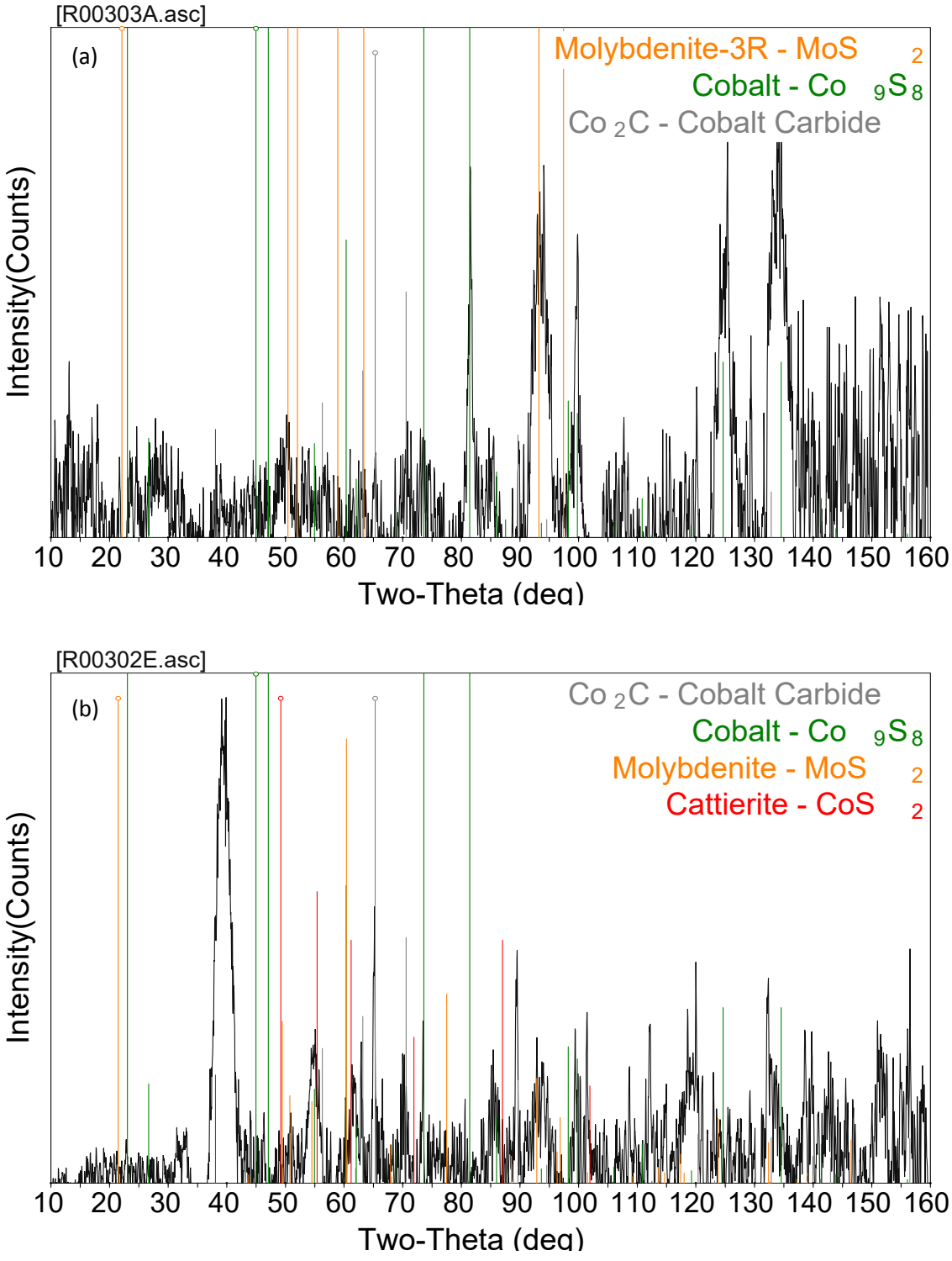

Figure 26. (a) XRD data collected on the ground powder of sample 3-4 illustrating the presence of Co_9S_8 and MoS_2 as well as the tickmarks for Co_2C for comparison. (b) XRD data collected at the exterior of a fractured pellet with the tickmarks of Co_9S_8, Co_2C, MoS_2, and CoS_2. The data was collected using Cr radiation (2.2897 Å).

When the diffractograms produced from XRD measurements at various points within a fractured pellet were analyzed, it was determined that the data collected at the fractured pellet exterior was different than the diffractograms produced from measurements within the pellet. However, at the exterior of the pellet, Co_2C was found (see Figure 26(b)), which was not detected at points inside the pellet. At the center of the pellet, only the presence of Co_9S_8 was confirmed. MoS_2 and CoS_2 were also potentially present throughout the pellet, but positive identification could not be made. The identification of the Co_2C only at the exterior of the pellet is a strong indication that only the outside of the pellet participated in any catalytic reactions.

3.2.2.7 Sample 9-1 (RF-101, used for mixed alcohol synthesis with MeOH and H_2S co-feed)

Sample 9-1 consisted of RF-101 that had been utilized for mixed alcohol synthesis for about 5 days. Methanol and 47 ppm H_2S were added to the feed stream in order to determine if the aging effects associated with added methanol could be mitigated through the simultaneous addition of a sulfiding agent. Similarly to the samples discussed previously, sample 9-1 was run both as ground powder as well as a fractured pellet.

XRD measurements on the ground powder sample of 9-1 showed the presence of Co_2C and Co_9S_8. Additionally, Montmorillonite, which was a major component of the Bentolite® binder, was possibly present (see Figure 27(a)).

In the center, Co_9S_8 and the binder were observed as likely matches as illustrated in Figure 27(b). Co_2C was not detected at the pellet center. In the data collected between the pellet center and exterior, the binder, Co_2C, and $Mo_{15}S_{19}$ were identified. Sulfides Co_4S_3 or Co_9S_8 were also deemed to be possible at this location. At the exterior, Co_9S_8, MoS_2, Co_2C, and Montmorillonite from the clay binder were identified.

3.2.2.8 Comparison of Co_2C content in samples 3-4 and 9-1

Co_2C formation was hypothesized by Range Fuels as a mechanism for catalyst deactivation. Methanol, when co-fed to the reactor with syngas, was known to have an aging effect on the catalyst. Thus, the methanol may have accelerated the formation of Co_2C. In order to mitigate or eliminate the growth of Co_2C, H_2S was added to the reactor during the run in an attempt to keep the catalyst sulfided, thereby eliminating the formation of Co_2C.

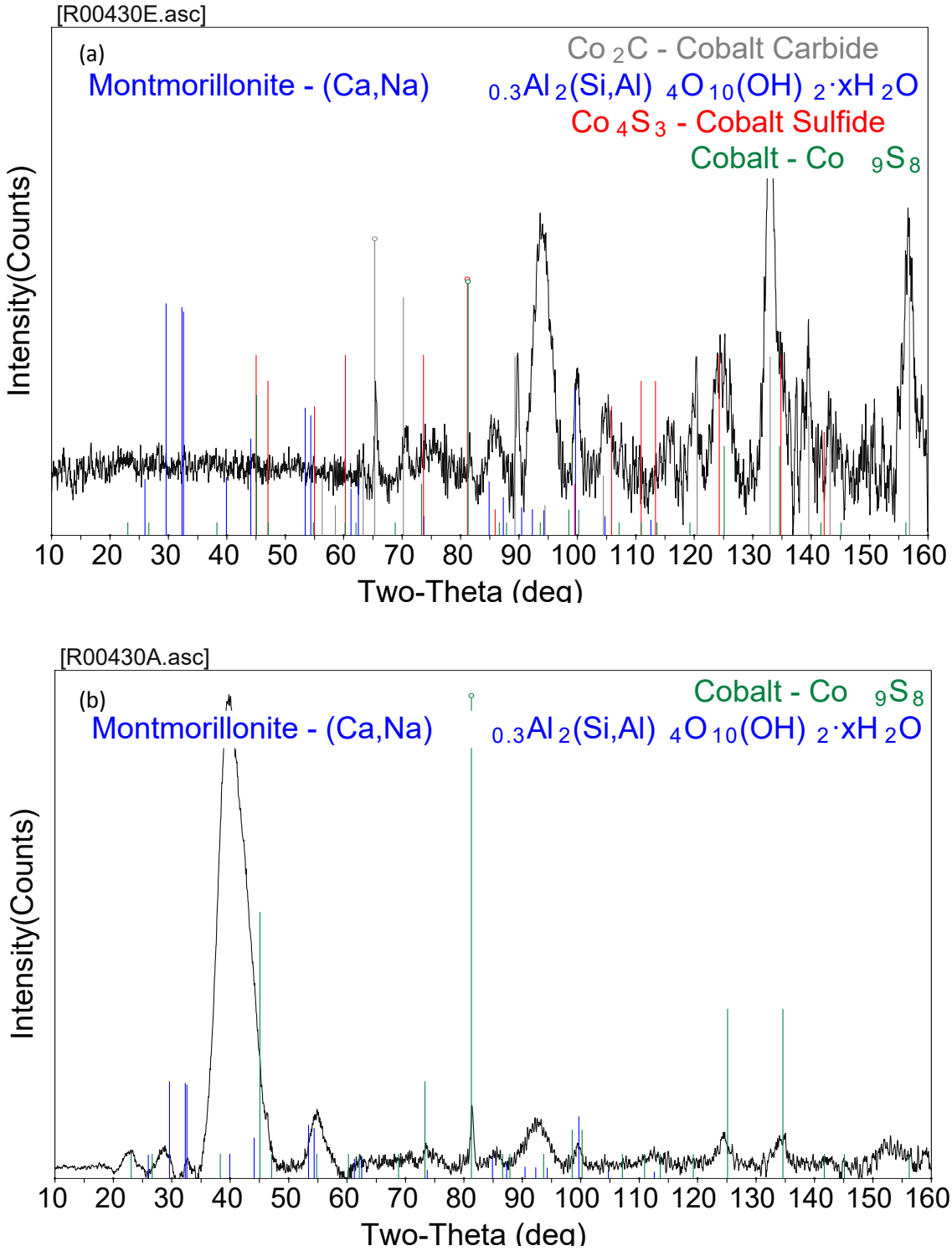

Figure 27. (a) XRD data collected on the ground powder of sample 9-1 showing the presence of Co_2C and Co_9S_8, as well as the possible presence of Montmorillonite from the clay binder. (b) Data collected at the pellet center with the tickmarks of Co_9S_8 and Montmorillonite from the binder. The data was collected using Cr radiation (2.2897 Å).

A determination of whether the addition of H_2S to the syngas feed stream would diminish or eliminate the concentration of measureable Co_2C at the exterior of the catalyst can be made by comparing samples 9-1 (methanol and H_2S co-feed) and 3-4 (methanol co-feed). This comparison revealed that there are similar concentrations of crystalline Co_2C at the exterior of both samples. Therefore, co-feeding 47 ppm H_2S did not inhibit the formation of the crystalline Co_2C phase (see Figure 28). Higher H_2S feed concentrations might be more effective.

As mentioned previously, Co_2C was not observed in samples 4-1 or 4-2, which had been activated but not utilized for mixed alcohol production for an extended period. However, Co_2C was observed radially throughout the pellets that had been utilized for mixed alcohol production for ~4200 h (samples 3-2 and 3-3). Therefore, Co_2C most likely forms with longer times on stream in the mixed alcohol synthesis reactor as well as during accelerated aging via co-feeding methanol regardless of the addition of 47 ppm H_2S to the feed stream.

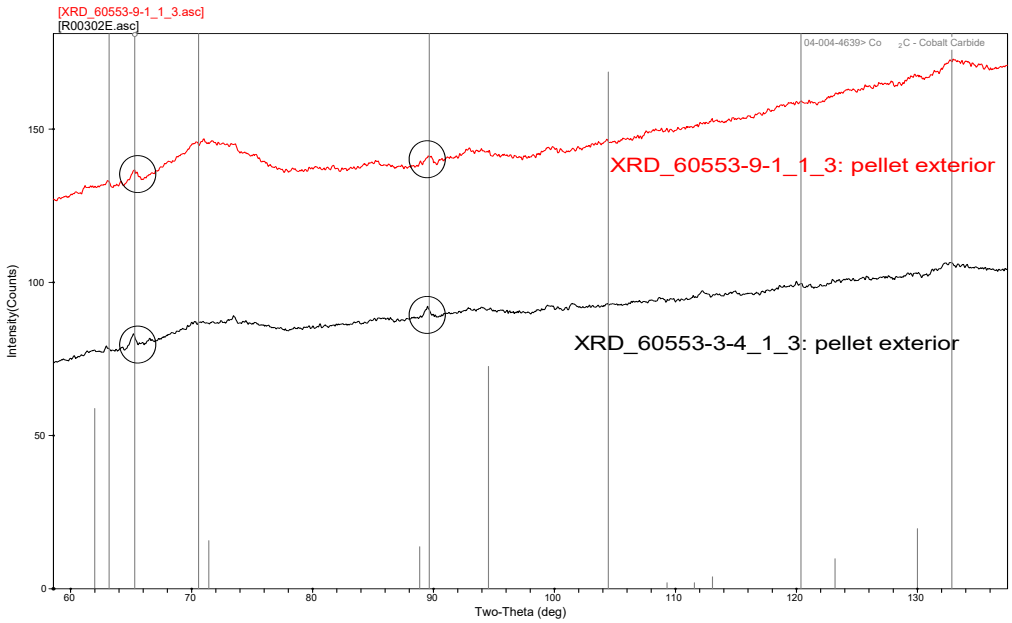

Figure 28. Comparison of the raw XRD patterns (not background subtracted) of samples 3-4 and 9-1 produced by XRD measurements at the pellet exteriors. The strongest Co_2C peaks are marked with black circles. No apparent difference was observed in the concentrations of Co_2C. Data collected using Cr radiation (2.2897 Å).

3.2.2.9 Analysis of Binder in Catalytic Samples

The Bentolite® binder consisted largely of Montmorillonite, which is a form of bentonite. Additionally, Tridymite (SiO_2) as well as forsterite (Mg_2SiO_4) were possibly present (see Figure 14). In fresh, unactivated RF-101 (sample 3-1), it is obvious that some features of the binder pattern contributed to the XRD spectrum of the pelletized sample (Figure 29). The binder may also have been present in the patterns of samples 4-1, 4-2, and 3-3 (see the reflection at 2-θ ~33° in Figure 30). However, the large amorphous humps present in many of the actual catalyst samples cannot be attributed to the binder, and are most likely due to an unknown amorphous content in the catalysts. It is interesting to note that the crystalline nature of the binder changes significantly upon activation, which may indicate that the binder is not inert.

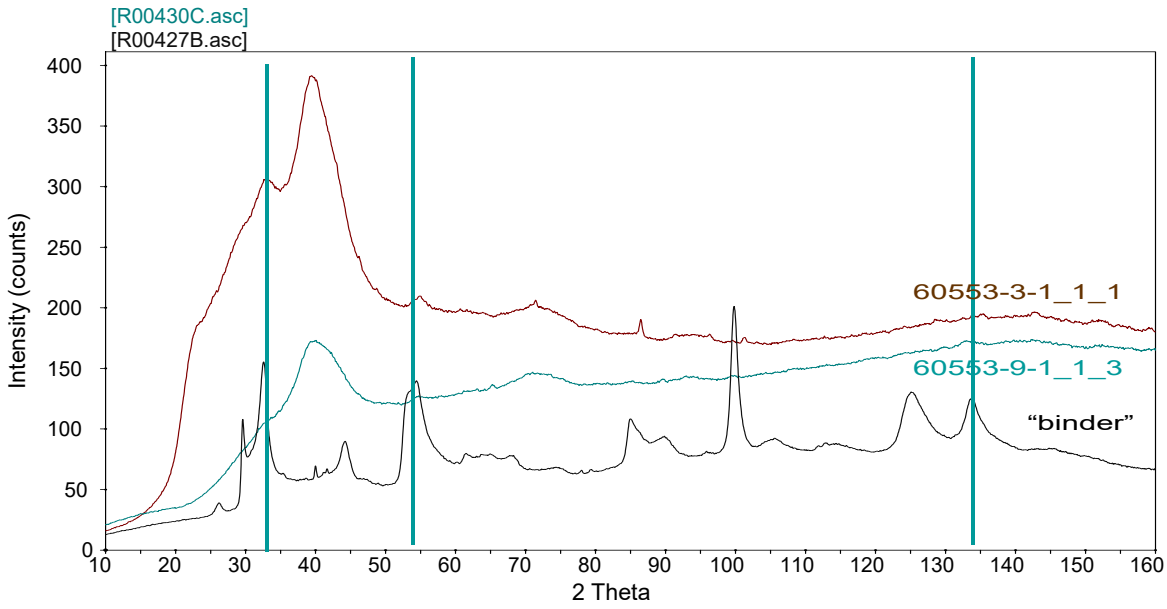

Figure 29. Overlay of catalyst raw patterns (not background subtracted) of 9-1 and 3-1, and the binder pattern. The major binder reflections coincident with catalyst reflections are marked with blue vertical lines. Data was collected using Cr radiation (2.2897 Å).

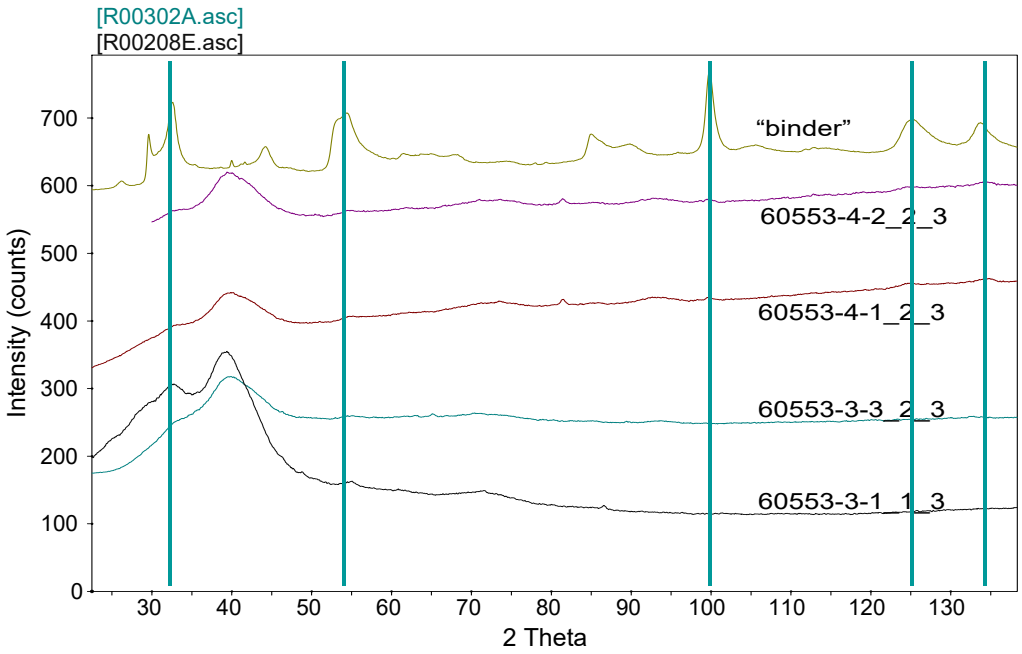

Figure 30. Overlay of catalyst raw patterns (not background subtracted) of samples 3-1, 3-3, 4-1, and 4-2, as well as the binder pattern. The major binder reflections coincident with catalyst reflections are marked with blue vertical lines. Data was collected using Cr radiation (2.2897 Å).

3.2.3 Summary of crystalline phases identified in all samples analyzed

The following is a brief synopsis of the crystalline phases identified in each of the analyzed samples.

3.2.3.1 Reference Samples

- **3-5** – *K_2MoS_4 reference material*: K_2MoS_4 was identified as the major phase but was not the only crystalline phase present. $CaSO_4$, as well as Si, C, and SiC may also have been present.
- **9-2** – *K_2CO_3 used in the preparation of RF-101*: K_2CO_3 was present with some $K_2CO_3 \cdot 1.5H_2O$.
- **9-3** – *Bentolite® binder*: Montmorillonite (bentonite; $(Ca,Na)_{0.3}Al_2(Si,Al)_4O_{10}(OH)_2 \cdot xH_2O$) was identified as the major crystalline phase with Tridymite (SiO_2) and forsterite (Mg_2SiO_4) also possibly present.
- **11-1** – *Co_9S_8 prepared in the open atmosphere*: The main phase was Co_9S_8 along with possibly CoS or S also present in small amounts.
- Time dependent Co_2C preparation reference samples
    - **15-1** – *Reduced Co*: The main phase was elemental Co with traces of remaining Co_3O_4.
    - **16-1** – *TOS 4 days in Co_2C reactor* : ~75 wt% Co and ~25 wt% Co_2C
    - **17-1** – *TOS 2 weeks in Co_2C reactor*: ~54 wt% Co and ~46 wt% Co_2C

- **18-1** – *TOS 3 weeks in Co_2C reactor*: ~37 wt% Co and ~63 wt% Co_2C
- **18-2** – *TOS 4.5 weeks in Co_2C reactor*: ~28 wt% Co and ~67 wt% Co_2C
- **19-1** – *TOS 6 weeks in Co_2C reactor*: ~20 wt% Co and ~77 wt% Co_2C

3.2.3.2 Catalyst Samples

- **3-1** – *Unactivated RF-101*: Only CoS_2 and MoS_2 identified in the ground powder. In addition to these, Co_9S_8 was found in the center of pellet, and only CoS_2 at the exterior. Very little difference was observed within the pellet.
- **4-1** – *Activated RF-101 not utilized for mixed alcohol synthesis for an extended period and located near the top of the reactor*: Co_9S_8 and MoS_2 were identified while CoS_2 was possible (although CoS_2 was not observed in the off-center scan). Co_2C, if present, was low in concentration and could only be observed in the ground powder
- **4-2** – *Activated RF-101 not utilized for mixed alcohol synthesis for an extended period and located near the bottom of the reactor*: Co_9S_8 and MoS_2 were identified. CoS_2 and possibly Co_2C were only seen closer to exterior but were lower in concentration as they were not detected in the exterior scan.
- **3-2** – *Activated RF-101 utilized for mixed alcohol synthesis for ~4200 h and located near the top of the reactor:* Co_9S_8 and Co_2C were identified as main phases from analysis of the ground powder. In contrast to other samples, Co_2C was not detected at the pellet exterior.
- **3-3** – *Activated RF-101 utilized for mixed alcohol synthesis for ~4200 h and located near the bottom of the reactor:* Co_2C was identified, Co_9S_8 was a possible match, and MoS_2 was likely at the pellet exterior.
- **3-4** – *Activated RF-101 utilized for mixed alcohol synthesis with a methanol co-feed*: Co_9S_8 was identified as a match while MoS_2 and CoS_2 were other possible matches. At the exterior, Co_2C was observed but was not seen inside the pellet.
- **9-1** – *Activated RF-101 utilized for mixed alcohol synthesis with a methanol and H_2S co-feed:* Co_2C, Co_9S_8, and clay binder were observed in the ground powder. Co_9S_8 was observed in the interior of the catalyst pellet. Peaks attributed to the binder, Co_2C, and most likely $Mo_{15}S_{19}$ were identified between the pellet center and exterior. Additionally, Co_9S_8 was a possible match between the center and exterior. At the pellet exterior, Co_9S_8, MoS_2, and binder reflections were observed. Additionally, Co_2C was observed at the pellet exterior.

3.3 XPS Analysis Results

X-Ray Photoelectron Spectroscopy (XPS) was performed on the catalyst samples received from Range Fuels as well as selected reference samples. XPS measurements are sensitive to electrons with relatively low energies incapable of passing through the material. Thus, electrons detected by XPS are only from atoms at or very near the sample surface. The energies of the observed electrons are characteristic of both the elemental and chemical makeup of the surface of the sample. In other words, XPS can identify and quantify the surface concentration of elements as well as relay information on the chemical state of the observed elements. Information pertaining to the chemical nature of the elements is deduced via the binding energy (BE) of the electrons of the observed elements. By measuring the BE of the electrons, it was possible to deduce the chemical state of the elements via comparison with literature reported reference material values in some samples.

Table 3 reports the concentration of elements in catalyst samples received from Range Fuels as determined by XPS measurements. The concentrations are normalized to 100%. All of the catalyst samples received from Range Fuels except samples 3-2 and 3-3 are reported in Table 3. Samples 3-2 and 3-3 were analyzed by XPS but were found to be contaminated by oxygen due to atmospheric storage of the samples after the reactor was unloaded and prior to delivery to PNNL. The oxygen contamination was manifested by Mo in the +6 oxidation state, which was not observed in any of the other catalyst samples. Since the quantified results are normalized, erroneously high concentrations of oxygen as well as other altered surface species (such as increased concentrations of S present as sulfate) would result in incorrectly quantified elemental concentrations. Thus, samples 3-2 and 3-3 were omitted from Table 3.

Several of the measurements in Table 3 were performed in duplicate in order to test the reproducibility of the observed quantification. Generally, the reproducibility was excellent and within $\pm$ 10%. However, a notable exception existed in the quantification of the sulfate measured at points inside the catalyst pellets of samples 4-1, 4-2, and 9-1, in which reproducibility was not as good and concentrations trended high.

The lack of reproducibility in the concentration of sulfur present as sulfate may indicate a non-homogeneous distribution with localized pockets of relatively higher sulfate concentrations. The source

Table 3. The normalized atomic concentrations of elements at the surface of various catalyst samples as measured by XPS.

Sample	Measurement Location[a]	Sampling[b]	C 1s	O 1s	S 2p[c]	S 2p[d]	K 2p	Co 2p3	Mo 3d
3-1	Exterior	P	34.9	30.6	0.6	20.4	2.3	3.5	7.6
3-1	Interior	P	34.9	31.1	0.8	19.8	2.4	3.6	7.4
4-1	Exterior	P	18.2	45.5	3.7	20.1	13.9	4.3	8.1
		D	19.5	44.7	3.2	20.4	13.4	4.2	8.1
4-1	Interior	P	17.5	41.7	5.3	21.7	15.1	4.8	9.0
		D	17.5	39.4	3.7	24.2	13.7	5.6	9.6
4-2	Exterior	P	19.3	44.9	3.5	20.0	13.1	4.6	7.7
		D	19.4	46.8	3.0	19.0	13.2	4.4	7.4
4-2	Interior	P	17.1	45.2	5.2	19.5	14.5	4.9	8.2
		D	17.8	42.7	3.9	21.8	13.4	5.2	8.7
3-4	Exterior	P	21.1	41.7	1.0	16.3	10.4	2.7	6.9
3-4	Interior	P	11.8	42.6	2.4	18.6	14.8	3.2	6.6
9-1	Exterior	P	22.2	39.5	2.7	22.3	14.6	3.6	9.8
		D	22.1	40.2	2.4	22.2	14.9	3.5	9.6
9-1	Interior	P	21.5	45.7	2.9	17.7	17.7	3.0	9.2
		D	21.5	42.3	4.5	19.3	18.7	2.3	10.1

[a]The location of the measurement on the pelletized sample
[b]The measurement reported; P = Primary and D = Duplicate
[c]Sulfur associated with the sample as sulfate
[d]Sulfur associate with the sample as sulfide

of these pockets of higher concentration is unknown. Sulfuric acid was used in the synthesis of the catalyst precursor, but sulfate from this source alone is not consistent with the XPS data because the unactivated catalyst precursor 3-1 contained less sulfate than activated and used catalysts. The increased concentration of sulfate is unlikely to have occurred because of air contamination[16] because these samples had not been exposed to air, as confirmed by EPR spectra (see below). In addition, if the

samples had been contaminated by air, the outside of the catalyst particles would be expected to have higher concentrations of sulfate. In contrast, the measured concentrations of sulfate at the exterior of the catalyst particles tended to be lower than the sulfate concentrations inside the catalyst pellets. It is unknown whether sulfate forms during activation or catalysis. It is also unknown if sulfate could be reduced under reaction conditions, although reports indicate that even Pt-catalyzed sulfate reduction occurs at much higher temperatures.[48]

Analysis of Table 3 also indicates that the K concentration in sample 3-1 (unactivated RF-101) was considerably lower than the activated catalyst samples. It is believed that this is because the potassium in 3-1 was most likely heterogeneously dispersed throughout the sample because the material was physically mixed and not yet activated. Lee et al.[14] reported that K_2CO_3 readily spread uniformly over MoS_2 under mixed alcohol synthesis reaction conditions. The distribution of the K throughout the RF-101 catalyst most likely results in the apparent increase in K concentration when comparing samples 3-1 (fresh RF-101) and 4-1 (activated RF-101).

Chemical information was also obtained through XPS measurements. Changes in the binding energy of electrons can indicate differences in the chemical nature and environment of the elements. Such differences are best analyzed via high resolution spectra focused on areas of elemental interest. For example, the Mo 3d electron region is illustrated in Figure 31. Furthermore, high resolution XPS plots are typically normalized and presented both “stacked” and “overlaid” in order to observe subtle differences in binding energies. Normalized stack and overlay plots of identical data are therefore presented. Of the catalyst samples received from Range Fuels, samples 3-2 and 3-3 were again omitted due to oxygen contamination.

The samples of RF-101 analyzed by XPS were not electrically conductive. Thus, the samples became charged while administering the electron beam during XPS analysis. Due to the fact that sample charging significantly alters the BE of the electrons, a charge reference was required in order to compare the samples. Initially, C was chosen as an internal charge reference. However, during the XPS investigation, it was determined that the chemical state of C was not constant throughout the catalysts. Instead, Mo was chosen as the charge reference due to the fact that Mo was always observed in the +4 oxidation state in the reported samples and appeared to be chemically stable. Therefore, all of the high resolution XPS spectra were charge referenced to the Mo 3 $d_{5/2}$ line at 228.5 eV. The features in

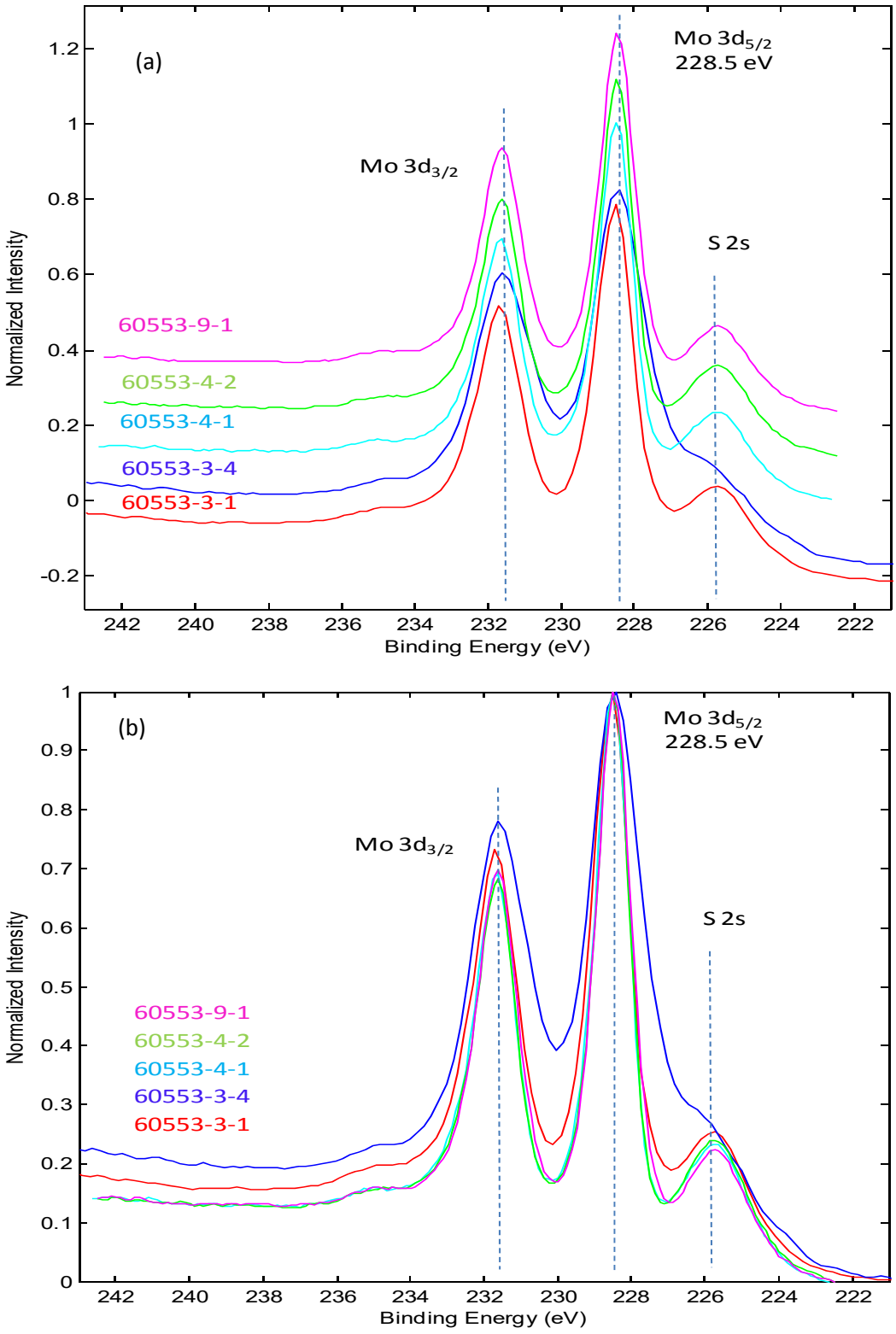

Figure 31. High energy resolution photoemission spectra of the Mo 3d region collected from the exterior of a catalyst pellet (a) Normalized stack plot. (b) Normalized overlay plot.

Figure 31 and Figure 32, which illustrate the high energy resolution spectra of the Mo 3d electrons, are aligned because they were used for charge referencing of the samples. Further justification for the selection of Mo as the charge reference of the XPS data is found in the lack of significant peak tailing or broadening in the Mo spectra presented in Figure 31 and Figure 32. The lack of significant peak trailing and or broadening in the spectra suggests a uniform Mo species.

The high resolution XPS region of the S 2p electrons is illustrated in measurements at the catalyst exterior in Figure 33 and at the catalyst pellet interior in Figure 34. XPS measurements taken at the exterior of the pellets indicate that there is likely a mixture of sulfur species present as S^{2-} (162.0 eV) and also possibly as a persulfide species (S_2^{2-}) due to the shoulder present at 162.5 eV.[20, 49] There are also apparent differences in the nature of the S at the exterior of the pellet when comparing sample 3-4 (methanol co-feed) with the other catalyst samples. The shoulder of the left side of the peak at higher BE, which is centered at approximately 162.5 eV, is not as well defined in sample 3-4 when compared with the other samples. This lack of definition is apparent in both the interior and exterior portions of the pellet (Figure 34). The missing shoulder feature may be indicative of a diminished concentration of the S_2^{2-} persulfide functionality. Range Fuels had hypothesized that the persulfide functionality may contribute in the mechanism of higher alcohol formation, so its absence may be related to the observed accelerated aging when methanol is co-fed.

Analysis of the sulfate feature in Figure 33 and Figure 34 also reveals slight differences in sample 3-4 when compared with other samples. The sulfate feature at 168.9 eV lines up reasonably well in samples 4-1 and 4-2 (activated RF-101 samples) and 9-1 (RF-101 with H_2S and methanol added during mixed alcohol synthesis testing). This indicates that the sulfate groups are of a similar nature in these samples. In contrast, the sulfate feature of the methanol aged catalyst 3-4 is shifted to lower binding energy, indicating a slight difference in the nature of the sulfate present. While it is difficult to deduce why the nature of the sulfate is different, it is interesting to observe that the sulfate peak in sample 3-4 appears to be more similar in binding energy to unactivated RF-101 (3-1) as opposed to any other activated catalyst sample.

The high resolution spectra of the Co 2p region of the exterior and interior regions of the catalyst pellet samples are shown in Figure 35 and Figure 36, respectively. Unfortunately, the oxidation state of Co in the catalyst samples was not revealed by XPS measurements as all of the Co species of interest have

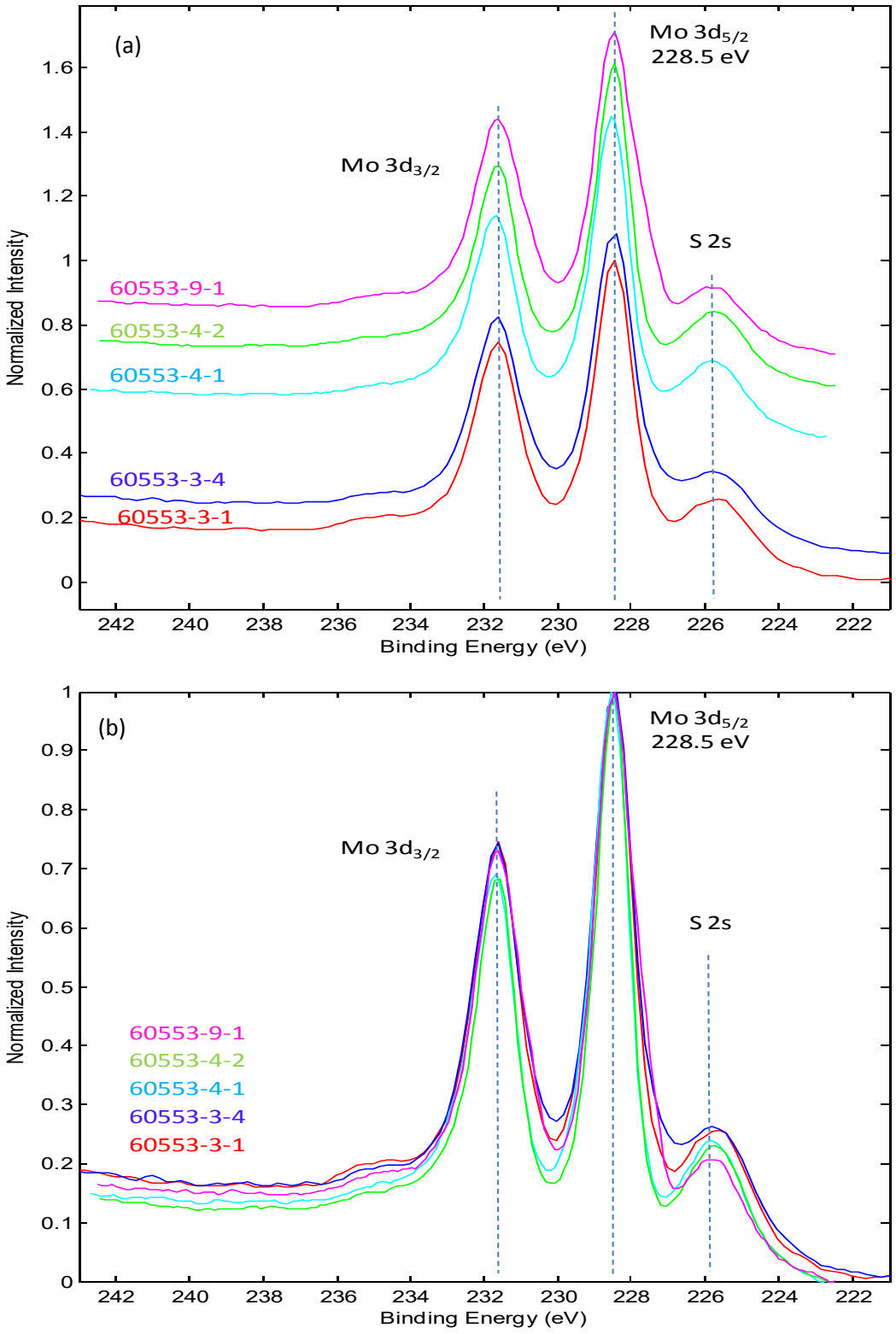

Figure 32. High energy resolution photoemission spectra of the Mo 3d region collected from the interior of a catalyst pellet (a) Normalized stack plot. (b) Normalized overlay plot.

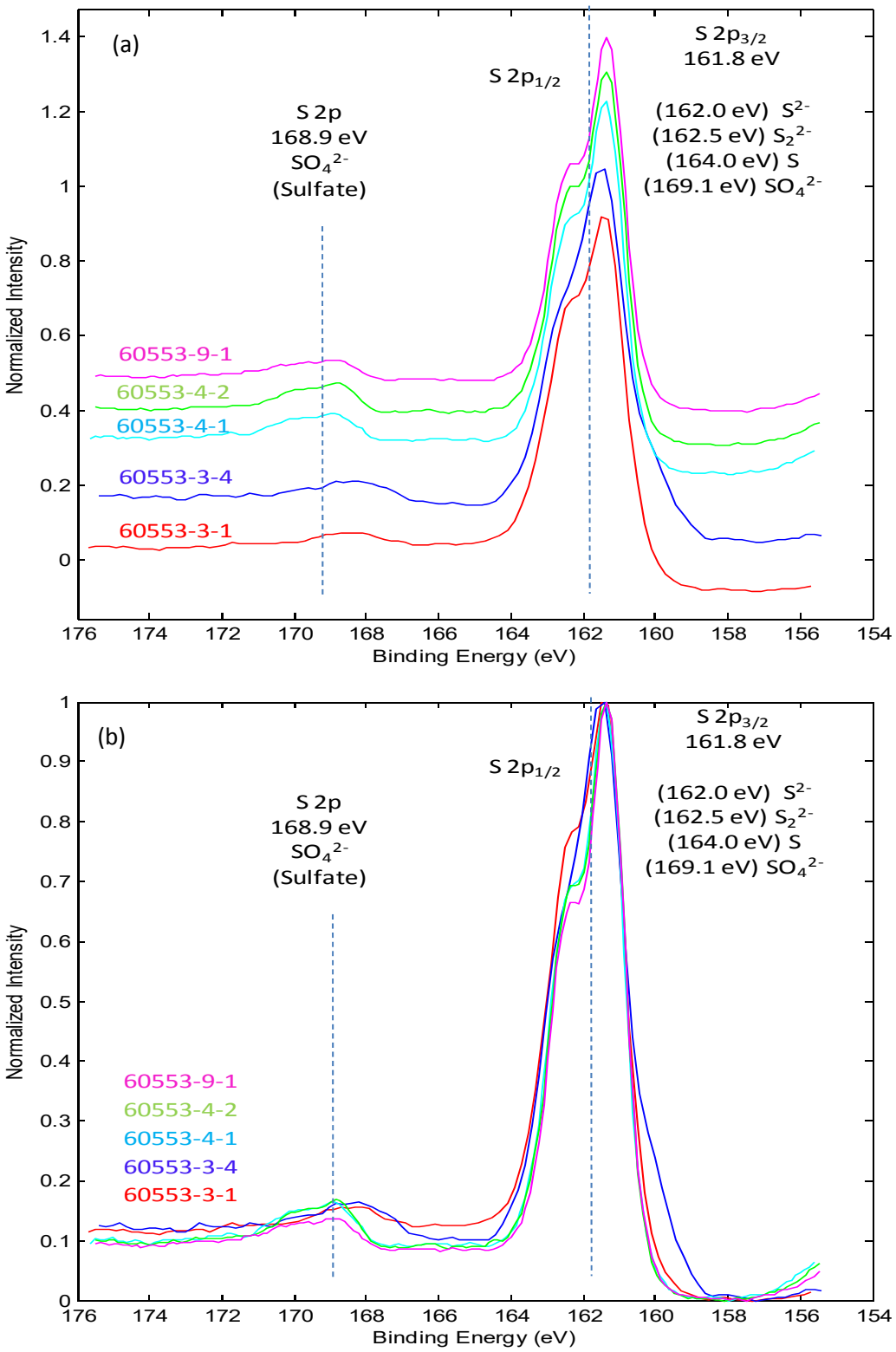

Figure 33. High energy resolution photoemission spectra of the S 2p region collected from the exterior of a catalyst pellet (a) Normalized stack plot. (b) Normalized overlay plot.

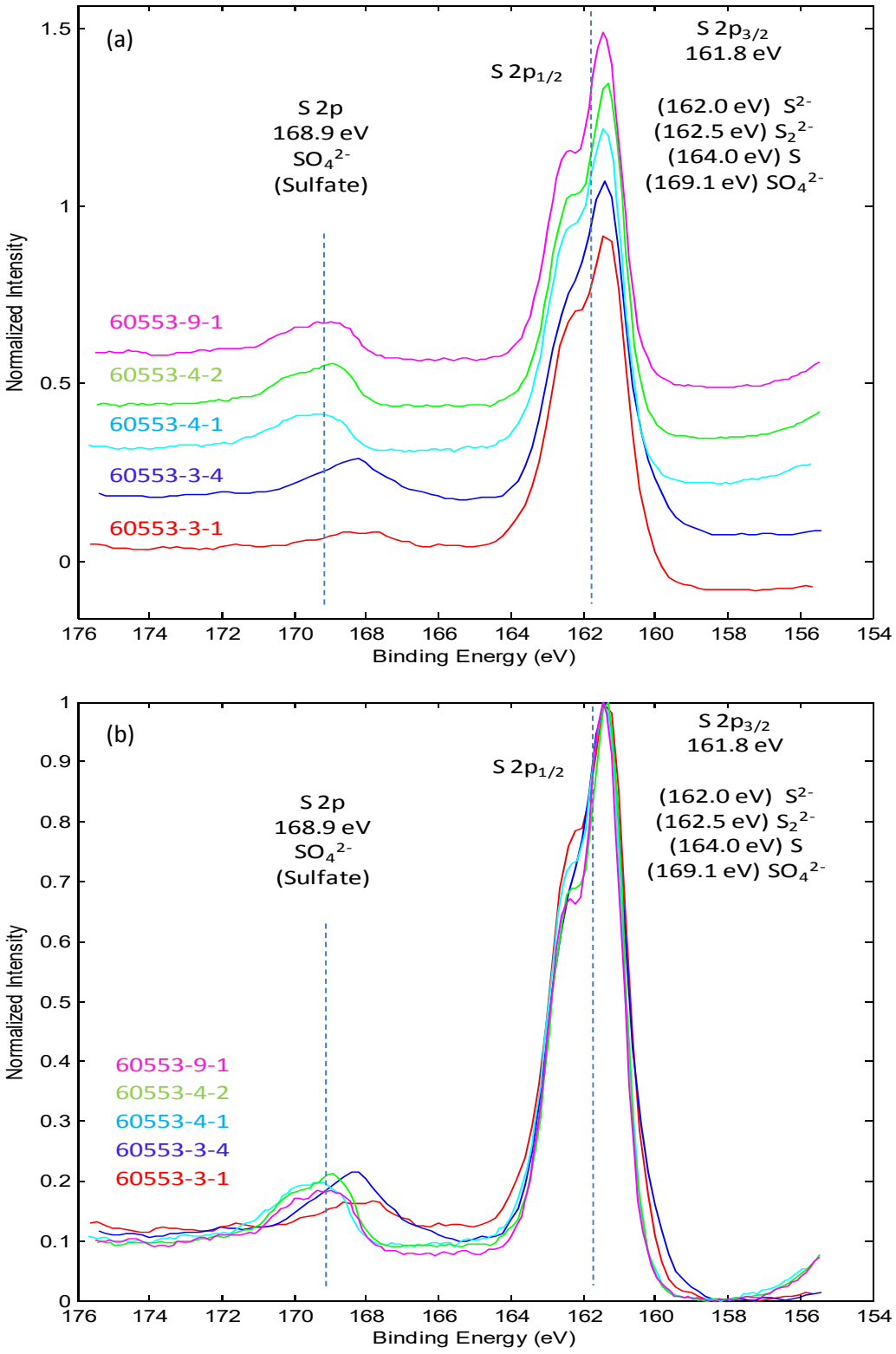

Figure 34. High energy resolution photoemission spectra of the S 2p region collected from the interior of a catalyst pellet (a) Normalized stack plot. (b) Normalized overlay plot.

nearly identical binding energies. For example, the major feature in the catalyst samples at 778.2 eV correlates with Co_9S_8 reference material 12-1 prepared by PNNL (not shown) as well as the reported literature value of Co_9S_8.[50] As illustrated in Figure 37, XPS analysis of metallic Co and Co_2C reference materials had similar features with the major response at 778.3 eV from the Co $2p_{3/2}$ electrons. Indeed, the binding energy of the 2p electrons in both metallic Co[51] and Co_2C[52] are reported to be 778.3 eV. Thus, elucidation of the state of the Co in the samples was not possible through XPS measurements.

While elucidation differentiation in the state of Co between Co(0), Co_9S_8, or Co_2C was not possible by XPS analysis, there were some observed differences in the Co 2p peak shape of certain samples. . Analysis of the normalized overlay plots of fresh RF-101 (3-1) and methanol aged samples (3-4) in Figure 35(b) and Figure 36(b) have an increased background in the XPS responses on the left side of the feature at 778.2 eV. The increased background may be indicative of an increased concentration of Co in the +2 oxidation state. Ramaswamy et al.[53] assigned a BE of 780.5 eV to Co^{+2} present as an oxide, probably CoO. XPS spectra of samples 3-2 and 3-3, which are known to have undergone air oxidation on storage, also show an increased background in this region, consistent with and increased concentration of oxidized cobalt. Alternatively, the increased background of the 3-1 and 3-4 samples in Figure 35(b) and Figure 36(b) could be due to an over layer on the surface of the sample, resulting in energy loss from the electrons and a change in the background relative to the other samples tested. Regarding the 3-4 sample, the over layer may be from carbon (coke) on the catalyst surface.

The high energy resolution XPS spectra for the K 2p and C 1s electrons are shown in Figure 38 and Figure 39. Figure 38 indicates that the state of the carbon and the potassium in samples 4-1, 4-2 and 9-1 are of a similar chemical nature at exterior and interior regions of the catalyst pellets. In contrast, the carbon signals in samples 3-1 and 3-4 are shifted to slightly lower binding energies. The difference in carbon binding energy between samples again illustrates the motivation for choosing Mo as the charge reference for the samples as opposed to carbon. The presence of carbon in the unactivated RF-101 sample (3-1) was likely from the K_2CO_3 potassium precursor, the binder material, or even atmospheric contamination. The carbon from the 3-4 sample was most likely carbon present after reaction, which was not carbonate. The results of the carbon XPS data suggests that the carbon present at the exterior

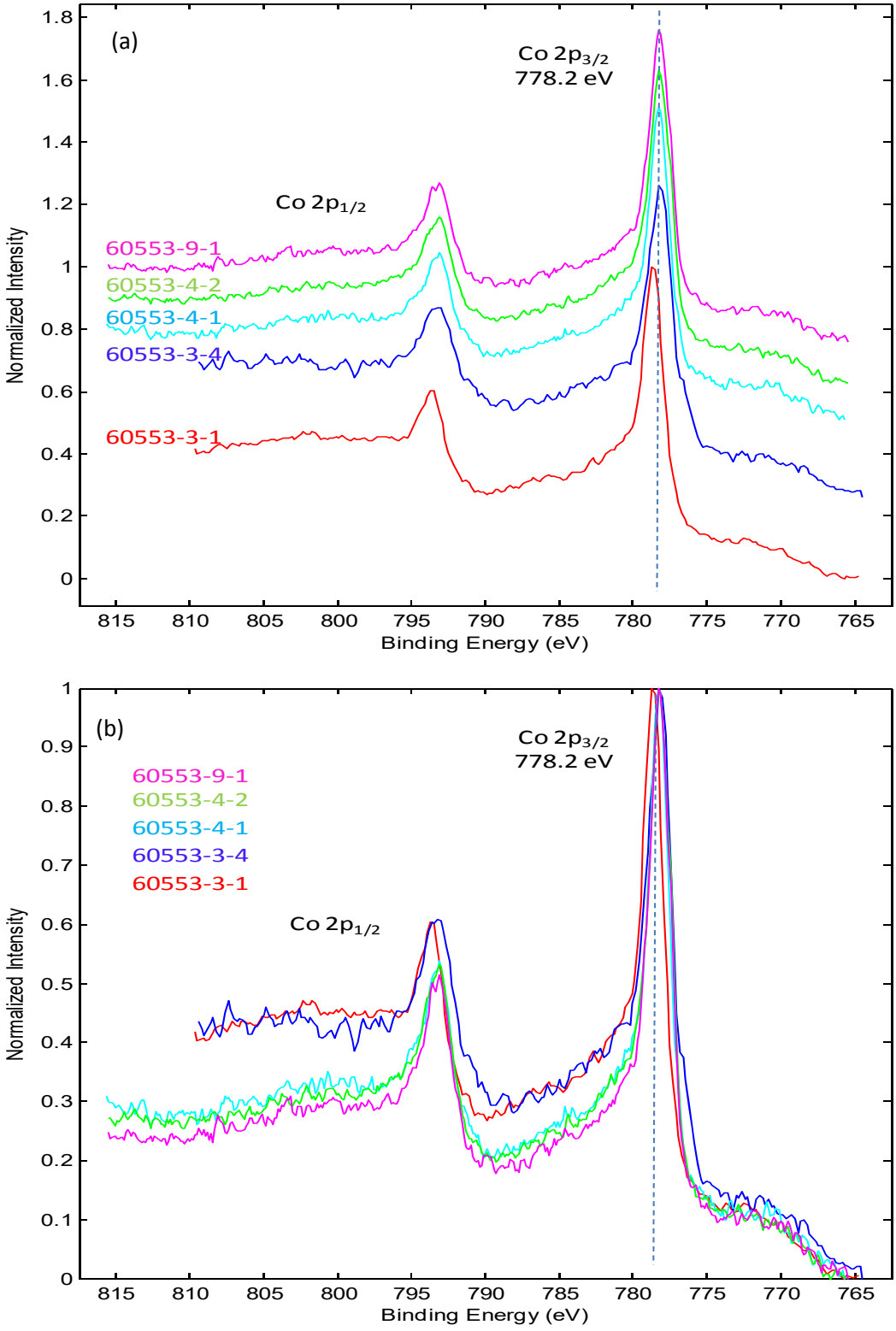

Figure 35. High energy resolution photoemission spectra of the Co 2p region collected from the outside of a catalyst pellet (a) Normalized stack plot. (b) Normalized overlay plot.

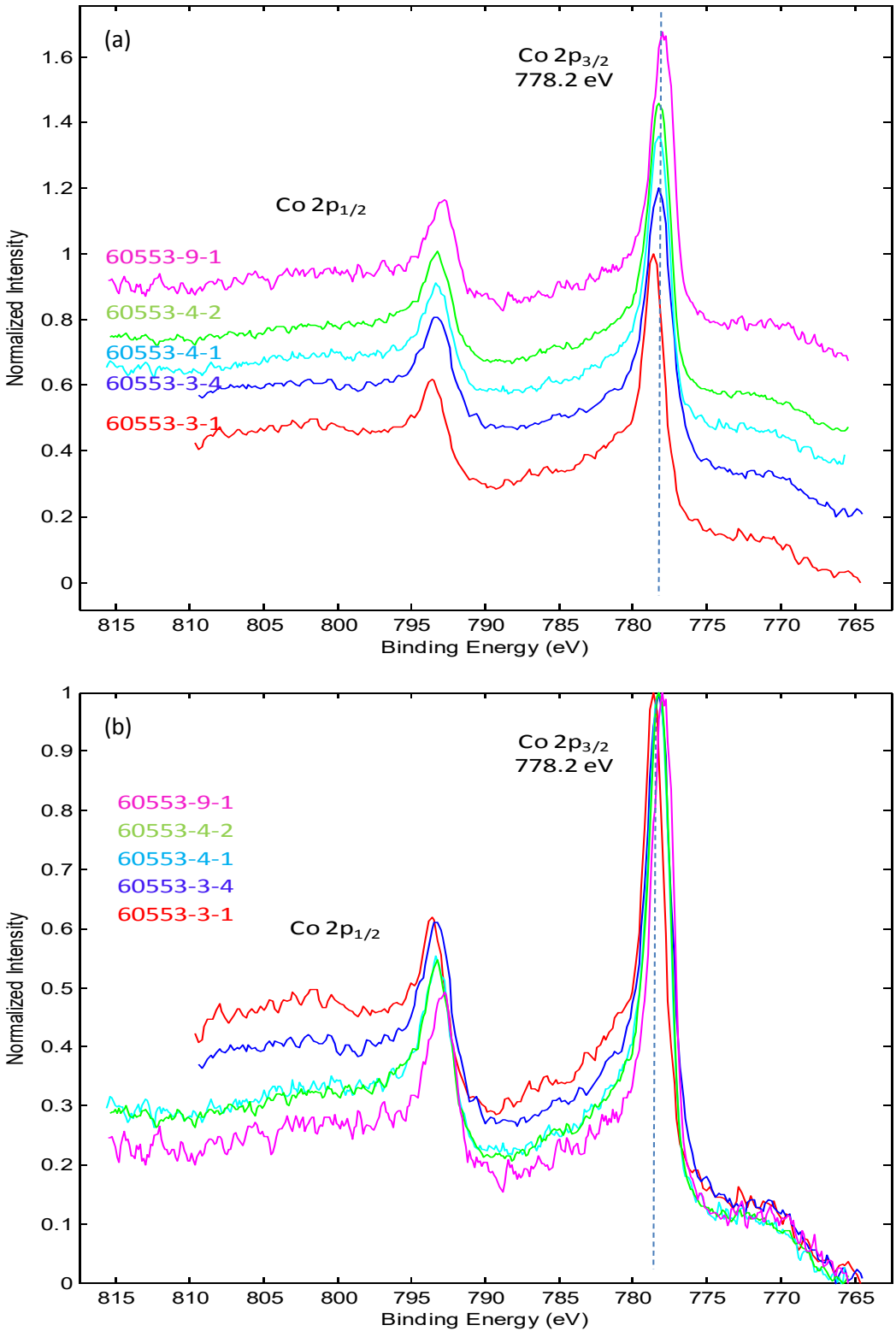

Figure 36. High energy resolution photoemission spectra of the Co 2p region collected from the inside of a catalyst pellet (a) Normalized stack plot. (b) Normalized overlay plot.

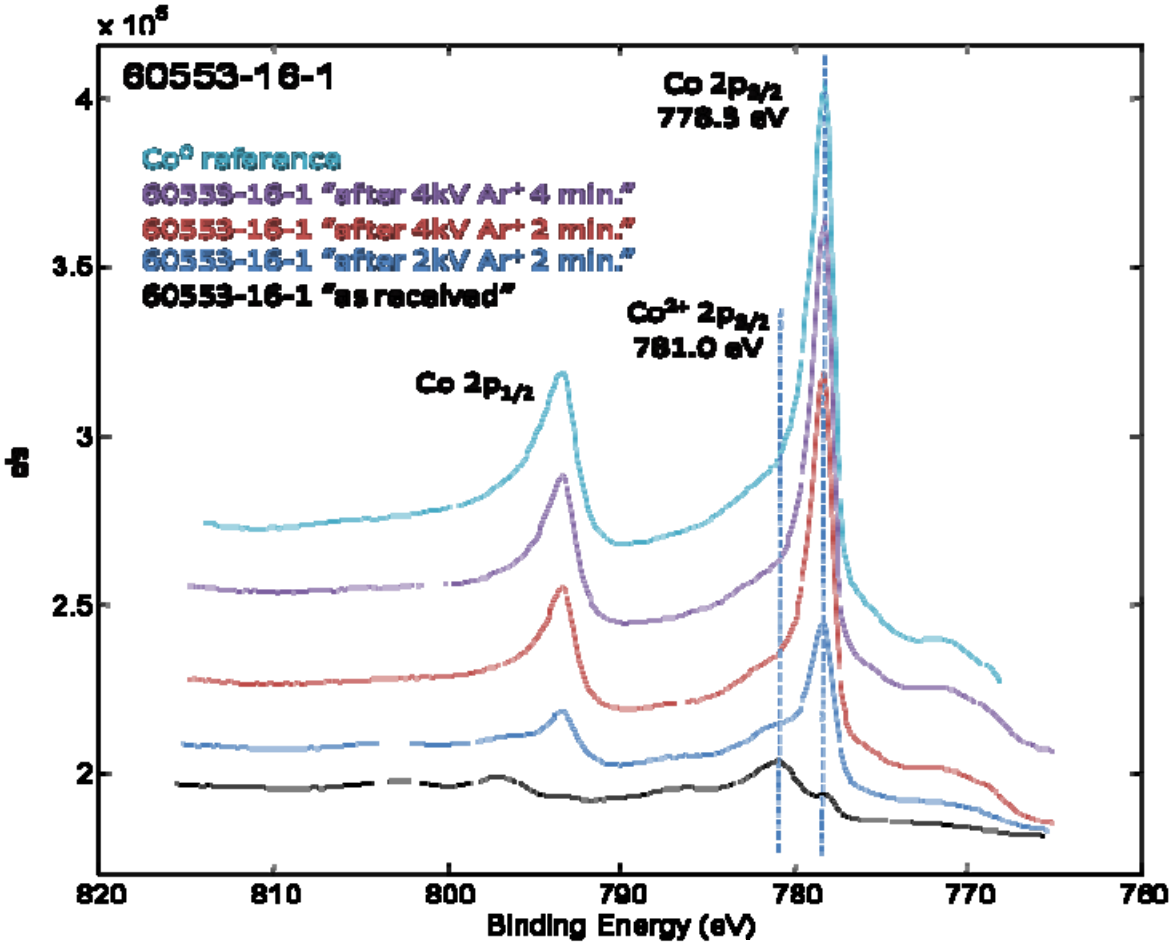

Figure 37. High energy resolution photoemission spectra of the Co 2p region collected from the reference sample 16-1 at various depths after Ar ion sputtering of the reference surface.

and interior of the methanol-aged catalyst may have been slightly more reduced than the carbon in the other activated samples in Figure 38.

The K 2p spectra of sample 4-1, 4-2 and 9-1 are also shown in Figure 38. The XPS spectra of the K region of samples 3-1 and 3-4 are plotted separately in Figure 39 in order to present the data on a more highly resolved ordinate. The binding energy of the K $2p_{3/2}$ electron in sample 3-1 is centered at about 292.2 eV, which matches the value reported in the literature for K_2CO_3.[54] K as K_2CO_3 was expected in sample 3-1 because the sample had not been activated.

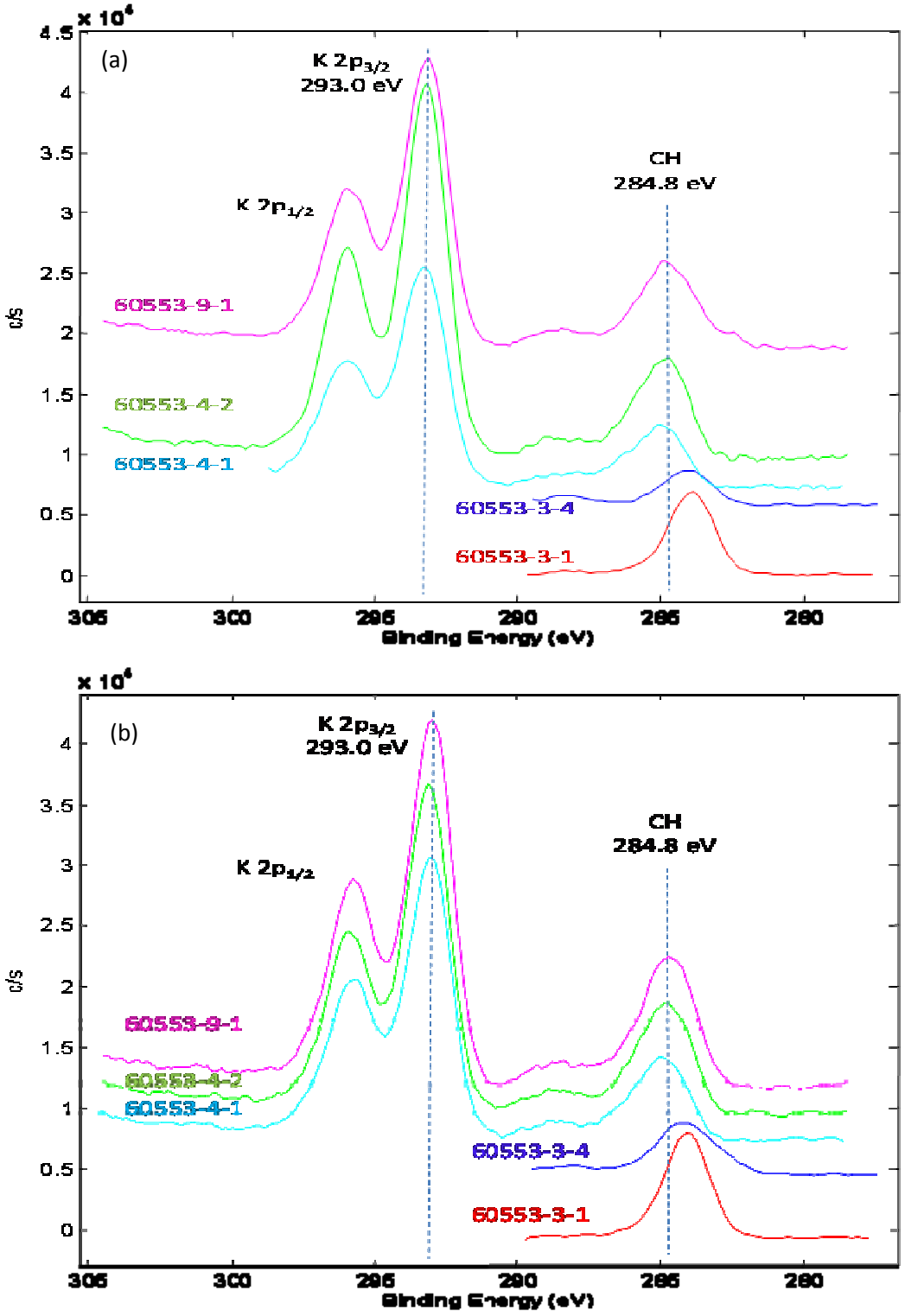

Figure 38. High energy resolution photoemission spectra of the K 2p and C 1s regions collected from the catalyst samples (a) Outside pellet surface. (b) Inside the pellet.

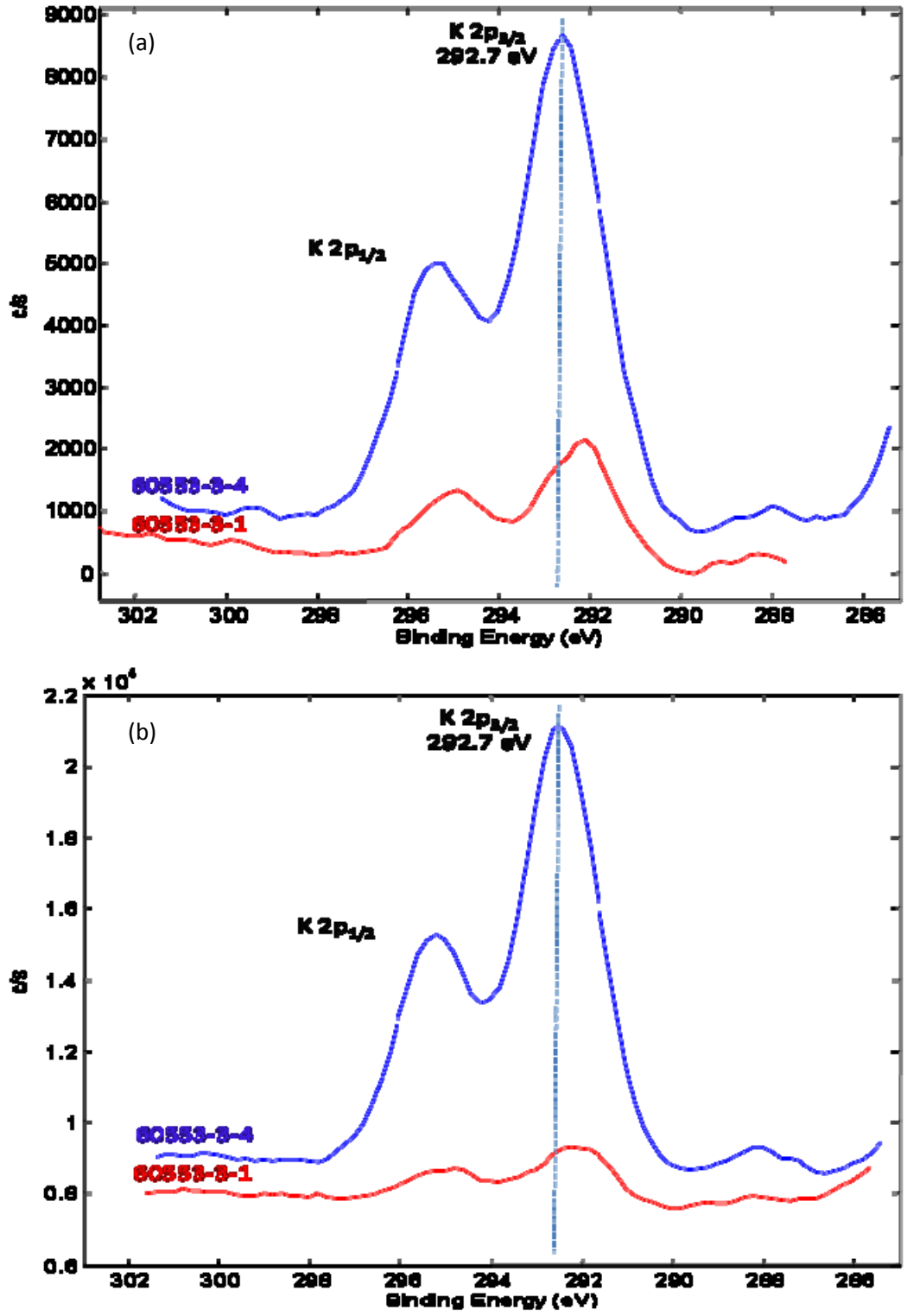

Figure 39. High energy resolution photoemission spectra of the K 2p region collected from the catalyst samples (a) Outside pellet surface. (b) Inside the pellet.

Samples 4-1, 4-2, and 9-1 have K $2p_{3/2}$ binding energies of 293.0 eV (Figure 38). DRIFTS analysis (see below) suggests the presence of formate in these samples, which may be consistent with the observed binding energy. While a K 2p binding energy could not be found in the literature for HCO_2K, the binding energy for the similar CH_3CO_2K is 292.9 eV.[55] The difference in binding energy for sample 3-1 contrasted to 4-1, 4-2, and 9-1 confirms that the carbonate decomposed upon activation as reported by Range Fuels. Furthermore, the K spectra of the activated samples suggest that K_2CO_3 does not re-form under reaction conditions or upon reactor cool down.

The K $2p_{3/2}$ electrons in sample 3-4 are shifted slightly lower to 292.7 eV. DRIFTS suggested that Sample 3-4 also contained formate, but the shift may suggest other potassium species are also present. More investigation is warranted into the changing chemical nature of the K while applying a methanol co-feed since the change in K could reveal a catalyst deactivation mechanism.

The XPS data collected on catalysts for the C 1s electrons, shown in Figure 38, were also analyzed. While the Co 2p spectra in Figure 35 and Figure 36 demonstrated that metallic Co and Co_2C were indistinguishable, Wang et al.[52] reported that the binding energy of the C 1s electrons of Co_2C had a binding energy of 283.5 eV. Unfortunately, a Co(0) reference sample tested by XPS and illustrated in Figure 40 exhibited a broad feature that encompassed the C-H and C-C region at 284.7 eV as well as the Co_2C region at 283.5 eV. The C on the Co(0) reference sample was likely from air contamination. The broadness of the Co(0) C 1s spectra demonstrated that it was not possible to distinguish between carbide due to Co_2C and other forms of carbon even in a fully reduced reference material.

Also presented in Figure 40 are the XPS results on sample 16-1, which was a sample collected during the preparation of Co_2C by the reaction of CO and Co. XPS analysis of sample 16-1 revealed that nearly all of the material at the surface of the sample was C with only a very small amount of Co. The sample was then sputtered with Ar ions for various times in order to analyze the sample as a function of depth. As the analysis depth within the sample increased, a shoulder developed in the C 1s spectra in Figure 40. The shoulder, which is approximately centered at 283.5 eV, suggests that Co_2C was present deeper within sample 16-1. The carbon deposited on the surface of the sample is likely amorphous as only Co(0) and Co_2C were identified by XRD analysis of the sample (Figure 17).

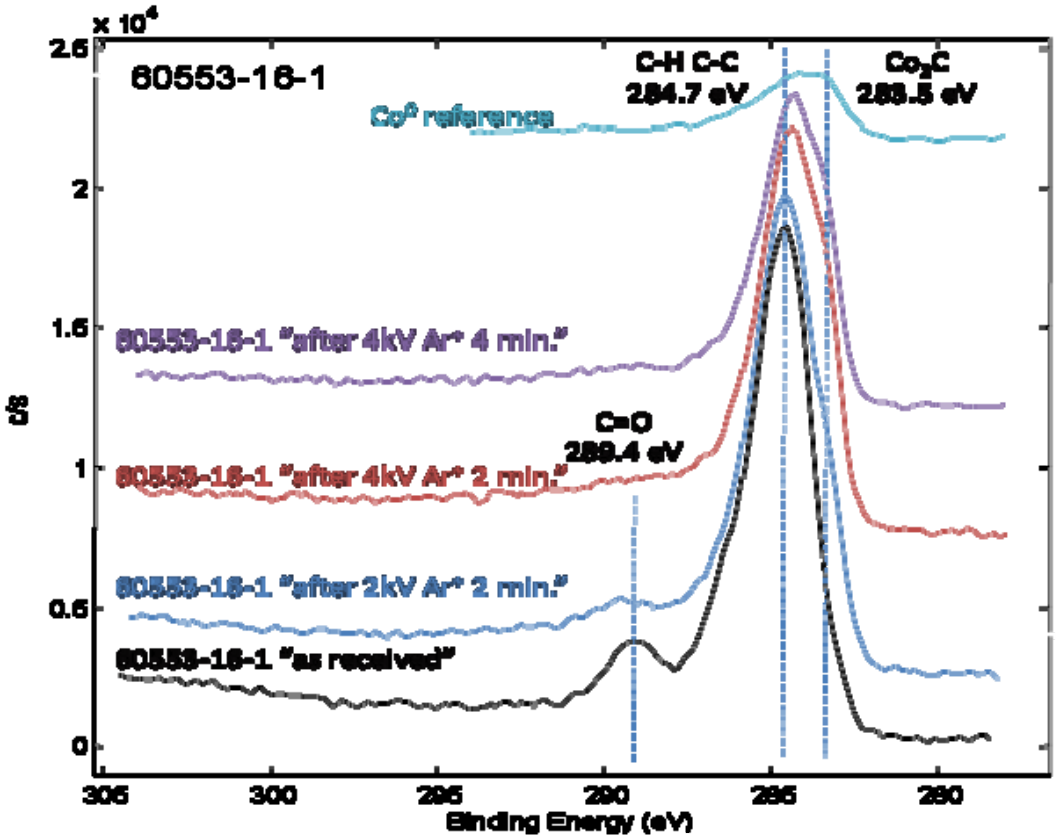

Figure 40. High energy resolution photoemission spectra of the C 1s region collected from the reference sample 16-1 at various depths after Ar ion sputtering of the reference surface.

3.4 EPR Analysis Results

Electron Paramagnetic Resonance (EPR) is an analytical technique for studying unpaired electrons such as those in free radicals or transition metal complexes. A number of paramagnetic species have been identified in Co-Mo-S systems, including Co(0), Co(I), Co(II), Mo(III), Mo(V), Co/Mo mixed species and sulfur-based radicals. While nearly all of the previously reported EPR investigations on sulfided catalysts have been applied to hydrodesulfurization catalysts, extrapolations to RF-101 mixed alcohol synthesis catalysts are relevant and informative.

In order to provide useful information in the analysis of catalytic samples, the EPR spectra from a number of reference compounds and starting materials were collected. The results are tabulated in Table 4. As expected, there were no paramagnetic species in the BentoLite® binder (9-3), K_2CO_3 (9-2), MoS_2, or Co_9S_8 prepared under N_2 (12-1).

Table 4. Summary of observations of EPR spectra collected on reference samples.

Sample ID	Sample Description	Observed EPR signal
9-3	Bentolite® Binder	None
9-2	K_2CO_3	None
12-1	Co_9S_8	None
19-1	Cobalt Carbide	CoC_2
CoS[a]	Co_6S_5, Co_4S_3	CoS
CoS_2[a]		CoS_2

[a]Commercial reference material

The data in Table 4 was applied to the analysis of the catalytic samples received from Range Fuels. Since the use of paramagnetic oxygen to induce EPR signals in catalytic material for spectroscopic reasons is well documented,[56] the EPR spectra from a series of catalyst samples were recorded at several temperatures with or without exposure to air. A summary of the observed spectra on the catalyst samples is tabulated in Table 5. The numbering system for the spectra [0, I, II, etc.] used in Table 5 and in the discussion is largely that of Woo et al.[57] The following results are discussed first in terms of observations for each catalyst tested, then later according to the types of signals observed in the EPR spectra.

Table 5. The summary of EPR signals observed during testing of the various catalyst samples.[a]

Sample ID	Sample Description	EPR signal						
		0	**I**	**II**	**III**	**IV**	**V**	**Other**
3-1	Unactivated RF-101							CoS_2?
4-1 4-2	Activated RF-101 Catalyst						N A	0_2, CoS? A
3-2 3-3	Catalyst after 4200 h TOS[b]	N A		N A	N A	N A		0_2, N A
3-4	Methanol Aged Catalyst	N A		A	A	A	N	0_2 A
9-1	Methanol and H_2S co-fed	N A					N A	
		Reported Species						
		Co(0)	**Mo(V)**	**S***	**Mo(III)**	**"MoSCo"**	**"Co(I)S"**	
	g value		1.93	2.002	2.05	2.11	2.19	

[a] N and A indicate a signal observed from a sample not exposed to air (N) or intentionally exposed to air (A) prior to EPR analysis.
[b] TOS = time on stream in the mixed alcohol synthesis reactor.

3.4.1 Analysis of Range Fuels Catalyst Samples

The spectrum of unactivated RF-101 (3-1) somewhat resembled that of the CoS reference compound. Upon activation and/or use, this spectrum does not appear in any other sample. Similarly, CoS was a phase observed in XRD spectra only for 3-1, but not in any of the other catalyst samples. The activated samples (4-1 and 4-2) exhibited an EPR spectrum with a single component, [V], as can be observed for 4-1 in Figure 41. Previous reports identified signal [V] as reduced Co(I) in a sulfur environment and has been denoted as "Co(I)S".[58-60] A sample of the catalyst 3-4, which was RF-101 aged with a methanol co-feed, shows the same Co(I)S spectrum, but with the addition of a very broad signal, [0], which spanned from 0 G to about 12,000 G. In studies of similar Co/Mo catalysts, the low field signal [0] has been reported to result from the presence of metallic cobalt (Co(0)).[58] Sample 9-1, which was operated with a co-feed of H_2S as well as methanol, exhibited a spectrum containing [0] that was nearly identical to that of sample 3-4 (Figure 41). In addition, the [0] signal was also observed in samples 3-2 and 3-3 (Figure 42).

The temperature dependence of the EPR spectra of sample 3-3, shown in Figure 42, and sample 3-4, shown in Figure 43, indicate superparamagnetic behavior associated with nanoparticles. In superparamagnetic nanoparticles, particles are small enough to comprise a single magnetic domain. Because the electron spin fluctuations average due to thermal effects, nanoparticles produce narrower EPR spectra at elevated temperatures that broaden at lower temperatures with a shift to lower field. The peak of signal [0] in Figure 42 and Figure 43 broadens and moves to lower field with decreasing temperature such that the peaks at 200 K and 100 K are below 0 G, which strongly indicates that the Co(0) present is in the form of superparamagnetic nanoparticles. In contrast, and not consistent with experimental observations, bulk Co EPR signals are broad at room temperature and narrow at lower temperature, accompanied by a spectrum shift to higher field to g=2 (about 3400 G at the frequency used).

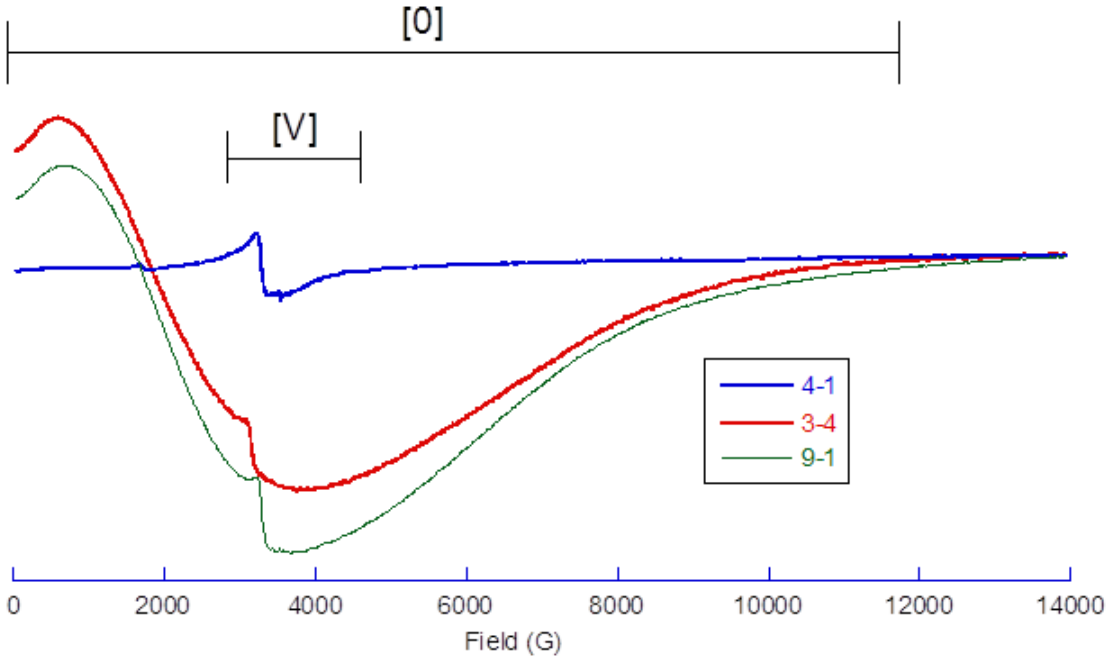

Figure 41. Room Temperature EPR spectra of samples 4-1,3-4, and 9-1. Signal [0] has been attributed to metallic Co[58] while signal [V] has been attributed to "Co(I)S."[58-60]

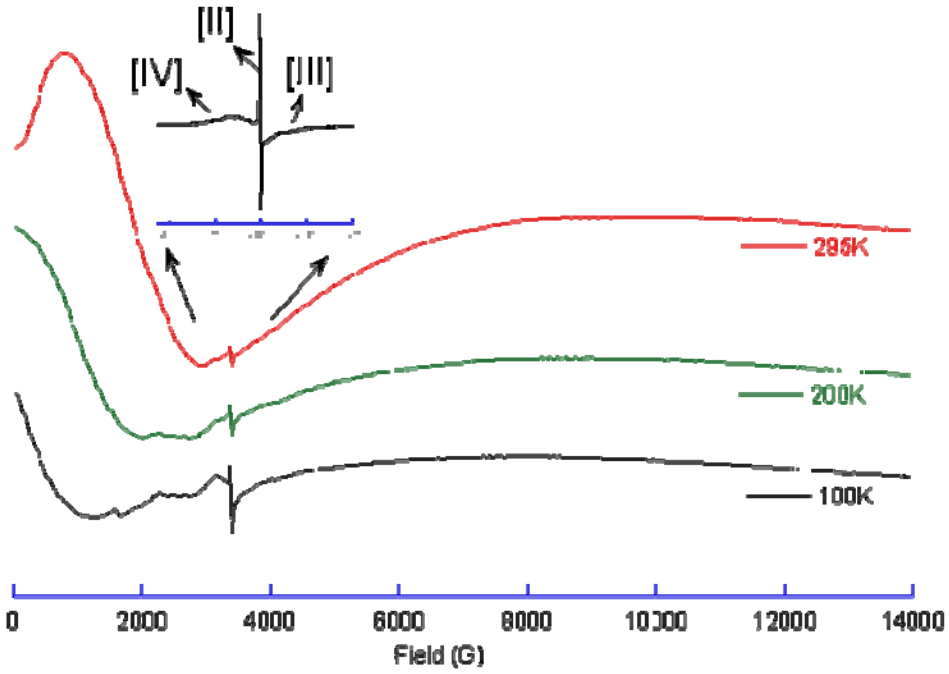

Figure 42. Variable temperature EPR spectra recorded during analysis of sample of 3-3. Inset shows expansion of the ~ g=2 region at room temperature.

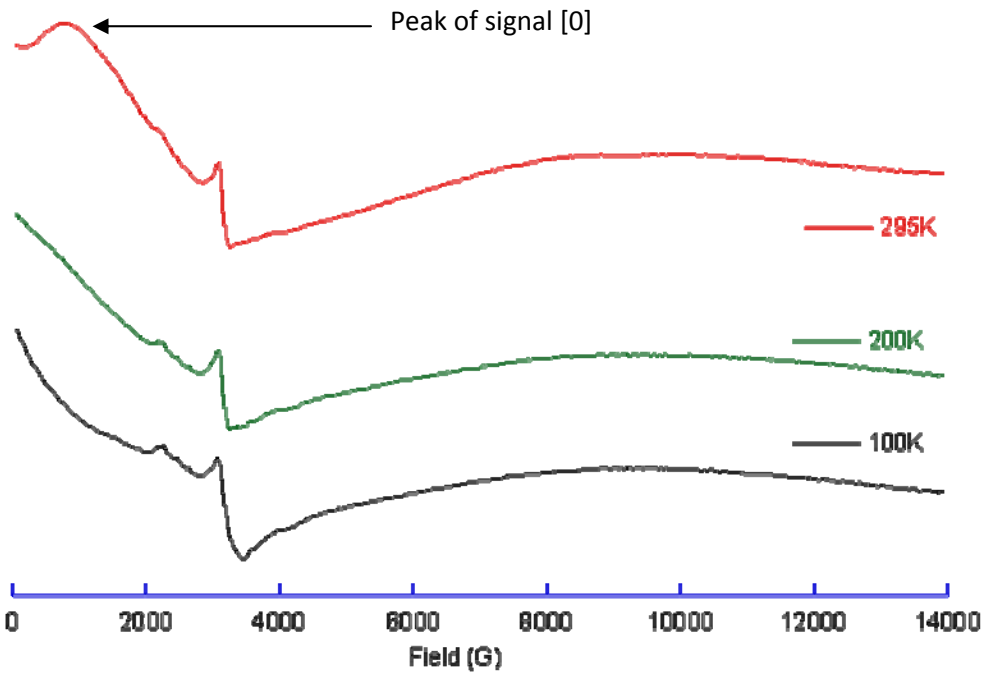

Figure 43. Variable temperature EPR spectra of sample 3-4, illustrating the temperature dependent nature of signal [0], which has been attributed to Co(0).[58]

As illustrated in Figure 42, the catalyst samples employed for extended periods of mixed alcohol synthesis (3-2 and 3-3) have feature [0], but not [V]. The EPR spectra for these samples instead have an overlapping set of three signals in the spectra: [II], [III] and [IV]. At temperatures below 15 K, a signal from adsorbed molecular oxygen is also observed. To test whether inadvertent exposure to air could modify the EPR spectrum of reduced catalysts, the tube containing a sample of 3-4 was unsealed and EPR spectra were periodically collected. Within minutes the spectrum began to include signals [II], [III] and [IV] (Figure 44), and over the course of several days the spectrum converted to that of 3-2 and 3-3 (in the 2000 to 4500 G range). Thus, it was highly probable that samples 3-2 and 3-3 were exposed to air prior to delivery to PNNL. These samples were kept in tightly sealed vials after unloading under inert conditions from the Range Fuels mixed alcohol synthesis reactors, but were stored outside the glovebox in air for several months.

Samples 4-1 and 9-1 were also exposed to air to further probe the nature of these materials. Figure 45 illustrates that sample 4-1 developed a new signal upon air exposure, which was independent of the loss of [V]. In the short term (days), this new signal resembled [IV], but over the course of weeks, as the

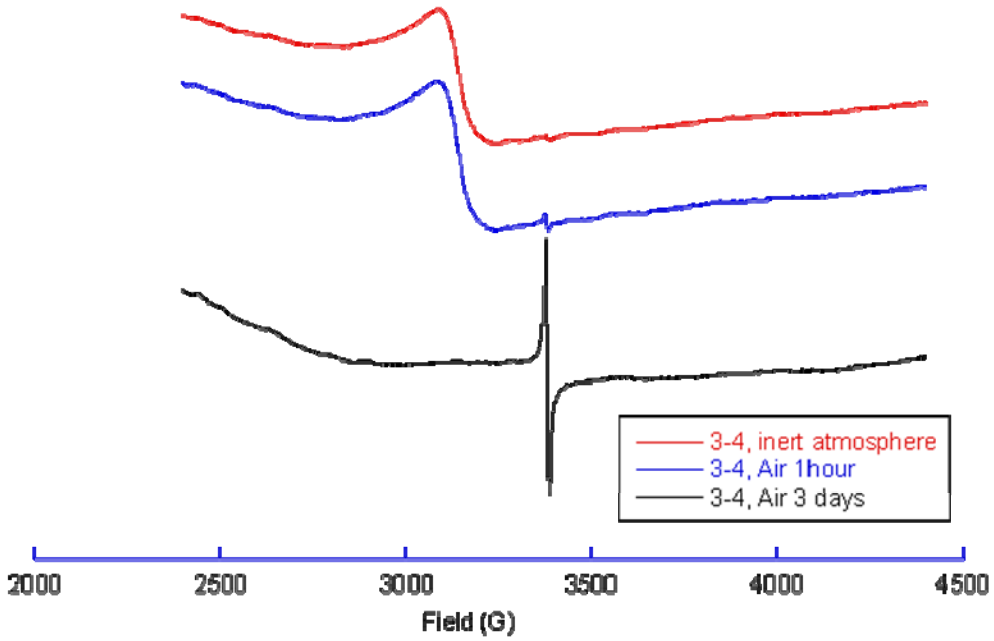

Figure 44. The changing nature of the room temperature EPR spectra of sample 3-4 after exposure to air at room temperature for various durations.

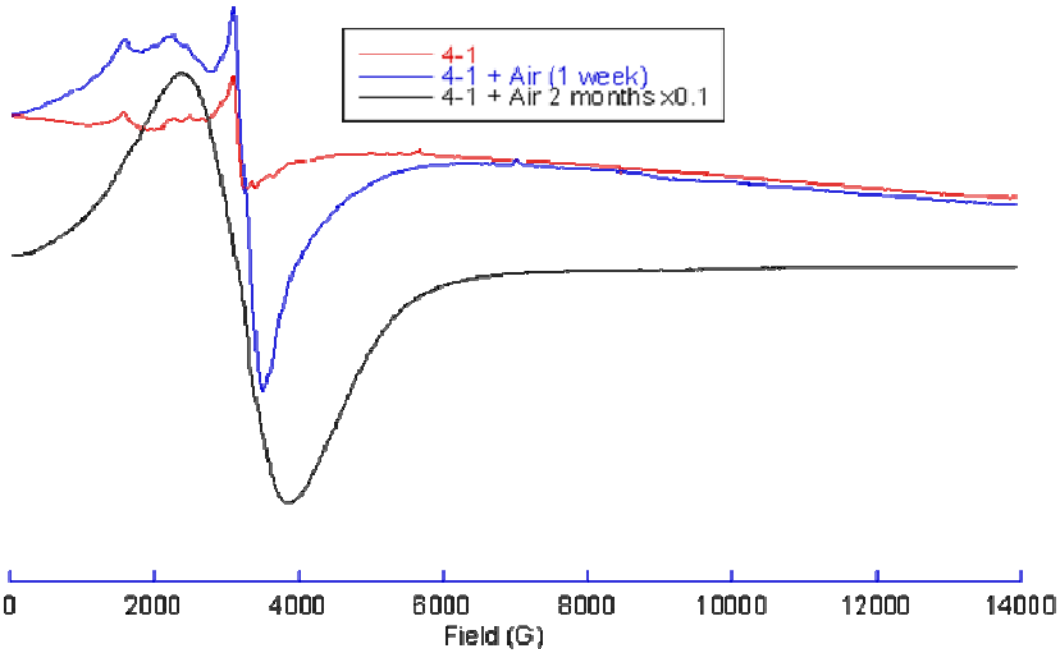

Figure 45. The changing nature of the EPR spectra of sample 4-1 after exposure to air at room temperature for various durations. The "x0.1" indicates the signal was divided by 10 for illustrative purposes.

sample oxidized, the spectrum most closely matched that obtained for the CoS reference material. Interestingly, sample 9-1 was unaffected by air in spite of having a spectrum identical to the air-sensitive 3-4. It is believed that the higher sulfur content in 9-1 may have inhibited air oxidation relative to the sulfur-deficient 3-4.

With evidence that the composition of the catalyst changes with use, samples from the more exposed exterior surfaces of catalyst sample 3-4 were compared with samples at the pellet interior (nearly identical sample weights were used). The results of the "spatially resolved" EPR testing are shown in Figure 46. Spectra of the exterior and interior samples gave nearly identical magnitudes of signal [V], but the difference in signal [0] was striking. The exterior sample exhibited a signal attributed to metallic Co approximately 4 times greater than the interior sample. This result is consistent with XRD and other results that suggested that the exterior of the catalyst was where the majority of the catalysis occurred, while the interior of the pellet did not participate to nearly the same degree.

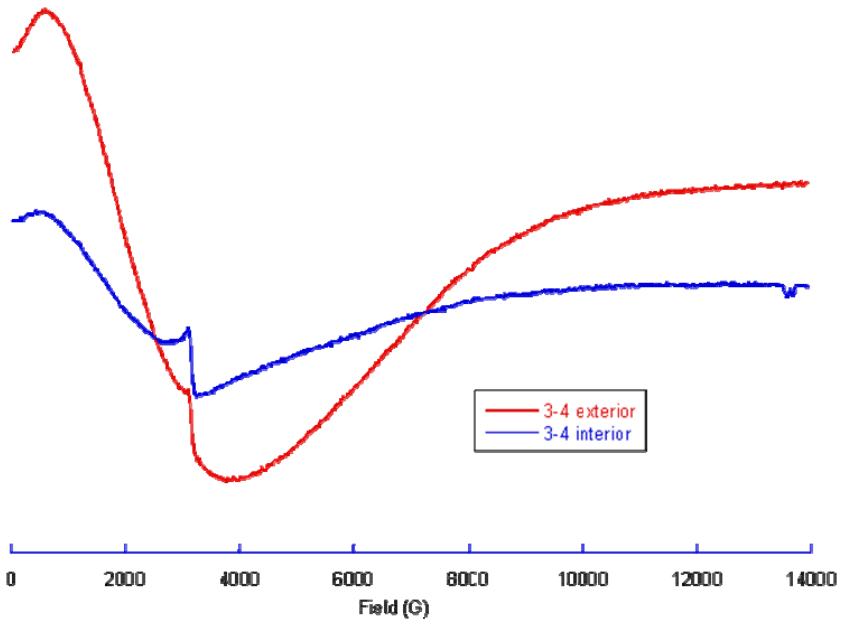

Figure 46. EPR spectra collected on portions of sample 3-4 near the pellet surface (exterior) and from the interior of the pellet**.**

3.4.2 EPR Spectra Analysis

The various EPR spectra obtained from the samples have been previously reported in the literature, though most reports only characterize new or freshly activated materials. The following sections detail a more in-depth discussion of the observed signals listed in Table 5.

3.4.2.1 Analysis of Signal [0]

Spectrum [0] has been previously reported as metallic cobalt in studies of cobalt deposited on alumina[53, 58]. Both Lojacono et al. [58] and Ramaswamy et al. [53] reported that cobalt oxides, such as CoO or Co_3O_4, were the likely precursors. Co^{2+} in tetrahedral positions in the alumina support did not reduce to Co(0) and Co^{2+} associated with the octahedral positions was not believed to be a Co(0) precursor. Based on this precedent, signal [0] is assumed to be Co(0). However, it should be pointed out that EPR spectra alone are not definitive and the signal could arise from another species.

Lojacono et al.[58] observed that reduction with H_2 as well as 90% H_2/10% H_2S produced the metallic Co(0) signal, although when H_2S was used, the signal was significantly diminished. Co(0) was only observed in the absence of Mo. Ramaswamy et al.[53] also observed [0] under reducing conditions (500°C, H_2), but only when sodium ions were included. The role of sodium was thought to involve blocking of sites on alumina, thereby promoting formation of Co-oxide phases. Ramaswamy et al. reported that Co(0) could not be confirmed with 1% S present as thiophene.

The pathway to Co(0) in the Range Fuels catalyst samples is unknown. The Range Fuels catalysts are different from the materials examined by Lojacano and Ramaswamy, who started with oxide phases. The Range Fuels materials are sulfided and more difficult to reduce beyond Co_9S_8, which is predicted to be the stable phase under sulfiding conditions. However, [0] is observed even when 47 ppm H_2S is introduced (9-1). The signal appears with time on stream, being absent in unactivated (3-1) and freshly activated (4-1, 4-2) materials but present in catalysts that have converted syngas for at least one week.

The possibility that the [0] signal arises from Co_2C was investigated. The behavior of sample 19-1, which contained ~77 wt% Co_2C and ~20 wt% Co metal, is shown in Figure 47. Figure 47 shows that the signal observed in this sample has a very different temperature profile from that observed for catalyst samples believed to contain nanoparticulate cobalt metal. In catalyst samples, the peak associated with signal

[0] moved to lower field at lower temperatures (Figure 43) associated with broadening of the signal and consistent with Co nanoparticles. However, the peak associated with the signal observed in sample 19-1 (Figure 47) behaved differently by moving to higher field as the temperature was decreased, indicating the presence of a bulk material. Thus, the signal of bulk Co_2C/Co(0) does not account for the signal [0] in the Range Fuels samples. The results do not rule out nanoparticulate Co_2C and no EPR spectra of any particle size of Co_2C appear in the literature. More work is needed to definitively identify the species responsible for [0].

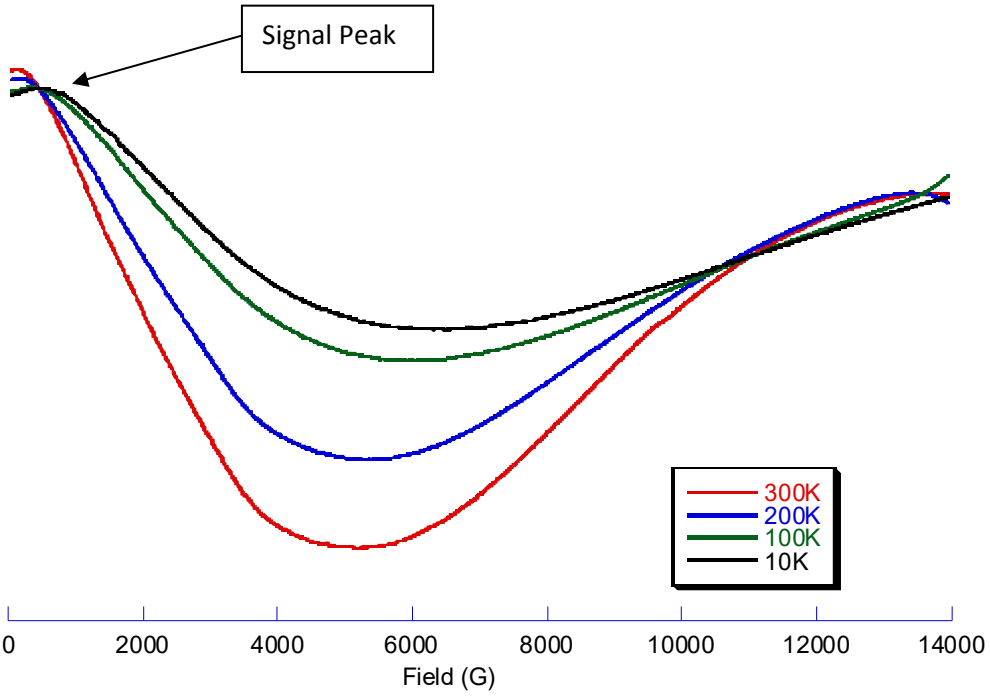

Figure 47. Variable Temperature EPR spectra of sample 19-1.

3.4.2.2 Analysis of Signal [I]

This signal is included, even though it was not observed in any sample, simply because it is so prevalent in the literature. This spectrum arises from Mo(V) interacting with alumina. Others have noted that it is absent under very strongly reducing conditions[57, 59] and in unsupported catalysts.[61] Derouane et al.[61] also noted that the signal decreased in intensity with higher cobalt ratios. In the Range Fuels catalysts, alumina was only present in low concentrations, so interaction with Mo was apparently minimal. As an aside, signals observed by others arising from interactions of Co^{+2} with alumina were also absent in the Range Fuels catalysts. Neither Co nor Mo showed any particular association with binder in SEM spectra.

3.4.2.3 Analysis of Signals [II], [III] and [IV]

These signals are grouped here because in the present investigation they are always observed simultaneously after exposure to air. EPR spectrum [II] was proposed in the literature to occur from sulfur-based radicals possibly due to association with an alumina support.[57, 61, 62] While the Range Fuels catalysts were not supported on alumina, alumina was present in the catalyst from the binder. It is unknown whether interactions of sulfur with other binder components might also give this signal. Spectrum [III] has been assigned to Mo(V)-thio species, probably at edge defects based on its appearance with unsupported MoS_2 catalysts.[61, 63] A mixed or synergistic "CoMoS" species is responsible for [IV],[57] though the oxidation state of the molybdenum has been suggested as Mo(III),[64] Mo(IV),[61] and Mo(V).[65] Not only do these spectra only occur in the samples that have been exposed to air, they do not develop in either the freshly activated samples (4-1 and 4-2) or the H_2S and methanol co-feed samples (9-1). This suggests that the precursors of the species responsible for signals [II], [III], and [IV] may be both sulfur deficient compared to the other paramagnetic species.

3.4.2.4 Analysis of Signal [V]

Spectrum [V] is a signal that was observed in all activated samples, except 3-2 and 3-3. Lojacano et al.[58] reported the appearance of this spectrum after H_2/H_2S then H_2 activation of Co/Al_2O_3 and $Co/Mo/Al_2O_3$ materials and also noted the disappearance of the signal upon exposure to air. Therefore, species responsible for [V] may have been present originally in samples 3-2 and 3-3, but destroyed by inadvertent exposure to air during storage. Hagenbach et al.[66] and Gajardo et al.[60] observed this EPR signal when Co_9S_8/MoS_2 mixtures were used as starting materials. Though Gajardo et al.[60] suggested that it could stem from either a low spin Co(III)S or a Co(I)S species, Bhaduri and Mitchell[59] reproduced this spectrum by treating $Co\text{-}S/Al_2O_3$ with the strong reducing agent $AlEt_3$. Gajardo et al.[60] correlated the appearance of this spectrum with XPS data indicating the presence of a reduced "Co_9S_8-like" species, formed by reduction with H_2. The species, therefore is denoted "Co(I)S".

Newly activated material (4-1 and 4-2) had only signal [V], indicating that activation converted the major part of the starting Co(II) sulfide to an EPR-silent species and a minor part to the "Co(I)S" species with spectrum [V]. Aged samples (3-2, 3-3, 3-4, and 9-1) gained a new signal, [0], suggesting that a large amount of the previously EPR silent cobalt was converted to metallic cobalt. Differences in the ratio of [V] to [0] in sample 3-4 show that this conversion takes place preferentially on the exterior of the pellet. A second change with aging is the sensitivity to air. When exposed to air, 4-1 gained a new signal

resembling CoS and lost [V] very slowly (time scale of weeks), whereas 3-4 lost [V] and gains [II], [III] and [IV] in minutes. Sample 9-1, aged with a co-feed of H_2S, had [0] like 3-4, but lost [V] very slowly and did not develop [II], [III] and [IV]. The difference in time scale of the modification with air could be due to either a difference in the depth of the air-sensitive species, or to the presence of a protective layer. Methanol was hypothesized by Range Fuels to accelerate aging of the catalyst through the stripping of S from the catalyst. Sample 3-4 was found through EDS analysis to be lower in S when compared with the other samples. Therefore, it is plausible that oxygen reacted with the 3-4 sample more rapidly than with the other samples because it was not as highly coordinated with S.

3.5 TEM Analysis Results

Transmission electron microscopy (TEM) analysis was performed on selected catalyst samples in order to understand the morphology of the catalysts at the tens-of-nanometers scale. Furthermore, specific analysis of the catalysts was undertaken in a search for metallic Co. Samples 4-1, 4-2, 3-4 and 9-1 were analyzed. While metallic Co was not identified in any of the samples, the absence of evidence was not conclusively linked to a lack of Co(0) due to the fact that TEM analysis may not have been able to detect fine grained, highly dispersed Co(0) nanoparticles embedded in the heterogeneous catalyst samples.

Sample 4-1 was composed of very weakly crystalline particles. EDS analysis of the sample collected simultaneously during TEM analysis revealed that the sample in Figure 48 is composed of S, Co, Mo, and K. While much of the sample was finely crystalline, some large crystalline particles were also seen. One such particle is shown in Figure 49. While the crystal in Figure 49 is believed to be represenattive of the sample, it cannot be ruled out that it was produced from electron beam crystallization during TEM analysis.

As shown in Figure 50, the microstructure of sample 4-2 was very uniform. The sample was composed of very weakly crystalline particles. EDS revealed a chemical composition of S, Co, Mo, K.

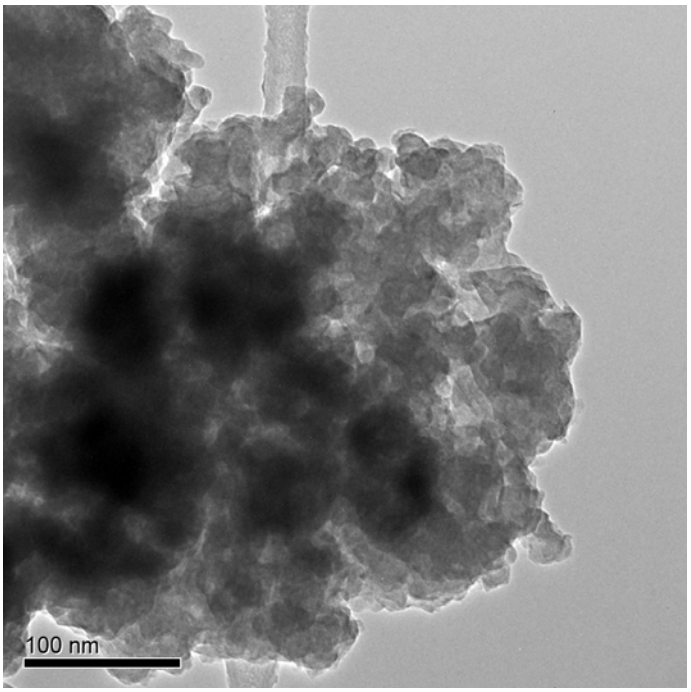

Figure 48. The microstructural features for sample 4-1. This sample was weakly crystalline. EDS analysis indicated that Mo, S, Co, and K were present.

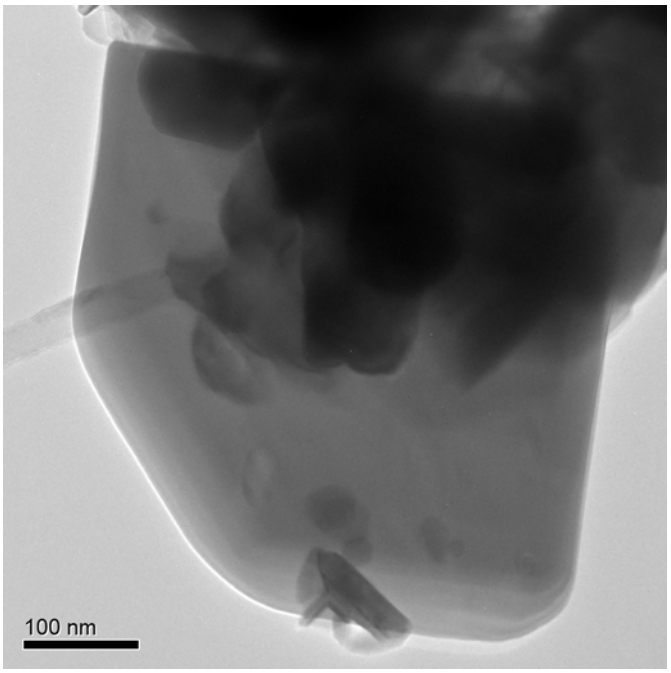

Figure 49. An alternative view of the sample 4-1, which revealed that large crystalline particles could be seen dispersed throughout the particle. EDS indicated that Mo, S, Co, and K were present.

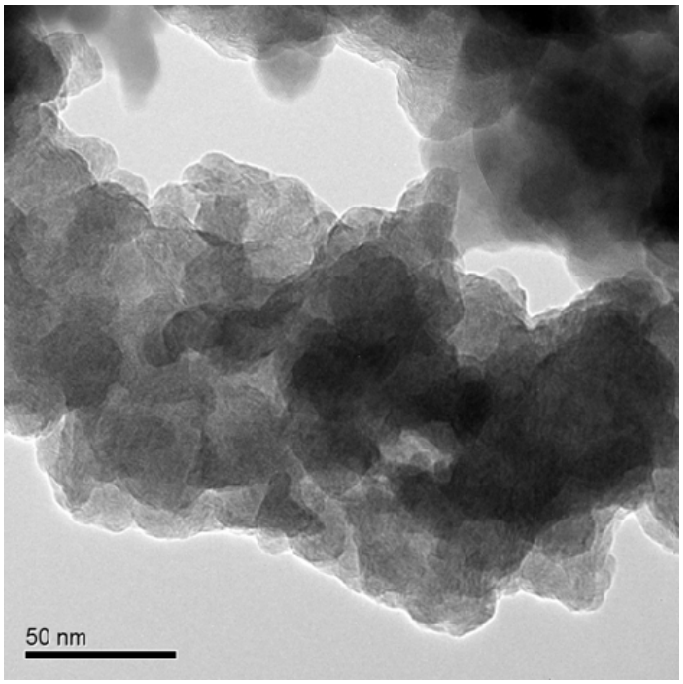

Figure 50. The microstructural features for sample 4-2, which was a weakly crystalline particle. EDS indicated the presence of S, Co, Mo, K.

The microstructural features for sample 3-4 are shown in Figure 51 and Figure 52. Structurally, this sample was composed of very weakly crystalline regions (Fig. 5) accompanied by regions with greater crystallinity (Fig. 6). The weakly crystalline region was nearly amorphous. EDS revealed that these two regions were similarly composed of S, Co, Mo, K. Although several locations were sampled, 3-4 showed no evidence of pure metallic Co particles.

The microstructural characteristics of sample 9-1 are shown in Figure 53. Structurally, this sample is composed of very fine particles. EDS reveals a chemical composition of S, Co, Mo, and K. As in the other samples analyzed by TEM, no Co metal particles could be identified in sample 9-1.

Overall, the catalyst samples illustrated a general and common structural feature in that they all appeared to possess a very fine particle size. Compositionally, they are all composed of S, Co, Mo, and K, although no quantitative analysis was carried out using EDS.

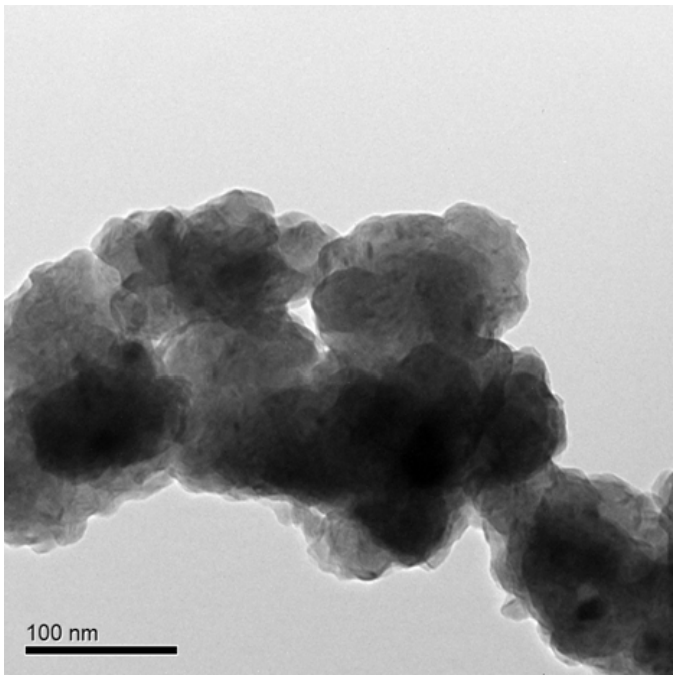

Figure 51. The microstructural features of a weakly crystalline region of sample 3-4. EDS measurements indicated the presence of Mo, Co, S and K.

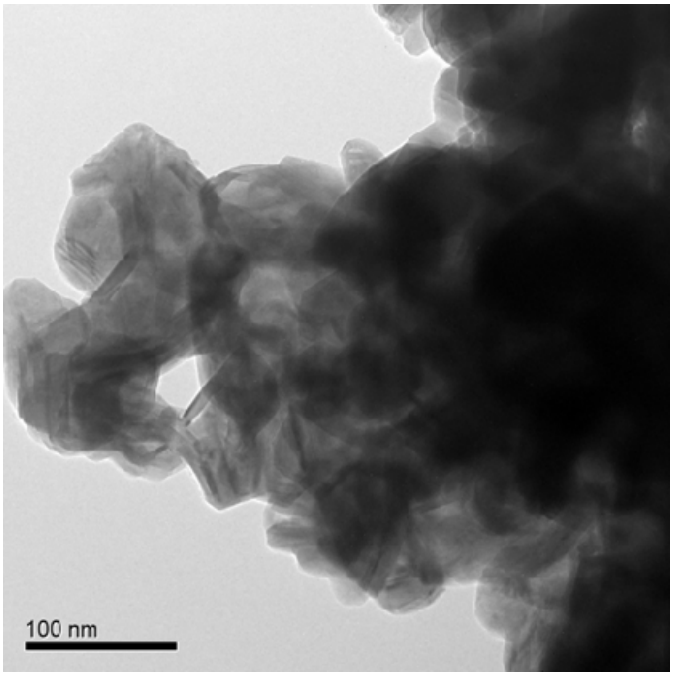

Figure 52. The microstructural features of a region of sample 3-4 with a highly crystalline characteristic. EDS measurements indicated the presence of Mo, Co, S and K.

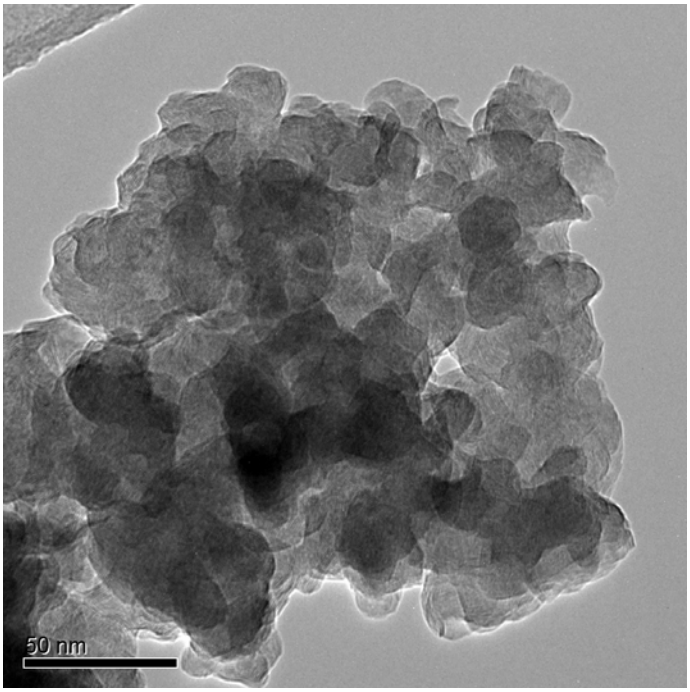

Figure 53. The microstructural features revealed by TEM analysis for sample 9-1. The sample was weakly crystalline and EDS measurements indicated Mo, Co, K and S were present.

3.6 DRIFTS Analysis Results

Diffuse reflectance infrared Fourier transform spectroscopy (DRIFTS) is an analytical technique that probes the chemical functionality of a solid surface thorough application of a spectrum of infrared light onto a solid surface, which is then reflected into a detector. Chemical functionality, whether organic or inorganic, can be excited by different wavelengths of IR light, resulting in molecule vibrations – bending or stretching movements of the molecules. The chemical functionality as well as the excited mode are specific and characteristic of the chemical species absorbing the light. The infrared light that is reflected into the detector is thus lacking in the wavelengths of IR light that were absorbed by the chemical functional groups. Hence, very specific information about the chemical species present on a solid surface can be achieved with DRIFTS analysis.

DRIFTS was used to analyze the physical and chemical characteristics of selected samples. Analyses were conducted on as-received catalysts, catalysts subjected to thermal cycling, and catalysts exposed to an atmosphere containing CO or O_2.

3.6.1 Examination of As-Received Catalyst Samples

An initial investigation was undertaken to compare two diverse catalyst samples with a MoS_2 reference material. The catalyst samples studied were 3-1 (unactivated catalyst) and 3-4 (methanol aged catalyst). Figure 54 illustrates the results of the measurements. The spectra produced by analysis of samples 3-1 and 3-4 have some features in common with the MoS_2 reference, such as the features at 620 cm^{-1} and 1142 cm^{-1}. It is interesting that the feature at 1142 cm^{-1} is much sharper in sample 3-4 than in 3-1 or the MoS_2 reference. This could be due to better defined domains (i.e. more crystalline) MoS_2 in sample 3-4.

Broad bands at 1400 and 1643 cm^{-1} present in 3-1 are consistent with bands reported by Woo[16, 67] for MoS_2 doped with K_2CO_3. K_2CO_3 would be expected in the unactivated Range Fuels catalysts since, like Woo, K_2CO_3 had been physically mixed into the MoS_2 catalyst precursor. In addition, K $2P_{3/2}$ binding energies discussed above were consistent with K_2CO_3.

However, the DRIFTS bands for sample 3-1 are actually more similar to those reported for bicarbonate. Ranges of frequencies for bicarbonate species on metal oxides occur at 1390-1480 and 1600-1659 cm^{-1},[68, 69] corresponding to the features at 1400 and 1643 cm^{-1}. The peak at 1643 cm^{-1}, in particular, is not consistent with peaks for carbonate, which are reported at 1475 and 1356 cm^{-1}.[68] XPS spectra were not consistent with bicarbonate. The K $2P_{2/3}$ binding energy for $KHCO_3$ is reported to be 292.9 eV,[54] which is not what is observed. XRD measurements on sample 3-1 did not identify either crystalline carbonate or bicarbonate, even though crystalline K_2CO_3 was physically mixed into the precipitated Mo/Co/sulfide catalyst precursor. Bicarbonate could potentially be formed during the preparation if carbonate were chemically converted by reaction with residual acid that was used in the precipitation.

Some of the bands presented in Figure 54 from the DRIFTS analysis of sample 3-4 (methanol co-feed) may be suggestive of an adsorbed formate species ($HCOO^-$). The catalyst precursor 3-1, which was not exposed to reaction conditions, did not show these bands. According to Amenomiya[70] and Hornes et al.,[68] adsorbed formate exhibits infrared features at 1558-1590 and 1330-1395 cm^{-1}. Similar features are observed for sample 3-4 in Figure 54 centered at 1582 and 1425 cm^{-1}. The broad peak centered at 1425 cm^{-1} resembles a feature observed by Koisumi et al.,[71] who suggested it was a composite of absorbances by formate and another species, such as methoxide. Surface formate is believed to be an intermediate

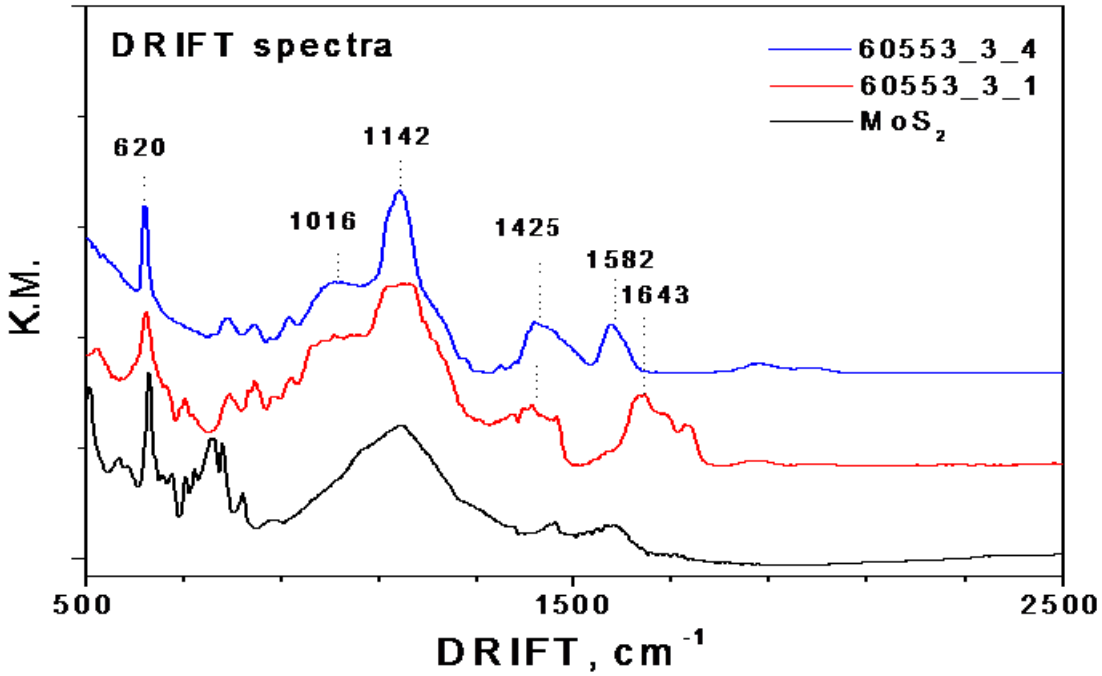

Figure 54. DRIFTS spectra of a MoS_2 reference material for comparison with samples 3-1 and 3-4. The spectra were collected in a He environment at room temperature.

in water-gas shift catalysis and Koizumi et al.[71] reported that adsorbed formate species can be converted to CO_2, CH_4, or methanol.

Sample 3-5, which was a K_2MoS_4 reference material supplied by Range Fuels, was also measured with DRIFTS. The feature at 1016 cm^{-1} observed in samples 3-1 and 3-4 in Figure 54 may be due to the presence of K_2MoS_4. The spectrum of K_2MoS_4 is discussed further below (Figure 57).

3.6.2 Thermal Cycling of Selected Catalysts

Thermal cycling of selected samples was initiated in order to investigate the thermal stability of observed DRIFTS features. Thermal cycling was expected to reveal if structural changes occurred in the catalyst and whether adsorbed species (such as formate) were stable on the catalyst surface.

The effect of thermal cycling on sample 4-1 (activated catalyst) was investigated. Figure 55 illustrates the effects of heating the sample in flowing He from room temperature to 300°C at 10°C/min with a 1 h

soak at 300°C followed by cooling back to room temperature. The features at 1420 and 1575 cm^{-1}, which may be due to adsorbed formate as discussed above, were again present in activated catalyst. These features decreased during the thermal cycle, suggesting formate decomposition as reported by Woo et al.[16]. Additionally, CO_2 was observed at 2300-2400 cm^{-1} on heating to 250°C and above (shown at 300°C in Figure 55). The CO_2 may have been formed during formate decomposition or may also have been related to the disappearance of the unknown features at 1850-2050 cm^{-1}, which also occurred at this temperature After 1 h at 300°C, the CO_2 was swept away by the He purge gas and did not appear in subsequent spectra.

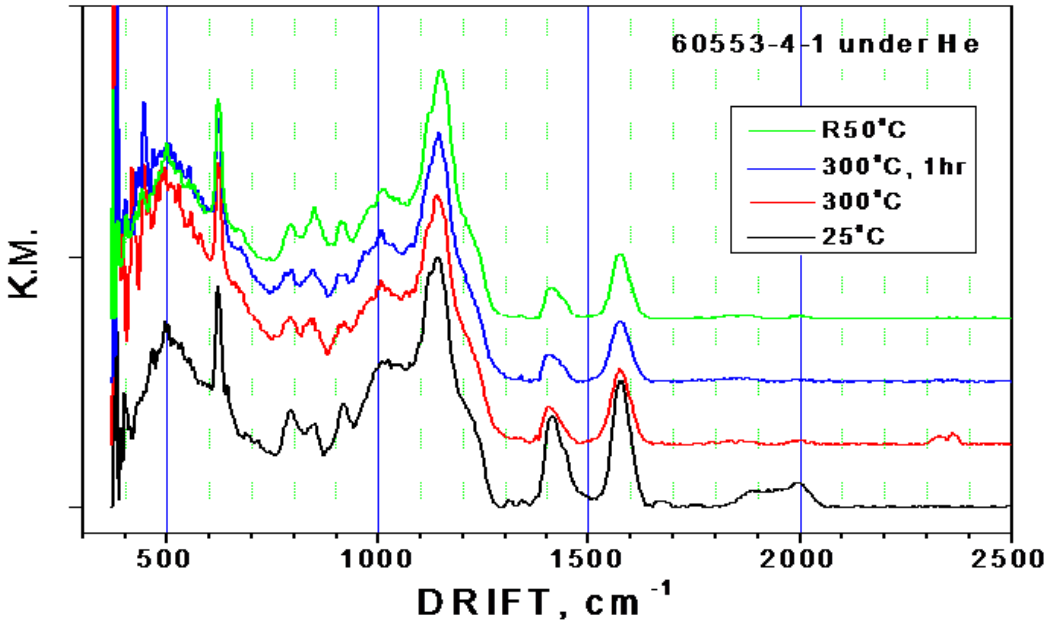

Figure 55. DRIFT spectra of sample 4-1 under He at room temperature, raised to 300°C, held for 1 h, then cooled to 50°C. Spectra baselines have been offset to more clearly show spectral features.

Next, the effect of thermal cycling on sample 3-4 was investigated under a He atmosphere. Features that changed appreciably are marked in Figure 56(a) and (b). The diminishment of the features at 1420 and 1575 cm^{-1} may again be from the decomposition of the adsorbed formate species. Figure 56(b) illustrates that the new features at 670 and 1000 cm^{-1} that developed during the thermal cycle heat-up in Figure 56(a) were still present when the sample was returned to room temperature. Thus, the change in the DRIFTS spectra observed during heating indicated that another irreversible structural process occurred. This process might be related to formation of K_2MoS_4, which has bands at 670 and 1000 cm^{-1}, or a related species.

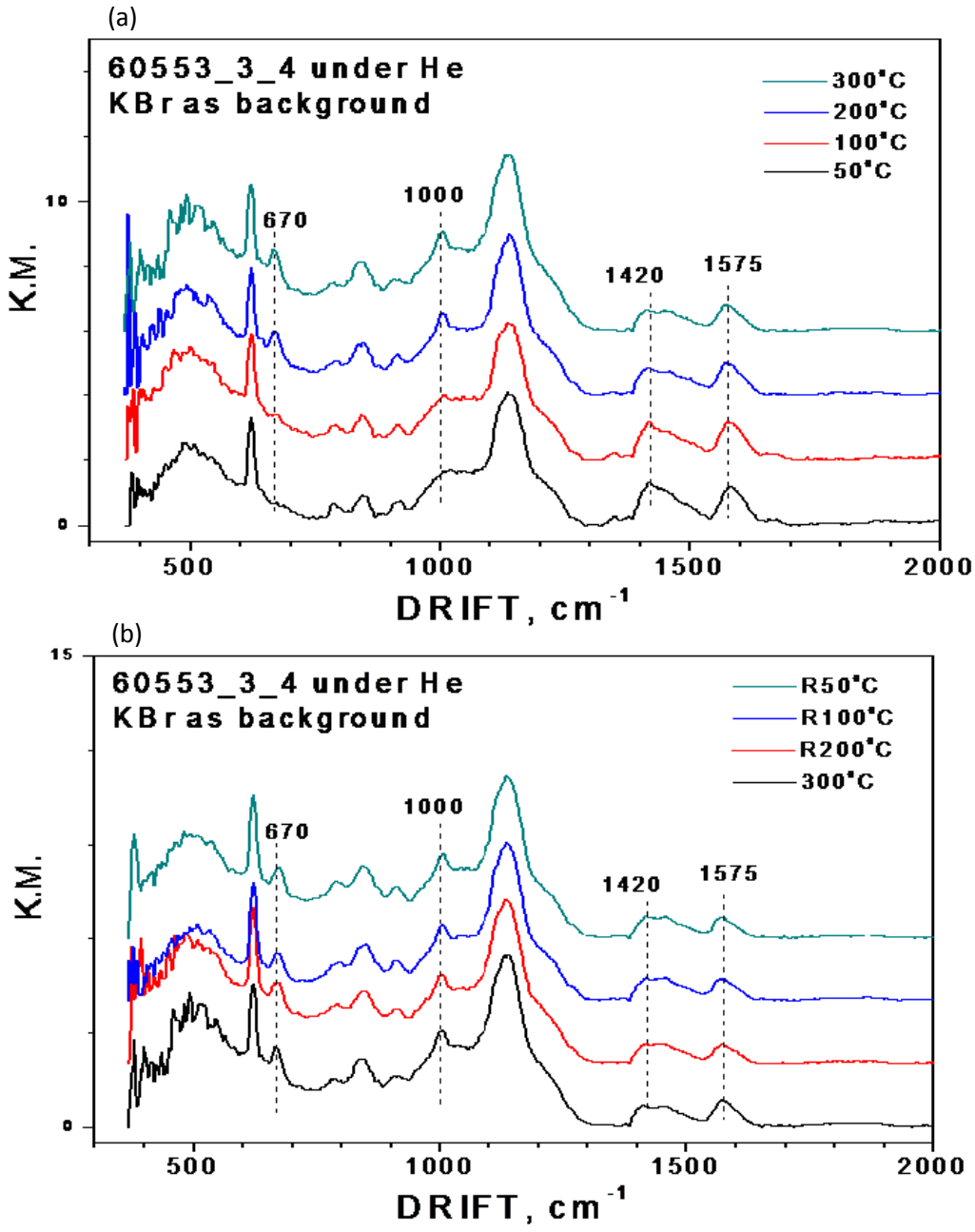

Figure 56. DRIFT spectra of sample 3-4 under flowing He (a) during heating of the sample at 10°C/min (b) during cooling of the sample at 10°C/min back to 50°C.

Figure 57 compares the spectra of the K_2MoS_4 and MoS_2 reference materials with the results of the DRIFTS analysis on sample 3-4 before and after the thermal cycle. The features at 618, 1132, 1420, and 1575 cm^{-1} were consistent with the characteristic bands shown in MoS_2 while the features at 670, 843, 910, 1000, and 1132 cm^{-1} were close to the bands from K_2MoS_4. It is interesting to note that the spectra

obtained after the heat treatment of sample 3-4 showed the growth of features associated with K_2MoS_4. How this species, or a species with similar infrared spectrum, could form on thermal treatment under an inert atmosphere is unknown.

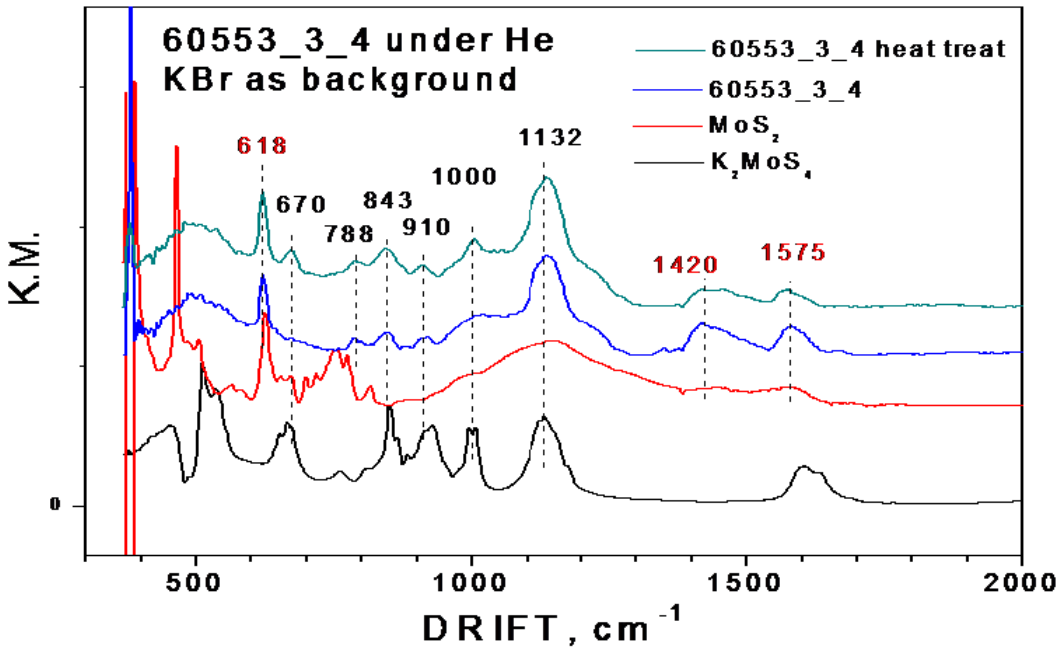

Figure 57. DRIFTS spectra of a fresh sample of 3-4, a sample of 3-4 after cycling to 300°C and subsequent cooling to room temperature at 10°C/min and the reference materials MoS_2 and K_2MoS_4.

3.6.3 DRIFTS CO Chemisorption Studies

Experiments were conducted to explore the interaction of CO with selected Range Fuels catalysts. Chemisorbed CO is reported to register DRIFTS features at about 2060 cm^{-1}.[71] CO chemisorption experiments on a sample of activated catalyst (4-1) showed that no chemisorbed CO was observed spectroscopically between 25 and 300°C (Figure 58). However, CO_2 was produced in the presence of CO with the rate of CO_2 formation apparently increasing with temperature. CO_2 first appeared at about 100°C. A much smaller amount of CO_2 was observed when 4-1 was heated to 300°C under He (Figure 55) with the onset of CO_2 formation being higher at about 250°C (not shown). Possible sources of CO_2 are discussed below.

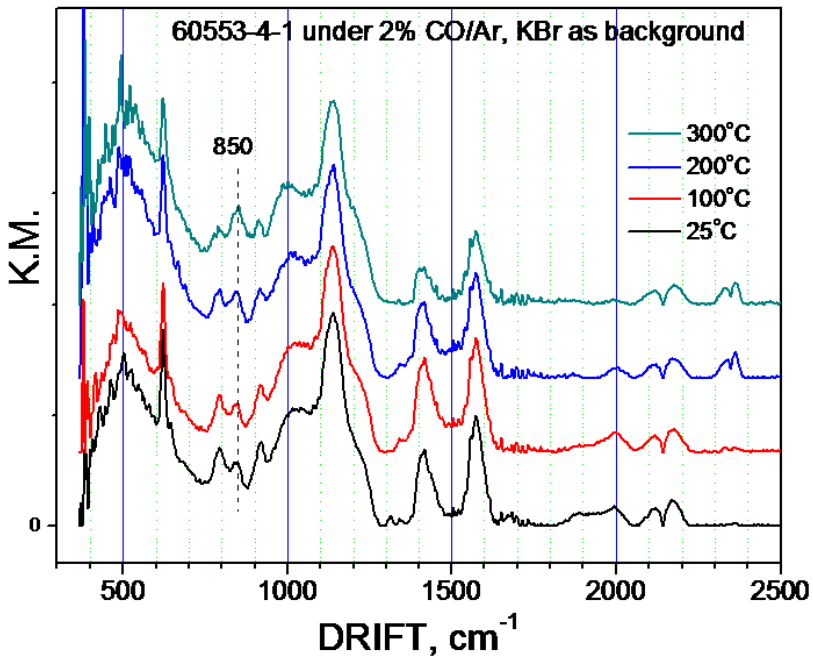

Figure 58. DRIFT spectra of sample 4-1 under 2% CO buffered in argon. The sample temperature was ramped to 300°C at 10°C/min.

Sample 3-4, the methanol aged RF-101, was subjected to a similar chemisorption experiment for comparison with sample 4-1. Like 4-1, no chemisorbed CO bands were observed on 3-4 during temperature ramping, as shown in Figure 59. In addition, CO_2 formation occurred at increasing temperatures in the presence of CO, but was absent when the sample was heated under He. The rate of CO_2 formation appeared to reach a maximum at 200-250°C, dropping off at 300°C. This type of behavior was also observed for sample 3-1, discussed below, but it is unknown whether this is an experimental artifact or a chemical phenomenon.

For fresh, unactivated catalyst (3-1), Figure 60 illustrates that at temperatures up to about 250°C very little CO was chemisorbed. However, unlike the previously discussed samples, at 250°C, the surface population of chemisorbed CO increased significantly as indicated by the growth of a new peak at 2070 cm^{-1}. The appearance of this band at higher temperatures suggests that either it was necessary to remove bound materials before CO could reach the surface or that ligand loss to form coordinately unsaturated metal sites was necessary for CO binding. Chemisorption of CO was reversible as evidenced by the extinction of the band after stopping the feed of CO and purging with Ar (not shown). This indicates that the bonding between CO and surface adsorption sites was relatively weak at 250-300°C.

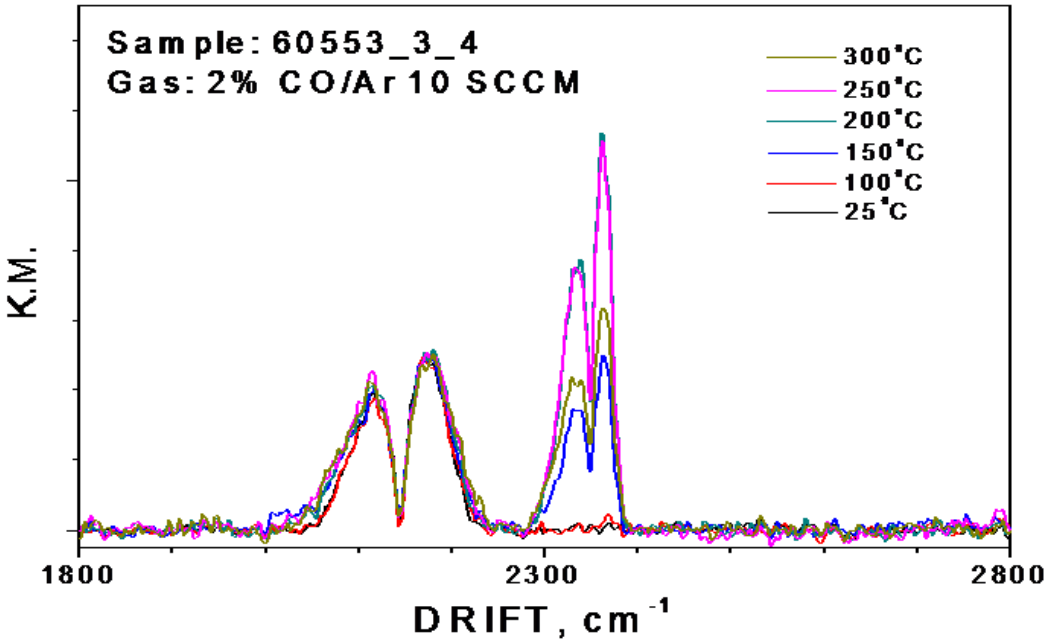

Figure 59. DRIFTS measurements of sample 3-4 under 2% CO buffered in Ar during ramping from room temperature to 300°C at 10°C/min.

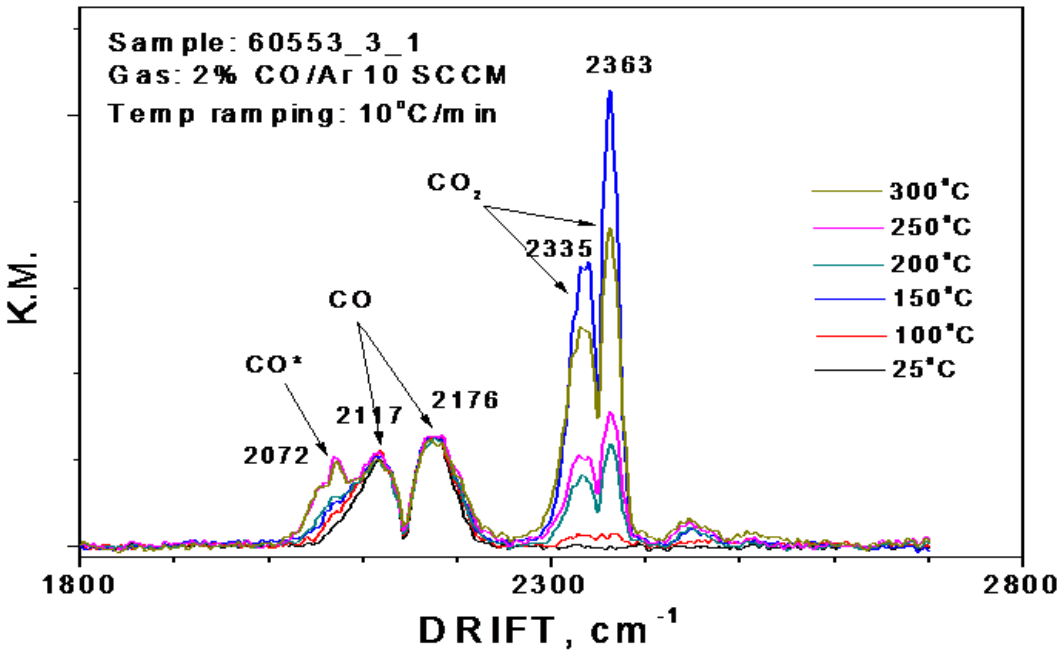

Figure 60. DRIFT spectra of sample 3-1 under 2% CO buffered in Ar. The spectrum produced from a sample of untreated 3-1 was used for background subtraction, so the bands shown arise from new surface species. The band at 2072 cm^{-1} labeled CO* is from chemisorbed CO on the catalyst surface. The temperature was ramped to 300°C at 10 °C/min.

Figure 60 also shows that, like the other samples, CO_2 was observed at elevated temperatures, with the onset being about 100°C.

There are at least three possible sources of CO_2 when heating these samples. Under He, CO_2 might be generated by thermal bimolecular decomposition of bicarbonate, which would form CO_2, water, and carbonate. This decomposition is known to occur at temperatures as low as 100-120°C. In the samples studied, under He, CO_2 doesn't appear until much higher temperatures, so either this process does not occur, or the higher temperature is needed to increase surface mobility.

CO_2 may have been produced from CO via the water-gas shift reaction ($CO + H_2O \rightarrow CO_2 + H_2$). If this were the case, the water would need to be present within the catalyst itself since none was added during the experiments. Samples 4-1 and 3-4 produced CO_2 at 300°C under flowing 2%Co/Ar for 1.5h and 2.0 h, respectively, with some loss in production rate with time (40% for 4-1 and 20% for 3-4, estimated).

Another possibility is that CO_2 may have been produced by the Boudouard reaction ($2\ CO \rightarrow CO_2 + C(s)$). This reaction can occur on Co metal surfaces as low as 225°C (Nakamura et al.[72]), with low temperatures favoring the CO_2 side of the equilibrium. There was no evidence of Co metal in 3-1 or 4-1 samples, but a shifted peak consistent with a small degree of CO interaction with metal at 100-150°C was observed in sample 3-1 (Figure 60). Further work is needed to determine which pathway(s) lead to CO_2 over these catalysts.

In addition to adsorbed CO, other new surface species are also formed when 3-1 was placed under flowing CO at 250°C (Figure 61). Many of the bands observed have not been assigned. However, bands at 1564 and 1387 cm^{-1} (top) appear to arise from surface formate, as observed before. The presence of a small absorption at 2935 cm^{-1} (bottom) is consistent with this assignment.

3.6.4 DRIFTS Oxidation Studies

A sample of activated RF-101 (4-1) under oxidizing conditions was investigated with DRIFTS. Figure 62 illustrates the effect of 1% O_2 buffered in Ar during a temperature ramp to 300°C at a heating rate of 10°C/min. The intensities of the bands at 670, 846, and 1006 cm^{-1}, which most likely correlate with

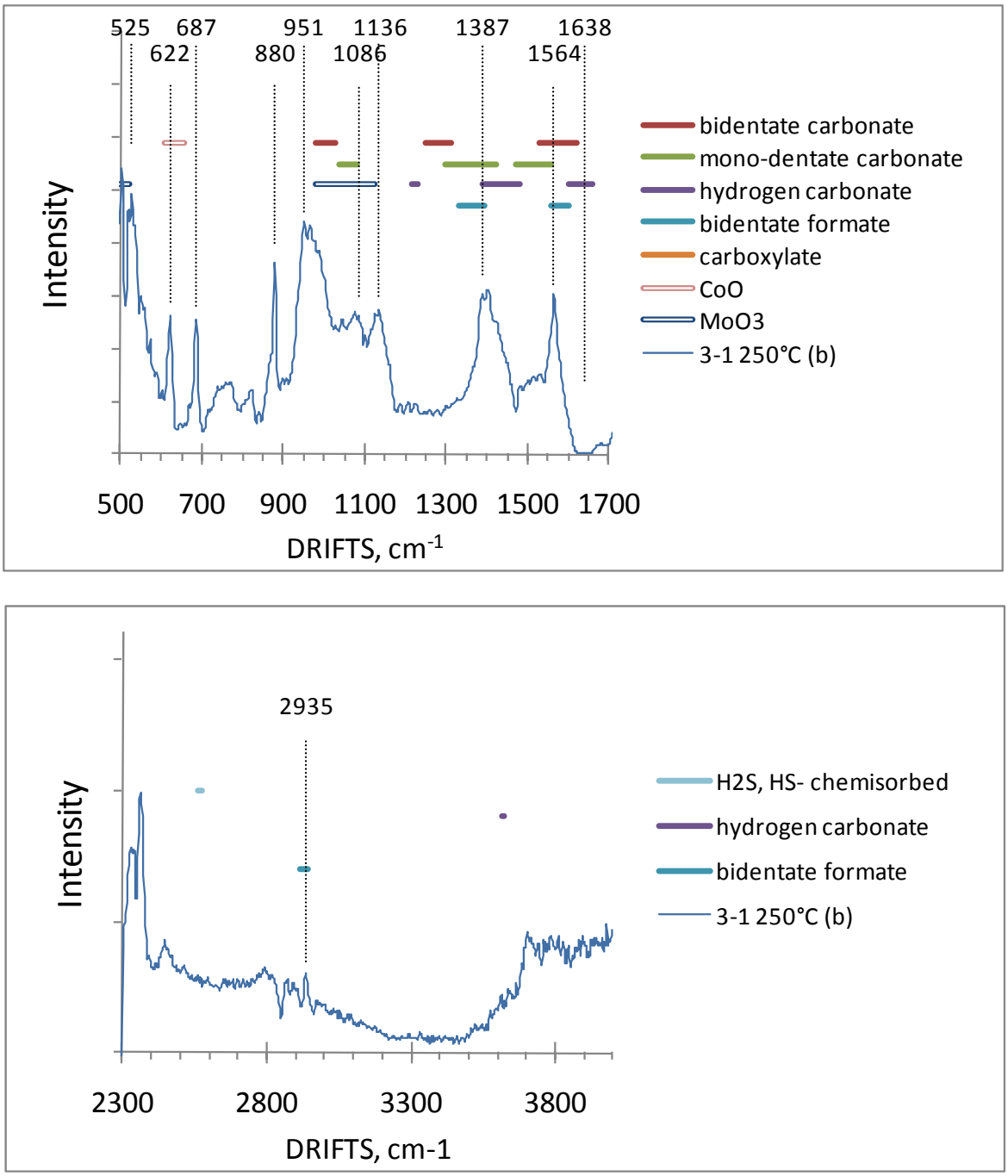

Figure 61. DRIFT spectra of sample 3-1 under 2% CO in Ar at 250°C. Fresh 3-1 is the background spectrum, so bands shown arise from new surface species. Bars represent reported ranges for species absorption bands as reported by Toops and Crocker[69] and Hornes et al.[68]

K_2MoS_4 (Figure 57), increased during ramping to 200°C. However, at 300°C, the bands suddenly diminish. The bands may have diminished due to sulfur lost in the oxidizing atmosphere. Alternatively, MoO_3 may have been formed from the desulfurization of MoS_2. According to Du et al.[73], MoO_3 exhibits a fundamental stretching vibration of crystalline vibration at 990 cm^{-1} characteristic overtones at 1100-1300 cm^{-1} and smaller overtones 1885-1970 cm^{-1}. The data in Figure 62 is at best inconclusive with respect to the possibility of MoO_3 due to convolution with other signals and the likely low concentration of MoO_3. However, the growth of peaks at 620 and 1100-1200 cm^{-1}, may be indicative of the formation of K_2SO_4.[16] XPS results performed on the same sample used to produce the spectra in Figure 62 did exhibit Mo^{6+} and a relatively high concentration of sulfate (~6 atomic%) compared with samples not exposed to oxygen. For comparison, a sample of 4-1 not subjected to oxidizing conditions at elevated temperatures exhibited only about 3.7 atomic% sulfate and no identifiable Mo^{6+}.

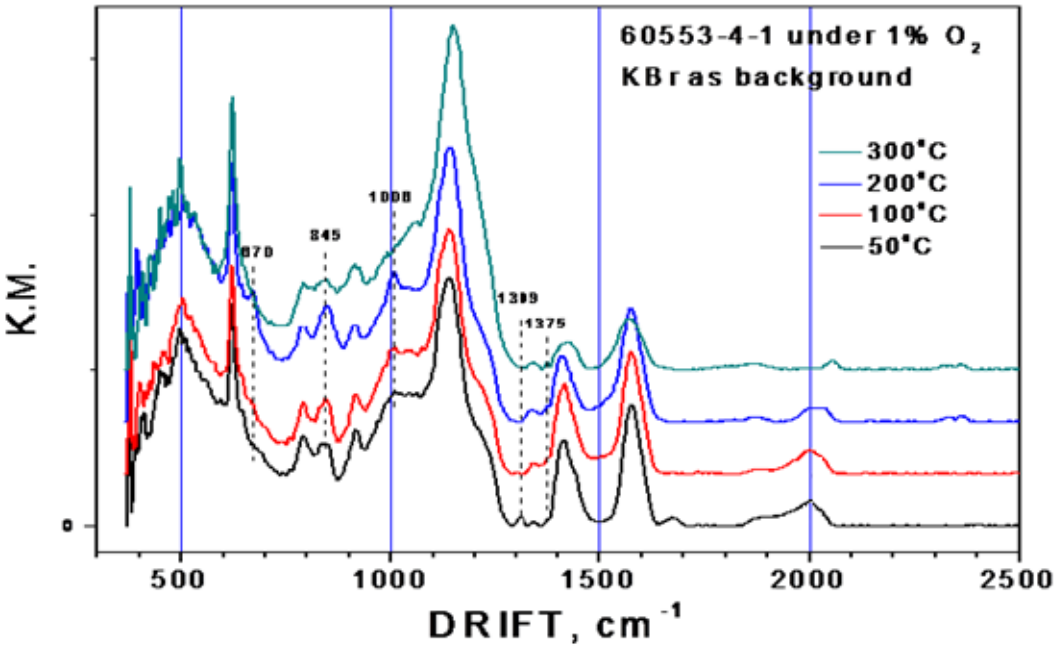

Figure 62. DRIFT spectra of sample 4-1 under 1% O_2 buffered in He.

3.7 TPR/TPD/CO Chemisorption Analysis Results

Temperature programmed reduction (TPR), desorption (TPD) and CO chemisorption experiments were performed on selected catalytic and reference samples. The experiments were performed in order to gain insight into the mechanism of catalyst deactivation under various flowing gases. MoS_2 was initially analyzed as a reference material. The catalyst samples analyzed were 3-2 (RF-101 used for long periods), 3-5 (K_2MoS_4 reference material) and 4-1 (activated RF-101). .

The MoS_2 reference material was considered first for comparison with the catalyst samples. The TPR profile of MoS_2 (Figure 63) supports the findings of Aoshima and Wise[74] who reported MoS_2 must be taken to at least 600°C before H_2 uptake is observed. The MoS_2 samples tested in this investigation showed similar behavior even after calcination at various temperatures in flowing He, as can be seen by the TPR profiles in Figure 63. Trial 010-100 registered a reading on the TCD slightly before 600°C while in trial 010-069 the TCD signal began to change closer to 700°C. In contrast, the temperature ramp of the fresh MoS_2 showed little to no change up to even 1000°C. Although the TCD cannot directly differentiate H_2 adsorption from H_2S desorption, the report by Dianis[75] as well as the report by Aoshima and Wise[74] asserted that reduction of MoS_2 will not take place without the release of significant amounts of sulfur. It is also interesting to note that while increasing the temperature with H_2 present did not result in H_2 uptake, pre-treatment under increasingly higher temperatures in He resulted in H_2 uptake at lower temperatures. Speculatively, the pre-treatment at higher temperatures in He may have altered the material in a manner that made S less strongly bound to the bulk MoS_2. This may have resulted in S being more susceptible to removal at lower temperatures.

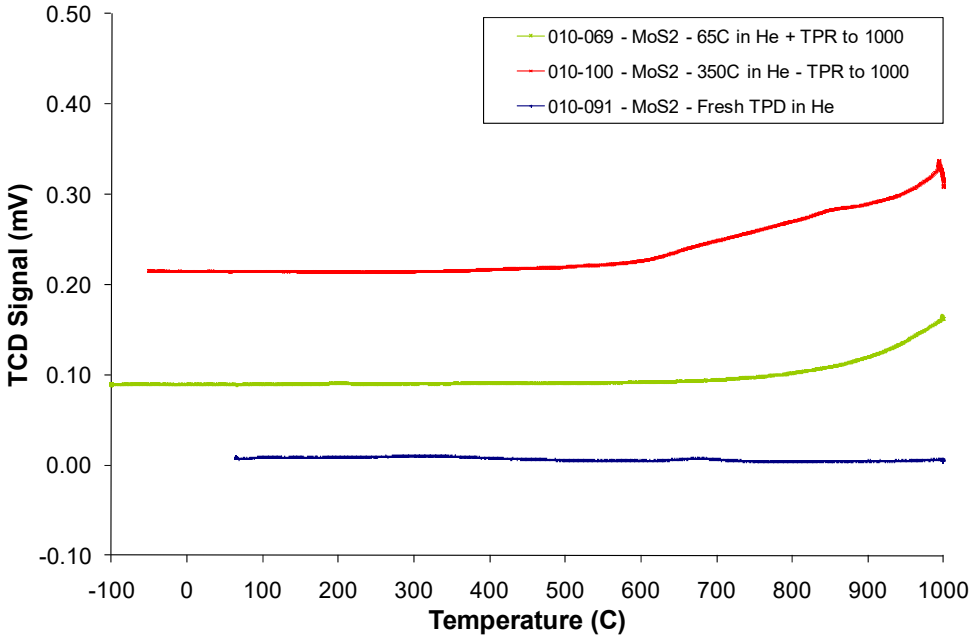

Figure 63. TPR profiles of fresh MoS_s or after subjection to He pretreatment at 65°C or 350°C in He. The TPR experiments were performed using 5% H_2 in Ar.

During TPR testing of the MoS_2 reference sample, accelerated deterioration of the thermocouple inside the tube was observed. The majority of the Micromeritics system's internal components are designed for sulfur resistance. However, the thermocouples are designed only to withstand numerous heating cycles and are not as resistant to corrosive gases. Under normal operating conditions, a thermocouple will last dozens of experiments but the thermocouples failed after only a few runs with sulfur containing samples. Thus, it seems likely that some sulfur loss was occurring, probably in the form of corrosive H_2S, which was manifested in the deterioration of the sample thermocouple.

CO chemisorption and subsequent temperature programmed desorption (TPD) experiments were also performed on the MoS_2 reference material. While it is apparent from Figure 64 that very little gas was desorbed from fresh MoS_2, CO saturation of a MoS_2 sample that had been pretreated at 65°C in He resulted in various periods of desorption from the sample even though only a small amount of CO (<1 μmol/g) was adsorbed by the material (see Table 6). Speculatively, the desorbed species may have been CO, which had adsorbed to Mo atoms, possibly at exposed edge sites, although this seems

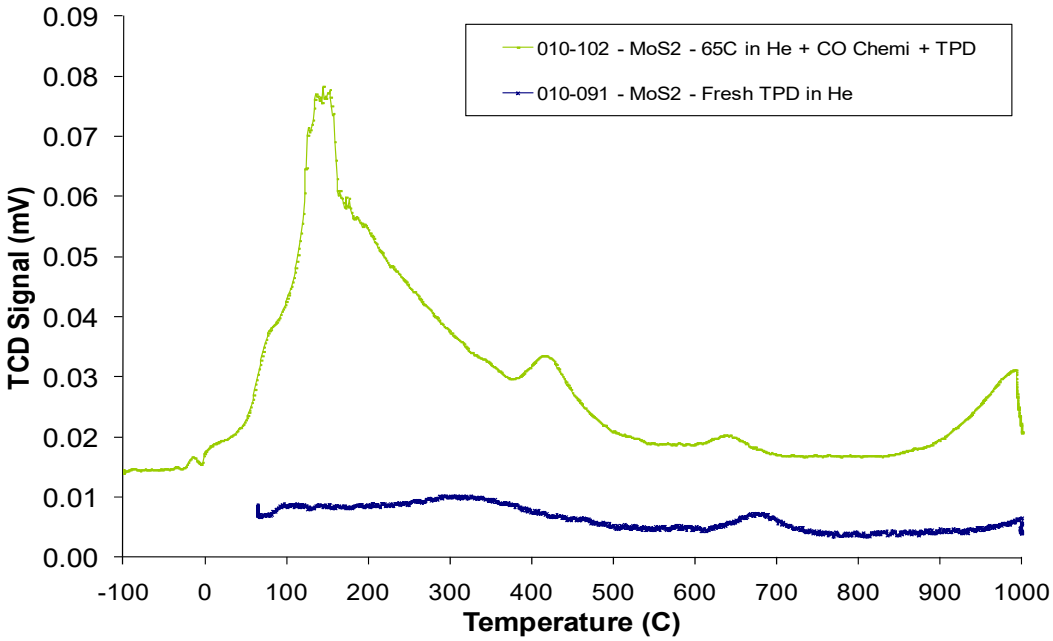

Figure 64. TPD profiles of fresh MoS_2 as well as MoS_2 pretreated at 65°C, saturated with CO and then subjected to TPD analysis.

Table 6. The amount of CO adsorbed during chemisorption experiments on various reference and catalyst samples subjected to different pretreatments.

Run ID	Material	Pretreatment	CO Adsorbed, μmol/g
010-102	MoS_2	65°C in He	<1
010-074	K_2MoS_4	350°C in He	<1
010-099	K_2MoS_4	65°C in He	<1
010-076	4-1	350°C in He	15.3
010-094	4-1	350°C TPR	24.0
010-026	3-2	350°C in He	2.0
010-025	3-4	350°C in He	8.1

unlikely as such a small amount of CO was adsorbed. Alternatively, adsorbed CO may have reacted with the S to form COS, which may have been a mechanism for S loss. The large peak at about 115°C in the CO-treated sample TPD in Figure 64 may be due to elemental sulfur, which has a melting point at 115°C.

Next, sample 3-5, the K_2MoS_4 reference material, was subjected to various temperature programmed tests. During the course of the tests, sulfur loss was readily observed in several samples by the formation of bright yellow droplets at the outlet of the sample tube. These droplets were seen during runs 010-092 (Figure 65) and 010-099 (Figure 66) and were assumed to be from elemental sulfur that condensed at the sample tube outlet after the sample was heated. The temperature at the outlet of the tube was constant at 110°C, which was just below the melting point of S at 115°C. Both of the tubes exhibiting the yellow droplets contained K_2MoS_4 and were taken to 1000°C under He without a subsequent TPR experiment. Sulfur droplets were most likely not observed after samples that terminated with TPR experiments because the H_2 reacted with the S to form H_2S, which was carried away in the flow gas stream. The source of the elemental S was likely a residual contaminant left over from the preparation of the K_2MoS_4. Visual inspection of the K_2MoS_4 material revealed that the sample appeared heterogeneous. Furthermore, XRD testing revealed that while K_2MoS_4 was the major crystalline phase, there were other impurities.

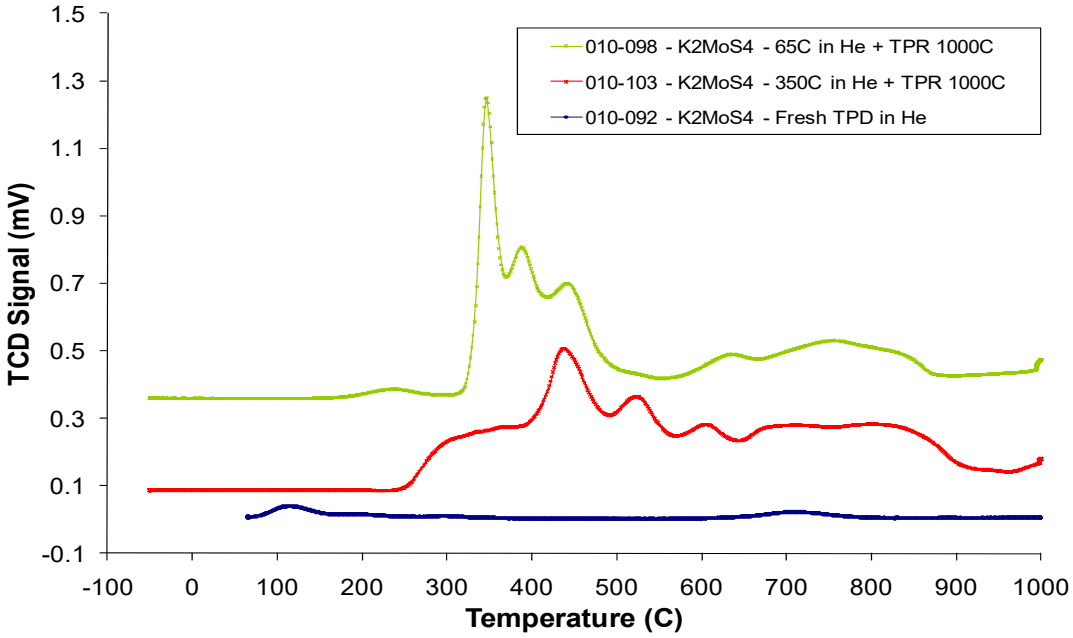

Figure 65. TPR profiles of fresh K_2MoS_4 or after pretreatment at 65°C or 350°C in He. The TPR experiments were performed using 5% H_2 in Ar.

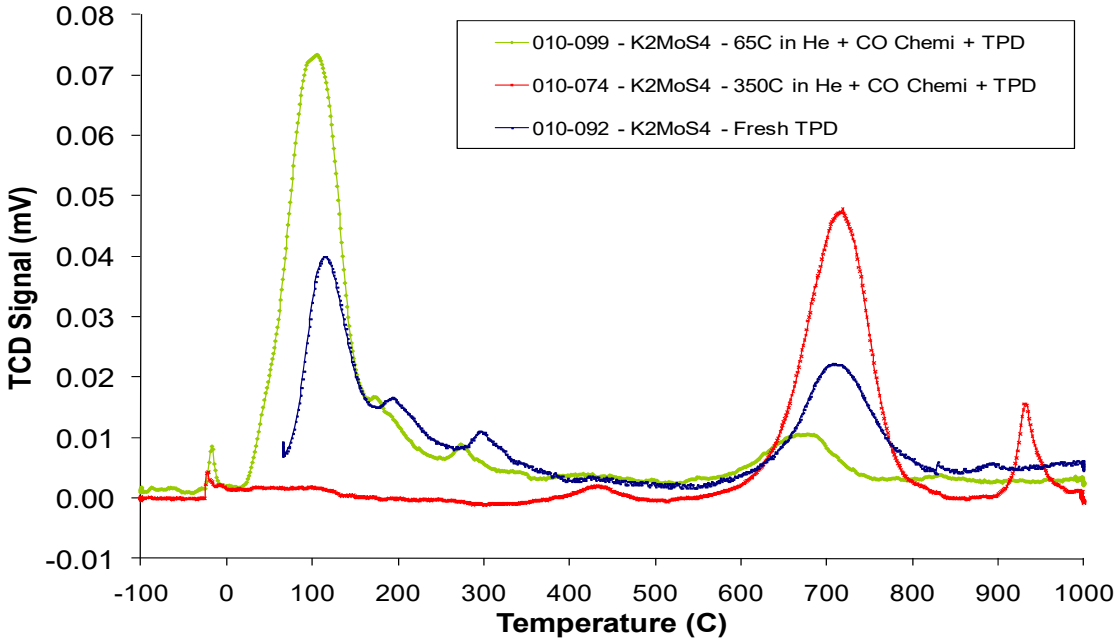

Figure 66. TPD profiles of fresh K_2MoS_4 as well as K_2MoS_4pretreated at 65°C or 300°C, saturated with CO and then subjected to TPD analysis.

Figure 66 gives a higher resolution of the 101-092 run, which was a TPD experiment on the fresh K_2MoS_4 reference. The peak at 115°C is likely due to the melting and subsequent evaporation of elemental S, which was most likely present in the sample as an impurity. The peak is also apparent in sample pretreated at 65°C. Elemental S was also probably in the sample pretreated at 350°C, but was lost during the pretreatment. Interestingly, in Figure 65, the sample pretreated at 65°C and then subjected to TPR did not exhibit the peak at 115°C

Catalyst samples were also investigated with temperature programmed experiments. First, a sample of activated catalyst (4-1) was investigated. TPR analysis on sample 4-1 indicated that there may be elemental sulfur present as evidenced by the blue peak centered at about 115°C in Figure 67. Comparison with the TPR traces of other reference materials in Figure 67 demonstrated few, if any, similarities in the traces of sample 4-1 with other reference materials. It is also interesting to note that TPR testing of the binder caused the baseline to shift during (red trace, Figure 67).

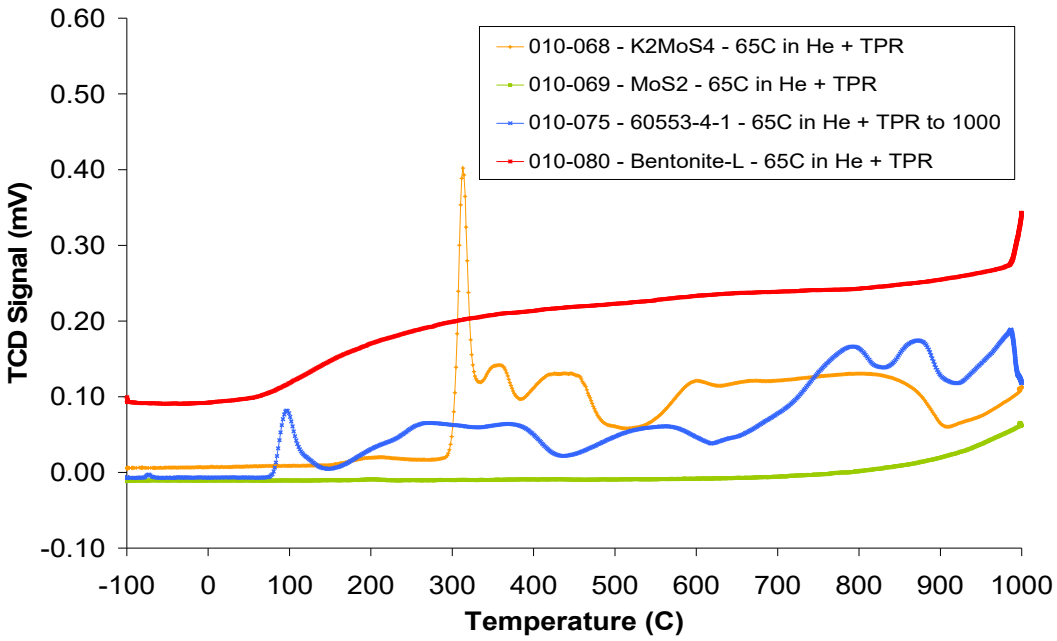

Figure 67. A comparison of the TPR profiles of K_2MoS_4, MoS_2, the Bentolite® binder and sample 4-1 (activated RF-1010) after pretreatment at 65°C in He. The TPR experiments were performed using 5% H_2 in Ar.

Sample 4-1 was also subjected to TPD experiments after various pretreatments. The results are plotted in Figure 68. Several periods of activity were recorded by the TCD during the TPD experiment with sample 4-1. The TPD performed after reduction to 350°C and subsequent CO saturation (red trace in Figure 68) exhibited similar features as the TPD of the unaltered 4-1 above 350°C. Interestingly, pretreatment at 350°C in He prior to CO saturation and subsequent TPD testing lowered the desorption temperature of what are presumably similar species to 400°C and 550°C (green trace in Figure 68). The pretreatment in He may have weakened the bonds between the desorbed species and the catalyst, resulting in diminished desorption temperatures.

According to Table 6, the pretreatment of sample 4-1 did affect the amount of CO chemisorbed during CO saturation. While the sample pretreated in He adsorbed about 15 μmol/g, the sample pretreated in H_2 via TPR testing took up 24 μmol/g. Speculatively, this increase in CO uptake may have been due to S loss, which could have resulted in more exposed metal sites capable of adsorbing CO. Since the mechanism of CO adsorption that results in mixed alcohol synthesis is not clearly understood, the increased uptake of CO may or may not be beneficial. However, when the CO chemisorption results of

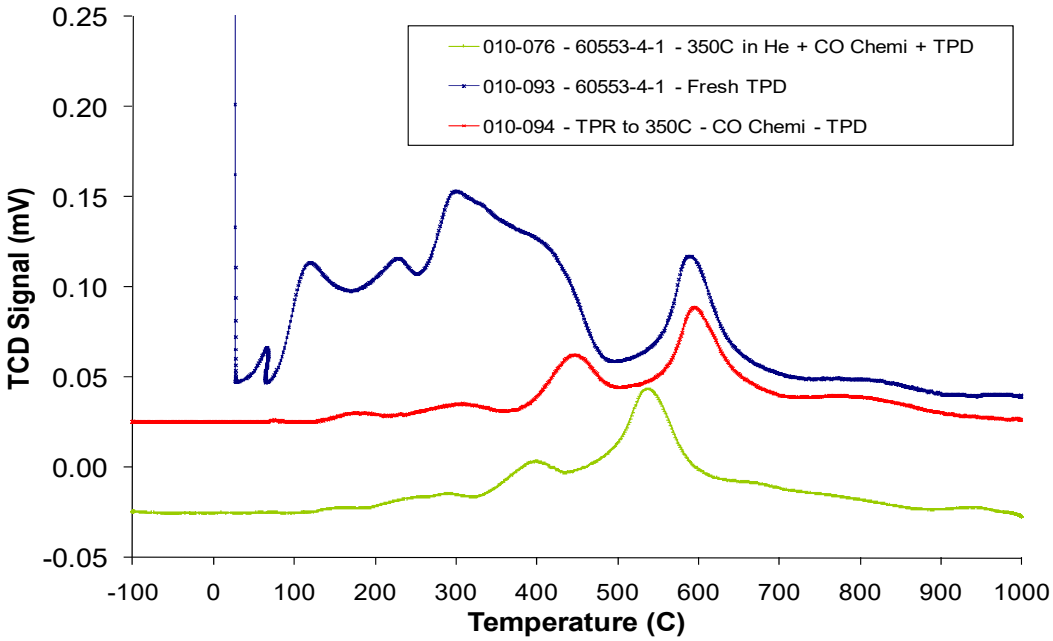

Figure 68. TPD profiles of sample 4-1 (activated RF-101) as well as 4-1 pretreated at 350°C in He or TPR tested to 350°C. The samples subjected to TPR or pretreated at 350°C were saturated with CO prior to TPD analysis.

sample 4-1 are compared with comparable experiments on 3-2 (catalyst utilized for mixed alcohol synthesis for 4200 h) and 3-4 (catalyst aged through methanol addition), it is possible that CO adsorption is greater with the activated catalyst and diminishes upon use in the mixed alcohol synthesis reactor. However, caution should be exercised when comparing the results obtained from sample 3-2 as the sample was inadvertently exposed to air prior to analysis.

Limited testing was also performed on samples 3-2 (catalyst subjected to mixed alcohol synthesis for 4200 h) and 3-4 (methanol aged catalyst). The TPD traces of the two samples, which had been subjected to CO chemisorption, are plotted in Figure 69. It is interesting to note that sample 3-2 exhibited what has been suggested above as elemental S loss at about 115°C. It is impossible to determine if a similar period of suspected sulfur loss was exhibited by sample 3-4 since the sample was pretreated at 350°C in air. On the other hand, if sample 3-4 did lose elemental sulfur during pretreatment in He, the loss was not necessitated by the presence of CO.

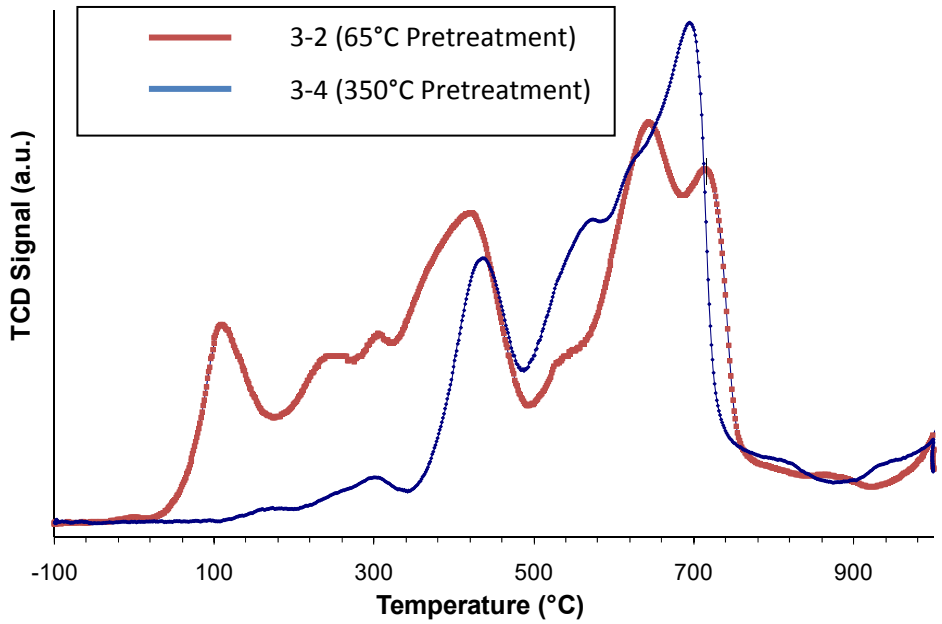

Figure 69. TPD traces of samples 3-2 (catalyst subjected to mixed alcohol synthesis for 4200 h) and 3-4 (methanol aged catalyst). Sample 3-2 was pretreated at 65°C in He while sample 3-4 was pretreated at 350°C in He. Both samples were then saturated with CO at -100°C and subjected to the TPD testing shown.

3.7.1.1 TPR of Metal Oxide References

Temperature programmed reduction (TPR) tests of Co and Mo oxide were also performed. Although the Co and Mo present in the active catalyst were sulfided, TPR experiments on bulk oxides were performed in order to understand if metal oxide reduction could take place if oxidation did occur. Figure 70 illustrates the reduction profile of Co (II) oxide. Figure 70 clearly shows that reduction was taking place by 300°C, which is the temperature used for the synthesis of mixed alcohols. Likewise, Figure 71 illustrates that a mixed valence Co (II,III) oxide material was also undergoing reduction by 300°C. In contrast, Figure 72 indicated that MoO_3 did not begin reduction until approximately 550°C. The MoO_3 sample continued to undergo reduction even up to 800°C when the TPR method was terminated. The results of the TPR tests on the Co and Mo bulk oxide references suggests that Co oxide could be reduced at 300°C but it is unlikely that Mo oxide would undergo reduction at these temperatures.

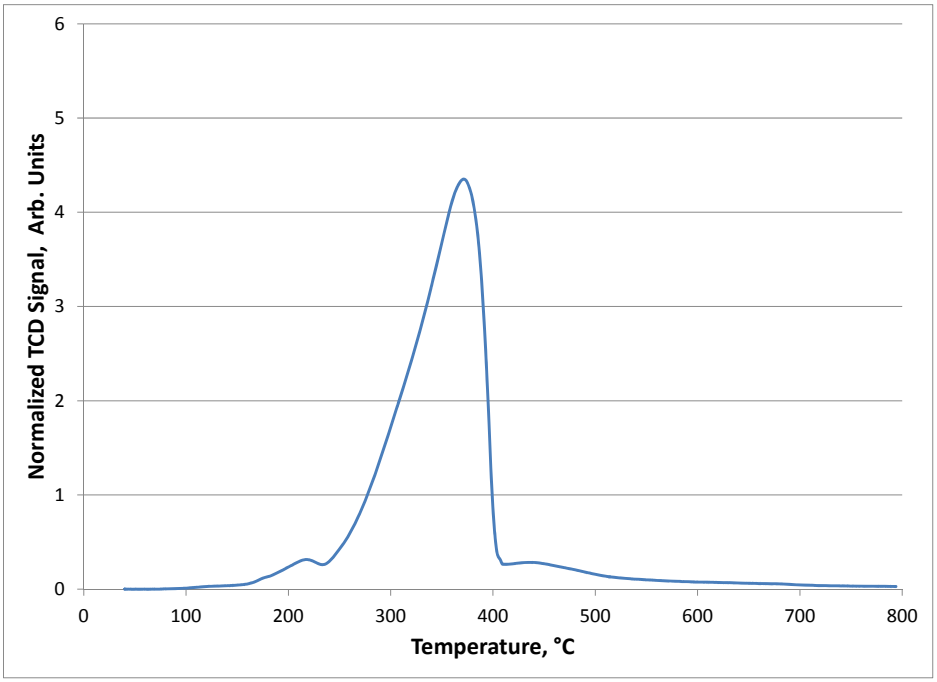

Figure 70. Temperature programmed reduction profile of the CoO reference material. The signal was normalized to the mass of the sample (0.1005 g).

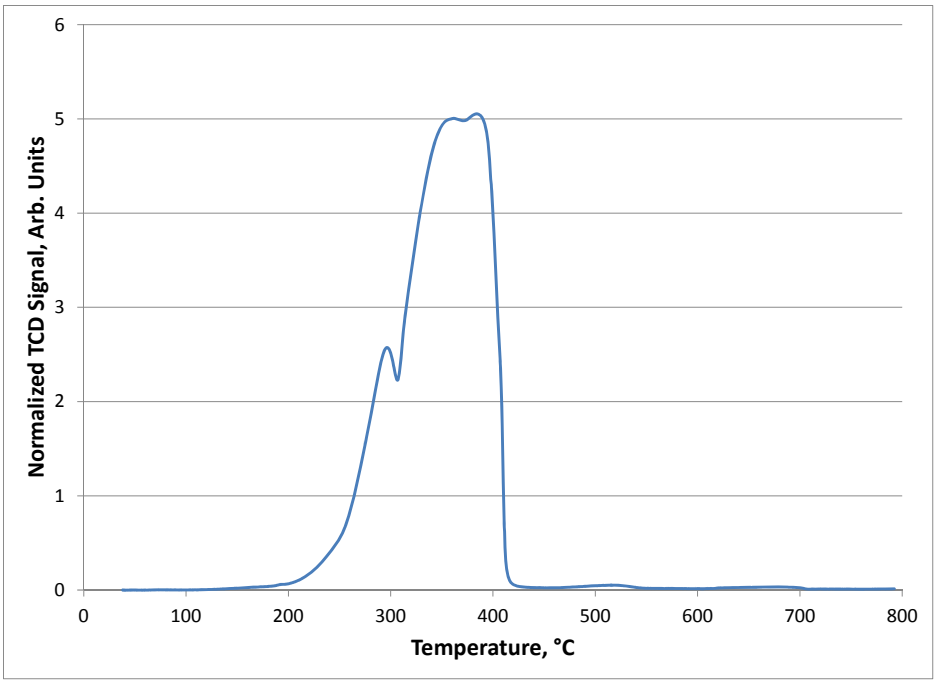

Figure 71. Temperature programmed reduction profile of the Co(II,III) oxide reference material. The signal was normalized to the mass of the sample (0.1088 g).

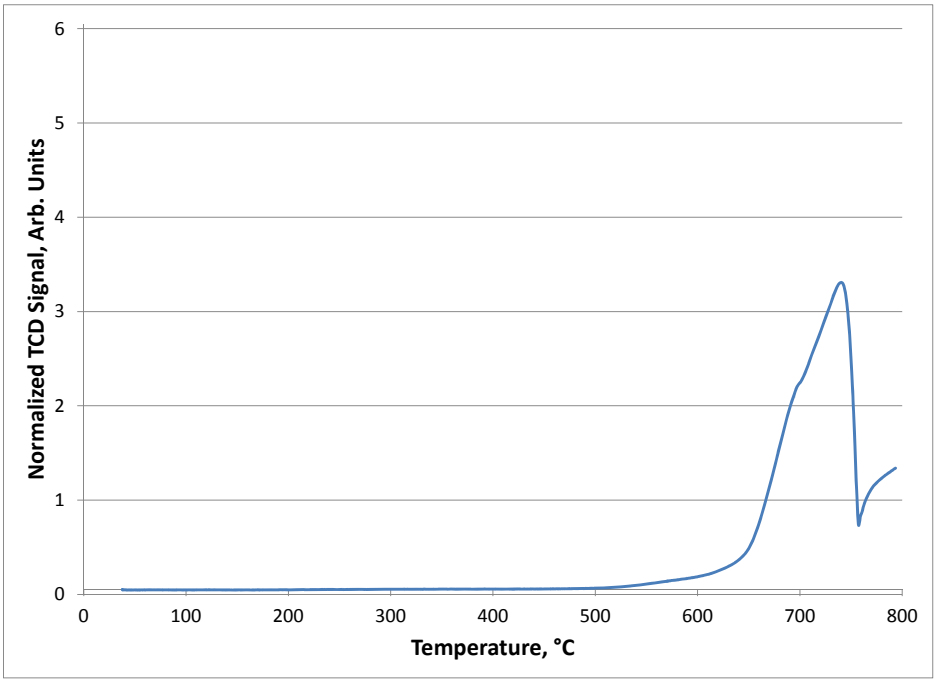

Figure 72. Temperature programmed reduction profile of the MoO_3 reference material. The signal was normalized to the mass of the sample (0.0938 g).

3.8 Computational Results

Periodic density functional theory calculations were performed to investigate the interaction potassium has with the Mo and S edges of the MoS_2(100) surface. Four sulfur coverage scenarios at the (100) surface were considered: 1) the “as-cleaved" bare Mo terminal edge and fully sulfided S terminal edge, 2) the 50% sulfided Mo edge and 50% sulfided S edge, 3) the non-stoichiometric 100% sulfided Mo edge and 100% sulfided S edge, and 4) 37.5% sulfided Mo edge and 50% sulfided S edge (effectively demonstrating a sulfur “vacancy" at the Mo edge). Both neutral and cationic (1+) potassium were considered; our electronic structure calculations indicate that neutral potassium readily donates its single valence electron to the MoS_2 structure, effectively behaving in a similar manner to the K+ systems. Potassium shows a tendency to maximize its interactions with the available sulfur atoms at the edge surface. Thus, at the “as-cleaved" surface, the most stable sites for potassium are over the S edge four-fold hollow sites. At the 50%-50% S-covered surface, potassium prefers to sit over the interstitial and coordinate with three sulfur atoms. At the 100%-100% S-covered surface, both sites over the interstitial coordinating four sulfur atoms and sites over four-fold S hollow sites on both edges are preferred. With a S “vacancy" at the Mo edge at the 37.5%-50% S-covered surface, potassium either prefers a higher sulfur concentration site away from the “vacancy" in the interstitial or coordinating with the two sulfur atoms on either side of the “vacancy".

3.8.1 Preferred K adsorption sites for the neutral and cationic systems

3.8.1.1 “As-cleaved" Mo0-S100 surface: Bare Mo edge and fully-sulfided S edge

Different sites on the Mo0-S100 surface shown in Figure 2a for both the neutral and the cationic systems were studied. The calculated adsorption energies are listed in Table 7. For the Mo0-S100 system, the most energetically stable site is the four-fold hollow site over the fully sulfided S edge surface Figure 73(a). K adsorption on the subsurface interstitial sites between two edges is not energetically stable. Moreover, we found that dramatic migration of the potassium from the initial tetragonal subsurface sites to an adjacent four-fold hollow site at the S edge, an S-S dimer is formed during the migration (Figure 73(b). Compared to the four-fold S hollow site with no S-S dimerization, K adsorbs at four-fold S hollow sites with neighboring S-S dimerization configurations are slightly more stable. This is consistent with a previous DFT study by Vojvodic et al.[44] where they found that alternating S-S dimerization patterns along the S edge were shown to be slightly more energetically stable than the fully undimerized S edge.

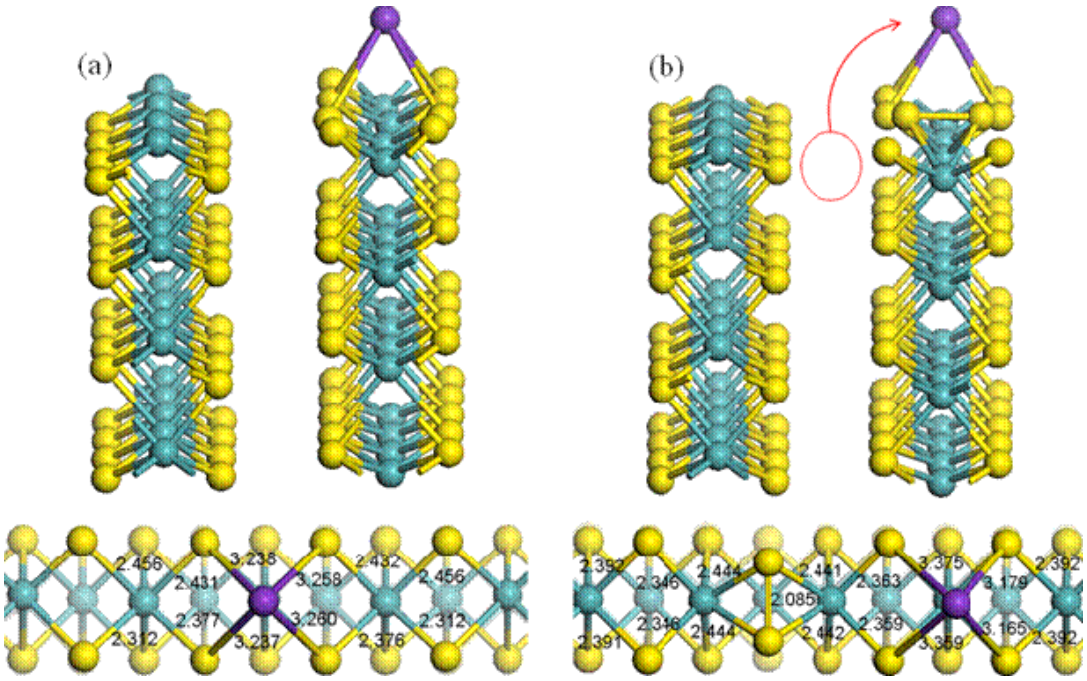

Figure 73. Local minimum energy structure for potassium atom over a sulfur hollow site on the S edge of the Mo0-S100 surface (left). Local minimum energy structure for potassium atom over a sulfur hollow site on the S edge with an adjacent disulfide dimer from migration of potassium out of a subsurface interstitial tetragonal site (empty circle denotes original position) during optimization (right). The K atom is represented by the purple ball. All distances listed in the figure are in Å.

As shown in Figure 73(a), the K–S distances for the neutral K adsorption (3.24-3.26 Å) are slightly shorter compared to those for the charged K system (3.29-3.33 Å) at the four-fold hollow site on the Mo0-S100 S edge surface. The average difference in K-S lengths for the charged versus neutral systems are summarized in Table 7. With the disulfide adjacent to the four-fold hollow adsorption site (Figure 73(b)), there is a broadening in the range of K–S bond lengths: 3.18-3.38 Å for the neutral system and 3.22-3.43 Å for the charged K system. The two K–S distances on the side of the hollow site that is closest to the disulfide dimer are longer than those farthest from the disulfide dimer. This may be due to the repulsive interaction between the positively charged potassium and disulfide species. Our calculated K–S distances are similar to the K–S distance of 3.20 Å in the antifluorite structure of K_2S.[76]

The second most energetically stable sites at the Mo0-S100 surface were found over the interstitial sites between two edges. One energetically stable configuration for both the neutral and cationic system was found through the migration of potassium out of a subsurface hexagonal interstitial site. As the subsurface S migrates from the tetrahedral subsurface site, the K atom induces the dimerization of two

Table 7. Stable neutral and cationic K adsorption sites, energies and Bader charges for the "as-cleaved" MoS_2 (100) edge surface (Mo0-S100).

	K (neutral system)				"K^+" (charged system)			
Adsorption Site K	**Adsorption Energy (eV)**	**Charge (e)**	**d_{K-S} (Å)**	**d_{K-Mo} (Å)**	**Adsorption Energy (eV)**	**Charge (e)**	**d_{K-S} (Å)**	**d_{K-Mo} (Å)**
Mo edge								
Mo atop (site 1)	-1.89	0.774		3.453	-0.65	0.838		3.631
Mo-Mo bridge (site 2)	-1.90	0.765		3.692 3.689	-0.69	0.816		3.846 3.862
S edge								
4-S hollow[a] (site 5)	-3.15	0.869	3.238 3.258 3.260 3.237		-1.84	0.877	3.333, 3.318, 3.328, 3.287	
4-S hollow with disulfided[b] (site 5)	-3.24	0.853	3.375 3.179 3.165 3.359		-2.06	0.868	3.433, 3.413, 3.239, 3.220	
Interstitial								
Above interstitial (site 8)	-2.82	0.846	2.987 2986, 3.520					
Above interstitial with disulfided (site 8)	-2.49	0.824	3.120 3.550	3.531	-1.21	0.870	3.223	3.753

[a]All initial site placements at the Mo edge that are not either Mo atop or Mo-Mo bridge sites are unstable and potassium migrates toward the S edge 4-S hollow sites during geometry optimization.
[b]Dimerization at S edge to create disulfide bonds is due to repulsion from potassium migrating out of subsurface sites, nudging sulfur atoms together during geometry optimization.

opposing S edge sulfur atoms. Unlike the migration process from the octahedral subsurface site discussed earlier, the K atom remains located over the interstitial and interacts with two sulfur atoms just below the terminal Mo atom layer at the Mo edge in the final configuration. Similarly, we note that the K–S distances for neutral K adsorption are slightly shorter than those of the charged system.

There is a weak interaction with the Mo on the other side of the interstitial (3.531 Å and 3.753 Å) for the neutral and cationic system, respectively. An energetically stable site is found over the interstitial with no dimer formed on the S-edge for only the neutral system case. Since the trend in K–S distances appears to be that the neutral system distances are shorter than those of the +1 charge system, the fixed distance between the MoS_2 edges is too short for a stable configuration over the interstitial in the +1 charge case. If the interstitial was allowed to expand, both the neutral and cationic system would prefer coordination between the S-edge surface and subsurface S atoms and the Mo-edge subsurface S atoms below the terminal Mo.

The least energetically stable sites on the Mo0-S100 surface were found directly over the atop Mo atop and bridging Mo–Mo sites of the bare Mo edge (Figure 74 (a) and (b), respectively) and nearly have the same adsorption energy. The Mo–K distances in these configurations are longer than the K–S distances in the cases where K is adsorbed over the S edge four-fold hollow or over the interstitial.

A number of ultra-high-vacuum experiments addressing the adsorption of the heavy alkali metals on the MoS_2(0001) basal surface can be found in the literature.[77-82] Though, these experiments only address alkali metal adsorption at the basal surface, some comparisons with the sulfur terminated edge surface and the sulfur-covered basal surface can be made. Kamaratos et al.[79] measured a ~3 eV desorption energy at low potassium coverage (θ_K < 0.5 ML) in their combined LEED, AES, EELS, and TDS experiments. Our lowest adsorption energies for the neutral system are similar to the basal surface estimation. Kamaratos[79] noted that this binding magnitude is close to that for ionic bonding of potassium, implying that the low-coverage adsorbed potassium is likely to be in an ionic state.

Alexiev et al.[83] studied lithium adsorbed at the surface of the "as-cleaved" MoS_2(100) edge surface with electronic structure methods. They found that potassium appears to have multiple sites it can stably adsorb. According to Alexiev et al.'s [83] calculations, lithium's only energetically favorable adsorption sites were found over the interstitial space, which would be favorable for facile diffusion of lithium into the interstitial spaces. Alexiev et al.'s calculations cannot be readily compared with experimental observations since lithium (and sodium) promotion is known to cause profound structural change to 2H-MoS_2, which is not the case for heavy alkali metals K, Rb, and Cs.[27,80] We note here that our calculations consider only the adsorption situation at 0 K. Climbing image nudged-elastic band[84] transition state

searches we conducted suggest that surface diffusion can readily occur at temperatures relevant to catalytic conditions. The maximum barrier to surface diffusion is ~3 kcal/mol.

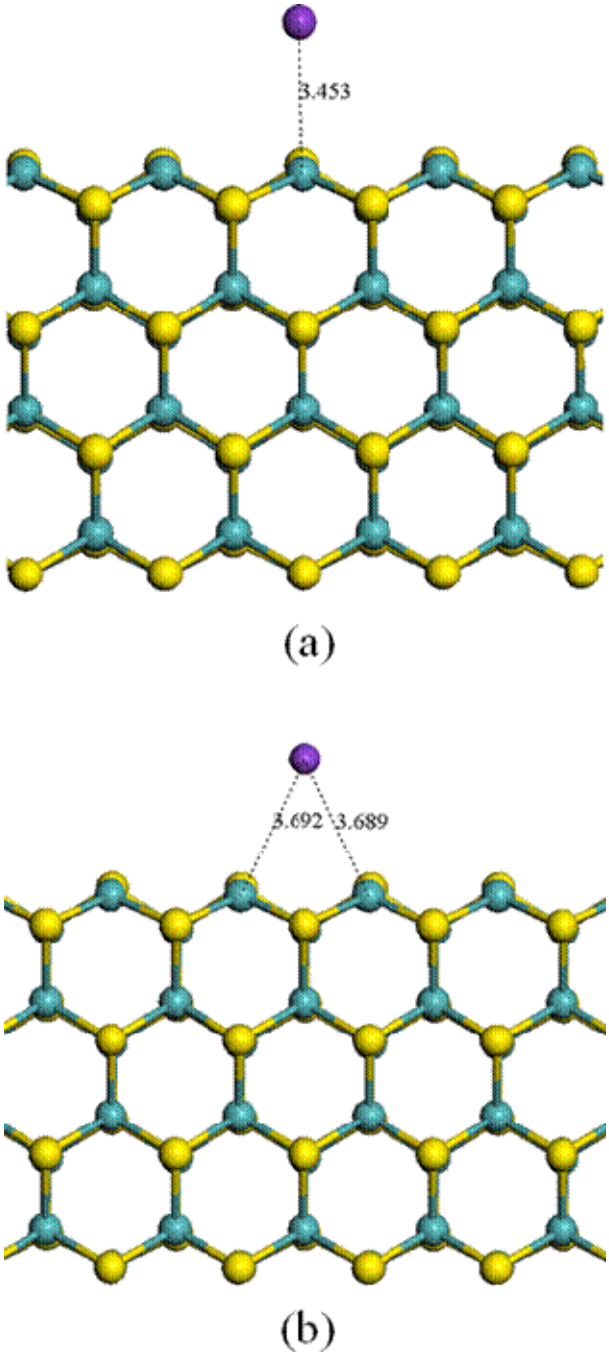

Figure 74. Local minimum energy structures for potassium over a Mo atop site (top) and a Mo bridging site (bottom) on the Mo0-S100 Mo edge structure.

Mo50-S50 surface: 50% sulfided Mo edge, 50% sulfided S edge

The only energetically stable sites for potassium at the Mo50-S50 surface are those over the interstitial where potassium coordinates with three sulfur atoms (see Table 8 and Figure 75). The stable sites either exhibit coordination of the potassium with two surface sulfur atoms at the Mo edge and one surface sulfur at the S edge (Figure 75(a)) or coordination of one Mo edge surface sulfur, one Mo edge subsurface sulfur and one S edge surface sulfur atom (Figure 75(b)). Energetically, these two configurations are nearly equally favorable. Since sites over the interstitial are the most stable, the potassium is expected to linearly decorate space over the interstitials either at the (100) edge surface or

Table 8. Stable neutral and cationic K adsorption sites and energies and Bader charges for the 50% sulfided Mo edge/50% sulfided S edge MoS_2(100) edge surface (Mo50-S50) and the 37.5% sulfided Mo edge/50% sulfided S edge MoS_2(100) edge surface (Mo37.5v-S50).

	K (neutral system)			**"K^+" (charged system)**		
Adsorption Site K	**Adsorption Energy (eV)**	**Charge (e)**	**d_{K-S} (Å)**	**Adsorption Energy (eV)**	**Charge (e)**	**d_{K-S} (Å)**
50%-50%, interstitial [a]						
Coordinated with 1 S of Mo edge & 2 S of S edge [b] **(site 5)**	-3.46	0.894	3.167 3.286 3.254	-1.64	0.890	3.19 3.529 3.372
Coordinated with 2 S of Mo edge & 1 S of S edge 1 [c] **(site 5)**	-3.37	0.863	3.370 3.197 3.169	-1.72	0.893	3.196 3.498 3.427
Coordinated with 2 S of Mo edge & 1 S of S edge 2 [d] **(site 5)**	-3.30	0.868	3.194 3.313 3.275	-1.72	0.893	3.373
37.5%-50% (Mo edge "vacancy")						
Interstitial [e] **(site 1)**	-3.06	0.795	3.502 3.428 3.222	-1.42	0.392	3.256 3.296 3.377
Over "vacancy" (site 2)	-2.55	0.854	3.199-3.202	-1.04	0.898	3.304

[a] All stable sites for potassium on the 50%-50% sulfided system are above the interstitial.
[b] Distortion of S-edge bridge S facilitates coordination of two S atoms with potassium.
[c] Potassium coordination with two topmost bridge S of Mo edge as well as one bridge sulfur on top of S edge.
[d] Potassium coordination with one bridge S on top of Mo edge and one prismatic sulfur directly below it at Mo edge as well as one bridge sulfur on top of S edge.
[e] Potassium migrates away from "vacancy" toward sulfur-rich part of surface.

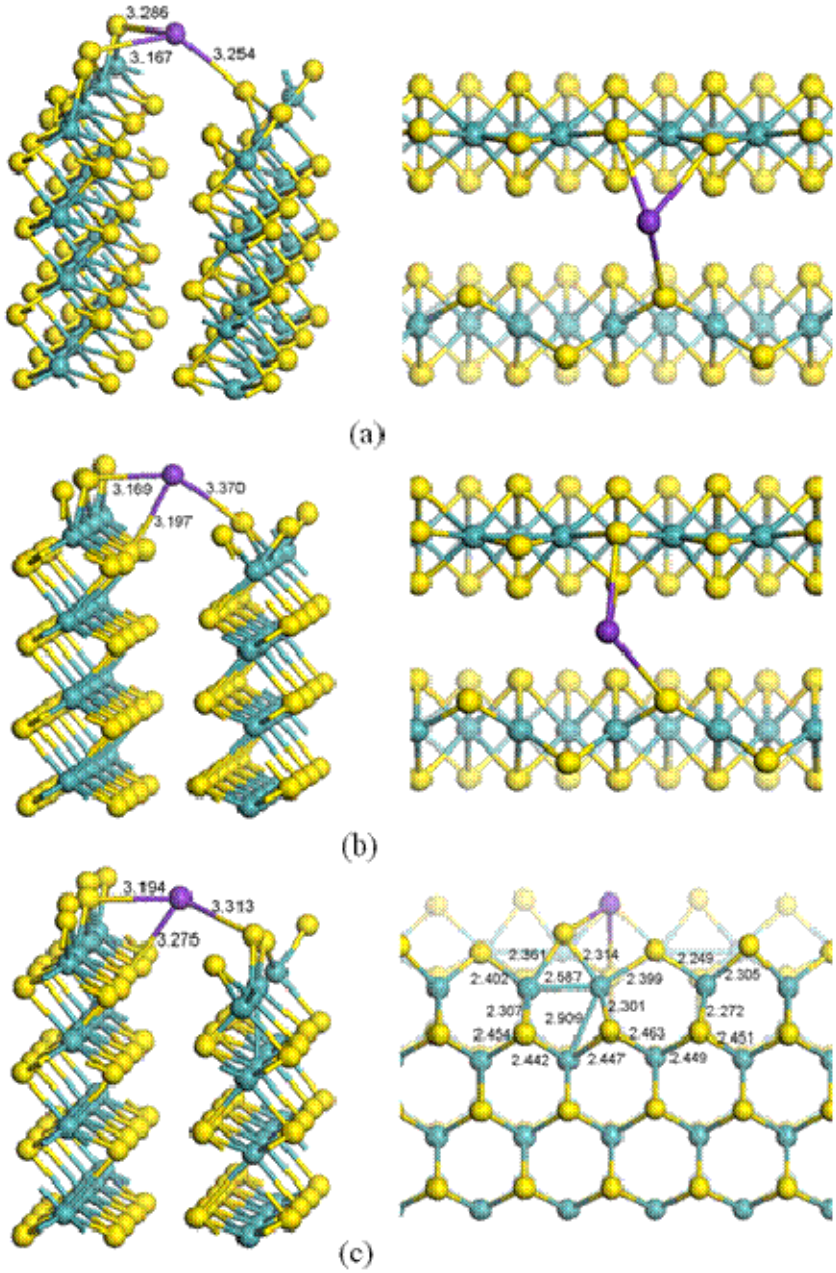

Figure 75. Local minimum energy structures for potassium over the interstitial of the Mo50-S50 structure. (a) potassium coordinates three sulfur atoms over the interstitial (two Mo edge surface sulfur atom and one S edge surface sulfur atom), (b) potassium coordinates three sulfur atoms over the interstitial (one Mo edge surface sulfur atom, one second-layer Mo edge sulfur atom, and one S edge surface sulfur atom), and (c) potassium starts in a subsurface interstitial (in this case the broadly distorted hexagonal site) and migrates to a three-fold sulfur-coordinated site over the interstitial.

at stepped terraces formed over basal surfaces with either $(10\bar{1}0)$ or $(\bar{1}010)$ edges. Because the potassium is confined to the sites over the interstitial, the sulfur and molybdenum sites at the MoS_2 edges will be relatively open to be approached by adsorbates although the long-ranged interaction of the large potassium ion will still influence the approach of adsorbates. This is not the case for K adsorbed on the 100% sulfided S edge surface where potassium can occupy four-fold sulfur-coordinated hollow sites and block potential sulfur and molybdenum adsorption sites.

If potassium migrates into the subsurface (as would occur in the intercalation process), hexagonal features at the subsurface can be distorted by the embedded K. This is shown in Figure 75(c). This appears to be slightly more energetically stable compared to potassium being merely being above the interstitial and inducing minimal strain to the MoS_2 lattice. This local distortion to a hexagonal structure is expected to affect the adsorption of syngas species such as CO and H_2 by subtly changing the electronic structure.

3.8.1.2 Mo37.5v-S50 MoS_2 surface: "vacancy" at 50% sulfided (37.5%) Mo edge, 50% sulfided S edge

The Mo37.5v-S50 surface model represents a sulfur atom "vacancy" at the 50% sulfided Mo edge, resulting in a bare Mo–Mo bridge site. Two stable K adsorption sites were identified. The first potassium adsorption configuration involves the adsorption of the potassium directly over the vacancy, coordinating with the two sulfur atoms on either side of the vacancy (Figure 76(a)). The second configuration involves potassium over the interstitial (Figure 76(b)). In this case, the potassium atom was initially placed over the interstitial close to the vacancy. The potassium migrated to the more negatively-charged sulfur-rich domain over the interstitial away from the more positively-charged vacancy. Our calculation results show that the K adsorbed over the sulfur-rich domain of the interstitial surface is more energetically favorable compared with that of the potassium directly over the vacancy interacting with the flanking sulfur on the Mo edge. In For the case of the K adsorbed directly over the vacancy site, the trend in K–S distances where the neutral system has slightly shorter distances than that of the charged system holds (3.20 Å for the neutral system case versus 3.30 Å for the charged system case). However, this trend does not precisely hold for the case where the potassium is over the interstitial away from the vacancy (3.22-3.50 Å for the neutral case versus 3.24-3.38 Å). Since potassium prefers sulfur-rich domains away from vacancy sites, vacancy sites may serve as methanation sites since Mo sites are associated with methanation.

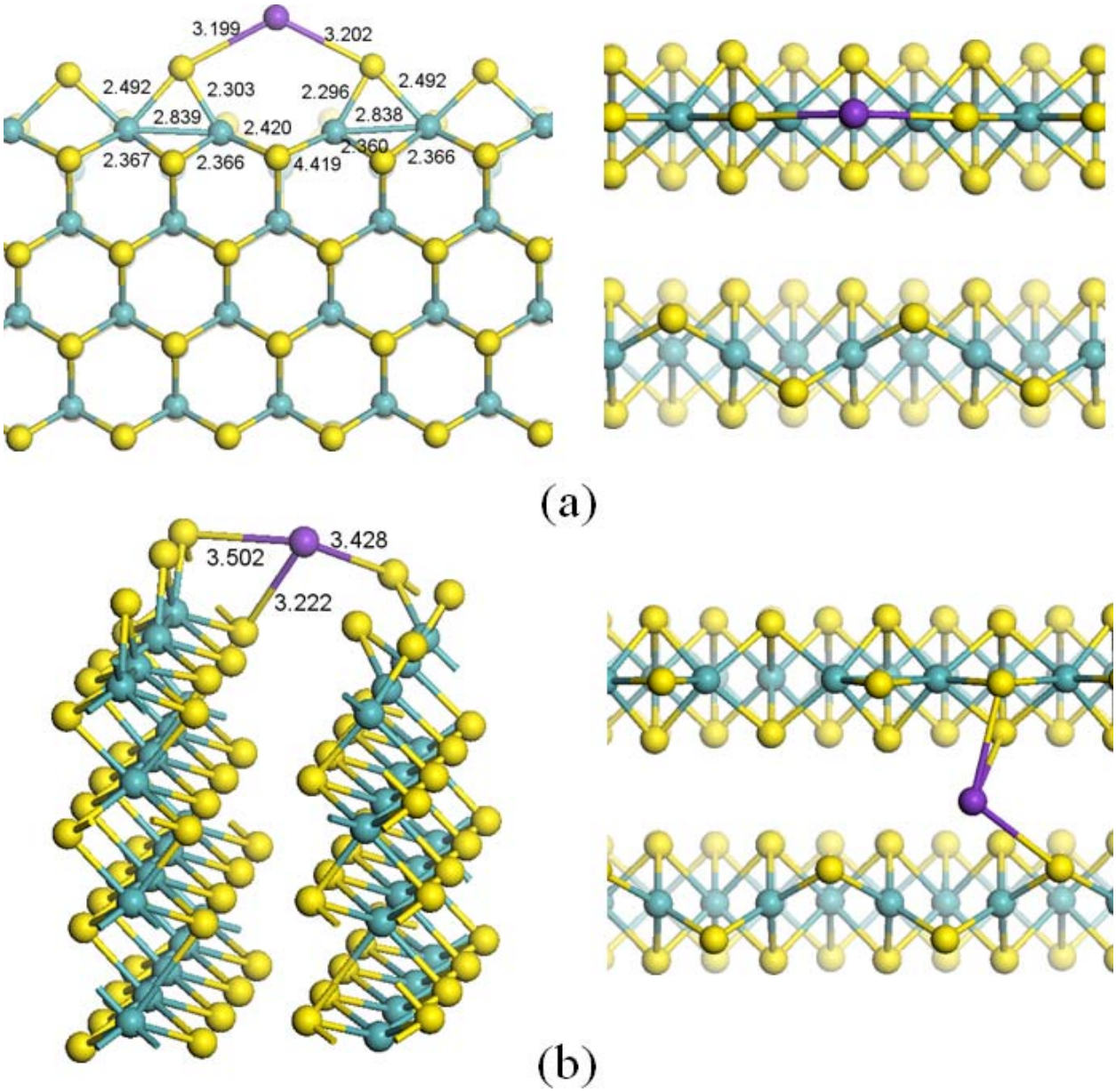

Figure 76. Local minimum energy structures for (a) potassium over sulfur "vacancy" at Mo edge of the Mo37.5v-S50 surface and (b) potassium over the interstitial three-fold coordinated by sulfur atoms away from the "vacancy" site.

3.8.1.3 Mo100-S100 surface: fully sulfided Mo edge, fully sulfided S edge

As with the Mo0-S100 surface system, a K adsorbed to the fully sulfided Mo and S edges (Mo100-S100) finds an energetically stable configuration over the four-fold sulfur hollow sites found on the fully sulfided S edge. Moreover, the disulfide dimers of the fully sulfided Mo edge provide pseudo-four-fold hollow sites where potassium finds a stable configuration (see Table 9 and Figure 77(a)). This configuration is not as stable as the four-fold site over the S edge. A stable potassium configuration was also found over the interstitial with potassium coordinating four sulfur atoms, two on either side of the

Table 9. Stable neutral and cationic K adsorption sites and energies and Bader charges for the non-stoichiometric 100% sulfided Mo edge/100% sulfided S edge MoS_2 (100) edge surface (Mo100-S100).

	K (neutral system)			"K^+" (charged system)		
Adsorption Site K	Adsorption Energy (eV)	Charge (e)	d_{K-S} (Å)	Adsorption Energy (eV)	Charge (e)	d_{K-S} (Å)
Mo edge						
4-fold disulfide-disulfide "hollow" (site 1)	-2.61	0.833	3.084 3.094 3.074 3.097	-1.16	0.894	3.204 3.194 3.221 3.220
S edge						
4-S hollow[a] (site 4)	-3.16	0.862	3.337 3.242 3.247 3.317	-1.72	0.879	3.310 3.410 3.387 3.318
Interstitial						
4-fold coordinations[b] (site 3)	-3.00	0.856				
4-fold coordination with S-edge disulfide 1[c] (site 3)			3.180 3.250 3.107 3.139	-0.97	0.836	2.978 2.939 3.203 3.147
4-fold coordination with S-edge disulfide 2[d] (site 3)	-3.13	0.842	3.070 3.245 3.121 3.298	-1.64	0.882	3.128 3.339, 3.254 3.431

[a]Identical to S edge four-fold S hollow sites in the Mo0-S100 system discussion.
[b]Potassium coordinated with sulfur atoms from two different disulfide at Mo edge and two sulfur on the same side of S edge.
[c]Potassium coordinated with one sulfur atom of disulfide at Mo edge and two sulfur in layer below it as well as one sulfur of newly formed disulfide at S edge.
[d]Potassium coordinated with two sulfur atoms of two different disulfide at Mo edge, one sulfur atom of the newly formed disulfide at the S edge and one non-dimer sulfur at S edge.

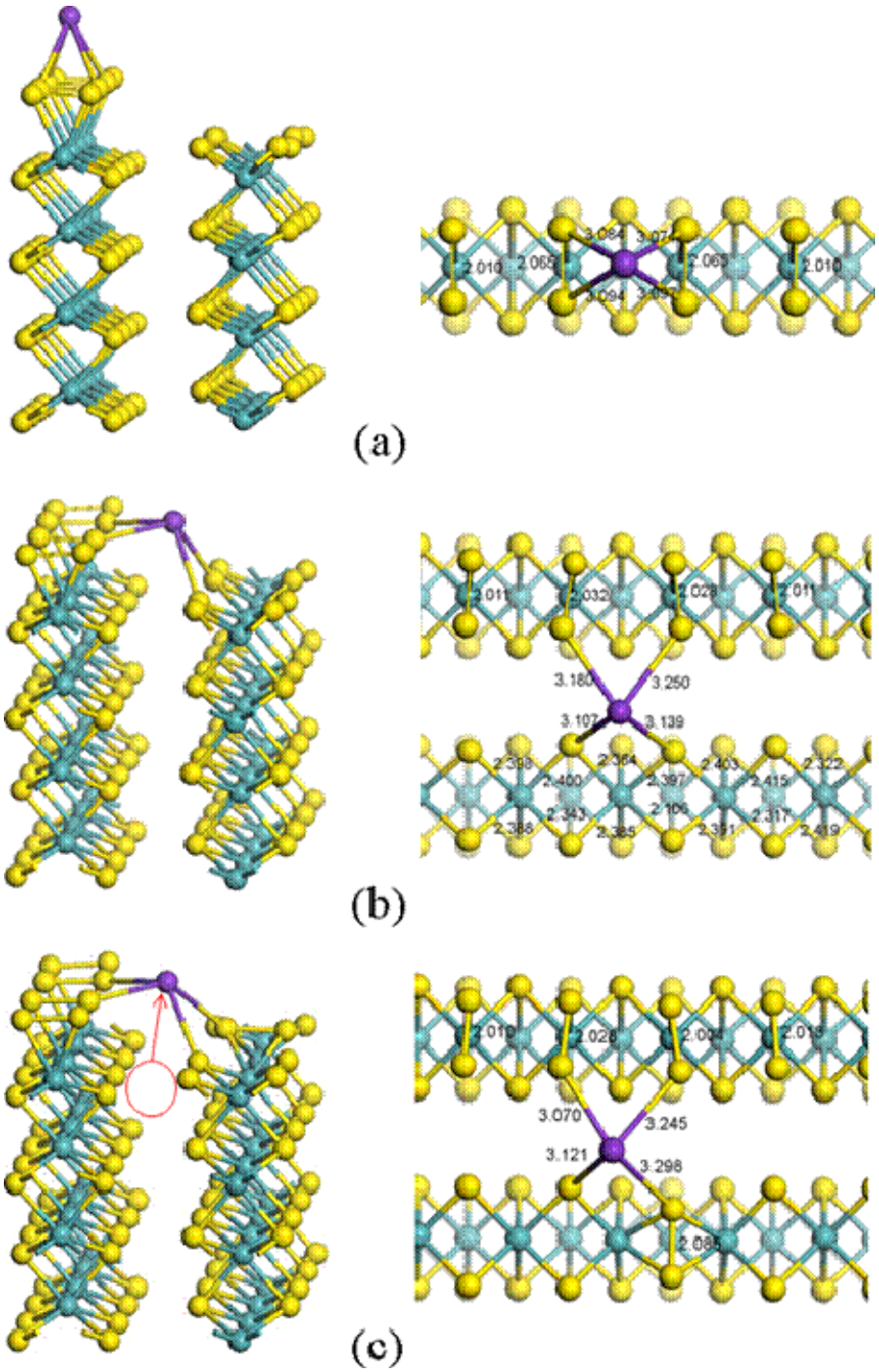

Figure 77. Local minimum energy structure for potassium (a) over a four-fold sulfur hollow on Mo edge (between two disulfide dimers) on the Mo100-S100 non-stoichiometric structure, (b) over the interstitial of the Mo100-S100 non-stoichiometric structure with potassium coordinated by four sulfur atoms (two on each edge surface), and (c) over the interstitial of the Mo100-S100 non-stoichiometric structure with potassium coordinated by four sulfur atoms (three on Mo edge and one on S edge) and a disulfide formed from the migration of the potassium out of a hexagonal subsurface site (open circle) to the surface over the interstitial during optimization.

interstitial (Figure 77(b)). Subsurface potassium site optimizations were attempted, and, as with the subsurface sites of the Mo0-S100 system, potassium migrated to the surface. In the case of the cationic charged system, potassium migration resulted in a four-coordinated potassium where one surface (in a S-S dimer) and two subsurface sulfur atoms at the Mo edge and one surface sulfur (in a S-S dimer) at the S edge. The K atom in this case is not fully over the interstitial, and there is some apparent strain from the K-MoS_2 wall repulsion pushing the MoS_2 sheets outward. As with the Mo0-S100 case, an S-S dimer at the S edge is formed from the K atom pushing the two S edge sulfur atoms together on the way out of the subsurface hexagonal site. On the other hand, a full migration of the potassium to the top over the interstitial was observed for the neutral system (Figure 77(c)). As with the cationic system case, an S-S dimer is formed from migration of the potassium out of the subsurface.

Finally, we want to briefly discuss the pseudo-intercalation of the potassium. Figure 78 shows the pseudo-intercalation of a single potassium well-below the surface/subsurface in the fully sulfide model system. With the crystallographic spacing of the MoS_2 sheets, the insertion of the potassium is only slightly favorable (-0.06 eV) for the neutral system and unfavorable (1.54 eV) in the charged system. Structurally, there is a slight bulging outward of the MoS_2 where the potassium is inserted; this is slightly more pronounced in the cationic case. The K–S distances are much shorter than the preferred 3.1-3.4 Å distances found at the edge surface, indicating that the interstitial spacing would need to expand to favorably accommodate intercalated potassium. Potassium, as well as lithium, sodium, rubidium, and cesium, are known to intercalate into the MoS_2 bulk between the van der Waals held MoS_2 sheets. For the heavier alkali metals (K, Rb, Cs), the 2H structure remains well-defined with a 35% increase in the c-axis (from 12.294 to 16.580 Å).[27]

3.8.2 Electronic and magnetic structure

For the bulk MoS_2, the sulfur atoms coordinate the molybdenum atoms in a trigonal prismatic configuration. This coordination results in a ligand field splitting of the Mo 4d orbitals into three groups: degenerate filled d_{xz} and d_{yz} (i.e., e_g or t_{2g}^{+}, t_{2g}^{-}), nondegenerate filled d_{z^2} (i.e., a_{1g} = t_{1g}^{0} ~ d_{z^2}), and degenerate unfilled d_{xy} and $d_{x^2-y^2}$ (i.e., e_g or t_{2g}^{+}, t_{2g}^{-}). The bottom of the conduction band is primarily composed of a combination of Mo 4d d_{z^2}, d_{xy}, and $d_{x^2-y^2}$ states.[80] Previous DFT studies[85]

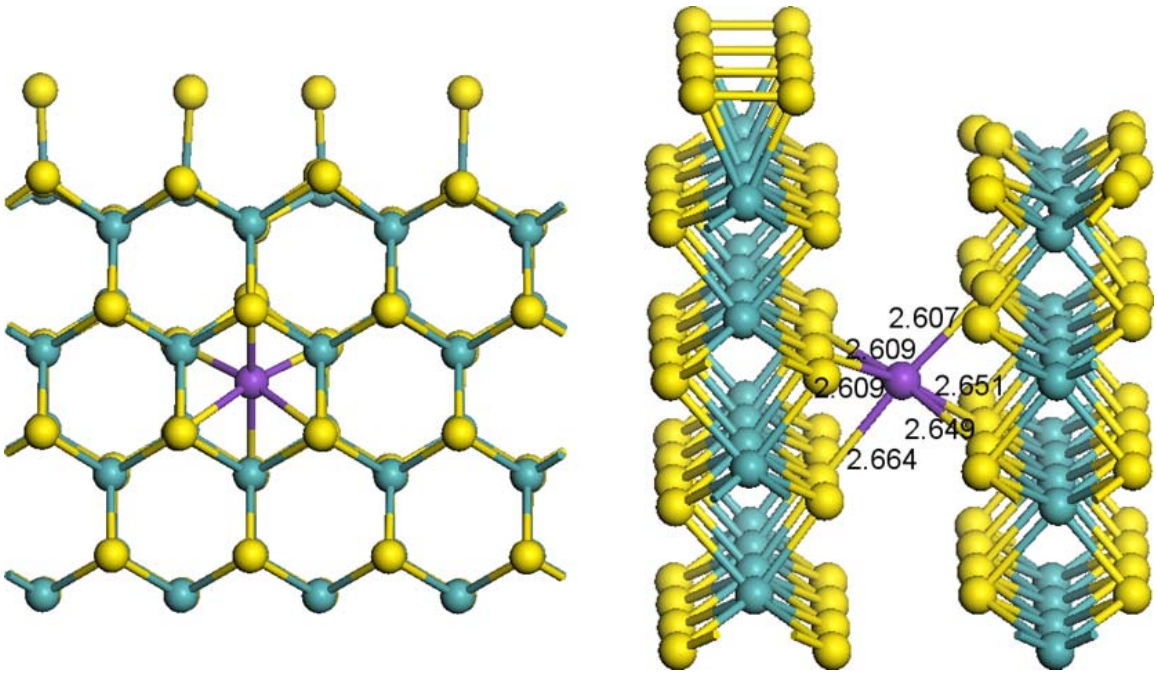

Figure 78. K atom deeply embedded in the interstitial of the Mo100-S100 non-stoichiometric structure.

have shown that the density of states shows a low-lying band of states around -16 to 13 eV, which is primarily attributed to the S 3s. The valence band, typically extending from -8 eV to the Fermi-level, is primarily composed of a mixture of Mo 4d states and S 3p states (the filled d_{z^2} mixes strongly with the 3p S orbitals). The conduction band from the top of the band gap to ~4 eV is also primarily composed of a mixture of Mo 4d and S 3p states. The S 3p states are dominant in the valence band up to the Fermi level and the Mo 4d orbitals dominate the conduction band above the band gap. The optical band-gap has been reported to be between 1 and 2 eV.[42] GGA-DFT calculations underestimate this band gap (0.7 eV).[85]

For the MoS_2(100) edge surface, unsaturated Mo and S atoms at the edge reduce the ligand-field splitting. The d_{z^2} states move up and the e_g states move down, and the Mo 4d states contribute to gap states.[85] With appreciable mixing of the S 3p and Mo e_g along with bonding-antibonding splitting, some S 3p state are pushed above the Fermi energy.[85] The metallic behavior of the edge surface from these "brim states" (as indicated by the closing of the band gap) has been demonstrated with STM experiments[86]and DFT simulations of Au supported MoS_2 nanoparticles.[26, 44, 85, 87, 88] For the unpromoted

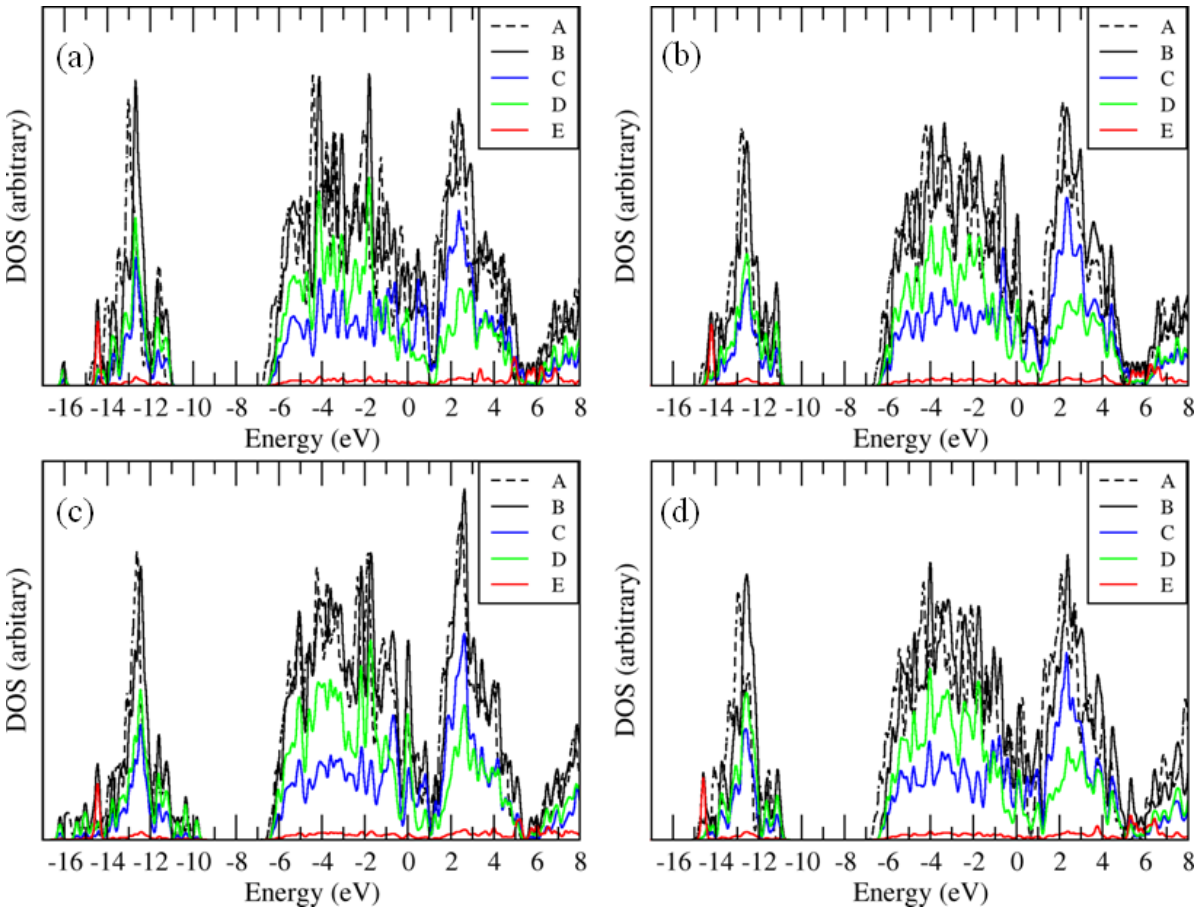

Figure 79. Total and projected density of states (DOS and PDOS, respectively) for the most stable configuration of K adsorbed on (a) Mo0-S100, (b) Mo50-S50, (c) Mo100-S100, and (d) Mo37.5v-S50 MoS_2(100) systems. A: Unpromoted total DOS, B: promoted total DOS, C: Mo LDOS, D: S LDOS, and E: K LDOS. Energies are relative to the Fermi energy of the unpromoted system at 0 eV.

MoS_2(100) edge surface system, our calculated total DOS is in agreement with the trends reported by Raybaud et al.,[85] and the lack of a band gap in our DOS analysis is in agreement with these earlier observations[86] and calculations[26, 44, 85, 87, 88] (dashed lines in Figure 79).

When promoted with potassium, the K LDOS (Figure 79) show a weak highly delocalized set of states around the Fermi level with a clearly discernable K 3p state resonance peak between -15 and -14 eV overlapping the MoS_2 valence states dominated by the S 3s states. For the Mo0-S100 lowest configuration with potassium over a four-fold S hollow adjacent to a S-S dimer (shown in Figure 73(b)), a few resonance peaks overlapping with the conduction band Mo d and S sp states that can be assigned to a mixture of 4s (~3.25 eV), 4p (~5 eV) and 3d (5-7 eV), connecting the upper part of the conduction band

to a higher manifold of states (dominated by the S 3d states), indicating hybridization of the K states with those of MoS_2 (DOS shown in Figure 79(a)). The DOS are qualitatively similar for the lowest configuration Mo50-S50 sulfided (Figure 75(c), DOS in Figure 79(b)), Mo100-S100 sulfided (Figure 77(c), DOS in Figure 79(c)), and Mo37.5-S50 (Mo edge "vacancy") sulfided (Figure 76(b), DOS in Figure 79(d)). There appears to be an overall 0.1-0.3 eV shift of the total DOS for the K-doped systems compared with that of the undoped systems. Alexiev et al. noted a similar, but larger, shift of the Li-doped MoS_2(100) DOS with respect to the undoped MoS_2(100) in their periodic Hartree-Fock calculations.[83] The presence of potassium, however, does not profoundly change the overall profile of the DOS, in qualitative agreement with the "rigid band" observations of heavy alkali metal *ns* electron charge injection into bottom of the conduction band of MoS_2 as demonstrated in valence angle-resolved x-ray photoelectron spectroscopy (ARXPS) experiments.[80] A donation of the highly delocalized K 4s charge to the surface may result in repulsion of the p and d electrons leading to a shift in the p and d density of states, as is seen with transition metal surfaces like Rh(111).[89] The DOS for the neutral and charged systems have nearly identical profiles.

Recent experimental observations and DFT calculations also indicate that the MoS_2 edge surface can demonstrate magnetic properties.[44-46] Though magnetic properties are not expected to significantly influence the catalytic properties of the surface, the magnetization of the edge is important in the interpretation of characterization data from ESR spectroscopy. Vojvodic et al. have recently shown in their DFT calculations that changes in sulfur atom coverage and sulfur orientation (e.g., undimerized, dimerized, trimers) at the undoped MoS_2 edge can induce changes in the magnetic properties of the edge surface.[44] They have shown that hybridization of the Mo 4d and the undimerized S 3p states results in a splitting of the S states at the S edge that is associated with a small local magnetic moment. Similar behavior was observed in our calculations shown in Figure 80. Figure 80 shows the LDOS for specific atom LDOS features of the lowest configuration Mo0-S100 case. Figure 80(a) shows the LDOS for the Mo atom directly below the adsorbed K atom at the four-fold S hollow on the S edge, and Figure 80(b) shows the LDOS for the four-fold S hollow atoms. Figure 80(c) shows the LDOS for two Mo atoms adjacent to the newly-formed S-S dimer, and Figure 80(d) shows the LDOS for the sulfur atom in the newly-formed dimer. Though there are examples of state splitting in most of the DOS analyses considered here, the inset in Figure 80(c) demonstrates one of the more profound examples.

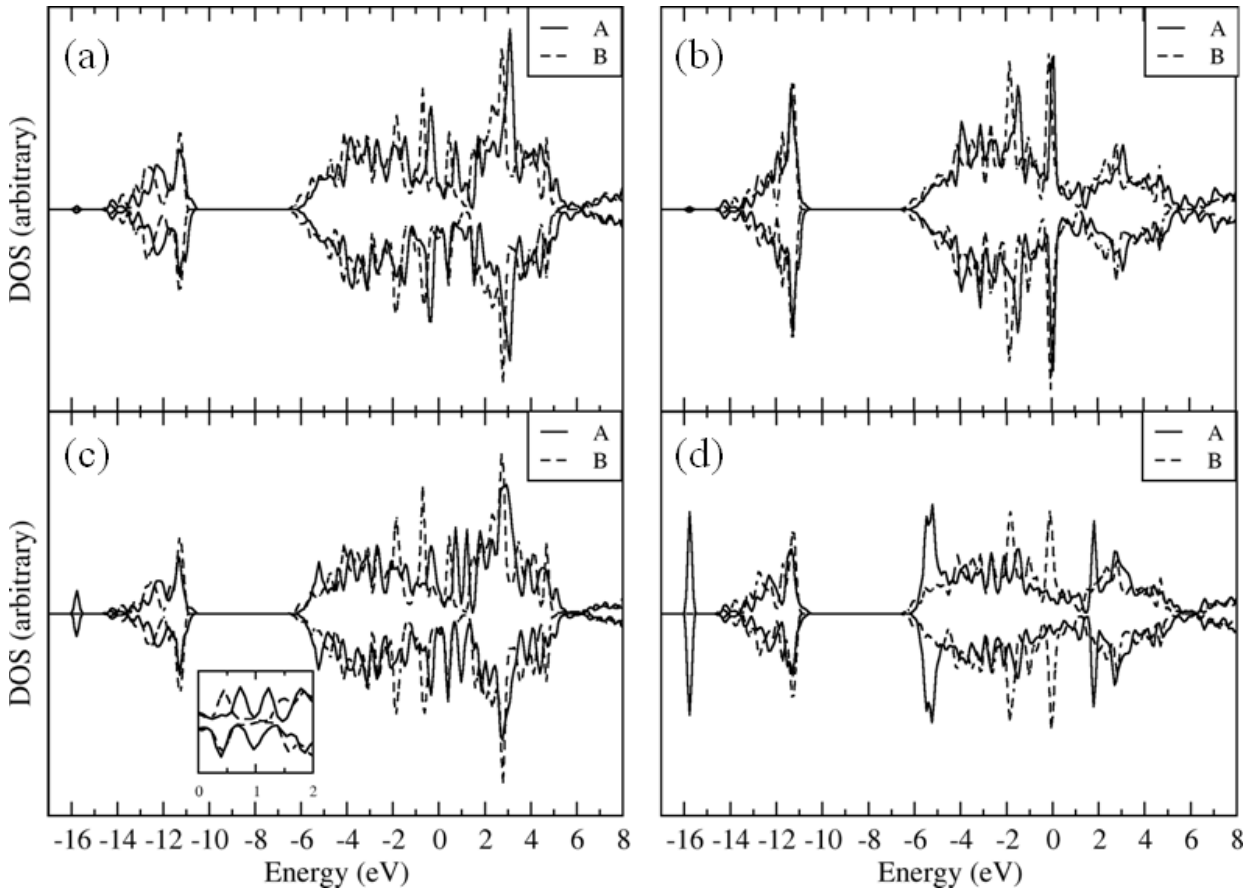

Figure 80. PDOS for the neutral K doped Mo0-S100 system with disulfide. (a) d band for the Mo atom under the four-sulfur hollow at the S edge, (b) d band for the two Mo atoms adjacent to the newly formed disulfide (inset shows splitting of the alpha and beta spin DOS), (c) sp band for the sulfur atoms of the four-sulfur hollow with the adsorbed K, and (d) sp band for the disulfide sulfur atoms. A: undoped system. B: K-doped system. Energies are relative to the Fermi energy of the unpromoted system at 0 eV

Bader charge analysis show that the potassium charge ranges from +0.39-0.89 |e| for both the neutral and charged systems (Table 7, Table 8, Table 9) indicating, in the neutral system case, a nearly incomplete transfer of charge to the MoS_2 edge and, in the charged system case, a small backfilling of the K 4s (except for the lowest Mo37.5v-S50 configuration over the interstitial where the charge on the K is a surprisingly small +0.39 |e|, which may be due to the close interaction with an Mo edge Mo atom). Most edge atoms show negligible >0.01 |e| magnitude changes in atom charge (indicating a delocalized increase in charge), and the lowest configuration Mo0-S100 case with no S-S dimer formation Figure 73(a) shows the most change in the atom charges (compared to the unpromoted system) for the K-coordinated sulfur atoms of the four-fold S hollow at the Sedge. These four-fold S

hollow sulfur atoms show a small increase in negative charge of -0.10 |e| to -0.12 |e| for the neutral system and -0.07 |e| to -0.11 |e| for the cationic charged system. There is also an increase in the negative charge of the Mo atom below the adsorbed potassium (-0.09 and -0.08 |e| for the charged case). Upon dimer formation from the subsurface migration of potassium, the charge difference profiles are nearly identical to the potassium-promoted, undimerized configuration with respect to the four-fold hollow S atoms that the potassium coordinates with and the Mo beneath the hollow site. Similar charge changes are found for the other surface models studied here. The creation of a dimer results in some charge redistribution among the Mo atoms bonded to the S-S dimer (gain of -0.07 and -0.11 |e| for the neutral case and -0.05 to -0.10 |e| for the charged system) and the S atoms in the dimer (loss of +0.19 to +0.30 |e| for the neutral system and +0.21 to +0.31 |e| for the charged system). There is also a small charge gain for the S edge Mo atoms not directly associated with the four-fold S hollow (-0.07 |e| for the neutral system and -0.05 |e| for the charged system) and the S-S dimer or the undimerized S pair not coordinated with the K (-0.07 and -0.06 |e| for the neutral system and -0.04 and -0.03 |e| for the charged system).

Interestingly, for the Mo0-S100 K-promoted, undimerized charged system with potassium over an S edge four-fold S hollow (depicted in top figure in Figure 73(a), an adjacent pair of flanking S edge sulfur atoms is closer to each other in what appears to be a "pre-dimer" configuration (2.73 Å opposed to 3.00 Å for the unpromoted system) with a decrease in negative charge of +0.05 and +0.07 |e| for the two sulfur atoms. Bader charge analysis of the spin density difference shows a fairly large 0.37 μ_B local magnetic moment on each of these pre-dimer sulfur atoms while the other S edge sulfur atoms show a slight -0.003 to -0.04 μ_B magnetic moment, which is close to the -0.03 μ_B magnetic moment per S edge sulfur atom of the unpromoted Mo0-S100 system. The relatively large magnetic moments on the undimerized S atoms of the cationic system are in qualitative agreement with the calculations of Vojvodic et al.[44] They postulated that the drive for lower energy S-S dimer configurations may be due to Peierls type instabilities that are potentially pronounced at the low-dimension edge surface of MoS_2.[44] Indeed, the presence of potassium in the charged Mo0-S100 system appears to modulate the magnetic configuration of the edge surface toward favorable S edge S-S dimerization. In agreement with Vojvodic et al.'s calculations, the bare Mo edge tends to have a ferromagnetic arrangement with local magnetic moments of -0.12 μ_B per Mo for the unpromoted case. Addition of potassium at the S edge influences the local magnetic moments of the Mo edge Mo atoms. For the neutral case, the local Mo atom magnetic moments decrease slightly (with the four Mo moments alternating -0.08, -0.09, -0.08,

-0.09 μ_B), and, for the charged case, they increase (with the four Mo moments alternating -0.13, -0.22, -0.11, -0.27 μ_B). The S edge Mo atoms also possess a small magnetic moment of -0.01 μ_B in the unpromoted case, -0.003 to -0.01 μ_B in the neutral potassium promoted case, and 0.02 to 0.11 μ_B in the charged potassium promoted case.

Upon dimerization of one S-S pair at the S edge in the Mo0-S100 model by potassium migration from the subsurface Figure 73(b) there are magnitude increases in the magnetic moments compared to the unpromoted, undimerized system on the Mo edge Mo (0.31-0.53 μ_B), S edge Mo (-0.02 to -0.04 μ_B), and the S edge S (-0.05 to -0.09 μ_B) atoms for the neutral system. Unlike the neutral system, the charged system stays ferromagnetic with an alternating -0.17, -0.06, -0.19, -0.05 μ_B pattern of Mo edge Mo moments. Like the neutral system, there is a magnitude increase in the magnetic moments of the S edge S (-0.07 to -0.12 μ_B) and Mo edge Mo (-0.02 to -0.06 μ_B).

Similar behavior is seen for the fully sulfided Mo and S surface, Mo100-S100 Figure 2(c). However, the fully sulfided Mo edge causes some notable differences to the magnetic properties of the MoS_2(100) system in contrast to the bare Mo edge system (Mo0-S100). In the undoped system, we see, as with the Mo0-S100 case with the addition of one K to the charged system, alternating “pre-dimers” with 2.729 and 2.732 Å distances at the S edge with -0.12 and -0.13 μ_B magnetic moments for one undimerized S-S pair and 0.46 and 0.46 μ_B for the other pair, giving an antiferromagnetic configuration. The associated S edge Mo-Mo pairs bonded to these S-S pairs have -0.22 and -0.23 μ_B magnetic moments for the first S-S pair mentioned above and slight moments of -0.01 μ_B each for the second S-S pair. The S-S dimers at the Mo edge have a ferromagnetic configuration with each S having a 0.11-0.12 μ_B local magnetic moment. Upon the addition of one neutral K atom (Figure 77(b), the local magnetic moments for the two “pre-dimers” decrease in magnitude to -0.11 μ_B per S in the first pair and 0.43-0.48 μ_B in the second pair (closest to the potassium atom). There is also a significant change in the adjacent Mo-Mo pairs’ magnetic moments to an antiferromagnetic configuration (-0.04 for each Mo in the first pair and 0.17 and 0.19 μ_B for the second pair). The magnetic moments on the Mo edge S-S dimers go to zero. A net charge gain from -0.03 to -0.13 e seen for most edge sulfur except for one sulfur in the pre-dimer adjacent to the adsorbed K atom but on the side opposite to the potassium that has a small +0.03 charge (the flanking S pairs appear to be polarized with the S closest to the positively charged K being more negative than the S on the opposing side). For the charged system, the only significant change in

local magnetic moments is seen with the pre-dimer S-S pair closest to the potassium where the local magnetic moment is zero for both S atoms and one of the associated Mo atoms (the other Mo changed sign to 0.01 μ_B). This is due to the adsorption of the K on the S edge four-fold S hollow where the pre-dimer comprised one side of the dimer (since the interstitial site is unstable for the charged system). Upon dimerization of one S edge pre-dimer by migration of a subsurface K for the neutral system (Figure 77(c)), all S edge S atoms have zero local magnetic moments, and all the Mo atoms have a ferromagnetic configuration with magnetic moments ranging from 0.10-0.23 μ_B. The S-S dimer S atoms as well as the Mo atoms on the S edge have zero local magnetic moments. Interestingly, the charged system with the S edge dimer formed from K migration from the subsurface has zero local magnetic moment for all edge atoms on both the Mo and S edges.

Finally, the unpromoted Mo50-S50 surface (Figure 2(b)) has local magnetic moments for only the edge Mo atoms ranging from 0.47-0.50 μ_B for the S edge Mo and 0.17-0.50 μ_B. Upon addition of one potassium atom (Figure 75(c)), both the neutral and charged systems show no magnetic moment for any of the edge atoms. When an edge S vacancy is opened up on the Mo edge, Mo37.5-S100 (Figure 76(b)), the Mo edge has zero magnetic moment for all edge atoms except for the S atoms on either side of the vacancy (-0.06 to -0.07 μ_B). The magnetic moments of the S atoms on the S edge range, in an alternating pattern, from -0.16 to -0.21 μ_B. The magnetic moments of the Mo atoms that comprise the S edge range, also in an alternating pattern, from -0.06 to -0.13 μ_B. Upon addition of potassium over the interstitial, the neutral and charged systems exhibit nearly the same magnetic behavior. The magnetic moments of the S atoms on either side of the Mo edge vacancy slightly decrease in magnitude (-0.05 to -0.06 μ_B for both the neutral and charged systems). The Mo atoms of S edge show an increase in magnetic moment magnitude (0.46 to 0.52 μ_B for the neutral and 0.47 to 0.51 μ_B for the charged systems), and the S edge S atoms each have a slight magnetic moment of -0.01 μ_B (the overall edge surface has an antiferromagnetic configuration).

3.8.3 Coverage effects

With increasing K coverage on the surface, it is expected that charge is built up in the conduction band, leading to less charge transfer from the K to the surface with the formation of a metallic adlayer of K. A number of K atoms were added to the Mo0-S100, Mo50-S50, and Mo100-S100 surfaces on the basis of the number available adsorption sites. Figure 81 depicts the optimized geometries for the highest K

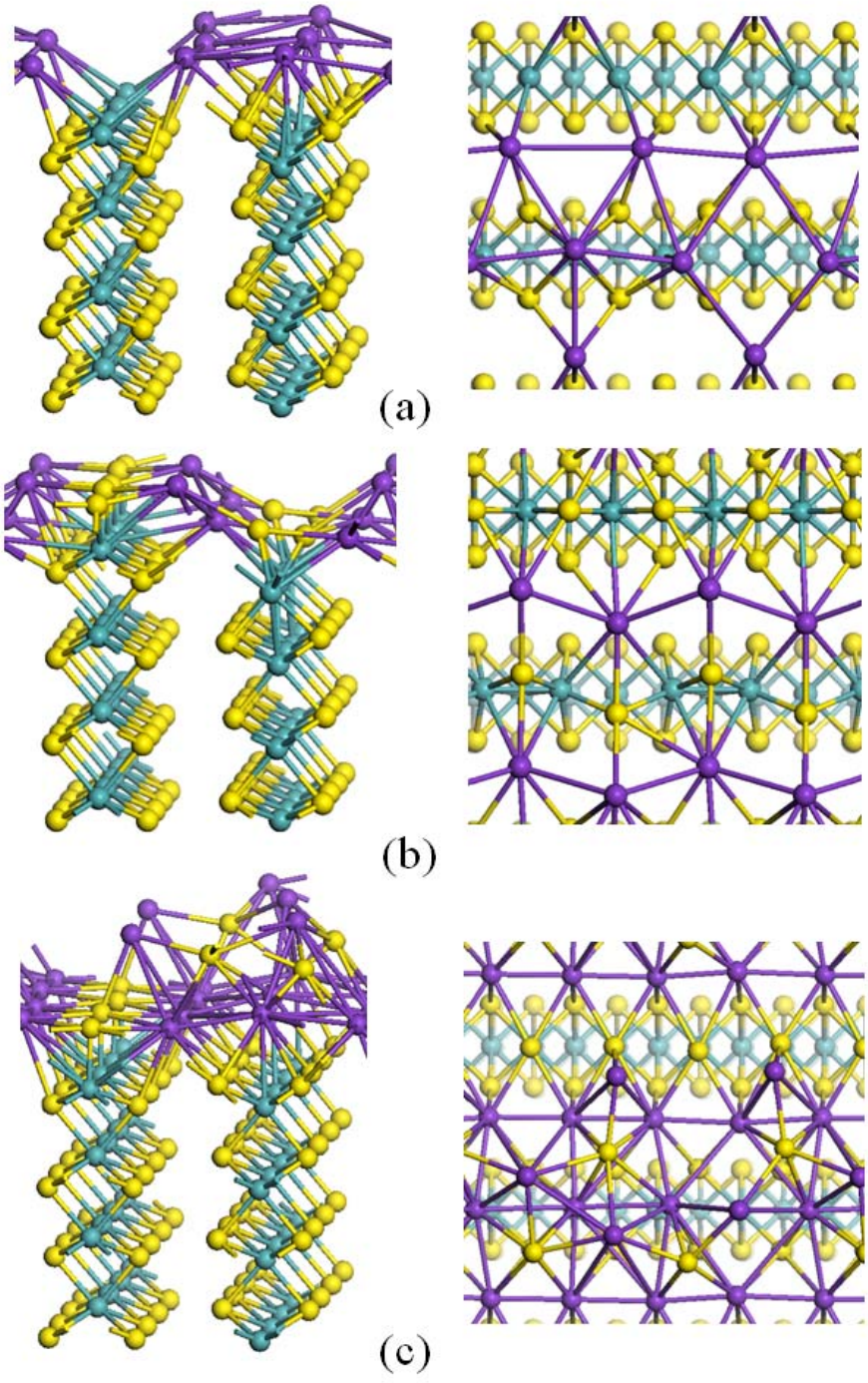

Figure 81. Optimized structures of MoS_2(100) surfaces at high K coverages: (a) Mo0-S100 (1 ML), (b) Mo50-S50 (1 ML), and (c) Mo100-S100 (2 ML).

coverages considered for the Mo0-S100, Mo50-S50, and Mo100-S100 surfaces (1, 1, and 2 monolayer (ML) coverages, respectively). Interestingly, upon optimization, the K-K distances for the highest potassium coverages considered for the Mo50-S50 and Mo100-S100 model surfaces (1 and 2 ML, respectively) are considerably shorter (3.66 and 3.69 Å, respectively) than the K-K distance of 4.61 Å for body centered cubic (bcc) bulk K. For the highest K coverage Mo100-S100 model (which is in excess of 1ML), we added potassium atoms to every available four-fold S hollow site on each edge as well as every four-coordinated S site above and along the interstitial site. Four Mo edge surface S were dislodged and formed sulfur-poor K-S phase on top of the potassium layer, and this configuration demonstrates that the Mo edge sulfur dimers are unstable with K coverages greater than 1 ML.

On closer inspection of the high K coverage Mo0-S100, Mo50-S50, and Mo100-S100 structure, the K atoms tend to organize as chains along the top of the van der Waals gap and over the fully sulfided S edge. For the high 2 ML K covered Mo100-S100 surface, the K-K distances of the chain structures are exceedingly short with average distance of 3.16 Å. This is also seen with the highest coverage Mo50-S50 model where the only stable adsorption sites at low coverage are located over the interstitial. The unusually shorter K-K distances can be due to increased 3d (transition-metal like) bonding character, which contributes to the anomalously short K-K distances for pure potassium metal and potassium alloys under high pressure.[90,91] The LDOS for potassium shows a dramatic increase in the number and intensity of accessible K 3d states in the conduction band, which start to appear about 1 eV above the Fermi level with this dramatic increase in potassium loading at the Mo100-S100 surface. This “chemical pressure” effect of compressed K-K distances relative to bcc bulk K may be a contributing factor in the favorable intercalation of potassium and other heavy alkali metals into the MoS_2 bulk and, possibly, the observed superconductivity phenomenon below ~7 K for these systems (which is beyond the scope of the present work and will not be discussed here).[27,92, 93]

Bader charge analysis demonstrates a decrease in charge transfer from the potassium to the surface (Table 10). This is accompanied by a decreasing magnitude in the adsorption energy per added potassium (Table 10). On the MoS_2(0001) basal plane, Kamaratos et al.[79] showed with low temperature (100 K) electron diffraction spectroscopy (LEEDS), AES, electron energy loss spectroscopy (EELS), and TDS measurements that, below a surface coverage of 0.5 monolayer (ML) where K likely adsorbs to the graphite-like hexagonal sites, the potassium is bound ionically to the basal surface.[79] Above 0.5 ML, an observed 3 eV K plasmon and low-energy desorption of 0.9 eV in Kamaratos et al.'s experiments indicate

Table 10. Adsorption energies, Bader charges, and work functions for various K coverages on the Mo0-S100, Mo50-S50, and Mo100-S100 surfaces. One monolayer is defined as one K atom per unit area of the surface up to eight total K atoms on the 4×1 area of the slab model surfaces considered here.

Coverage (ML)	Adsorption Energy (eV per K)	Average K Charge(e)	Average work Function, Φ (eV)
Mo0-S100			
unpromoted system			5.0
0.125a	-3.24	0.853	4.4
0.25	-2.68	0.807	3.8
0.5	-2.51	0.774	3.4
1	-2.04	0.598	3.1
Mo50-S50			
unpromoted system			5.6
0.125[a]	-3.46	0.863	5.0
0.25	-3.21	0.854	4.4
0.375	-3.00	0.848	4.1
0.5	-2.88	0.834	3.9
0.625	-2.72	0.816	3.8
0.75	-2.60	0.802	3.8
1	-2.35	0.777	3.3
Mo100-S100			
unpromoted system			5.0
0.125[a]	-3.16	0.842	4.6
0.25	-2.62	0.780	3.9
0.5	-2.61	0.742	3.2
1	-2.00	0.398	3.3
2[b]	-2.29	0.557	3.3

[a]Lowest energy configuration.
[b]Sulfur coverage of 100% sulfided Mo edge reduces to 50% coverage with S-poor K_xS_y cluster formation over the edge surface.

the formation of metallic layers of potassium. Dramatic decreases in the work function for potassium adsorbed at the basal plane with low coverage also indicate transfer of the K 4s charge to MoS_2.[77] The calculated work function for the MoS_2(100) edge with the Mo0-S100 and Mo100-S100 sulfur coverages (Table 10) are within the error bars of the measured work function for the MoS_2 basal surface (4.8±0.5 eV[94]). The Mo50-S50 sulfided edge surface calculated work function is 0.3 eV above this range. However, we must note that there are no measurements reported specifically addressing the edge surface, and there are some important differences between adsorption of potassium on the basal surface versus that of the edge surface. The basal surface DOS indicates that it is not metallic like the edge surface, behaving more like the semiconducting bulk system. At low coverage, the addition of potassium results in a gap state just above the MoS_2 valence band from the transfer of the K 4s electron

to MoS_2.[80] This is accompanied by a sharp decrease in the work function of ~1.2 eV at low coverage ($\Theta <$ 0.5 ML).[77] As more potassium is added at low temperature, a metal layer of potassium forms, and the reduction in work function is much more gradual.[77] In the case of the edge surface with three S coverages (Mo100-S0, Mo50-S50, and Mo100-S100), we see a decrease in the work function with increasing potassium coverage (Table 10), but the decrease is less dramatic at low coverage compared to that for the basal surface. This may be due to the edge surface not requiring a transition from insulating to conducting since it is inherently metallic. The Mo0-S100 and Mo100-S100 sulfided systems have more dramatic work function decreases than that of the Mo50-S50 sulfided system. Kamaratos et al. also note that, at room temperature, no potassium metallicity is observed, indicating that potassium readily intercalates into the bulk.[77, 79] Thus, at the elevated catalytic conditions expected for alcohol synthesis, intercalation of potassium would be relevant with increased loading of potassium.

The similar coverage effect on the K interaction with the MoS_2 edge surface is also found in other semiconductor and metal systems. For example, MoS_2 shares some structural similarities to the hexagonal graphite basal plane, and there is similar behavior with respect to the adsorption of potassium over the hexagonal sites of the graphite sheet where theoretical electronic structure studies of potassium coverage on graphite, a reduced 4s charge transfer from potassium to the graphite conduction band with increasing K coverage.[95,96] Similar to MoS_2,[77, 79, 80] the graphite system at low K coverage shows completely ionized K^+ and their delocalized screening charge from the donated electron in the graphite surface form large dipoles and a large work function reduction of the graphite surface. At low coverage, there is a long-ranged repulsive interaction between the K^+ due to electrostatic repulsion and to the filling of the graphite π^* states by charge donation from the potassium. This behavior at low coverage is also seen in metal system such as Rh(111), and, at high coverage, MoS_2 and metal systems show similar behavior with respect to formation of metallic K adlayers and clustering.[89]

3.8.4 Brief discussion of K promotion on catalytic properties of MoS_2-based catalyst

In this study, we are focused only on the interactions of K at the edge surfaces and near-surface interstitial sites where catalytic activity is thought to be most prevalent for MoS_2(100)-based catalysts. The most efficacious salt is one that allows for K^+ to effectively spread over the MoS_2 surface.[13, 16, 17, 97] K_2CO_3 is observed to be one of the most effective salts for the spreading of K^+ (likely due to carbonate decomposition into CO_2 and K_2O). Alkali metal promoters (e.g., potassium metal or potassium from K_2O) are thought to donate the alkali metal unpaired electron to group VIII metal systems such as

rhodium.[98,99] This electron donation is then thought to promote back-bonding into π*-orbitals of adsorbate systems such as CO, N_2, and NO.[99] As a result, this facilitates the dissociation of the diatomic species such as adsorbed hydrogen and enhances the stability of reaction intermediates. For the semiconductor MoS_2 material with metallic edge state behavior, injection of the alkali electron into the MoS_2 conduction band can be considered to be a quasi-metallic catalyst material with similar catalytic behavior to that of K-promoted transition metal systems such as rhodium.[89] However, unlike pure group VIII metal systems, the availability of Mo metal centers for strong adsorption of CO is hindered by the presence of sulfur and potassium. With moderate to high sulfur coverage as well as potassium coverage, weak molecular adsorption of CO that leads to direct hydrogenation may be favored over CO dissociation that leads to subsequent methanation reactions. Indeed, K-promoted MoS_2 is thought to be a bifunctional catalyst where H_2 dissociation occurs on the MoS_2 edge surfaces and CO is molecularly adsorbed by K^+ with direct CO hydrogenation dominant.[8, 100] For the K-promoted Rh(111) system, the delocalized electron of *s* orbital character injected by the K into the metal system is observed to cause "poisoning" toward dissociative H_2 adsorption due to repulsion between the delocalized *s* charge of the surface and the 1*s* character of the approaching H_2.[89] This may also apply to the metallic MoS_2(100) edge surface.

In this work, substantial migration of the K^+ or neutral K is observed. The preferable configuration for K/K^+ is to maximize its interactions with sulfur. On the bare Mo-terminal surface of the Mo0-S100 model, stable local minima were found for K directly atop Mo atoms or directly over bridging Mo-Mo sites. However, these minima are ~1 eV higher than those for K adsorbed at a four-fold sulfur hollow site over the S edge surface. Thermal fluctuations may easily cause the migration of K to more sulfur-rich regions of the surface. Adsorption of K in subsurface hexagonal or tetrahedral sites is not stable with the experimental crystallographic spacing of the MoS_2. Expansion of the interstitial is required to accommodate K at the hexagonal interstitial sites.

Unlike other promoters such as Ni and Co, which have short-range interactions with sulfur at the edge (~2.4 Å[101]) and are integrated tightly into the edge surface (influencing the morphology of crystallites),[88, 102] the interaction of potassium with the MoS_2 edge surface are long-ranged interaction with very little perturbation to the edge surface structures. The mechanism of enhanced alcohol selectivity may be due to K^+ obstruction of Mo sites responsible for methanation via CO adsorption leading to CO dissociation.

Further computational work was also performed relating to K-modified MoS_2 catalysts. Periodic density functional theory calculations were performed to explore the effect of potassium doping of the MoS_2(100) edge surface on the adsorption of CO and H species. Potassium doping of the MoS_2(100) with sulfide coverages of 0% at the Mo edge and 100% at the S edge ("as-cleaved" surface), 50% at the Mo edge and 50% at the S edge surface, 37.5% at the Mo edge and 50% at the S edge surface (S "vacancy" at Mo edge), and 100% at both the S edge and Mo edge were studied previous. CO and H adsorbates were placed at potential sites on the most stable potassium site configuration determined from the previous study. In addition to available Mo and S adsorption sites, CO also adsorbs, albeit more weakly, to surface potassium. Interestingly, the oxygen atom end of CO appears to bind to the potassium with almost the same adsorption energy as the carbon atom end. Though the binding of CO to K is weaker, the binding distance of either the C or the O end of CO with K is longer than those for the available Mo or S sites. This suggests that potassium can play an active role as a catalytic center, competing with and physically blocking the available edge Mo and S sites for CO adsorption. Charge donation of the K 4s electron to the MoS_2 conduction band appears to slightly enhance the adsorption of CO at available Mo and S sites. As for H_2, the nonpolar and repulsive 1s H_2 molecule is unlikely to interact directly with the surface K. H_2 most likely adsorbs dissociatively on the Mo and S sites; however, the presence of the large potassium species can limit H_2's access to these sites.

Periodic density functional theory calculations were also performed to study the structural and electronic properties of potassium intercalated in bulk 2H-MoS_2. The interstitial van der Waals spacing between a 2x2 supercell 2H-MoS_2 bulk structure was incrementally loaded with potassium atoms in the hexagonal sites to create K_xMoS_2 structures where x=0.125, 0.25, 0.375, 0.5, 0.625, 0.75, 0.875, and 1. The interstitial space must expand to accommodate the large potassium atoms, and the smallest doping concentration of x=0.125 has the largest interstitial spacing. There is a small gradual contraction of the interstitial spacing as the loading of potassium increases. This interstitial contraction is correlated with an in-plane expansion of the MoS_2 sheets in the a and b directions. According to our calculations, a 2ax2a ordering of the potassium in the interstitial spacing between MoS_2 layers gives the best agreement with available published experimental XRD lattice measurements. Potassium readily donates its 4s electron to the conduction band of the MoS_2,and the potassium-loaded MoS_2 system becomes metallic in character. An interplay between loading and the degree of potassium metallicity and ionicity in the MoS_2 system is discussed.

4 Discussion

The purpose of the intensive characterization and computation efforts undertaken at PNNL was to assist Range Fuels in their efforts to improve their KCoMoS-based mixed alcohols catalyst. Specifically, the three goals of the current investigation were:

1. Increase the selectivity of alcohols while decreasing hydrocarbon selectivity
2. Improve catalyst lifetime
3. Increase catalyst activity

In discussions between PNNL and Range Fuels staff, Range Fuels reported that catalyst activity did not greatly diminish with increasing time on stream, although this would be an issue for very long times on stream. Instead, the major effect observed was a change in selectivity from producing alcohols to hydrocarbons. Thus, physical and chemical changes were thought to occur in the catalyst during mixed alcohol synthesis.

Several processes contributing to the shift in selectivity appear to operate. These include a loss of S from the catalyst; segregation of potassium, especially at long time-on-stream (TOS); clustering of cobalt; and formation of cobalt metal.

In contrast to sulfur often acting as a poisoning agent in precious metal catalysts, its presence is necessary to the activity of hydrodesulfurization (HDS) and hydrotreating catalysts, which share similarities with the KCoMoS based catalyst of interest. Sulfur loss is one potential cause of decreased performance in CoMoS hydrotreating catalysts catalysts.[103] Loss of sulfur from sulfided catalysts can be induced by H_2 during reduction[75] or by oxygenates in the feedstock.[103] Indeed, Range reported that catalysts that had been "aged" through the addition of methanol as a co-feed with the syngas exhibited a sudden increase in dimethyl sulfide (DMS) as a product. The increased concentration of DMS as a product represents S loss from the catalyst.

The amount of sulfide present in selected Range Fuels catalysts at various points throughout the pellet was determined through XPS measurements (Table 3). The concentration of sulfide in freshly-activated samples 4-1 and 4-2 was found to be fairly consistent at about 20 atom% throughout the catalyst pellet.

In contrast, the concentration of the sulfide at the outside of sample 3-4 (methanol added) was much less at only 16.3 at%. Interestingly, the sulfide concentration was slightly higher in the interior of 3-4 at 18.6 at%. The decrease in sulfur present as sulfide at the exterior of the pellet suggested that the addition of the methanol to the reactant stream had resulted in the loss of sulfur from the catalyst.

Sample 9-1, which included methanol as well as H_2S in the reactant stream, exhibited a higher sulfide concentration compared to 4-1 and 4-2 at the pellet exterior of about 22 at%. It is also noteworthy to observe that sample 9-1 exhibited slightly lower sulfide concentrations at the interior of the pellet approximately on par with the 3-4 sample. One explanation for the radial change in sulfide concentration in sample 9-1 could be that gas does not efficiently diffuse throughout the pellet, resulting in mass transport limitations and an inefficient use of catalytic material.

High energy resolution XPS plots of the S 2p region were also suggestive of a change in the nature of the sulfide due to methanol aging. As shown in Figure 33 and Figure 34, the nature of the sulfide in sample 3-4 is different from the other samples illustrated. More specifically, the shoulder on the sulfide peak at approximately 162.5 eV is less pronounced in sample 3-4 than in the other samples. Chen et al.[20] attribute the 162.5 eV peak to S_2^{2-} S 2p electrons.

The interior measurement of sample 9-1, which exhibited lower sulfide concentration on par with that observed for sample 3-4, does exhibit the shoulder near 162.5 eV (see Figure 34(a)). Thus, a lower sulfide concentration does not directly correlate with a lack of S_2^{2-} functionality. The XPS evidence indicates that the characteristics of the sulfide present in the 3-4 sample are different from other samples, which strongly suggests its changed nature.

Characterization gave information about the location of the potassium modifier within the catalysts. In the preparation of K-promoted MoS_2 mixed alcohol synthesis catalysts, alternate potassium precursors have been reported to give contrasting effects.[14] Potassium added through the addition of K_2CO_3, KOH, and K_2S have been reported to separate from their anions and spread uniformly over a MoS_2 surface during catalyst activation. The uniform distribution of the K over the MoS_2 catalyst surface was reported to enhance alcohol selectivity. In contrast, K_2SO_4 and KCl maintained their chemical states and exhibited a non-uniform distribution on the MoS_2 surface.[14] The uneven spreading of the K resulted in an

enhanced selectivity for hydrocarbon growth over time with exposure to syngas. Thus, well-distributed K may be required in order to produce a selective mixed alcohol synthesis catalyst.

Table 11 presents a representative example from the work of Lee et al.[14] showing that when MoS_2 is doped with K_2CO_3, hydrocarbon selectivity greatly decreases and alcohol selectivity increases. Conversely, K segregation in a mixed alcohol catalyst would remove K from the active sites, leading to an increase in selectivity to hydrocarbons and a decrease in selectivity to alcohols.

Table 11. Representative literature example taken from Lee et al.[14] showing the effect of K doping on syngas conversion to hydrocarbons and alcohols.

Catalyst[1]	CO Conv.	% Sel HC	% Sel ROH	C_{2+}/C_1	
				HC	R-OH
MoS_2	35.3	99.2	0.8	0.72	0.00
K_2CO_3/MoS_2	8.4	38.8	61.2	0.25	0.70

[1]Conditions: 300°C, 220 psi, H_2/CO = 1.0 (K/Mo molar ratio = 0.4)

The RF-101 catalyst prepared and tested by Range Fuels and studied at PNNL were prepared with K_2CO_3. Range Fuels reported that the carbonate most likely decomposed during catalyst activation. In agreement with Lee et al.,[14] Range Fuels staff also reported that the K spread uniformly throughout the catalyst. SEM/EDS testing at PNNL of activated RF-101 (sample 4-1, Figure 4) confirmed that K appeared to be distributed evenly throughout the catalyst.

However, SEM/EDS evidence suggested that K segregated into the Bentolite® binder under mixed alcohol synthesis conditions. The Bentolite® was confirmed via XRD measurements to contain Montmorillonite clay (Figure 14), which has been reported to possess cation exchange abilities.[104] SEM/EDS analysis of sample 3-2 (Figure 6), which was on stream for 2,400 h, illustrates regions with a strong association of K with the Si and O in the binder. Based on the SEM/EDS evidence, it appears that the clay-based binder may, over time, become a K sink, which likely has a negative impact on the

performance of the catalyst. K segregation is likely a major cause of selectivity changes, especially in catalysts with very long time on stream.

Samples of other catalysts treated at shorter TOS under a variety of processing conditions do not show this strong association of K and silica. At the resolution of the instrumentation, K is not segregated and it appears to be evenly distributed across the catalysts. In these catalysts, although we do not know about accessibility of K to the active sites, it seems unlikely that the observed change in selectivity is a result of K segregation and immobilization. The presumption is that the K remains mobile, since its distribution appears to be the same as that attained upon activation.

In addition to the effect of the clay-based binder on the segregation of K, the addition of clay to K-Co-Mo-S mixed alcohol synthesis catalysts has been reported to increase hydrocarbon and CO_2 production at higher temperatures.[23]

The location and chemical nature of the Co in the catalytic samples was of particular interest throughout the current investigation. Co is added to the catalyst to enhance the alcohol formation activity as well as the formation of C_{2+} alcohols. Gang et al.[105] reported that Co addition to a carbon-supported K-MoS_2 catalyst (3:1 molar ratio Mo:Co) approximately doubled the alcohol activity while also increasing the selectivity of ethanol in the liquid product by nearly a factor of two (Table 12). Conversely, removal of Co from the active site of a KCoMoS catalyst, such as by segregation and clustering, is expected to decrease the yield of ethanol.

Table 12. Representative literature example showing the effect of Co doping of K-MoS_2 catalysts on syngas conversion to hydrocarbons and alcohols.[105]

Catalyst	g ROH/g cat•h	% HC (CO_2-free)	% ROH (CO_2-free)	wt% ROH	
				C_1	C_{2+}
K-MoS_2/C	0.12	15.0	85.0	50.2	17.8
Co-K-MoS_2/C	0.20	13.0	87.8	50.0	28.4

While the addition of Co is beneficial, the physical effect it has on the catalyst in the formation of active sites is unclear. Chianelli and Berhault[9] reported that Co and Mo sulfides are immiscible and, furthermore, under catalytic conditions, the metal sulfides are phase separated into the stable Co_9S_8 and MoS_2 phases. Lauritsen et al.[88] reported that Co was substituted for Mo atoms at edge sites on single-layer MoS_2 nanoclusters, as illustrated in Figure 82. The Co substitution at MoS_2 edges is most likely analogous to the "pseudo-intercalation" mechanism discussed by Chianelli and Berhault[9] to describe the CoMoS "phase" that is formed by Co at the edge of MoS_2. They also mention[9] that MoS_2 catalysts with a higher edge/surface ratio require a greater concentration of Co to maximize the CoMoS phase and reach maximum activity.

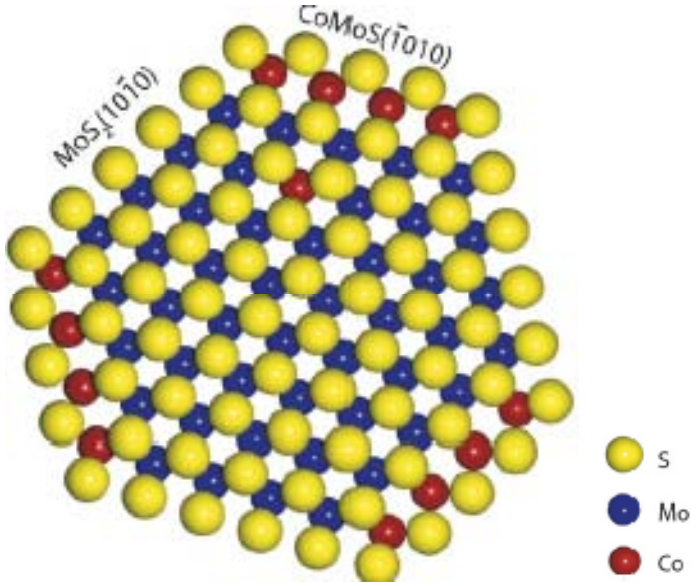

Figure 82. An illustrative representation of the CoMoS phase taken from Lauritzen et al.[88]

Co segregation removes Co from these edge sites, resulting in poor promotion and decreased activity. In addition, the segregated cobalt forms new phases that likely have different activities and selectivities to products. Cobalt clustering was observed in Range Fuels catalyst samples, which no doubt contributed to the observed change in selectivity from alcohols to methane.

Cobalt segregation occurred at short TOS, even in freshly activated catalysts. Whereas Co in the unactivated sample 3-1 was uniformly distributed, catalyst activation resulted in material containing

crystalline Co_9S_8 as detected by XRD. The size of these crystals was below the SEM detection threshold. In the SEM, the Co distribution appeared uniform and there was a strong correlation between Co and sulfur.

Co aggregates were present in all catalysts used for syngas conversion. At long TOS (4,200 h), Co clustering was especially apparent (Figure 6 and Figure 7). SEM could not identify the Co species present, but it did suggest that there were some species present that were not associated with sulfur and others that likely were associated with sulfur. Thus, comparing Figure 7(c) and Figure 7(e) it is apparent that there are regions with high Co concentrations that correspond to regions with low sulfur. A different view of the same catalyst in Figure 6 does not show this correspondence, suggesting that multiple Co species are likely present.

XRD spectra identified the nature of the crystalline Co species in the catalysts. Consistent with the multiple Co species observed with SEM/EDS, these species are primarily Co_9S_8 and Co_2C. Table 13 shows the distribution of these species across the pellet radius for each catalyst. Co_9S_8 forms during activation and is found throughout the pellet for all samples. It was difficult to detect in the 4,200 h samples, suggesting it may convert to other species.

Table 13. Mapping of the location of Co_2C and Co_9S_8 across the catalyst pellet radius by XRD.

	Co_2C			**Co_9S_8**		
Catalyst Sample	**Exterior**	**Mid**	**Center**	**Exterior**	**Mid**	**Center**
Unactivated	-	-	-	-	-	-
Activated, short TOS	-	-	-	+	+	+
MeOH co-feed	+	-	-	?	+	+
MeOH + H_2S	+	+	-	+	+	+
4,200h TOS	+	+	+	?	?	?

Key: + = positive ID; - = no evidence; ? = possibly present

In contrast, Co_2C did not form until the catalyst had been on line for about a week. The carbide appeared first at the catalyst surface and was not observed at the center of the pellets until about 4,200 h TOS, indicating that the center of the catalyst pellets did not participate to the same extent as the outer surface of the catalyst. The presence of 47 ppm H_2S in the feed apparently did not inhibit the formation of either Co_2C or Co_9S_8.

The formation of Co_9S_8 cannot explain the observed change in selectivity from alcohols to methane. Co_9S_8 is reported to be inactive for alcohol and hydrocarbon synthesis from syngas.[106] Co_2C is reported to be a good higher alcohol synthesis catalyst.[107, 108] In addition, it is also reported to be a poor Fischer-Tropsch catalyst.[109, 110] Therefore, the formation of Co_2C also may not explain the observed changes in selectivity. Sintering of Co to these crystalline species is likely related to long-term loss of activity. The formation of these species represents potential loss of Co from active sites and an inefficient use of metal.

Perhaps the largest probable contributor to the increasing methane selectivity is the formation of cobalt metal. Co metal is a good Fischer-Tropsch catalyst .[109, 110] Nano-particulate Co metal was identified in EPR spectra based on the observed superparamagnetic behavior in temperature-dependence experiments. This behavior and the signal line shape distinguished it from other potential species, such as Co_2C and Co_9S_8. Co metal was observed in catalysts used for syngas conversion, but not in the freshly activated catalyst (Figure 41). More Co metal was found at the exterior surface of the catalyst pellets than in the middle, again consistent with most of the conversion occurring at the pellet surface (Figure 46). In addition, the presence of 47 ppm H_2S did not inhibit formation of the metal (Figure 41).

Co metal was not observed in XRD spectra, indicating that sintering of the nanoparticles was slow relative to follow-on reactions, such as reaction with CO to form Co_2C[30] or reaction with H_2S to cobalt sulfides. Similarly, Lojacono et al.[58] observed that Co metal formed during reduction of cobalt oxides on alumina under flowing H_2/H_2S could be detected by EPR, but not by XRD, indicating that the Co metal particles were small, say less than 40Å.[53] The thermodynamically stable Co phase in the presence of even low concentrations of H_2S is reported to be Co_9S_8, not cobalt metal,[111-113] suggesting that its formation and conversion are dynamic processes.

The process forming cobalt metal is unknown. Co_2C can be reduced under H_2 to cobalt metal, but Co_2C is apparently a stable phase under syngas since it crystallizes to particles observable by XRD. Thermally, under H_2, CoS_2 is reduced to Co_3S_4 and on to Co_9S_8.[114] TPR studies[115] show that Co_9S_8 does not reduce below 500°C (Figure 83). The small reduction at 250°C is attributed to excess sulfur on the Co_9S_8 surface. It's unlikely that the higher H_2 pressure in the syngas reactor would decrease the reduction temperature to the operating temperature of 300°C.

It may be possible that an electrochemical reduction takes place. It is known that alkali metals can intercalate into the MoS_2 layers. Synthetically, this is accomplished by treating MoS_2 with a reducing agent such as butyl lithium. It can also be carried out electrochemically by making the MoS_2 a cathode in an alkali metal salt electrolyte. The intercalated metal has a binding energy more like the metal than the ion as shown in Table 14 for the lithium intercalate.

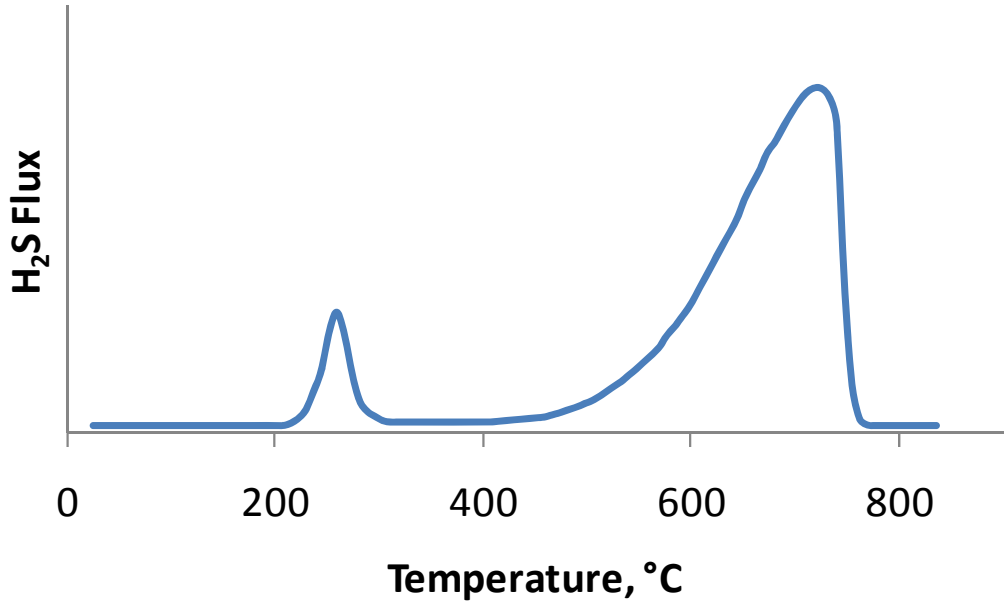

Figure 83. Temperature-programmed reduction pattern of Co_9S_8.[115]

Table 14. Binding energies for Li-intercalated MoS_2, Li metal, and LiCl.[117]

Species	Binding Energy (E_b), eV
$Li_{0.8}MoS_2$	55.6
Li metal	55.5
LiCl	58.1

Range Fuels has observed intercalation of potassium into MoS_2 in experiments using in situ XRD (Figure 84). The intercalation was only observed at temperatures above about 250°C in the presence of an effective alkali metal promoter and under an atmosphere of H_2 or H_2/CO. Intercalation did not occur under CO or N_2. H_2, therefore, appears to drive the intercalation. As for the lithium example above, the intercalated potassium is expected to be a strong reducing agent, similar to potassium metal.

The electrochemistry of cobalt sulfides is known[116] and the voltage-composition relationship for Li_xMoS_2 has been reported.[117] Therefore, a cell potential can be estimated for the reduction of Co_9S_8 to cobalt metal involving lithium intercalates.

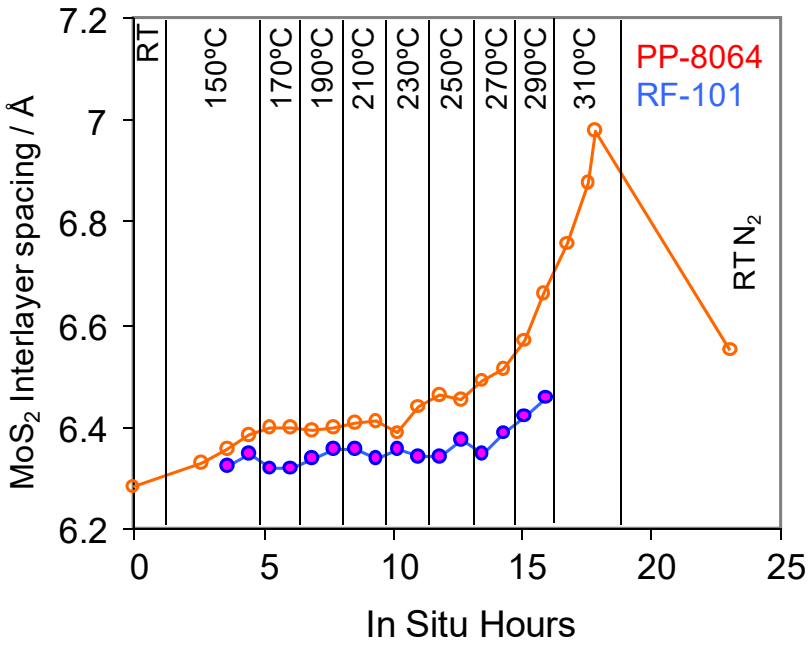

Figure 84. Expansion of the MoS_2 interlayer spacing caused by K intercalation.

A study of the electrochemistry of CoS_2 electrodes in molten LiCl-KCl (400°C) determined the following potentials versus the lithium electrode:

$3CoS_2 + 4Li \;<>\; Co_3S_4 + 2Li_2S$	1.398 V at 400°C	
$3Co_3S_4 + 8Li \;<>\; Co_9S_8 + 4Li_2S$	1.336 V at 400°C	
$Co_9S_8 + 16Li \;<>\; 9Co + 8Li_2S$	1.069 V at 400°C	Eq 1

From the Li_xMoS_2 voltage-composition curve (Figure 85) for x=0.8, a potential of -1V is estimated (at ambient temperature) according to the following equation:

$Li_{0.8}MoS_2 \;<>\; MoS_2 + 0.8Li$	~ -1V at ambient	Eq 2

Combining Eqs 1 and 2, a cell potential of 0.069 is estimated (Eq 3). Since E>0, and $\Delta G = -nFE$, then G<0, and the reaction is predicted to be favorable. Therefore, for lithium, the reduction of Co_9S_8 to metal is possible. Lithium (3.02 V) and potassium (2.92 V) have similar standard oxidation potentials, so it may also be possible for potassium to reduce Co_9S_8 to cobalt metal.

$Co_9S_8 + nLi_{0.8}MoS_2 \;<>\; 9Co + nMoS_2 + 8Li_2S$	~ 0.069 V	Eq 3

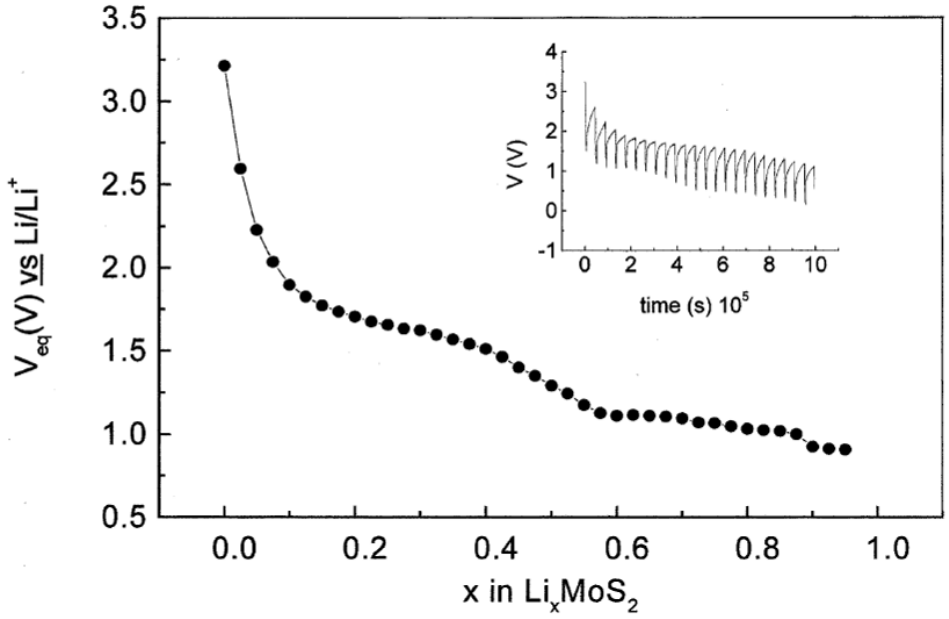

Figure 85. Li_xMoS_2 voltage-compositioncurve.[117]

The mechanism for the H_2-driven intercalation of potassium is unknown. However, it may be related to the presence of persulfide in these catalysts, which has been observed in XPS spectra (Figure 34). Our computational studies indicate that addition of potassium to a sulfur edge induces persulfide formation with internal redox shifting electron density to the molybdenum. Potassium can move further into the layers by coupled charge and ion transport (Figure 86). In addition, persulfide ligands can be hydrogenated to thiol groups under mild conditions.[118] Deprotonation by base and reformation of persulfide, induced by potassium ion, injects potassium into the layers. These steps are illustrated in Figure 87.

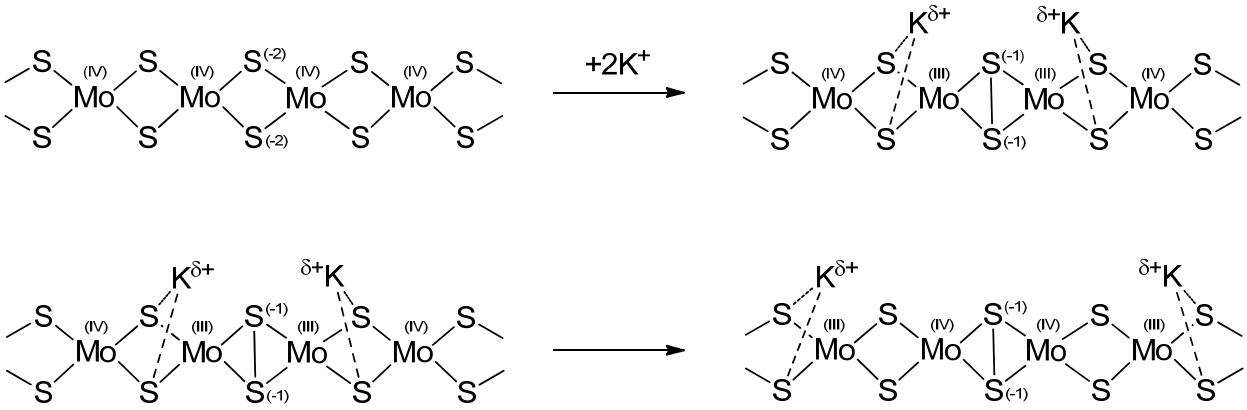

Figure 86. Potassium-induced persulfide formation and coupled transport

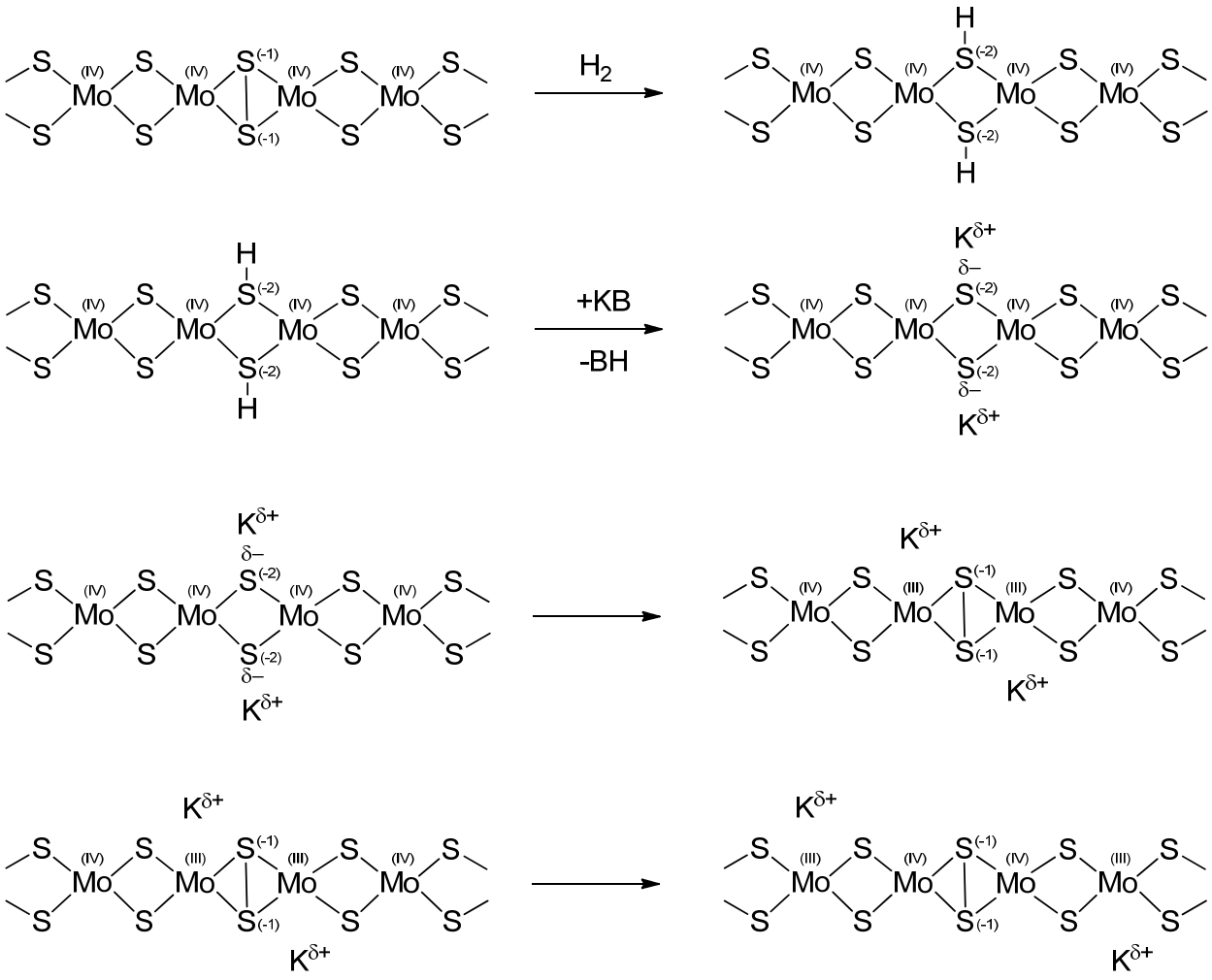

Figure 87. Possible mechanism for H_2-driven potassium intercalation into MoS_2.

5 Conclusions and Recommendations

This study identified modes of deactivation and selectivity change from alcohols to hydrocarbons for Range Fuel's K-Co-Mo-S higher alcohol synthesis catalyst. Undesirable K segregation into the catalyst binder likely increases hydrocarbon selectivity, especially for catalysts that have been on stream for a long time. Segregation of the Co promoter from the active site and clustering to other phases is expected to decrease the ethanol yield and decrease catalyst activity. The Co phases formed are inactive (Co_9S_8) or have different selectivities to products (Co_2C, Co(0)). The formation of cobalt metal is believed to be a major contributor to the increased selectivity to methane.

The catalyst composition and form may not be ideal. Only the exterior surface of the bulk catalyst appears to be used in the catalysis. This results in a lower activity than might otherwise be obtained and represents an inefficient use of expensive metal components in the catalyst. As mentioned, the cation-exchange material as a binder may decrease selectivity with time. Excess Co in the catalyst recipe forms Co_9S_8, one possible precursor to Co(0), a good Fischer-Tropsch catalyst.

Some steps could be taken to address the technical challenges of preventing promoter (K and Co) segregation, avoiding paths to cobalt metal, and using metals more efficiently, thereby improving the performance of the catalyst. A supported catalyst would use catalytic materials more efficiently and avoid early formation of Co_9S_8. Nearly all of the catalyst would be accessible to the syngas, minimizing the cost of materials per pound of product. Higher surface areas could be attained, increasing overall catalyst activity. Use of a binder other than Bentolite (or other cation exchange materials) could slow the loss of potassium from the active sites, thereby improving long-term activity and selectivity to ethanol. A surface-supported catalyst likely would not need a binder at all, further decreasing costs. Careful control of the Co:Mo ratio would minimize the formation of Co_9S_8 and would minimize metal costs. Minimization of Co_9S_8 formation may also decrease formation of cobalt metal, which would decrease hydrocarbon (methane) formation. Keeping the catalyst sulfided is also an important strategy that Range Fuels is already aware of. Finally, use of mono-layer MoS_2 in the catalyst preparations could reduce the amount of potassium that intercalates, thereby decreasing the amount of cobalt metal that forms.

Implementation of these recommendations could lead to higher and more stable catalyst activities, enhancing catalyst longevity. Selectivity to ethanol would also be stabilized and methane yields decreased. Catalyst costs per pound of ethanol could be decreased by more efficiently using expensive metal catalyst components and by increasing activity.

5.1 Subject Invention Derived Under the CRADA

One invention report was filed as a result of this work and disclosed to Range Fuels, Inc. on February 17, 2011:

- 17005-E, "Elimination of the Formation of Cobalt Metal in MoS2-based Higher Alcohol Synthesis Catalysts"

6 Definitions

DRIFTS	Diffuse Reflectance Infrared Fourier Transform Spectroscopy
EDS	Energy Dispersive Spectroscopy
EPR	Electron Paramagnetic Resonance
FTIR	Fourier Transform Infrared Spectroscopy
SEM	Scanning Electron Microscopy
TEM	Transmission Electron Microscopy
TPD	Temperature Programmed Desorption
TPR	Temperature Programmed Reduction
XPS	X-Ray Photoelectron Spectroscopy
XRD	X-Ray Diffraction

7 References

1. Afanasiev, P., Synthetic approaches to the molybdenum sulfide materials. *C. R. Chimie* **2008,** 11, 159-182.

2. Subramani, V.; Gangwal, S. K., A Review of Recent Literature to Search for an Efficient Catalytic Process for the Conversion of Syngas to Ethanol. *Energy & Fuels* **2008,** 22, 814-839.

3. Quarderer, Q. J.; Cochram, G. A. Catalytic process for producing mixed alcohols from hydrogen and carbon monoxide. September 1984, **1984**.

4. Jackson, G. R.; Mahajan, D. Method for production of mixed alcohols from synthesis gas. 6,248,796, June 19, 2001, **2001**.

5. Kinkade, N. E. Process for producing alcohols from carbon momoxide and hydrogen and carbon monoxide. July 1985, **1985**.

6. Kinkade, N. E. Tantalum-containing catalyst useful for producing alcohols from synthesis gas. 4,994,498, February 1991, **1991**.

7. Stevens, R. R. Process for producing alcohols from synthesis gas. 4,882,360, November 1989, **1989**.

8. Santiesteban, J. G.; Bogdan, C. E.; Herman, R. G.; Klier, K. In *Mechanism of C1-C4 Alcohol Synthesis Over Alkali/MoS_2 and Alkali/Co/MoS_2 Catalysts*, 9th International Congress of Catalysis, Ottawa, CA, 1988; Phillips, M. J.; Ternan, M., Eds. Calgary Chemical Institute of Canada: Ottawa, CA, 1988; pp 561-568.

9. Chianelli, R. R.; Berhault, G., Symmetrical synergism and the role of carbon in transition metal sulfide catalytic materials. *Catalysis Today* **1999,** 53, (3), 357-366.

10. Wivel, C.; Candia, R.; Clausen, B. S.; Mørup, S.; Topsøe, H., On the catalytic significance of a Co---Mo---S phase in Co---Mo/Al_2O_3 hydrodesulfurization catalysts: Combined in situ Mössbauer emission spectroscopy and activity studies. *Journal of Catalysis* **1981,** 68, (2), 453-463.

11. Surisetty, V. R.; Dalai, A. K.; Kozinski, J., Synthesis of higher alcohols from synthesis gas over Co-promoted alkali-modified MoS_2 catalysts supported on MWCNTs. *Applied Catalysis A: General* **2010,** 385, (1-2), 153-162.

12. Iranmahboob, J.; Toghiani, H.; Hill, D. O., Dispersion of alkali on the surface of Co-MoS_2/clay catalyst: a comparison of K and Cs as a promoter for synthesis of alcohol. *Applied Catalysis A: General* **2003,** 247, (2), 207-218.

13. Iranmahboob, J.; Hill, D. O.; Toghiani, H., Characterization of K_2CO_3/Co-MoS_2 catalyst by XRD, XPS, SEM, and EDS. *Applied Surface Science* **2001,** 185, (1-2), 72-78.

14. Lee, J. S.; Kim, S.; Lee, K. H.; Nam, I.-S.; Chung, J. S.; Kim, Y. G.; Woo, H. C., Role of alkali promoters in K/MoS_2 catalysts for CO-H_2 reactions. *Applied Catalysis A: General* **1994,** 110, (1), 11-25.

15. Lee, J. S.; Kim, S.; Kim, Y. G., Electronic and geometric effects of alkali promoters in CO hydrogenation over K/Mo_2C catalysts. *Topics in Catalysis* **1995,** 2, (1), 127-140.

16. Woo, H. C.; Nam, I.-S.; Lee, J. S.; Chung, J. S.; Lee, K. H.; Kim, Y. G., Room-temperature oxidation of K_2CO_3/MoS_2 catalysts and its effects on alcohol synthesis from CO and H_2. *Journal of Catalysis* **1992,** 138, (2), 525-535.

17. Woo, H. C.; Kirn, Y. G.; Nam, I.-S.; Chung, J. S.; Lee, J. S., Oxidized K_2CO_3/MoS_2 as a novel sulfur-resistant catalyst for Fischer-Tropsch reaction. *Catalysis Letters* **1993,** 20, (3), 221-229.

18. Xiao, H.; Li, D.; Li, W.; Sun, Y., Study of induction period over K_2CO_3/MoS_2 catalyst for higher alcohols synthesis. *Fuel Processing Technology* **2010,** 91, (4), 383-387.

19. Surisetty, V. R.; Tavasoli, A.; Dalai, A. K., Synthesis of higher alcohols from syngas over alkali promoted MoS_2 catalysts supported on multi-walled carbon nanotubes. *Applied Catalysis A: General* **2009,** 365, (2), 243-251.

20. Chen, A.; Wang, Q.; Li, Q.; Hao, Y.; Fang, W.; Yang, Y., Direct synthesis of methanethiol from H_2S-rich syngas over sulfided Mo-based catalysts. *Journal of Molecular Catalysis A: Chemical* **2008,** 283, (1-2), 69-76.

21. Xiang, M.; Li, D.; Li, W.; Zhong, B.; Sun, Y., Potassium and nickel doped beta-Mo_2C catalysts for mixed alcohols synthesis via syngas. *Catalysis Communications* **2007,** 8, (3), 513-518.

22. Santiesteban, J. G.; Bogdan, C. E.; Herman, R. G.; Klier, K. In *Mechanism of C_1-C_4 alcohol synthesis over alkali/MoS_2 and alkali/Co/MoS_2 catalysts.*, Proceedings of the 9th International Congress on Catalysis, 1988; Phillips, M. J.; Ternan, M., Eds. 1988; p 561.

23. Iranmahboob, J.; Toghiani, H.; Hill, D. O.; Nadim, F., The influence of clay on K_2CO_3/Co-MoS_2 catalyst in the production of higher alcohol fuel. *Fuel Processing Technology* **2002,** 79, (1), 71-75.

24. Yang, Y. Q.; Yuan, Y. Z.; Dai, S. J.; Wang, B.; Zhang, H. B., The catalytic properties of supported K_2MoS_4/SiO_2 catalyst for methanethiol synthesis from high H_2S-content syngas. *Catal. Lett.* **1998,** 54, 64-68.

25. Yang, Y. Q.; Yang, H.; Wang, Q.; Yu, L. J.; Wang, C.; Dai, S. J.; Yuan, Y. Z., Study of the supported K_2MoO_4 catalyst for methanethiol synthesis by on step from high H_2S-containing syngas. *Catalysis Letters* **2001,** 74, 221-225.

26. Lauritsen, J. V.; Kibsgaard, J.; Helveg, S.; Topsoe, H.; Clausen, B. S.; Laegsgaard, E.; Besenbacher, F., Size-dependent structure of MoS_2 nanocrystals. *Nat Nano* **2007,** 2, (1), 53-58.

27. Somoano, R. B.; Hadek, V.; Rembaum, A., Alkali metal intercalates of molybdenum disulfide. *J. Chem. Phys.* **1973,** 58, 697-701.

28. Zak, A.; Feldman, Y.; Lyakhovitskaya, V.; Leitus, G.; Popovitz-Biro, R.; Wachtel, E.; Cohen, H.; Reich, S.; Tenne, R., Alkali metal intercalated fullerene-like MS_2 (M = W, Mo) Nanoparticles and their properties. *J. Am. Chem. Soc.* **2002,** 124, 4747-4758.

29. Liu, X., Hydrothermal synthesis and characterization of nickel and cobalt sulfides nanocrystallines. *Materials Science and Engineering B* **2005,** 119, (1), 19-24.

30. Hofer, L. J. E.; Peebles, W. C., Preparation and X-Ray Diffraction Studies of a New Cobalt Carbide1. *Journal of the American Chemical Society* **1947,** 69, (4), 893-899.

31. Clarke, J.; Jack, K. H., The Preparation and the Crystal Structures of Cobalt Nitride, Co_2N of Cobalt Carbonitrides, $Co_2(C, N)$, and of Cobalt Carbide, Co_2C. *Chemistry and Industry* **1951,** 46, 1004.

32. Mazancova, E.; Mazanec, K., Contribution to the Physical Metallurgy Analysis of New High-Strength Mn Alloys. *Metal* **2007,** 22-24, (5), 1-8.

33. Goedecker, S.; Teter, M.; Hutter, J., Separable dual-space Gaussian pseudopotentials. *Physical Review B* **1996,** 54, (3), 1703.

34. Hartwigsen, C.; Goedecker, S.; Hutter, J., Relativistic separable dual-space Gaussian pseudopotentials from H to Rn. *Physical Review B* **1998,** 58, (7), 3641.

35. Krack, M., Pseudopotentials for H to Kr optimized for gradient-corrected exchange-correlation functionals. *Theoretical Chemistry Accounts: Theory, Computation, and Modeling (Theoretica Chimica Acta)* **2005,** 114, (1), 145-152.

36. VandeVondele, J.; Hutter, J., Gaussian basis sets for accurate calculations on molecular systems in gas and condensed phases. *J. Chem. Phys.* **2007,** 127, 114105.

37. Perdew, J. P.; Burke, K.; Ernzerhof, M., Generalized gradient approximation made simple. *Phys. Rev. Lett.* **1996,** 77, 3865.

38. Henkelman, G.; Arnaldsson, A.; Jónsson, H., A fast and robust algorithm for Bader decomposition of charge density. *Computational Materials Science* **2006,** 36, (3), 354-360.

39. Sanville, E.; Kenny, S. D.; Smith, R.; Henkelman, G., Improved grid-based algorithm for Bader charge allocation. *Journal of Computational Chemistry* **2007,** 28, (5), 899-908.

40. Tang, W.; et al., A grid-based Bader analysis algorithm without lattice bias. *Journal of Physics: Condensed Matter* **2009,** 21, (8), 084204.

41. Wilson, J. A.; Yoffe, A. D., The transition metal dichalcogenides discussion and interpretation of the observed optical, electrical and structural properties. *Adv. Phys.* **1969,** 18, 193-335.

42. Mattheiss, L. F., Band Structures of Transition-Metal-Dichalcogenide Layer Compounds. *Phys. Rev. B* **1973,** 8, 3719-3740.

43. Raybaud, P.; Hafner, J.; Kresse, G.; Kasztelan, S.; Toulhoat, H., Ab Initio study of the H_2-H_2S/MoS_2 gas-solid interface: the nature of the catalytically active sites. *J. Catal.* **2000,** 189, 129-146.

44. Vojvodic, A.; Hinnemann, B.; oslash; rskov, J. K., Magnetic edge states in MoS_2 characterized using density-functional theory. *Physical Review B* **2009,** 80, (12), 125416.

45. Zhang, J.; Soon, J. M.; Loh, K. P.; Yin, J.; Ding, J.; Sullivian, M. B.; Wu, P., Magnetic Molybdenum Disulfide Nanosheet Films. *Nano Letters* **2007,** 7, (8), 2370-2376.

46. Botello-Mendez, A. R.; et al., Metallic and ferromagnetic edges in molybdenum disulfide nanoribbons. *Nanotechnology* **2009,** 20, (32), 325703.

47. Chen, Y.; Chang, Y., Thermodynamics and phase relationships of transition metal-sulfur systems: I. The cobalt-sulfur system. *Metallurgical and Materials Transactions B* **1978,** 9, (1), 61-67.

48. Mao, R.; Xiao, S.; Si Le, T., Thermal stability of the Pt bearing sulfate-promoted zirconia in the presence of hydrogen. *Catalysis Letters* **1995,** 35, (1), 107-118.

49. Afanasiev, P., The influence of reducing and sulfiding conditions on the properties of unsupported MoS_2-based catalysts. *Journal of Catalysis* **2010,** 269, (2), 269-280.

50. Gandubert, A. D.; Legens, C.; Guillaume, D.; Rebours, S.; Payen, E., X-ray Photoelectron Spectroscopy Surface Quantification of Sulfided CoMoP Catalysts - Relation Between Activity and Promoted Sites - Part I: Influence of the Co/Mo Ratio. *Oil & Gas Science and Technology - Rev. IFP* **2007,** 62, (1), 79-89.

51. Lebugle, A.; et al., Experimental L and M Core Level Binding Energies for the Metals 22 Ti to 30 Zn. *Physica Scripta* **1981,** 23, (5A), 825.

52. Wang, H.; Wong, S. P.; Cheung, W. Y.; Ke, N.; Wen, G. H.; Zhang, X. X.; Kwok, R. W. M., Magnetic properties and structure evolution of amorphous Co--C nanocomposite films prepared by pulsed filtered vacuum arc deposition. *Journal of Applied Physics* **2000,** 88, (8), 4919-4921.

53. Ramaswamy, A. V.; Sivasanker, S.; Ratnasamy, P., Interaction between Active Components and Support in Co-Mo-Al_2O_3 System .3. Magnetic and Electron-Spin Resonance Spectroscopic Study of Influence of Sodium on Nature of Cobalt. *Journal of Catalysis* **1976,** 42, (1), 107-114.

54. Shchukarev, A.; Korolkov, D., XPS Study of group IA carbonates. *Central European Journal of Chemistry* **2004,** 2, (2), 347-362.

55. Jerome, R.; Teyssie, P.; Pireaux, J. J.; Verbist, J. J., Surface analysis of polymers end-capped with metal carboxylates using x-ray photoelectron spectroscopy. *Applied Surface Science* **1986,** 27, (1), 93-105.

56. Derouane, E. G.; Pedersen, E.; Clausen, B. S.; Gabelica, Z.; Topsoe, H., Electron-Paramagnetic-Res Studies on the Influence of No Adsorption on Sulfided Co-Mo Hydrodesulfurization Catalysts. *Journal of Catalysis* **1987,** 107, (2), 587-588.

57. Woo, S. I.; Kim, S. I.; Kim, C. H., Characterization of hydrodesulfurization catalyst prepared by impregnating cobalt nitrate solution onto the sulfided MoO_3/Al_2O_3 catalyst. *Korean Journal of Chemical Engineering* **1995,** 12, (5), 497-502.

58. Lojacono, M.; Verbeek, J. L.; Schuit, G. C. A., Magnetic and Spectroscopic Investigations on Cobalt-Alumina and Cobalt-Molybdenum-Alumina - Electron-Spin Resonance of Oxidized, Sulfided, and Reduced Catalysts. *Journal of Catalysis* **1973,** 29, (3), 463-474.

59. Bhaduri, M.; Mitchell, P. C. H., The Effect of Treatment with Triethylaluminum on the Hydrogenation and Hydrodesulfurization Activity of Molybdenum, Cobalt, and Nickel Sulfide Catalysts. *Journal of Catalysis* **1982,** 77, (1), 132-140.

60. Gajardo, P.; Mathieux, A.; Grange, P.; Delmon, B., Structure and Catalytic Activity of $CoMo/\gamma\text{-}Al_2O_3$ and $CoMo/SiO_2$ Hydrodesulfurization Catalysts - an XPS and Electron-Spin-Resonance Characterization of Sulfided Used Catalysts. *Applied Catalysis* **1982,** 3, (4), 347-376.

61. Derouane, E. G.; Pedersen, E.; Clausen, B. S.; Gabelica, Z.; Candia, R.; Topsoe, H., Electron-Paramagnetic-Res Studies on Unsupported and Alumina-Supported Sulfided Co Mo Hydrodesulfurization Catalysts. *Journal of Catalysis* **1986,** 99, (2), 253-261.

62. Seshadri, K. S.; Massoth, F. E.; Petrakis, L., Electron Spin Resonance and Microbalance Study of Sulfided Molybdena-Alumina Catalysts. *Journal of Catalysis* **1970,** 19, (2), 95-&.

63. Silbernagel, B. G.; Pecoraro, T. A.; Chianelli, R. R., Electron-Spin Resonance of Supported and Unsupported Molybdenum Hydrotreating Catalysts .1. Model System Studies. *Journal of Catalysis* **1982,** 78, (2), 380-388.

64. Konings, A. J. A.; Valster, A.; Debeer, V. H. J.; Prins, R., Hydrodesulfurization Catalysts Prepared from $X(MS_4)_2^{(2-)}$ Thioheteroanions Containing Ni or Co and Mo or W - Correlation of Electron-Spin-Resonance Signal Intensity with Thiophene Conversion. *Journal of Catalysis* **1982,** 76, (2), 466-472.

65. Oliver, S. W.; Smith, T. D.; Pilbrow, J. R.; Pratt, K. C.; Christov, V., An Electron-Spin Resonance Study of the Catalyzed Hydrodesulfurization of Thiophene Using Sulfided Molybdenum Oxide on a Zirconia Support. *Journal of Catalysis* **1988,** 111, (1), 88-93.

66. Hagenbach, G.; Menguy, P.; Delmon, B., Presentation of Electronic Paramagnetic Resonance Signal Connecge)) Presentation of Electronic Paramagnetic Resonance Signal Connected to Maxima of Various Catalytic Activities of Masses Composed of Cobalt and Molybdenum Sulfides. *Comptes Rendus Hebdomadaires Des Seances De L Academie Des Sciences Serie C* **1971,** 273, (19), 1220-&.

67. Woo, H. C.; Kim, J. C.; Nam, I.-S.; Lee, J. S.; Chung, J. S.; Kim, Y. G., Surface species on the oxidized K_2CO_3/MoS_2 and their effects on catalytic carbon monoxide hydrogenation. *Applied Catalysis A: General* **1993,** 104, (2), 199-214.

68. Hornés, A.; Bera, P.; Cámara, A. L.; Gamarra, D.; Munuera, G.; Martínez-Arias, A., CO-TPR-DRIFTS-MS in situ study of $CuO/Ce_{1-x}Tb_xO_{2-y}$ (x = 0, 0.2 and 0.5) catalysts: Support effects on redox properties and CO oxidation catalysis. *Journal of Catalysis* **2009,** 268, (2), 367-375.

69. Toops, T. J.; Crocker, M., New sulfur adsorbents derived from layered double hydroxides: II. DRIFTS study of COS and H_2S adsorption. *Applied Catalysis B: Environmental* **2008,** 82, (3-4), 199-207.

70. Amenomiya, Y., Active sites of solid acidic catalysts : III. Infrared study of the water gas conversion reaction on alumina. *Journal of Catalysis* **1979,** 57, (1), 64-71.

71. Koizumi, N.; Bian, G.; Murai, K.; Ozaki, T.; Yamada, M., In situ DRIFT studies of sulfided K-Mo/γ-Al_2O_3 catalysts. *Journal of Molecular Catalysis A: Chemical* **2004,** 207, (2), 173-182.

72. Nakamura, J.; Toyoshima, I.; Tanaka, K.-i., Formation of carbidic and graphite carbon from CO on polycrystalline cobalt. *Surface Science* **1988,** 201, (1-2), 185-194.

73. Du, X.; Dong, L.; Li, C.; Liang, Y.; Chen, Y., Diffuse Reflectance Infrared Fourier Transform and Raman Spectroscopic Studies of MoO_3 Dispersed on CeO_2 Support. *Langmuir* **1999,** 15, (5), 1693-1697.

74. Aoshima, A.; Wise, H., Hydrodesulfurization Activity and Electronic Properties of Molybdenum Sulfide Catalyst. *Journal of Catalysis* **1974,** 34, (1), 145-151.

75. Dianis, W. P., Characterization of metal sulfide Fischer-Tropsch catalysts by temperature programmed desorption. *Applied Catalysis* **1987,** 30, (1), 99-121.

76. Zintl, E.; Harder, A.; Dauth, B., Gitterstruktur der Oxyde, Sulfide, Selenide und Telluride des Lithiums, Natriums und Kaliums. *Z. Elektrochem.* **1934,** 40, (8), 588-593.

77. Papageorgopoulos, C. A.; Kamaratos, M.; Kennou, S.; Vlachos, D., The behavior of K on the basal plane of MoS_2. *Surface Science* **1991,** 251-252, 1057-1061.

78. Papageorgopoulos, C.; Kamaratos, M.; Kennou, S.; Vlachos, D., Coadsorption of K and O_2 on MoS_2(0001). *Surface Science* **1992,** 277, (3), 273-281.

79. Kamaratos, M.; et al., Potassium adsorption on MoS_2 (0001) at low temperature. *Journal of Physics: Condensed Matter* **1993,** 5, (5), 535.

80. Park, K. T.; Kong, J., Chemistry and Physics of Alkali Metals on MoS_2 Surfaces. *Topics in Catalysis* **2002,** 18, (3), 175-181.

81. Park, K. T.; Kong, J.; Klier, K., Angle-Resolved X-ray Photoelectron Spectroscopy of in Situ Deposited Li on MoS_2(0002). *The Journal of Physical Chemistry B* **2000,** 104, (14), 3145-3154.

82. Park, K. T.; Richards-Babb, M.; Freund, M. S.; Weiss, J.; Klier, K., Surface Structure of Single-Crystal MoS_2(0002) and Cs/MoS_2(0002) by X-ray Photoelectron Diffraction. *The Journal of Physical Chemistry* **1996,** 100, (25), 10739-10745.

83. Alexiev, V.; Prins, R.; Weber, T., Ab initio study of MoS_2 and Li adsorbed on the (1010) face of MoS_2. *Phys. Chem. Chem. Phys.* **2000,** 2, 1815-1827.

84. Henkelman, G.; Uberuaga, B. P.; Jonsson, H., A climbing image nudged elastic band method for finding saddle points and minimum energy paths. *J. Chem. Phys.* **2000,** 113, (22), 9901-9904.

85. Raybaud, P.; Hafner, J.; Kresse, G.; Toulhoat, H., Structural and electronic properties of the MoS_2(1010) edge-surface. *Surface Science* **1998,** 407, (1-3), 237-250.

86. Helveg, S.; Lauritsen, J. V.; Lægsgaard, E.; Stensgaard, I.; Norskov, J. K.; Clausen, B. S.; Topsøe, H.; Besenbacher, F., Atomic-Scale Structure of Single-Layer MoS_2 Nanoclusters. *Phys. Rev. Lett.* **2000,** 84, 951-954.

87. Bollinger, M. V.; Lauritsen, J. V.; Jacobsen, K. W.; oslash; rskov, J. K.; Helveg, S.; Besenbacher, F., One-Dimensional Metallic Edge States in MoS_2. *Physical Review Letters* **2001,** 87, (19), 196803.

88. Lauritsen, J. V.; Kibsgaard, J.; Olesen, G. H.; Moses, P. G.; Hinnemann, B.; Helveg, S.; Nørskov, J. K.; Clausen, B. S.; Topsøe, H.; Lægsgaard, E.; Besenbacher, F., Location and coordination of promoter atoms in Co- and Ni-promoted MoS_2-based hydrotreating catalysts. *Journal of Catalysis* **2007,** 249, (2), 220-233.

89. Liu, Z. P.; Hu, P., An insight into alkali promotion: a density functional theory study of CO dissociation on K/Rh(111). *J. Am. Chem. Soc.* **2001,** 123, 12596-12604.

90. Parker, L. J.; Atou, T.; Badding, J. V., Transition Element-Like Chemistry for Potassium Under Pressure. *Science* **1996,** 273, 95-97.

91. Atou, T.; Hasegawa, M.; Parker, L. J.; Badding, J. V., Unusual Chemical Behavior for Potassium under Pressure: Potassium-Silver Compounds. *J. Am. Chem. Soc.* **1996,** 118, 12104-12108.

92. Somoano, R. B.; Rembaum, A., Superconductivity in intercalated molybdenum disulfide. *Phys. Rev. Lett.* **1971,** 27, 402-404.

93. Woollam, J. A.; Somoano, R. B., Superconducting critical fields of alkali and alkaline-earth intercalates of MoS_2. *Phys. Rev. B* **1976,** 13, 3843-3853.

94. Papageorgopoulos, C. A., Adsorption of Cs and O_2 on MoS_2 *Surf. Sci.* **1978,** 75, 17-28.

95. Lamoen, D.; Persson, B. N. J., Adsorption of potassium and oxygen on graphite: A theoretical study. *J. Chem. Phys.* **1998,** 108, 3332-3341.

96. Lou, L.; Österlund, L.; Hellsing, B., Electronic structure and kinetics of K on graphite. *J. Chem. Phys.* **2000,** 112, 4788-4796.

97. Christensen, J. M.; Mortensen, P. M.; Trane, R.; Jensen, P. A.; Jensen, A. D., Effects of H_2S and process conditions in the synthesis of mixed alcohols from syngas over alkali promoted cobalt-molybdenum sulfide. *Applied Catalysis A: General* **2009,** 366, (1), 29-43.

98. Crowell, J. E.; Somorjai, G. A., The Effect of Potassium on the Chemisorption of Carbon Monoxide on the Rh(111) Crystal Face. *Applications of Surface Science* **1984,** 19, 73391.

99. Hagen, J., *Industrial Catalysis: a Practical Approach*. Wiley: 1999.

100. Youchang, X.; Naasz, B. M.; Somorjai, G. A., Alcohol Synthesis from CO and H_2 over Molybdenum sulfide. The Effect of Pressure and Promotion by Potassium Carbonate. *Appl. Catal.* **1986,** 27, 233-241.

101. Sierraalta, A.; Herize, A.; Añez, R., Interaction of H_2S with the X/MoS_2 Surface (X=Zn, Cu, Ni, Co). A Theoretical Study. *J. Phys. Chem. A* **2001,** 105, 6519–6525.

102. Krebs, E.; Daudin, A.; Raybaud, P., A DFT study of CoMoS and NiMoS catalysts from Nano-crystallite morphology to selective hydrodesulfurization. *Oil & Gas Science and Technology - Rev. IFP* **2009,** 64, (6), 707-718.

103. Yoshimura, Y.; Shimada, H.; Sato, T.; Kubota, M.; Nishijima, A., Initial Catalyst Deactivation in the Hydrotreatment of Coal Liquid over Ni-Mo and Co-Mo-Gamma-Al_2O_3 Catalysts. *Applied Catalysis* **1987,** 29, (1), 125-140.

104. Crooks, J. E.; El-Daly, H.; El-Sheikh, M. Y.; Habib, A.-F. M.; Zaki, A. B., Kinetics of ion-exchange on montmorillonite clays. *International Journal of Chemical Kinetics* **1993,** 25, (3), 161-168.

105. Gang, L.; Chengfang, Z.; Yanqing, C.; Zhibin, Z.; Yianhui, N.; Linjun, C.; Fong, Y., Synthesis of mixed alcohols from CO_2 contained syngas on supported molybdenum sulfide catalysts. *Applied Catalysis A: General* **1997,** 150, (2), 243-252.

106. Li, Z.; Fu, Y.; Bao, J.; Jiang, M.; Hu, T.; Liu, T.; Xie, Y.-n., Effect of cobalt promoter on Co-Mo-K/C catalysts used for mixed alcohol synthesis. *Applied Catalysis A: General* **2001,** 220, (1-2), 21-30.

107. Volkova, G. G.; Yurieva, T. M.; Plyasova, L. M.; Naumova, M. I.; Zaikovskii, V. I., Role of the Cu-Co alloy and cobalt carbide in higher alcohol synthesis. *Journal of Molecular Catalysis A: Chemical* **2000,** 158, (1), 389-393.

108. Jiao, G.; Ding, Y.; Zhu, H.; Li, X.; Dong, W.; Li, J.; LÜ, Y., Effect of the Reduction Temperature of Co-La-Zr/AC on the Synthesis of Higher Alcohols from Syngas. *Chinese J Catal* **2009,** 30, (2), 92-94.

109. Khodakov, A. Y.; Chu, W.; Fongarland, P., Advances in the Development of Novel Cobalt Fischer-Tropsch Catalysts for Synthesis of Long-Chain Hydrocarbons and Clean Fuels. *Chemical Reviews* **2007,** 107, (5), 1692-1744.

110. Ducreux, O.; Rebours, B.; Lynch, J.; Roy-Auberger, M.; Bazin, D., Microstructure of supported cobalt Fischer-Tropsch catalysts. *Oil & Gas Science and Technology - Rev. IFP* **2009,** 64, (1), 49-62.

111. Hoodless, R. C.; Moyes, R. B.; Wells, P. B., D-tracer study of butadiene hydrogenation and tetrahydrothiophen hydrodesulphurisation catalysed by Co_9S_8. *Catalysis Today* **2006,** 114, (4), 377-382.

112. Castner, D. G.; Watson, P. R., X-ray absorption spectroscopy and x-ray photoelectron spectroscopy studies of cobalt catalysts. 3. Sulfidation properties in hydrogen sulfide/hydrogen. *The Journal of Physical Chemistry* **1991,** 95, (17), 6617-6623.

113. Richardson, J. T., Magnetic Study of Cobalt Molybdenum Oxide Catalysts. *Industrial & Engineering Chemistry Fundamentals* **1964,** 3, (2), 154-158.

114. Iranmahboob, J.; Hill, D. O., Alcohol Synthesis from Syngas over K_2CO_3/CoS/MoS_2 on Activated Carbon. *Catalysis Letters* **2002,** 78, (1), 49-55.

115. Bezverkhyy, I.; Danot, M.; Afanasiev, P., New Low-Temperature Preparations of Some Simple and Mixed Co and Ni Dispersed Sulfides and Their Chemical Behavior in Reducing Atmosphere. *Inorganic Chemistry* **2003,** 42, (5), 1764-1768.

116. Preto, S. K.; Tomczuk, Z.; von Winbush, S.; Roche, M. F., Reactions of FeS_2, CoS_2, and NiS_2 Electrodes in Molten LiCl-KCl Electrolytes. *Journal of The Electrochemical Society* **1983,** 130, (2), 264-273.

117. Benavente, E.; Santa Ana, M. A.; Mendizábal, F.; González, G., Intercalation chemistry of molybdenum disulfide. *Coordination Chemistry Reviews* **2002,** 224, (1-2), 87-109.

118. Byskov, L. S.; Bollinger, M.; Nørskov, J. K.; Clausen, B. S.; Topsøe, H., Molecular aspects of the H2 activation on MoS_2 based catalysts -- the role of dynamic surface arrangements. *Journal of Molecular Catalysis A: Chemical* **2000,** 163, (1-2), 117-122.